

043810-F

N 7 2 - 2 5 6 8 3

THE UNIVERSITY OF MICHIGAN

**COLLEGE OF ENGINEERING
DEPARTMENT OF NUCLEAR ENGINEERING**

Final Report

Niobium Hyperfine Structure in Crystal Calcium Tungstate

**CASE FILE
COPY**

**DER LING TSENG
CHIHIRO KIKUCHI**

Under Contract with:

**National Aeronautics and Space Administration
Grant No. NGR 23-005-004
Washington, D. C.**

Administered through:

April 1972

OFFICE OF RESEARCH ADMINISTRATION • ANN ARBOR

THE UNIVERSITY OF MICHIGAN

COLLEGE OF ENGINEERING
Department of Nuclear Engineering

Final Report

NIOBIUM HYPERFINE STRUCTURE IN
CRYSTAL CALCIUM TUNGSTATE

Der Ling Tseng
Chihiro Kikuchi

ORA Project 043810

supported by:

NATIONAL AERONAUTICS AND SPACE ADMINISTRATION
Grant No. NGR-23-005-004
WASHINGTON, D.C.

administered through:

OFFICE OF RESEARCH ADMINISTRATION ANN ARBOR

April 1972

ABSTRACT

A study of the niobium hyperfine structure in single crystal calcium tungstate has been made by the combination of the technique of electron paramagnetic resonance and electron nuclear double resonance (EPR/ENDOR). The microwave frequency was about 9.4 GHz and the radio frequency from 20 MHz to 70 MHz. The rare earth ions Nd^{3+} , U^{3+} , or Tm^{3+} were added as the charge compensator for Nb^{5+} .

To create niobium paramagnetic centers, the sample was irradiated at 77°K with a 10 thousand curie Co-60 gamma source for 1 to 2 hours at a dose rate of 200 K rads per hour and then transferred quickly into the cavity.

In a general direction of magnetic field, the spectra showed 4 sets of 10 main lines corresponding to 4 non-equivalent sites of niobium with $I = 9/2$. These 4 sets of lines coalesced into 2 sets of 10 in the ab-plane and into a single set of 10 along the c-axis. This symmetry suggested that the tungsten ions are substituted by the niobium ions in the crystal. Secondary lines arising from forbidden transitions were also observed. The variation of the intensities of the allowed and forbidden spectra revealed the dominance of the quadrupole interaction. The vanishing of the forbidden doublets along particular directions suggested the principal axes of quadrupole interaction. The separations of the forbidden doublets indicate that the hyperfine structure constant A and the quadrupole coupling constant Q_z have the same sign. The

magnitude and direction of the principal values of g -, A -, q - and g_n - tensors were evaluated to be

	θ	ϕ
$g_x = 2.0133 \pm .0028$	28°	208°
$g_y = 2.0077 \pm .0002$	90°	-62°
$g_z = 2.0534 \pm .0010$	62°	28°
$A_x = 81.0 \pm 0.9$ MHz	27.5°	225°
$A_y = 75.2 \pm 1.2$ MHz	90°	-45°
$A_z = 88.4 \pm 1.4$ MHz	62.5°	45°
$Q_x = -0.561 \pm .023$ MHz	57°	225°
$Q_y = -0.835 \pm .025$ MHz	90°	-45°
$Q_z = +1.392 \pm .050$ MHz	33°	45°
$g_n = 1.366 \pm .036$	--	--

From these experimental results, arguments lead to the tentative charge compensation scheme of a Nb^{5+} ion substituting for a W^{6+} ion at the center of the unit cell of $CaWO_4$ coupled to an impurity located at one of these corners of the same unit cell.

ACKNOWLEDGMENTS

It is the pleasure of the author to thank Professor Chihiro Kikuchi for his initiation of this research, his continued guidance throughout the course of the work, as well as his patience in polishing the language used in this dissertation.

His sincere appreciation is extended to Dr. David R. Mason for his tireless advice in the experimental work, computer calculation and part of the wording of Chapters IV and V.

He would also like to express his deep gratitude to Dr. Robert H. Borcherts for his enthusiastic assistance in setting up the ENDOR network, and his valuable suggestion in working out the energy level formula.

He especially wishes to thank Dr. Keh-Chang Chu for his constant help and interesting discussions during the course of experimental work.

Many thanks are due to Mr. Chao-Yang Huang for the courtesy of his unpublished angular variation plots: Figs. 24 and 25.

The technical and administrative assistance provided by the entire staff of the Phoenix Memorial Laboratory are deeply appreciated.

He is indebted to Dr. Inan Chen and Dr. Nasser Mahootian for their kind help when they were with the University of Michigan.

The financial assistance provided by the Andrew A. Kucher Scholarship in Nuclear Engineering is gratefully acknowledged.

Acknowledgments are extended to National Tsing Hua University, Taiwan, China, as well as Agency for International Development, Washington, D.C./C.M. for their financial support provided in the early stages of this study, and their willing cooperation throughout the work.

Finally, the most heartfelt gratitude is due to his family in Taiwan, China, especially his wife Wei-Lang. Without their patience and continuous encouragement, this thesis would not be possible.

TABLE OF CONTENTS

	Page
ACKNOWLEDGMENTS.....	ii
LIST OF FIGURES.....	vii
LIST OF TABLES.....	x
 Chapter	
I. INTRODUCTION.....	1
II. SPIN HAMILTONIAN.....	5
A. Derivation of Spin Hamiltonian.....	5
B. General Discussion of the Spin Hamiltonian.....	11
III. FORMULATION OF EPR AND ENDOR MEASUREMENTS.....	16
A. Energy Levels.....	16
1. Spin Hamiltonian Expressed in the g-Tensor Principal Axis System.....	16
2. Quadrupole Dominated Hamiltonian.....	20
B. EPR Signal.....	24
1. g-value.....	24
2. A-value.....	25
C. Forbidden EPR System.....	26
1. Position of EPR Forbidden Lines.....	33
2. Relative Intensity of Allowed EPR Lines.....	35
IV. ELECTRON NUCLEAR DOUBLE RESONANCE.....	39
A. Qualitative Description.....	39
B. ENDOR Signal.....	43
C. The Assumption of Negative A-Value.....	49
V. EXPERIMENTAL SETUP.....	53

Chapter	Page
A. EPR Spectrometer.....	53
B. The ENDOR Arrangement.....	57
1. The Signal Generator.....	57
2. The Voltage Amplifier.....	58
3. The Power Amplifier.....	58
4. The Cavity.....	59
C. The Sample.....	62
D. Operation Procedure.....	64
1. EPR Measurement.....	64
2. ENDOR Measurement.....	64
VI. EXPERIMENTAL RESULTS.....	72
A. EPR.....	72
1. Samples.....	72
2. Spectra.....	72
3. Data Analysis.....	74
a. Determination of g- and A- Tensor Principal Axes.....	74
b. g- and A- Values.....	75
c. Adjacent HF line Separation.....	77
d. Fit of the g^2 - Equation.....	78
e. Q_{33} and g_n from forbidden doublets.....	78
B. ENDOR.....	108
1. ENDOR Frequency Identification.....	108
2. ENDOR Frequency Plot.....	109
3. Quadrupole Principal Axes and Values.....	111
4. Nuclear g-Value.....	113
5. The A-value.....	113
VII. DISCUSSION AND CONCLUSION.....	142
A. Various Charge Compensators.....	142
B. Temperature Effect.....	142
C. Sign of A and Q.....	143
D. Field Gradient of Nb ⁴⁺ Site.....	144

Chapter	Page
E. Orientation of Z_g , Z_A and Z_Q Axes.....	147
F. Conclusion.....	148
APPENDICES.....	153
A. Derivation of Energy Level Formula.....	153
1. Zeeman Term.....	156
2. Hyperfine Term.....	161
3. Quadrupole Term.....	171
4. Nuclear Zeeman Term.....	176
5. Summary.....	179
B. Relation Between Principal Coordinates and Crystal Symmetry Coordinates.....	179
REFERENCES.....	184

LIST OF FIGURES

Figure	Page
1. A composite spectrum of allowed and forbidden EPR lines showing the relative line intensities and line positions.....	38
2. Spin population for thermal equilibrium and partially saturated cases.....	42
3. Magnet and Dewar System.....	56
4. Details of a Lava cavity and the magnetic field of mode TE_{011}	60
5. Cavity system of ENDOR experiments.....	67
6. A unit cell of $CaWO_4$	68
7. a) WO_4^{--} tetrahedron, b) Projection of WO_4^{--} on the ab-plane.....	69
8. Laue picture of c-axis.....	70
9. Laue picture of a-axis.....	70
10. Block diagram of the EPR/ENDOR system.....	71
11. Spectrum a) along c-axis.....	81
12. Spectrum b) along a-axis.....	82
13. Spectrum c) along Z_g -axis.....	83
14. Spectrum d) along Y_Q or Y_A -axis; $\langle 110 \rangle$ direction...	84
15. Spectrum e) along Z_Q -axis.....	85
16. Spectrum f) ENDOR pattern, c-axis, $m = +\frac{1}{2}$	86
17. Separation of Forbidden Doublets along c-axis.....	87
18. g' -value, angular variation in ab-plane.....	88

Figure	Page
19. A'-value, angular variation in ab-plane.....	89
20. g'-value, angular variation in ac-plane.....	90
21. A'-value, angular variation in ac-plane.....	91
22. g'-value, angular variation in d-plane (28°).....	92
23. A'-value, angular variation in d-plane (28°).....	93
24. g'-value, angular variation in (110)-plane.....	94
25. A'-value, angular variation in (110)-plane.....	95
26. g-value vs. m (i) d-plane (28°).....	96
27. g-value vs. m (ii) (110)-plane.....	97
28. Adjacent line separation, c-axis.....	98
29. Fit of g^2 -Equation.....	99
30. A-value vs. m, c-axis.....	101
31. A-value vs. m, X_g -axis.....	102
32. A-value vs. m, Y_g -axis.....	103
33. A-value vs. m, Z_g -axis.....	104
34. A-value vs. m, X_Q -axis.....	105
35. A-value vs. m, Y_Q -axis.....	106
36. A-value vs. m, Z_Q -axis.....	107
37a. ENDOR Frequency Identification.....	121
37b. Idealized Energy Level Diagram.....	122
38. ENDOR frequency vs. m, X_Q -axis.....	123
39. ENDOR frequency vs. m, Y_Q -axis.....	124
40. ENDOR frequency vs. m, Z_Q -axis.....	125
41. ENDOR frequency vs. m, c-axis.....	126
42. ENDOR frequency vs. m, X_g -axis.....	127

Figure	Page
43. ENDOR frequency vs. m , Y_g -axis.....	128
44. ENDOR frequency vs. m , Z_g -axis.....	129
45. Quadrupole coupling constants vs. m , X_Q -axis.....	130
46. Quadrupole coupling constants vs. m , Y_Q -axis.....	131
47. Quadrupole coupling constants vs. m , Z_Q -axis.....	132
48. Quadrupole coupling constants vs. m , c-axis.....	133
49. Quadrupole coupling constants vs. m , X_g -axis.....	134
50. Quadrupole coupling constants vs. m , Y_g -axis.....	135
51. Quadrupole coupling constants vs. m , Z_g -axis.....	136
52. g_n vs. m , X_Q -axis.....	137
53. g_n vs. m , Y_Q -axis.....	138
54. g_n vs. m , Z_Q -axis.....	139
55. g_n vs. m , c-axis.....	140
56. A vs. m , measured by ENDOR along the principal axes of quadrupole.....	141
57. Three cones confining the X, Y, and Z axes of g-, A- and Q- tensors.....	151
58. (110) plane of crystal $CaWO_4$ showing the principal axes of Q in relation to the W ion to be substituted by the compensator ion Nd^{3+}	152

LIST OF TABLES

Table	Page
1. Principal values of A and g.....	80
2. g^2 versus $\cos^2 \textcircled{H}$	100
3. The W values fit to the Expressions of Eq. (66).....	118
4. Fitting of ENDOR frequencies to Eq. (86).....	119
5. Constants of Spin Hamiltonian.....	120
6. Relations Between the separation of Forbidden Doublet and the Sign of A and Q.....	150

Errata

<u>Page</u>	<u>Line</u>	<u>Present reading</u>	<u>Correct reading</u>
2	bottom	= 0.2 barn	= -0.2 barn
4	24	Fig. 57	Fig. 58
11	Eq. (9)	$H = \dots + A_{ij} S_i S_j$	$H = \dots + A_{ij} S_i I_j$
14	Eq. (12), Eq. (13)	$H = \dots$	$H = \dots$
17	first	$H = \dots$	$H = \dots$
21	Eq. (22)	$H = \dots$	$H = \dots$
34	20	this statement	the former statement
54	17	sbatility	stability
61	20	SWG #30	AWG #28
100	top	$\cos^2 H$	$\cos^2 (H)$
106	bottom		Y_Q -axis
116	24		too - delete
137		g_r	g_n
140		l approx	1st approx.
141	bottom curve	X_Q^-	Y_Q^-
143	2	Wahsh's	Walsh's
145	3	see page 15	see page 11
186	Ref. 33	J. Lamé	J. Lambe
187	Ref. 46	Abrazam	Abraham

Chapter I

Introduction

The purpose of this study is to present the details of the Niobium-93 hyperfine structure reported briefly in an earlier note.⁽¹⁾ As is now well known, the interest in Nb (Niobium) stems from the fact that its use as the charge compensator in CaWO_4 for the trivalent Nd^{3+} ions results in the simplification of the fluorescent spectrum and also in lowering the threshold for laser action.^(2, 3)

Niobium^(4, 5) was first discovered by C. Hatchett, an English chemist, in 1801 when he examined a heavy black stone which formed part of a collection presented to the British Museum. This stone was said to be discovered somewhere near Connecticut and was named columbium. In 1844, another chemist, Rose, announced the discovery of what he considered to be a new element and named it niobium, derived from the name of the goddess Niobe, the daughter of Tantalus. Eventually it was established that columbium and niobium were the same element. In 1949 niobium was chosen as the international name, however, a number of American scientists still prefer the name columbium. Niobium almost always occurs together with tantalum in nature because of their chemical similarity. The interest in niobium as an industrial element was stimulated by its low neutron adsorption cross section and high-temperature strength which led to its use as a cladding material for reactor fuel elements. This

interest was further extended to niobium-base alloys for high-temperature applications in missiles.

A portion of the periodic table near Nb is shown below. The elements under column VB are V, Nb and Ta. The normal valence state of these elements is 5+, with the closed electron shell structure of Ar-, Kr- and Hf⁴⁺ - core respectively. The notation to the right of the table indicates the orbit of the paramagnetic electron. Thus the electron configurations of V⁴⁺, Nb⁴⁺ and Ta⁴⁺ are expected to be Ar 3d¹, Kr 4d¹, and Hf⁴⁺ 5d¹ respectively. This table makes clear the logic for first studying V⁴⁺ in CaWO₄, as was done by N. Mahootian in his doctoral thesis (6, 7).

IIA	IIIB	IVB	VB	VIB	Electron Shell
Ca	Sc	Ti	V	Cr	(3d)
Sr	Y	Zr	Nb	Mo	(4d)
Ba	-	Hf	Ta	W	(5d)

In the periodic table, niobium is the 41st element belonging to the second series of transition elements with the 4d shell only partially filled. It contains 41 protons and 52 neutrons with a natural abundance of 100% of Nb-93. As a free atom, Nb-93 has the following characteristics: (8, 67)

electron configuration	= (Kr)4d ⁴ 5s
nuclear spin, I	= 9/2
nuclear magnetic moment, μ	= 6.1435, $g_n = 1.3652$
quadrupole moment, Q	= 0.2 barn

If during crystal growth, a small amount of Nb is added to the melt (in concentrations of the order of 1% or less), Nb is known to enter the W-site, forming the diamagnetic radical, NbO_4^{3-} . The four oxygens about the Nb ion form a squashed tetrahedron (bisphenoid) and the Nb is located near the center of the bisphenoid. The Nb can then be thought of as being Nb^{5+} , with the closed electron shell structure of Kr.

Upon gamma-irradiation, the niobate radicals become paramagnetic. The properties of paramagnetic niobium (Nb^{4+}) are in many respects similar to those of the orthovanadate radical (VO_4^{3-}) in CaWO_4 (6, 7, 10). One difference, however, is the stability. Whereas V^{4+} in CaWO_4 is stable at room temperature, Nb^{4+} requires dry ice temperature (195°K) or lower for stabilization. (1, 6, 7) It was indicated that the Nb ion is near the center of the oxygen bisphenoid. The evidence that the Nb is not at the center is provided by the EPR (electron paramagnetic resonance) spectrum at 77°K or lower. The nuclear spin I of Nb-93 is 9/2, so that the EPR spectrum of Nb^{4+} is expected to consist of 10 lines of nearly equal intensity and spacing, if all Nb ions are equivalent. Observation shows that there are 4 groups of 10 lines, for a general direction of the magnetic field, indicating, therefore that the Nb ions are locked in positions away from the bisphenoid center. At a higher temperature, say at 195°K, the Nb ion is able to "hop" from one displaced site to another, as evidenced by the fact that a single group of 10 lines is observed. (1)

Several other factors contribute to the complexity of the Nb^{4+} EPR spectrum. One is the forbidden structure, i.e. the doublets

at approximately midway between the principal allowed lines (see Fig. 11). It turns out that the nuclear quadrupole moment is responsible for the presence of these lines. Another factor is the non-coincidence of the g -, A -, and Q -tensor principal axes. The relation among these axes is rather complex and will be discussed in later chapters.

The analysis of the spectrum is therefore extremely difficult. This problem is, however, solved by the combination of the ENDOR and EPR technique. In the following chapters, we will develop a theory for this technique. Since the experimental results are described, as usual, by a phenomenological spin Hamiltonian, we will, first of all, give an explanation of how the spin Hamiltonian is obtained. Then the spin Hamiltonian is diagonalized to give the energy level formula which, in turn, leads to the formula of EPR signal. The ENDOR technique is next introduced and followed by the formulation of ENDOR signal. These formulas, being functions of the parameters of spin Hamiltonian, are the basis for the explanation of the spectrum. These spin Hamiltonian constants, including g , A , Q , and g_n obtained from the EPR and ENDOR measurements are tabulated in Tables 1 and 5. These experimental results are investigated and discussed together with the symmetry properties of the CaWO_4 crystal. Finally, the conclusion leads to a tentative charge compensation scheme as shown in Fig. 57, that is, a Nb ion substitutes the W ion at the center of the unit cell while a charge compensator ion, e.g. Nd, might substitute for the W ion at the corner of the same cell.

Chapter II

SPIN HAMILTONIAN

Since the discovery of the electron spin resonance phenomenon in paramagnetic ions by Zavoisky in 1945, the theory of paramagnetic resonance has been treated in detail by many authors. (11-22) There are the review papers by Kikuchi and Spence, (77) Bleaney and Stevens, (23) and Bowers and Owens. (24) However, for the sake of completeness and convenience, a brief discussion of the spin Hamiltonian will be given.

A. Derivation of Spin Hamiltonian

The interaction energy of an ion in a crystal field, having n electrons with nuclear spin I , nuclear magnetic moment μ_n , and quadrupole moment Q , can be described by the Hamiltonian: (13)

$$W = W_F + V_C + W_{ls} + W_{ss} + W_H + W_N + W_Q - g_n \beta_n \bar{H} \cdot \bar{I} \quad (1)$$

where

$$W_F = \sum_k^n \left(\frac{p^2}{2m} - \frac{ze^2}{r_k} \right) + \sum_{k,j}^n \frac{e^2}{r_{kj}} \sim 10^5 \text{ cm}^{-1} \quad (\text{Free ion})$$

$$V_C = \sum_k^{\text{ligands}} V(r_k) \quad (\text{Crystal field})$$

$$W_{ls} = \sum_{jk}^n a_{jk} \bar{l}_j \cdot \bar{s}_k + b_{jk} \bar{l}_j \cdot \bar{l}_k + c_{jk} \bar{s}_j \cdot \bar{s}_k \sim 10^3 \text{ cm}^{-1}$$

(Electron spin-orbit coupling)

$$W_{ss} = g_e^2 \beta_e^2 \sum_{jk}^n \left[\frac{\bar{S}_j \cdot \bar{S}_k}{r_{jk}^3} - \frac{3(\bar{r}_{jk} \cdot \bar{S}_j)(\bar{r}_{jk} \cdot \bar{S}_k)}{r_{jk}^5} \right] \text{-----} \sim 1 \text{ cm}^{-1}$$

(Electron dipole-dipole coupling)

$$W_H = \sum_k^{\text{unpaired electrons}} \beta_e (\bar{l}_k + g_e \bar{S}_k) \cdot \bar{H}$$

(Interaction with external magnetic field)

$$W_N = g_e \beta_e g_n \beta_n \left[\sum_k^n \left\{ \frac{(\bar{l}_k - \bar{S}_k) \cdot \bar{I}}{r_k^3} + \frac{3(\bar{r}_k \cdot \bar{S}_k)(\bar{r}_k \cdot \bar{I})}{r_k^5} \right\} + \frac{8\pi \delta(r_k)}{3} (\bar{S}_k \cdot \bar{I}) \right] \text{-----} \sim 10^{-2} \text{ cm}^{-1}$$

(Hyperfine coupling)

$$W_Q = \frac{e^2 Q}{2I(2I-1)} \left[\sum_k^n \left(\frac{I(I+1)}{r_k^3} - \frac{3(r_k \cdot I)^2}{r_k^5} \right) \right] \text{-----} \sim 10^{-3} \text{ cm}^{-1}$$

(Electric quadrupole coupling)

k and j refer to the electrons in the ion. The last term of Eq. (1) is the direct interaction of nucleus with the external magnetic field \bar{H} . Here P_k is the linear momentum and \bar{r}_k is the radius vector extending from the nucleus to the electron; a_{jk} , b_{jk} , c_{jk} are constants; \bar{l}_k , \bar{S}_k the orbital momentum and spin of the k^{th} electron, respectively; g_e , β_e refer to the electron spectroscopic splitting factor and Bohr magneton; g_n , β_n the nuclear spectroscopic splitting factor, and nuclear magneton; and e and m are the electronic charge and mass, respectively.

For the convenience of perturbation calculations, the crystalline field V_c is classified into three ranges, namely: the strong (10^4 cm^{-1}), the medium (10^3 cm^{-1}) and the weak (10^2 cm^{-1}) approximately according to

$$\text{strong: } \sum_{kj}^n \frac{e^2}{r_{kj}} < V_c < \sum_k^n \frac{Ze^2}{r_k}$$

$$\text{Medium: } W_{1s} < V_c < \sum_{kj}^n \frac{e^2}{r_{kj}}$$

$$\text{Weak: } V_c < W_{1s}$$

The weak field case applies, for example, to rare earth salts; the medium field to the 3d group hydrated salts, and the strong field to the 4d and 5d group complex where some degree of covalent bonding exists between the paramagnetic electron and the surrounding negative ions.

Setting

$$W' = W_{1s} + W_{ss} + W_H + W_N + W_Q - g_n \beta_n \bar{H} \cdot \bar{I} \quad (2)$$

equation (1) can be written as

$$W = W_F + V_c + W' \quad (3)$$

The spin Hamiltonian is derived from the actual Hamiltonian, Eq. (3) by carrying out the perturbation calculations term by term under the assumption of a medium crystalline field. A detailed description is long and has been treated in references. (13, 23, 24, 47, 48) We shall therefore confine ourselves to a brief sketch.

Assuming the terms W' and V_c are negligible compared to the coulomb energy $\sum_{kj}^n \frac{e^2}{r_{kj}}$, the term W_F in Eq. (3) is treated by the self consistent field method in which the coulomb interactions of

electrons are assumed to move independently of each other within the restriction of exclusion principle. The eigenstates which this gives are the "configurations" in which the individual electron orbits are specified, e.g. $3d^3 \ ^4F$. The next perturbation is that which comes from the crystalline potential V_C . The problem is then one of finding how the field perturbs the orbital levels. This is accomplished by first assuming that the crystalline potential satisfies the Laplace's equation $\nabla^2 V_C = 0$ and expanding the potential in spherical harmonics. Advantage is then taken of the crystal symmetry to simplify the terms in the expansion of V_C . The eigenvalue problem for $W_F + V_C$ is solved by means of the secular equations involving the matrix elements of V_C connecting the various eigenstates of W_F corresponding to the lowest level. In this way one arrives at a manifold of eigenstates of $W_F + V_C$ and the corresponding eigenvalues. These constitute the various orbital levels split by the crystal field. Further splitting may be caused by the spin-orbit interaction $W_{ls} + W_{ss}$. If we were to diagonalize the Hamiltonian W taking into account the term $V_C + W_{ls} + W_{ss}$ we could find that the energy levels are very complicated mixture of the various orbital and spin wave functions of the free ion. This procedure is complicated but has been used by Van Vleck,⁽⁴⁹⁾ Schlapp and Penney,⁽⁵⁰⁾ and others. We do not follow this procedure. Instead, the matrix elements of W' in Eq. (3) are determined within the ground manifold of the field splittings by the operator equivalent method of Stevens.⁽⁵¹⁻⁵³⁾ In this method, the position coordinates in the various terms of W' are transformed into the angular momentum operators L, S which are considered non-commuting

constants within the manifold. Contributions from closed shells vanish leaving only terms from the 3d electrons. The results of the transformations is to produce a total perturbation Hamiltonian represented by⁽⁴⁸⁾

$$\begin{aligned}
 W' = & (\lambda - 1/2 \rho) (L \cdot S) - \rho (L \cdot S)^2 + \beta_e H (L + g_e S) \\
 & + P \left\{ (L \cdot I) + \left[\xi L(L+1) - K \right] (S \cdot I) \right. \\
 & \left. - \frac{3}{2} \xi (L \cdot S) (L \cdot I) - \frac{3}{2} \xi (L \cdot I) (L \cdot S) \right\} \\
 & + \bar{Q} \left[(L \cdot I)^2 + \frac{1}{2} (L \cdot I) \right] - g_n \beta_n (H \cdot I) \quad (4)
 \end{aligned}$$

where λ = a spin-orbit constant for the given ion.
(in erg)

ρ = a proportionality constant of the W_{SS} term,
(in erg)

K = a proportionality constant of the delta-function term
(dimensionless)

$$P = g_e g_n \beta_e \beta_n / r^3 \quad (\text{in erg}) \quad (5)$$

$$\bar{Q} = \frac{3ne^2 Q}{2I(2I-1)r^3} \quad (\text{in erg}) \quad (6)$$

r = the effective radius of the 3d shell

Q = the usual quadrupole moment^(68, 70)

$$\xi = \frac{(2\ell+1) - 4S}{S(2\ell+1)(2\ell+3)(2L-1)} \text{ for } \ell = 2, \text{ (dimensionless).}$$

$$\eta = \pm 2S\xi \quad (\text{dimensionless})$$

The shell is less than half full, \longrightarrow "+"

The shell is more than half full, \longrightarrow "-"

The further development of the derivation depends on whether or not the lowest level of the crystal splittings is degenerate. The

following treatment assumes the lowest orbital level to be a singlet, i.e., the only degeneracy is that arising from the electronic and nuclear spins. The change in energy of the orbital singlet ground state due to W' in Eq. (4) is calculated to the second order perturbation theory using only the orbital part of wave function. The result is that, instead of obtaining the perturbed energy as usual, an expression is obtained which eliminates the orbital operator leaving a Hamiltonian with only spin operators, S and I ,⁽¹³⁾ i.e.

$$\begin{aligned}
 W' = & (-\lambda^2 \Lambda_{ij} - \rho \ell_{ij}) S_i S_j + g_e \beta_e (\delta_{ij} - \lambda \Lambda_{ij}) H_i S_j \\
 & - P(K \delta_{ij} + 3 \xi \ell_{ij} + \lambda \Lambda_{ij} - 3 \xi \lambda \mu_{ij}) S_i I_j \\
 & + \bar{Q} \ell_{ij} I_i I_j - (g_n \beta_n + R_{ij}) H_i I_j
 \end{aligned} \tag{7}$$

where

$$\Lambda_{ij} = \Lambda_{ji} = \sum_{n \neq 0} \frac{\langle 0 | L_i | n \rangle \langle n | L_j | 0 \rangle}{E_n - E_0} \quad (\text{in erg}^{-1})$$

$$\mu_{ij} = -\frac{1}{2} i \epsilon_{ikl} \sum_{n \neq 0} \frac{\langle 0 | L_l | n \rangle \langle n | L_j L_k + L_k L_j | 0 \rangle}{E_n - E_0} \quad (\text{in erg}^{-1})$$

$$\mu_{ii} = 0$$

$$\ell'_{ij} = \frac{1}{2} \langle 0 | L_i L_j + L_j L_i | 0 \rangle = \frac{1}{3} L(L+1) \delta_{ij} + \ell_{ij} \tag{8}$$

$$\ell_{ii} = 0$$

$$R_{ij} = P \Lambda_{ij} g_e \beta_e$$

$$i, j = x, y, z$$

E_0, E_n being the energy levels due to field splitting, the index 0 referring to the lowest level.

$|0\rangle$ = the ground orbital state with energy E_0

$|n\rangle$ = the excited orbital state with energy $E_n, n = 1, 2, 3, \dots$

Writing in the abbreviated form, with $\beta \equiv \beta_e$,

$$H = D_{ij}S_iS_j + \beta g_{ij}H_iS_j + A_{ij}S_iS_j \\ + Q_{ij}I_iI_j - (\beta n g_n + R_{ij})H_iI_j \quad (9)$$

Eq. (9) is the general spin Hamiltonian, where the tensors are defined as

$$D_{ij} = -(\lambda^2 \Lambda_{ij} + \rho \ell_{ij}) \quad (\text{in erg})$$

$$g_{ij} = g_e(\delta_{ij} - \lambda \Lambda_{ij}) \quad (\text{dimensionless})$$

$$A_{ij} = -P(K\delta_{ij} + 3\xi \ell_{ij} + 2\lambda \Lambda_{ij} - 3\xi \lambda \mu_{ij}) \quad (\text{in erg}) \quad (10)$$

$$Q_{ij} = \bar{Q} \ell'_{ij} = \frac{3ne^2q}{2I(2I-1)r^3} \ell'_{ij} \quad (\text{in erg}) \quad (11)$$

Note that along Z-axis we have ⁽¹³⁾

$$Q_{zz} = \frac{3e^2qQ}{4I(2I-1)} \quad (11')$$

which is the conventional form of quadrupole coupling constant, and where the parameter q is defined as the field gradient at the nucleus:

$$eq \equiv \frac{\partial^2 V}{\partial Z^2}$$

B. General Discussion of the Spin Hamiltonian

The tensor D_{ij} comes from the second order effects of the

crystal field Λ_{ij} , the spin-orbit coupling λ , and the spin-spin interaction \mathcal{P} . D_{ij} describes how the level splits in the zero magnetic field in the absence of nuclear interaction and contributes to the fine structure. g_{ij} is called the spectroscopic splitting factor. The term $\beta g_{ij} H_i S_j$ represents the Zeeman energy. The tensor g_{ij} indicates that the spin is no longer completely free. The change is due to the spin-orbit coupling λ of the paramagnetic ion and the second order effects of the crystal field Λ_{ij} . The magnetic interaction between the electrons and the nucleus is described by the hyperfine coupling tensor A_{ij} . Its anisotropy comes from the second order effects of crystal fields Λ_{ij} and μ_{ij} incorporated with spin-orbit coupling λ and the electronic configuration constant ξ of the paramagnetic electrons. The dipolar hyperfine interaction affects A_{ij} through the constant ξ as well as the effective radius r of the 3d shell contained in P. The Fermi contact hyperfine interaction originate from unpaired S electrons is taken care of by the constant K. The quadrupole interaction enters the spin Hamiltonian through the tensor Q_{ij} of which the anisotropy is due to the orbital contribution μ_{ij} . The electronic configuration effects the Q_{ij} through r^{-3} and η . The direct interaction between the magnetic field and the nuclear moment is taken into account by the factor $-(g_n \beta_n + R_{ij})$. The second term, R_{ij} is anisotropic and is equal to $P g_e \beta_e \Lambda_{ij}$ or $\Lambda_{ij} (g_e \beta_e)^2 g_n \beta_n / r^3$ which depends on the crystal field splitting due to Λ_{ij} . R_{ij} is conventionally referred as the "pseudo field" term. It is usually small compared to $g_n \beta_n$ when the field splitting $E_n - E_0$ is large, but R_{ij} and $g_n \beta_n$ can be of the same order of magnitude if the field splitting

is small (p. 72-73 of ref. 13). In this case it becomes hard to estimate the g_n from the measured value of the quantity $-(g_n\beta_n + R_{ij})$ without a detailed knowledge of the field splittings and the ionic radius r . It will be noticed that the term quadratic in magnetic field $\beta_e^2 \Lambda_{ij} H_i H_j$, has been neglected for it contains no spin variables and is unimportant for spin resonance.

The spin Hamiltonian has been deduced for the case of iron group under the assumption of a medium field (see p. 7). The question arises whether there is a similar spin Hamiltonian for cases in which the crystal field splittings are (1) small compared with the spin-orbit couplings (as in rare-earth salts), or (2) large (as in the covalent bonding complex). Elliott and Stevens^(52, 54-58) have considered the first problem and concluded that equation (9) can explain most of the experimental results. Equation (9) also keeps its forms in the covalent bonding case with only the following quantitative modification:⁽¹³⁾

a) The covalent bond modifies the orbital contribution to the g-factor.

b) There is a change in the second order contribution of the spin-orbit coupling to the g-factor.

c) The hyperfine coefficient A is reduced.

d) There may be a superhyperfine interaction between the magnetic electron and the surrounding nuclei. Consequently, in all the cases the spin Hamiltonian Eq. (9) is phenomenologically correct. There are only quantitative corrections made to coefficients D , g , A , etc., but no changes on the qualitative nature of the representation.

Another property of the spin Hamiltonian is that its coefficients must conform to the local symmetry about the ion in the crystal. If the symmetry is high, the spin-Hamiltonian takes a simpler form. The beauty of the spin-Hamiltonian lies in the fact that its employment makes it possible to give a shorthand description of the resonance properties of an ion in terms of a relatively small number of coefficients which can be determined experimentally. Since the EPR spectrum reflects the symmetry of each magnetic complex, it is often possible to guess the form of the spin-Hamiltonian from the symmetry properties with practically no detailed knowledge of the crystal field. From the observed parameters one then forms a model of the crystal field to explain the spin-Hamiltonian.

In the following we wish to rewrite the spin-Hamiltonian, Eq. (9) in a more convenient form.

$$\begin{aligned}
 H = & \underline{S} \cdot \underline{D} \cdot \underline{S} + \beta \underline{H} \cdot \underline{g} \cdot \underline{S} + \underline{S} \cdot \underline{A} \cdot \underline{I} \\
 & + \underline{I} \cdot \underline{Q} \cdot \underline{I} - \beta_n g_n \underline{H} \cdot \underline{I} - \underline{H} \cdot \underline{R} \cdot \underline{I}
 \end{aligned} \tag{12}$$

where \underline{D} , \underline{g} , \underline{A} , \underline{Q} , and \underline{R} are tensors to be determined experimentally. For the case of $S = 1/2$ the fine structure term vanishes. We also combine the "pseudo" field \underline{R} term with the nuclear direct interaction term and write the modified g_n as g_n' .

Then Eq. (12) simplifies to

$$H = \beta \underline{H} \cdot \underline{g} \cdot \underline{S} + \underline{S} \cdot \underline{A} \cdot \underline{I} + \underline{I} \cdot \underline{Q} \cdot \underline{I} - \beta_n \underline{H} \cdot \underline{g}_n' \cdot \underline{I} \tag{13}$$

Eq. (13) will be used as the starting point for the calculation of energy levels and EPR and ENDOR signals of the paramagnetic

Nb⁴⁺ ion in the CaWO₄ crystal.

Chapter III

FORMULATION OF EPR AND ENDOR MEASUREMENTS

The formulas needed to interpret the EPR and ENDOR measurements are obtained after making a few minor modifications of the results given in the thesis by R. H. Borcherts. (59, 60) We start with the spin Hamiltonian, Eq. (14), in which the principal axes of the g -, A -, Q - and g_n -tensors are assumed to be coincident. The electron Zeeman term is diagonalized first by the coordinate transformation technique. The remaining terms, namely the hyperfine, the nuclear quadrupole, and the direct interaction terms, being at least one order of magnitude smaller are calculated to the second order. The angular dependence of the allowed EPR lines are obtained by making use of the selection rule $\Delta M = \pm 1$, $\Delta m = 0$. The formulas for the ENDOR signal are obtained by considering $\Delta M = 0$, $\Delta m = \pm 1$. The main results are outlined in the following sections. The details of the derivation are given in Appendix A.

A. Energy Levels

1. Hamiltonian Expressed in the g -Tensor Principal Axis System

For rhombic symmetry, the spin Hamiltonian takes the form

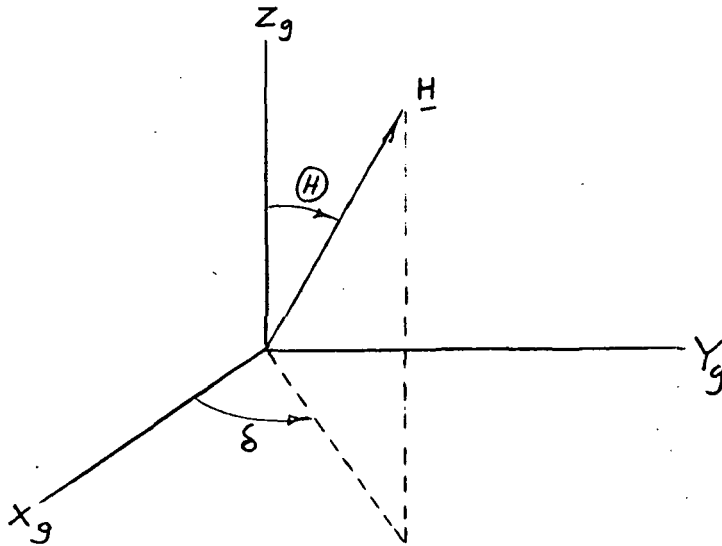
$$H = \beta (g_z H_z S_z + g_x H_x S_x + g_y H_y S_y)$$

$$+ A_z I_z S_z + A_x I_x S_x + A_y I_y S_y$$

$$+ Q' [I_z^2 - \frac{1}{3} I(I+1)] + Q'' (I_x^2 - I_y^2)$$

$$- \beta_n (g_n^z H_z I_z + g_n^x H_x I_x + g_n^y H_y I_y)$$

(14)



We define

$$H_x = H \sin (H) \cos \delta$$

$$H_y = H \sin (H) \sin \delta \quad (15)$$

$$H_z = H \cos (H)$$

$$g_{\perp}^2 = g_x^2 \cos^2 \delta + g_y^2 \sin^2 \delta \quad (16)$$

$$g^2 = g_z^2 \cos^2 (H) + g_{\perp}^2 \sin^2 (H) \quad (17)$$

$$A_{\perp}^2 g_{\perp}^2 = A_x^2 g_x^2 \cos^2 \delta + A_y^2 g_y^2 \sin^2 \delta \quad (18)$$

and

$$\begin{aligned}
f_1 &= \frac{1}{g\beta H_0} \frac{g_{\perp}^2}{K^2 g^2} \sin^2(H) [(A_z^2 - A_{\perp}^2) \frac{g_z^2}{g^2} \cos^2(H) + (A_x^2 - A_y^2) \frac{g_x^2 g_y^2}{g_{\perp}^2} \sin^2 \delta \cos^2 \delta] \\
f_2 &= \frac{1}{g\beta H_0} [A_{\perp}^2 (\frac{A_z^2 - K^2}{K^2}) + (A_x^2 + A_y^2 + 2 \frac{A_z}{K} A_x A_y) - \frac{(A_x^2 - A_y^2)^2}{K^2} \frac{g_x^2 g_y^2}{g_{\perp}^2} \sin^2(H) \sin^2 \delta \cos^2 \delta] \\
f_3 &= \frac{1}{g\beta H_0} [A_{\perp}^2 (\frac{A_z^2 - K^2}{K^2}) + (A_x^2 + A_y^2 - 2 \frac{A_z}{K} A_x A_y) - \frac{(A_x^2 - A_y^2)^2}{K^2} \frac{g_x^2 g_y^2}{g_{\perp}^2} \sin^2(H) \sin^2 \delta \cos^2 \delta] \\
f_4 &= Q' (1 - \frac{3}{2} \frac{A_z^2 g_{\perp}^2}{K^2 g^2} \sin^2(H)) + Q'' \frac{3}{2} \frac{\sin^2(H)}{K^2 g^2} (A_x^2 g_x^2 \cos^2 \delta - A_y^2 g_y^2 \sin^2 \delta) \\
f_5 &= \frac{1}{K} \left\{ [Q' \frac{A_z^2 g_{\perp}^2}{4K^2 g^2} \sin^2(H) + \frac{Q''}{4A_{\perp}^2 g_{\perp}^2} (1 + \frac{A_z^2 g_z^2}{K^2 g^2} \cos^2(H)) (A_x^2 g_x^2 \cos^2 \delta - \right. \\
&\quad \left. A_y^2 g_y^2 \sin^2 \delta)]^2 + Q''^2 \frac{A_z^2 A_x^2 A_y^2}{K^2 A_{\perp}^4} \cdot \frac{g_z^2 g_x^2 g_y^2}{g_{\perp}^4} \cos^2(H) \sin^2 \delta \cos^2 \delta \right\} \\
f_6 &= \frac{1}{K} \left\{ \frac{A_z^2 g_z^2 \sin^2(H) \cos^2(H)}{4K^4 A_{\perp}^2 g_{\perp}^4 g^2} [Q' A_{\perp}^2 g_{\perp}^2 - Q'' (A_x^2 g_x^2 \cos^2 \delta - A_y^2 g_y^2 \sin^2 \delta)]^2 \right. \\
&\quad \left. + Q''^2 \cdot \frac{A_x^2 A_y^2}{K^2 A_{\perp}^2} \cdot \frac{g_x^2 g_y^2}{g_{\perp}^2} \sin^2(H) \sin^2 \delta \cos^2 \delta \right\} \\
f_7 &= \frac{1}{Kg} [\sin^2(H) (A_x g_x g_h^x \cos^2 \delta + A_y g_y g_h^y \sin^2 \delta) + A_z g_z g_h^z \cos^2(H)] \\
f_8 &= \frac{\sin^2(H)}{K A_{\perp}^2 g_{\perp}^2} \left[\frac{\cos^2(H)}{K^2 g^2} (A_z A_x g_z g_x g_h^x \cos^2 \delta + A_z A_y g_z g_y g_h^y \sin^2 \delta - A_{\perp} g_{\perp}^2 \mathfrak{H}^2) \right. \\
&\quad \left. + \sin^2 \delta \cos^2 \delta (A_y g_y g_h^x - A_x g_x g_h^y)^2 \right]. \tag{21}
\end{aligned}$$

We have taken the perturbation denominator in the second order hyperfine terms as $(g\beta H_0)$. The significance of the field H_0 is that in the absence of the hyperfine splitting all the EPR lines

would coincide and occur at this field. The resonant condition satisfies the relation $h\nu_e = g\beta H_0$. In case $f_4 \ll k$, Eq. (20) can be simplified to Eq. (20') by neglecting the terms containing f_4 in the denominators

$$\begin{aligned}
 E_{Mm} = & g\beta HM + MmK + \frac{1}{2} Mm^2 f_1 \\
 & + \frac{1}{8} [-s(s+1)m + I(I+1)M + Mm(M-m)] f_2 \\
 & + \frac{1}{8} [s(s+1)m + I(I+1)M - Mm(M+m)] f_3 \\
 & + [m^2 - \frac{1}{3} I(I+1)] f_4 \\
 & + \frac{2m[2I(I+1) - 2m^2 - 1]}{M} f_5 \\
 & + \frac{2m[-4I(I+1) + 8m^2 + 1]}{M} f_6 \\
 & - m\beta_n H f_7 + \frac{m}{2M} \beta_n^2 H^2 f_8
 \end{aligned} \tag{20'}$$

We will use Eq. (20') to derive an expression for the values of g - and A - tensors.

2. Quadrupole Dominated Hamiltonian

The formulas of energy level, Eq. (20) and Eq. (20'), can be valid only if all the tensors, g , A , Q and g_n , have coincident principal axes. If, on the other hand, the principal axes do not coincide, Eq. (14) will contain additional off-diagonal elements and the resulting formula for energy levels will be much more complicated. However, in a special case as we are treating here, the previous formulas can still be used with only a small modification. This special case has two prominent features, namely:

- 1) The contribution of the quadrupole coupling term $\underline{I} \cdot \underline{Q} \cdot \underline{I}$ is much smaller than that of $\underline{S} \cdot \underline{A} \cdot \underline{I}$ term and/or $\underline{H} \cdot \underline{g} \cdot \underline{S}$ term,
- 2) The anisotropy of the tensors g , A and g_n are all small. Only Q is strongly anisotropic.

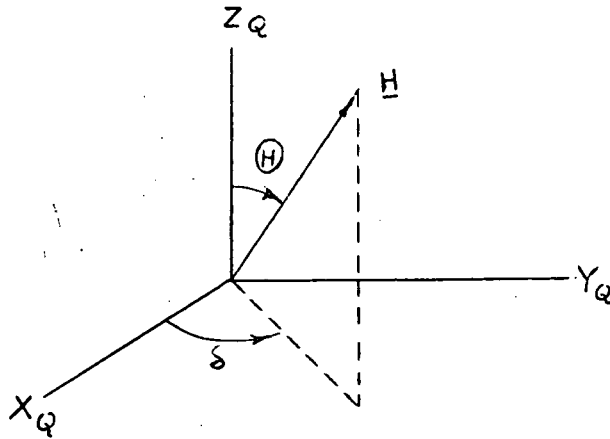
Under these conditions, the Hamiltonian, Eq. (14) can be written as

$$H = \beta g \underline{H} \cdot \underline{S} + A \underline{S} \cdot \underline{I} - \beta_n g_n \underline{H} \cdot \underline{I} + Q' [I_z^2 - \frac{1}{3} I(I+1)] + Q'' (I_x^2 - I_y^2) \quad (22)$$

where X , Y , Z denote the principal axes of Q -tensor and

$$Q' \equiv Q_z - \frac{1}{2} (Q_x + Q_y)$$

$$Q'' \equiv \frac{1}{2} (Q_x - Q_y) \quad (23)$$



The result of diagonalization of Eq. (22) to the second order of perturbation can be obtained directly from Eq. (20) or (20') by putting $g_x = g_y = g_z = g$, $A_x = A_y = A_z = A$ and $g'_{nx} = g'_{ny} = g'_{nz} = g_n$. Thus Eq. (20) becomes

$$\begin{aligned}
E_{Mm} &= g\beta HM + AMm - \beta_n g_n Hm \\
&+ \frac{-s(s+1)m + I(I+1)M + M^2m - Mm^2}{2 h\nu_e} A^2 \\
&+ [m^2 - \frac{1}{3} I(I+1)] f_4 \\
&+ \frac{A[I(I+1) - m(m+1)][I(I+1) - (m+1)(m+2)]}{-2MA - 4(m+1) f_4} f_5 \\
&+ \frac{A[I(I+1) - m(m+1)][I(I+1) - (M-1)(m-2)]}{2MA + 4(m-1) f_4} f_5 \\
&+ \frac{A(2m+1)^2 [I(I+1) - m(m+1)]}{-MA - (2m+1) f_4} f_6 \\
&+ \frac{A(2m-1)^2 [I(I+1) - m(m-1)]}{MA + (2m-1) f_4} f_6
\end{aligned} \tag{24}$$

where

$$\begin{aligned}
f_4 &= Q'(1 - \frac{3}{2} \sin^2 \textcircled{H}) + Q'' \frac{3}{2} \sin^2 \textcircled{H} (\cos^2 \delta - \sin^2 \delta) \\
f_5 &= \frac{1}{A} \left\{ \left[\frac{Q'}{4} \sin^2 \textcircled{H} + \frac{Q''}{4} (1 + \cos^2 \textcircled{H}) (\cos^2 \delta - \sin^2 \delta) \right]^2 \right. \\
&\quad \left. + Q''^2 \cos^2 \textcircled{H} \sin^2 \delta \cos^2 \delta \right\} \\
f_6 &= \frac{1}{A} \left\{ \sin^2 \textcircled{H} \cos^2 \textcircled{H} [Q' - Q'' (\cos^2 \delta - \sin^2 \delta)]^2 \right. \\
&\quad \left. + Q''^2 \sin^2 \textcircled{H} \sin^2 \delta \cos^2 \delta \right\}
\end{aligned} \tag{25}$$

Note that $f_1=f_3=f_8=0$ and we have written out K , f_2 and f_7 explicitly in terms of A , A^2 and g_n respectively in Eq. (24). Again if we make the assumption, $f_4 \ll A$, to simplify the denominators of Eq. (24), we obtain Eq. (24'):

$$\begin{aligned}
E_{Mm} &= \beta g_{HM} + AMm - \beta_n g_n Hm \\
&+ \frac{-s(s+1)m + I(I+1)M + M^2m - Mm^2}{2 h\nu_e} A^2 \\
&+ [m^2 - \frac{1}{3} I(I+1)] f_4 \\
&+ \frac{2m[2I(I+1) - 2m^2 - 1]}{M} f_5 \\
&+ \frac{2m[-4I(I+1) + 8m^2 + 1]}{M} f_6 \tag{24'}
\end{aligned}$$

We will use the simpler equation (24') to derive an expression for the values of Q -, A -, and g_n - tensors. In general, Eq. (24) will give us more accurate values for these tensors than Eq. (24'). However, in certain cases, as will be seen later, Eq. (24') offers the same accuracy as does Eq. (24).

Before concluding this section, it is to be noted that had we written Eq. (22) as (22')

$$\begin{aligned}
H &= \beta g_{H \cdot \underline{S}} + A \underline{S \cdot \underline{I}} - \beta_n g_n \underline{H \cdot \underline{I}} \\
&+ Q_{11} I_1^2 + Q_{22} I_2^2 + Q_{33} I_3^2 + Q_{12} (I_1 I_2 + I_2 I_1) \\
&+ Q_{23} (I_2 I_3 + I_3 I_2) + Q_{31} (I_3 I_1 + I_1 I_3) \tag{22'}
\end{aligned}$$

its diagonalization would give us the same expression as Eq. (24').

But in this case, f_4 , f_5 , and f_6 would take the following form:

$$\begin{aligned}
f_4 &= Q_{33} - \frac{1}{2} (Q_{11} + Q_{22}) = \frac{3}{2} Q_{33} \\
f_5 &= \frac{(Q_{11} - Q_{22})^2 - 4Q_{12}^2}{16A} \\
f_6 &= \frac{Q_{13}^2 + Q_{23}^2}{4A} \tag{25'}
\end{aligned}$$

where the quadrupole coupling constant Q_{33} is taken along the direction of the external d.c. magnetic field, and we have made use of the relation $Q_{11} + Q_{22} + Q_{33} = 0$.

B. EPR Signal

The EPR signal $h\nu_e$ is related to the d.c. field H_m according to Eq. (26) which is derived from Eq. (20') using the selection rule $\Delta m = 0$ and for a general direction of the d.c. magnetic field.

$$\begin{aligned}
 h\nu_e &= E_{\frac{1}{2}m} - E_{-\frac{1}{2}m} \\
 &= g\beta H_m + mA + \frac{1}{2} m^2 f_1 \\
 &\quad + \frac{1}{8} [I(I+1) - m^2] (f_2 + f_3) \\
 &\quad + 8 m [2I(I+1) - 2m^2 - 1] f_5 \\
 &\quad + 8 m [-4I(I+1) + 8m^2 + 1] f_6 \\
 &\quad + 2 m \beta_n^2 \frac{H^2}{m} f_8
 \end{aligned} \tag{26}$$

where we have written A in place of K.

1. g-value

From Eq. (26) we obtain

$$\begin{aligned}
 h\nu_e &= g\beta \frac{H_m + H_{-m}}{2} + \frac{1}{2} I(I+1) f_1 \\
 &\quad + \frac{I(I+1) - m^2}{2(2m+1)} [(H_{m+1} + H_{-(m+1)}) - (H_m + H_{-m})] g\beta
 \end{aligned} \tag{27}$$

If we neglect the second term containing f_1 and define

$$H_0 = \frac{h\nu_e}{g\beta}, \text{ we will have}$$

$$H_0 = \frac{1}{2} (H_m + H_{-m}) + \frac{I(I+1) - m^2}{2(2m+1)} \cdot [(H_{m+1} + H_{-(m+1)}) - (H_m + H_{-m})] \quad (28)$$

$$\text{and} \quad g = \frac{h}{\beta} \frac{\nu_e}{H_0} \quad (29)$$

Eqs. (28) and (29) indicate that the g-value can be calculated simply from the measurement of the EPR field. Along the g-tensor principal axes, f_1 is zero, hence its omission does not introduce an error in Eq. (28). Along other directions, f_1 is not zero, but according to measurements, it has a value of about only 0.1 gauss due to the A-tensor anisotropy. Thus the omission of the f_1 -term introduces an error of at most .04% in the g-value. For a rough estimate of the g-value, Eq. (28) can be approximated by

$$H_0' = \frac{1}{2} (H_m + H_{-m}) \quad (30)$$

which gives an error of $\pm .3\%$ in the g-value. The second term in Eq. (28) enters as a correction from the second order perturbation of the hyperfine interaction. This term remains even if the A-tensor were assumed isotropic.

2. A-value

From Eq. (26) we have

$$\begin{aligned} g\beta \frac{H_{-m} - H_m}{2m} &= A + 8 [2I(I+1) - 2m^2 - 1] f_5 \\ &+ 8 [-4I(I+1) + 8m^2 + 1] f_6 \\ &+ \beta_n^2 (H_m^2 + H_{-m}^2) f_8 \end{aligned} \quad (31)$$

The last term, containing f_8 in Eq. (31), comes from the second

order perturbation of the g_n -tensor. Measurements reveal that the anisotropies of g , g_n , and A are 3, 5, and 10% respectively. Therefore f_8 is mainly determined by the anisotropy of A -tensor. Taking $g \approx 2.02$, $g_n \approx 1.35$ and $A \approx 75$ to 89 MHz, we estimate from f_8 of Eq. (21) that

$$\beta_n^2 (H_m^2 + H_{-m}^2) f_8 \leq 0.01 \text{ MHz}$$

which is much smaller than A . Hence we neglect the last term of Eq. (31) and obtain

$$A = g\beta \frac{H_{-m} - H_m}{2m} - 8 [2I(I+1) - 2m^2 - 1] f_5 - 8 [-4I(I+1) + 8m^2 + 1] f_6 \quad (32)$$

The values of f_5 and f_6 needed to evaluate A in Eq. (32), were estimated from the results of Eq. (25). These results, to be sure, apply to the case of isotropic g and A , but the use of the results is justified because the g - and A - tensor anisotropies are only 5% or less. The values for Q' and Q'' were taken from ENDOR measurements. Thus from Eq. (25) we estimate that

$$f_5 \text{ and } f_6 \leq 0.01 \text{ MHz}$$

C. Forbidden EPR Spectra

A characteristic of the Nb^{4+} EPR spectrum is its forbidden structure, i.e. the occurrence of doublets midway between the more intense allowed ($\Delta M = 1$, $\Delta m = 0$) HFS lines. Consequently a theory for the positions of the first forbidden lines ($\Delta M = \pm 1$, $\Delta m = \pm 1$), and the relative intensities of the allowed and the forbidden lines

will be developed.

From perturbation theory, it follows that for

$$\mathcal{H}\Psi = E\Psi \quad (34)$$

where

$$\mathcal{H} = \mathcal{H}_0 + \mathcal{K}' \quad (35)$$

and

$$\mathcal{H}_0 \mu_k = E_{ok} \mu_k \quad (36)$$

then

$$\psi \approx \mu_k + \sum_{n \neq k}' \frac{\langle n | \mathcal{K}' | k \rangle}{E_{ok} - E_{on}} \mu_n \quad (37)$$

$$E \approx E_{ok} + \langle k | \mathcal{K}' | k \rangle + \sum_{n \neq k}' \frac{|\langle n | \mathcal{K}' | k \rangle|^2}{E_{ok} - E_{on}} \quad (38)$$

and

$$P(k \rightarrow n) \propto |\langle n | \mathcal{K}'' | k \rangle|^2 \quad (39)$$

where $P(k \rightarrow n)$ is the probability of transition from state k to n , and \mathcal{K}'' is the "amplitude" of the harmonic time dependent perturbation.

For the specific problem of concern here, we have from Eq.

(13)

$$\mathcal{H} = \beta \underline{H} \cdot \underline{g} \cdot \underline{S} + \underline{S} \cdot \underline{A} \cdot \underline{I} - \beta_n \underline{H} \cdot \underline{g}'_n \cdot \underline{I} + \underline{I} \cdot \underline{Q} \cdot \underline{I} \quad (35')$$

with

$$H_0 = \beta \underline{H} \cdot \underline{g} \cdot \underline{S}$$

such that

$$H_0 \Psi_M = g\beta H M \Psi_M \quad (36')$$

We note first of all that

$$[H, S^2] = [H, I^2] = [I^2, S^2] = 0 \quad (40)$$

so that the unperturbed basis functions can be built up by taking linear combinations of the electron spin functions φ_M and nuclear spin functions χ_m , which satisfy

$$S^2 \varphi_M = s(s+1) \varphi_M$$

$$S_z \varphi_M = M \varphi_M$$

$$I^2 \chi_m = I(I+1) \chi_m$$

$$I_z \chi_m = m \chi_m \quad (41)$$

For the linear combination of the φ_M 's, we take ψ_M 's which are the eigenfunctions of

$$\beta \underline{H} \cdot \underline{g} \cdot \underline{S} \psi_M = Mg\beta H \psi_M \quad (42)$$

For the linear combination of the χ_m 's, we take ϕ_m 's such that

$$\langle M = + \frac{1}{2} | S_z | M = + \frac{1}{2} \rangle \cdot \underline{A} \cdot \underline{I} \phi_m = \Delta E_m \phi_m \quad (43)$$

Thus the eigenfunctions ψ_{Mm} or $|Mm\rangle$ of the operator Eq. (51') are

to be expanded in terms of

$$\psi_{\frac{1}{2}} \phi_m \text{ and } \psi_{-\frac{1}{2}} \phi_m \quad (44)$$

In the above, because of the discussions to follow, we have taken the electron spin S to be $1/2$. The first order eigenfunctions and the eigenvalues to the second order, then, are given by

$$\psi_{\frac{1}{2}m} = \psi_{\frac{1}{2}} \left[\phi_m + \sum_{m'} \frac{\langle m' | \underline{I} \cdot \underline{Q} \cdot \underline{I} - \beta_n \underline{H} \cdot \underline{g}_n \cdot \underline{I} | m \rangle}{\Delta E_m - \Delta E_{m'}} \phi_{m'} \right] \quad (45)$$

$$E_{\frac{1}{2}m} = \frac{1}{2} g \beta H + \Delta E_m + \langle m | \underline{I} \cdot \underline{Q} \cdot \underline{I} - \beta_n \underline{H} \cdot \underline{g}_n \cdot \underline{I} | m \rangle + \sum_{m'} \frac{|\langle m' | \underline{I} \cdot \underline{Q} \cdot \underline{I} - \beta_n \underline{H} \cdot \underline{g}_n \cdot \underline{I} | m \rangle|^2}{\Delta E_m - \Delta E_{m'}} \quad (46)$$

and for $M = -\frac{1}{2}$,

$$\psi_{-\frac{1}{2}m} = \psi_{-\frac{1}{2}} \left[\phi_m + \sum_{m'} \frac{\langle m' | \underline{I} \cdot \underline{Q} \cdot \underline{I} - \beta_n \underline{H} \cdot \underline{g}_n \cdot \underline{I} | m \rangle}{-\Delta E_m + \Delta E_{m'}} \phi_{m'} \right] \quad (47)$$

$$E_{-\frac{1}{2}m} = -\frac{1}{2} g \beta H - \Delta E_m + \langle m | \underline{I} \cdot \underline{Q} \cdot \underline{I} - \beta_n \underline{H} \cdot \underline{g}_n \cdot \underline{I} | m \rangle + \sum_{m'} \frac{|\langle m' | \underline{I} \cdot \underline{Q} \cdot \underline{I} - \beta_n \underline{H} \cdot \underline{g}_n \cdot \underline{I} | m \rangle|^2}{-\Delta E_m + \Delta E_{m'}} \quad (48)$$

In Eqs. (46) and (48), we have not included the second order contributions coming from the off-diagonal elements of HFS interaction, $\underline{S} \cdot \underline{A} \cdot \underline{I}$. We shall consider these corrections when a quantitative treatment is to be made. However, experimental result tells us that such contributions appear to be small for Nb^{4+} .

The transitions among the several levels in the EPR spectrum

are indicated by the electron magnetic dipole interaction

$$\mathcal{H}' = g\beta \underline{H}' \cdot \underline{S} \quad (49)$$

where H' is the amplitude of the oscillating microwave magnetic field. This field is assumed to be perpendicular to the axis of quantization. Then from Eqs. (39), (45), (47), and (49) we find that the transition probability, and therefore the intensity, is

$$\begin{aligned} P(-\frac{1}{2} m \rightarrow \frac{1}{2} m) &\propto |\langle \frac{1}{2} m | S_+ | -\frac{1}{2} m \rangle|^2 \\ &\approx \left| 1 - \sum_{m'} \left| \frac{\langle m' | \underline{I} \cdot \underline{Q} \cdot \underline{I} - \beta_n \underline{H} \cdot \underline{g}_n \cdot \underline{I} | m \rangle}{\Delta E_m - \Delta E_{m'}} \right|^2 \right|^2 \\ &\approx 1 - 2 \sum_{m'} \left| \frac{\langle m' | \underline{I} \cdot \underline{Q} \cdot \underline{I} - \beta_n \underline{H} \cdot \underline{g}_n \cdot \underline{I} | m \rangle}{\Delta E_m - \Delta E_{m'}} \right|^2 \end{aligned} \quad (50)$$

The above expression applies to the allowed, $\Delta m = 0$ HFS lines. For the first forbidden transition ($\Delta m = \pm 1$),

$$\begin{aligned} P(-\frac{1}{2} m \rightarrow \frac{1}{2} m + 1) &\propto |\langle \frac{1}{2} m + 1 | S_+ | -\frac{1}{2} m \rangle|^2 \\ &\approx 4 \left| \frac{\langle m + 1 | \underline{I} \cdot \underline{Q} \cdot \underline{I} - \beta_n \underline{H} \cdot \underline{g}_n \cdot \underline{I} | m \rangle}{\Delta E_{m+1} - \Delta E_m} \right|^2 \end{aligned} \quad (51)$$

If the nuclear Zeeman term $\beta_n \underline{H} \cdot \underline{g}_n \cdot \underline{I}$ is dominant in (51) we will have

$$\begin{aligned} P(-\frac{1}{2} m \rightarrow \frac{1}{2} m + 1) &\propto \left| \frac{\langle m + 1 | I_+ | m \rangle}{\Delta E_{m+1} - \Delta E_m} \right|^2 \\ &\propto [I(I+1) - m(m+1)] \frac{\beta_n^2 (\underline{H} \cdot \underline{g}_n)^2}{|\Delta E_{m+1} - \Delta E_m|^2} \end{aligned} \quad (52)$$

If the quadrupole coupling term, $\underline{I} \cdot \underline{Q} \cdot \underline{I}$ is dominant in Eq. (51), we

will have

$$P(-\frac{1}{2} m \rightarrow \frac{1}{2} m+1) \propto \left| \frac{\langle m+1 | \underline{I} \cdot \underline{Q} \cdot \underline{I} | m \rangle}{\Delta E_{m+1} - \Delta E_m} \right|^2 \quad (53)$$

Since the quadrupole interaction term can be written in the form

$$\begin{aligned} \underline{I} \cdot \underline{Q} \cdot \underline{I} &= \frac{1}{2} (Q_{11} + Q_{22}) I^2 + [Q_{33} - \frac{1}{2} (Q_{11} + Q_{22})] I_Z^2 \\ &+ \frac{1}{2} (Q_{13} - i Q_{23}) (I_+ I_Z + I_Z I_+) \\ &+ \frac{1}{2} (Q_{13} + i Q_{23}) (I_- I_Z + I_Z I_-) \\ &+ \frac{1}{4} (Q_{11} - Q_{22} - 2iQ_{12}) I_+^2 + \frac{1}{4} (Q_{11} - Q_{22} + 2iQ_{12}) I_-^2 \end{aligned} \quad (54)$$

we get

$$\begin{aligned} \langle m+1 | \underline{I} \cdot \underline{Q} \cdot \underline{I} | m \rangle &= \frac{1}{2} (Q_{13} - iQ_{23}) \langle m+1 | I_Z I_+ + I_+ I_Z | m \rangle \\ &= \frac{1}{2} (Q_{13} - iQ_{23}) (2m+1) \sqrt{I(I+1) - m(m+1)} \end{aligned} \quad (55)$$

Putting Eq. (55) into Eq. (53) and assuming

$$\Delta E_{m+1} - \Delta E_m \approx \frac{A}{2} \text{ we find}$$

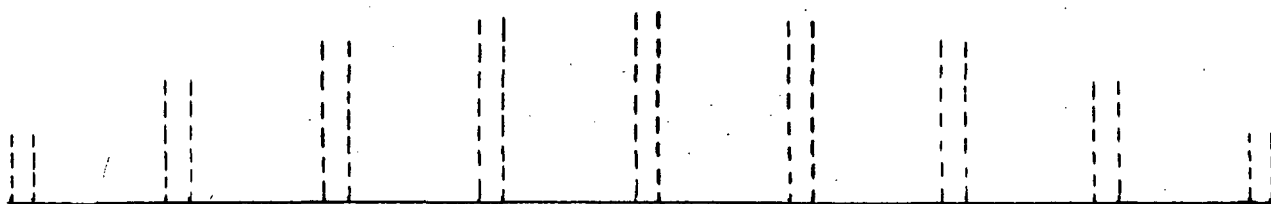
$$\begin{aligned} P(-\frac{1}{2} m \rightarrow \frac{1}{2} m+1) &\propto \frac{Q_{13}^2 + Q_{23}^2}{A^2} (2m+1)^2 [I(I+1) - m(m+1)] \\ &\propto (2m+1)^2 [I(I+1) - m(m+1)] \end{aligned} \quad (56)$$

For ^{93}Nb , ($I = 9/2$), we have, from (52), the relative intensity of the forbidden lines:

$$9 : 16 : 21 : 24 : 25 : 24 : 21 : 16 : 9$$

From Eq. (56), the relative intensity of the forbidden lines is

$$24 : 24 : 14 : 4 : 0 : 4 : 14 : 24 : 24$$



(a) $\beta_n \underline{H} \cdot \underline{g}_n' \cdot \underline{I}$ - term dominant



(b) $\underline{I} \cdot \underline{Q} \cdot \underline{I}$ - term dominant

The relative intensities are plotted in Figs. (a), and (b), in which the doublet is due to the transitions $P(-\frac{1}{2}, m \rightarrow +\frac{1}{2}, m+1)$ and $P(-\frac{1}{2}, m \rightarrow \frac{1}{2}, m-1)$. The experimental evidence is that Fig. (b) matches the structure of the Nb^{4+} forbidden EPR spectrum. It is noted that, from Eq. (56), the line intensity of the forbidden transitions is a function of the off-diagonal quadrupole coupling elements, $(Q_{13}^2 + Q_{23}^2)$, and that if the magnetic field is aligned with one of the principal axes of quadrupole, the off-diagonal elements will be zero. Therefore, the forbidden EPR lines will disappear if the spectrum is taken along one of the quadrupole principal axes (See Figs. 14 and 15). This is, in fact, the way by which these principal axes are experimentally found.

1. Position of EPR Forbidden Lines

In order to understand the EPR spectrum of Nb^{4+} , two more points should be noted: (1) the position of the forbidden lines and (2) the relative line intensity of the allowed EPR lines. In the following, we will discuss the position of forbidden lines first.

Using the selection rule $\Delta M = 1$ and $\Delta m = \pm 1$, we obtain Eq. (57) from Eq. (20'):

$$\begin{aligned}
 h\nu_e &= E_{\frac{1}{2}m} - E_{-\frac{1}{2}m\pm 1} \\
 &= g\beta H_m^{\pm} + (m \pm \frac{1}{2})A + (\mp 2m - 1) f_4 \pm \beta_n H_m^{\pm} f_7 \\
 &\quad + \frac{1}{2}(m \pm m + \frac{1}{2}) f_1 \\
 &\quad - \frac{1}{8}(m^2 \pm m - \frac{95}{4})(f_2 + f_3) \\
 &\quad - 4[2(m \pm 1)^3 + 2m^3 - \frac{97}{2}(2m+1)] f_5 \\
 &\quad + 4[8(m \pm 1)^3 + 8m^3 - 98(2m+1)] f_6 \\
 &\quad + (2m \pm 1)\beta_n^2 (H_m^{\pm})^2 f_8
 \end{aligned} \tag{57}$$

where we have used the relation $I = 9/2$ and have written the resonant d.c. field as H_m^{\pm} corresponding to the forbidden transitions $(\frac{1}{2}m) \rightarrow (-\frac{1}{2}m + 1)$. Eq. (57) leads to the line separation of the forbidden doublets:

$$\begin{aligned}
 g\beta(H_m^+ - H_{m+1}^-) &= 2(2m+1) f_4 - \beta_n(H_{m+1}^- + H_m^+) f_7 \\
 &\quad - \frac{1}{8}(f_2 - f_3)
 \end{aligned} \tag{58}$$

where we have assumed that the second order term of the nuclear interaction $\beta_n^2 (H_m^\pm)^2 f_8$ is negligible compared to the first order term $\beta_n H_m^\pm f_7$. Assuming again that A and g_n are isotropic, and that the Hamiltonian Eq. (22) has been diagonalized along the magnetic field, then

$$f_4 = \frac{3}{2} Q_{33}$$

$$f_7 = g_n$$

$$f_2 - f_3 = \frac{4A^2}{h\nu_e} \quad (59)$$

Thus

$$g\beta (H_m^+ - H_{m+1}^-) = 3(2m+1)Q_{33} - \beta_n g_n (H_{m+1}^- + H_m^+) - \frac{A^2}{2h\nu_e} \quad (60)$$

It is worth to point out a fact that if the sign of A is +, then the position of EPR lines of the + m is at the low field side, while that of the - m at the high field side. Thus, from Eq. (60), if Q_{33} is also +, the line separation of the forbidden doublet will be larger at the high field side. In other words, if A and Q are of the same sign, the larger line separation of the forbidden doublet will occur at the high field side; if A and Q are opposite in sign, the larger separation occurs at the low field side. Experimental results have confirmed this statement.

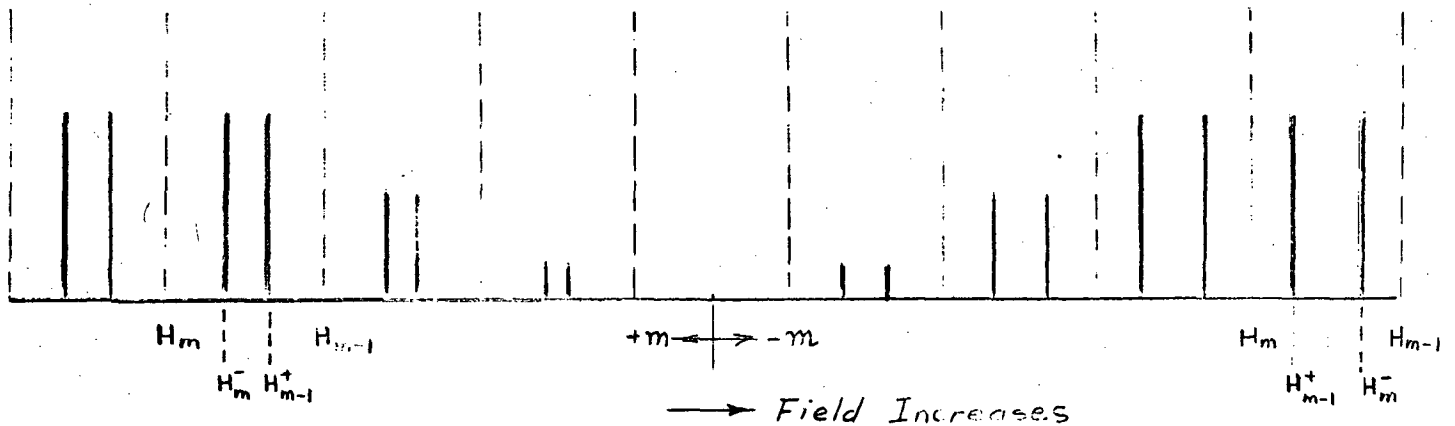
The relative position of the forbidden doublets with respect to the position of the allowed lines can be estimated by considering the first order terms of Eqs. (26) and (57):

Allowed: $h\nu_e = g\beta H_m + mA$

Forbidden: $h\nu_e = g\beta H_m^- + (m-\frac{1}{2})A + (2m-1)f_4 - \beta_n H_m^- f_7$

Forbidden: $h\nu_e = g\beta H_{m-1}^+ + (m-\frac{1}{2})A - (2m-1)f_4 + \beta_n H_{m-1}^+ f_7$

In the x-band operation the magnitudes of the last two terms of the forbidden spectrum are of the same order, but they are one order of magnitude smaller than that of the second term containing A. Therefore the spectrum of the forbidden lines is expected to look like Fig. (c) below:



(c) The Position of Forbidden Lines

In this figure, the dotted and solid vertical lines indicate the allowed and first forbidden lines respectively.

2. Relative Intensity of Allowed EPR Lines

The intensities of the allowed lines can be explained from the result of Eq. (50). If we assume that the term $\beta_n H \cdot g_n' \cdot I$ is negligible compared to the term $\underline{I} \cdot \underline{Q} \cdot \underline{I}$, then Eq. (50) becomes

$$\begin{aligned}
P(-\frac{1}{2} m \rightarrow \frac{1}{2} m) &\propto 1 - 2 \sum_{m'} \left| \frac{\langle m' | \underline{I} \cdot \underline{Q} \cdot \underline{I} | m \rangle}{\Delta E_m - \Delta E_{m'}} \right|^2 \\
&\approx 1 - \frac{2}{|\Delta E_m - \Delta E_{m+1}|^2} \left\{ \left| \langle m+1 | \underline{I} \cdot \underline{Q} \cdot \underline{I} | m \rangle \right|^2 + \left| \langle m-1 | \underline{I} \cdot \underline{Q} \cdot \underline{I} | m \rangle \right|^2 \right\} \\
&= 1 - \frac{Q_{13}^2 + Q_{23}^2}{2|\Delta E_m - \Delta E_{m+1}|^2} \left\{ (2m+1)^2 [I(I+1) - m(m+1)] \right. \\
&\quad \left. + (2m-1)^2 [I(I+1) - m(m-1)] \right\} \tag{61}
\end{aligned}$$

where we have made use of Eq. (54) and have neglected the contribution of the second forbidden transitions. The last step should not be taken for the explanation of the spectrum along one of the principal axes of quadrupole. Assuming $\Delta E_m - \Delta E_{m+1} \approx -\frac{A}{2}$, and $I = 9/2$ we obtain

$$\begin{aligned}
P(-\frac{1}{2} m \rightarrow \frac{1}{2} m) &\propto 1 - \frac{2(Q_{13}^2 + Q_{23}^2)}{A^2} \left\{ (2m+1)^2 \left[\frac{99}{4} - m(m+1) \right] \right. \\
&\quad \left. + (2m-1)^2 \left[\frac{99}{4} - m(m-1) \right] \right\} \tag{62}
\end{aligned}$$

Consequently, the reduction in intensities of the lines $m = 9/2, -7/2, \dots, +7/2, +9/2$, from unity is proportional to

$$12 : 24 : 19 : 9 : 2 : 2 : 9 : 19 : 24 : 12.$$

Along one of the principal axes of quadrupole, Eq. (61) becomes

$$\begin{aligned}
P(-\frac{1}{2} m \rightarrow \frac{1}{2} m) &\propto 1 - \frac{2}{|\Delta E_m - \Delta E_{m+2}|^2} \left\{ \left| \langle m+2 | \underline{I} \cdot \underline{Q} \cdot \underline{I} | m \rangle \right|^2 \right. \\
&\quad \left. + \left| \langle m-2 | \underline{I} \cdot \underline{Q} \cdot \underline{I} | m \rangle \right|^2 \right\}
\end{aligned}$$

$$\begin{aligned}
&= 1 - \frac{(Q_{11} - Q_{22})^2}{8 |\Delta E_m - \Delta E_{m+2}|^2} \left[\frac{99}{4} - m(m+1) \right] \left[\frac{99}{4} - (m+1)(m+2) \right] \\
&\quad + \left[\frac{99}{4} - m(m-1) \right] \left[\frac{99}{4} - (m-1)(m-2) \right] \quad (63)
\end{aligned}$$

Making the approximation $\Delta E_m - \Delta E_{m+2} \sim -A$, we have

$$\begin{aligned}
P\left(-\frac{1}{2}m \rightarrow \frac{1}{2}m\right) &\propto 1 - \frac{(Q_{11} - Q_{22})^2}{8A^2} \left\{ \left[\frac{99}{4} - m(m+1) \right] \left[\frac{99}{4} - (m+1)(m+2) \right] \right. \\
&\quad \left. + \left[\frac{99}{4} - m(m-1) \right] \left[\frac{99}{4} - (m-1)(m-2) \right] \right\} \quad (64)
\end{aligned}$$

for $m = -9/2, -7/2, \dots, +9/2$. Consequently, the reduction intensities of lines $m = -9/2, \dots, +9/2$ from unity, along the principal axes of quadrupole is proportional to

$$6 : 14 : 27 : 39 : 46 : 46 : 39 : 27 : 14 : 6$$

Combining the result of Eq. (62) with Fig. (c) we arrive at the conclusion that at a general angle the spectrum looks like Fig. 1 which can be compared with the spectrum of Fig. 11 taken at the c-axis of the CaWO_4 crystal.

(A and Q are of the same sign.)

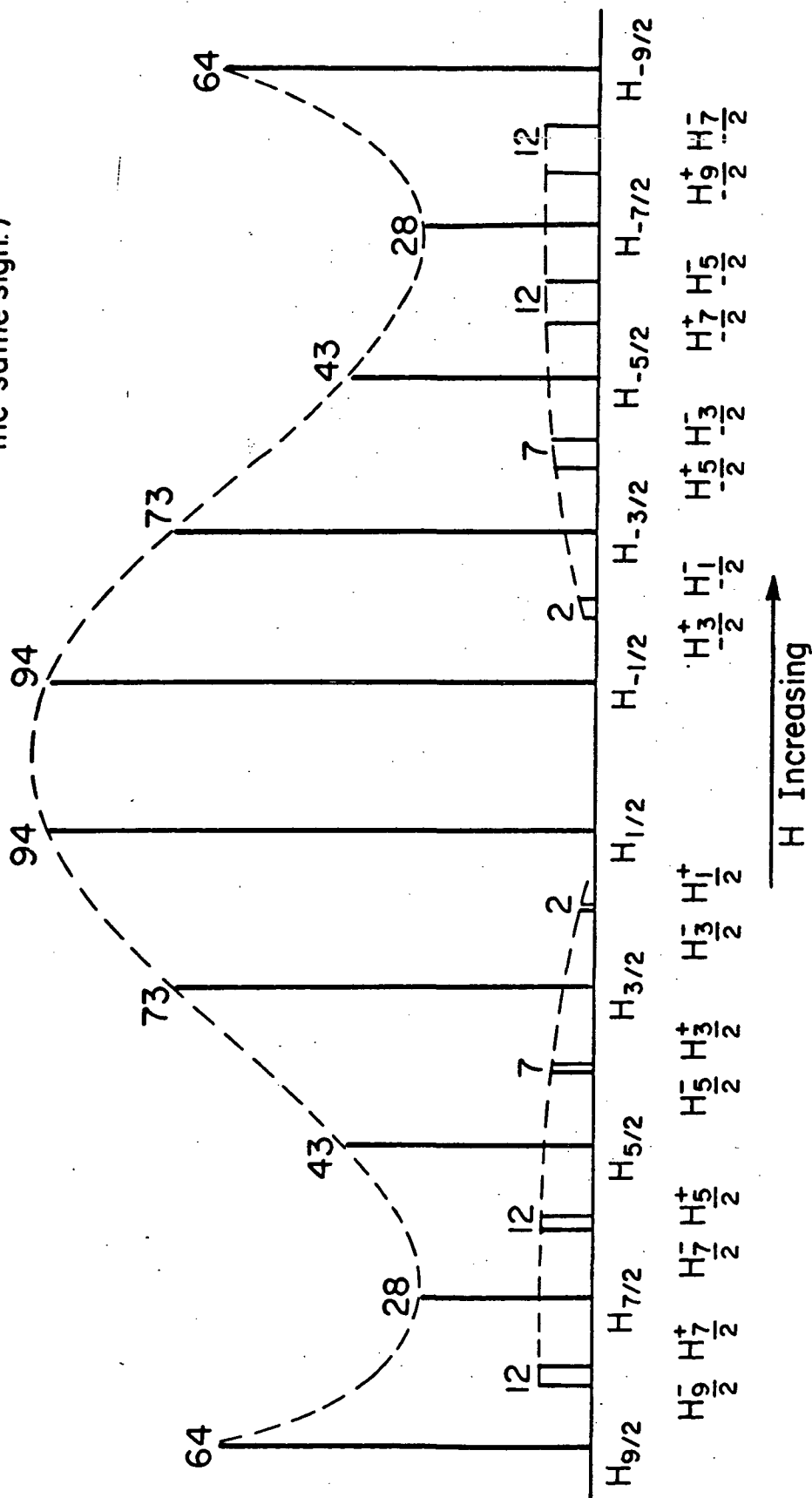


Fig. 1. A composite spectrum of allowed and forbidden EPR lines showing the relative line intensities and line positions.

Chapter IV

ELECTRON NUCLEAR DOUBLE RESONANCE

A. Qualitative Description

The electron nuclear double resonance technique, known as ENDOR was introduced by Feher in 1956.^(25, 26, 27) Originally the ENDOR technique was applied with great success to the study of the electronic structure of F centers in KCl⁽²⁸⁾ and of donors (Sb, P and As) in silocon.^(29, 31, 32) More recently this technique has been used in a variety of fields^(30, 33-45) especially where the EPR lines are inhomogeneously broadened by hyperfine or superhyperfine interactions. The experiment consists of monitoring the change in intensity of a partially saturated EPR signal induced by the application of a radio frequency field to the sample at the appropriate nuclear resonance frequency. The change in intensity of the EPR signal is caused by the alteration of the spin population when transition occur between the hyperfine levels. The particular advantage of the ENDOR technique is the accuracy with which hyperfine separations, the quadrupole coupling, and the nuclear gyromagnetic ratio can be measured and hence the possible observation of second order perturbations on the energy levels of the system.

To explain the technique, consider an ion which has a two fold electron spin degeneracy of the ground state so that in a magnetic field there are two energy levels that can be labeled

$M = \pm \frac{1}{2}$. Let us assume for simplicity, that the nuclear spin of the ion is $I = 3/2$ which will cause a splitting of each of the electron spin levels into four with $m = 3/2, +\frac{1}{2}, -\frac{1}{2}, -3/2$. The eight ground state levels can thus be described by using the notation (M, m) . In thermal equilibrium the electron populations of these levels in ascending order of energy can be represented by N_1, N_2, \dots, N_8 , (see Figure 2). The relationship of the population with the energy level is described by the Boltzmann equation

$$\frac{N'}{N} = e^{-(E_{N'} - E_N)/kT}$$

Let us assume that a d.c. magnetic field of the appropriate intensity is applied to the sample such that the EPR transition is observed between the levels $(-\frac{1}{2}, +\frac{1}{2})$ and $(+\frac{1}{2}, +\frac{1}{2})$ when the microwave frequency ν_e is 9,300 MHz. Let us also assume that the frequency ν_n for all the hyperfine transitions is about 45 MHz and the sample temperature T is 4.2°K. Then when the system is in the thermal equilibrium

$$\frac{N_7}{N_2} = 0.9045, \quad \frac{N_1}{N_2} = 0.9995$$

Thus there is a relatively large population difference between the levels for the EPR signal and a small difference for neighboring hyperfine transitions. Through the exchange of the spin energy with the lattice the increased population in the upper state due to the applied microwave field will attempt to return to thermal equilibrium. If the rate of promotion of the spins from the lower state is greater than the return to the ground state through the

spin lattice interaction, the population difference will gradually decrease. This phenomenon is called saturation and is said to be "complete" when the population difference is zero. Using the Boltzmann equation an effective spin temperature T_s can be defined which describes the population difference n between the two levels.⁽⁴⁶⁾ The ratio n/n_0 is called the saturation factor,⁽¹⁴⁾ where n_0 is the population difference in thermal equilibrium and $T_s = T / (n/n_0)$. For illustration, let us suppose that the microwave power is adjusted so that the saturation factor is 40% corresponding to a spin temperature of $T_s = 10.5^\circ\text{K}$ for the EPR line. Fig. 2 shows the population of the various levels relative to the ground state when the system is in thermal equilibrium and with a 40% saturation factor. It is obvious that the population of the level $(\frac{1}{2}, \frac{1}{2})$ is now larger than its neighboring levels $(\frac{1}{2} - \frac{1}{2})$ and $(\frac{1}{2}, 3/2)$ whilst the level $(-\frac{1}{2}, \frac{1}{2})$ has a lower population than its neighbors. The rate of energy absorption P is proportional to the population difference for levels separated by energy $h\nu_e$:

$$P = nwh\nu_e$$

where w is the transition probability and n is the population difference. The strength of EPR signal is proportional to P . Thus upon saturation the EPR signal is reduced in intensity.

The application of a radio frequency signal ν_n can cause transitions between levels with $\Delta m = \pm 1$ and $\Delta m = 0$. Since the population of the spin state $(-\frac{1}{2}, \frac{1}{2})$ is substantially less than that of $(-\frac{1}{2}, -\frac{1}{2})$ and $(-\frac{1}{2}, 3/2)$ transitions are induced from the latter levels to the $(-\frac{1}{2}, \frac{1}{2})$ state. Thus the population of the

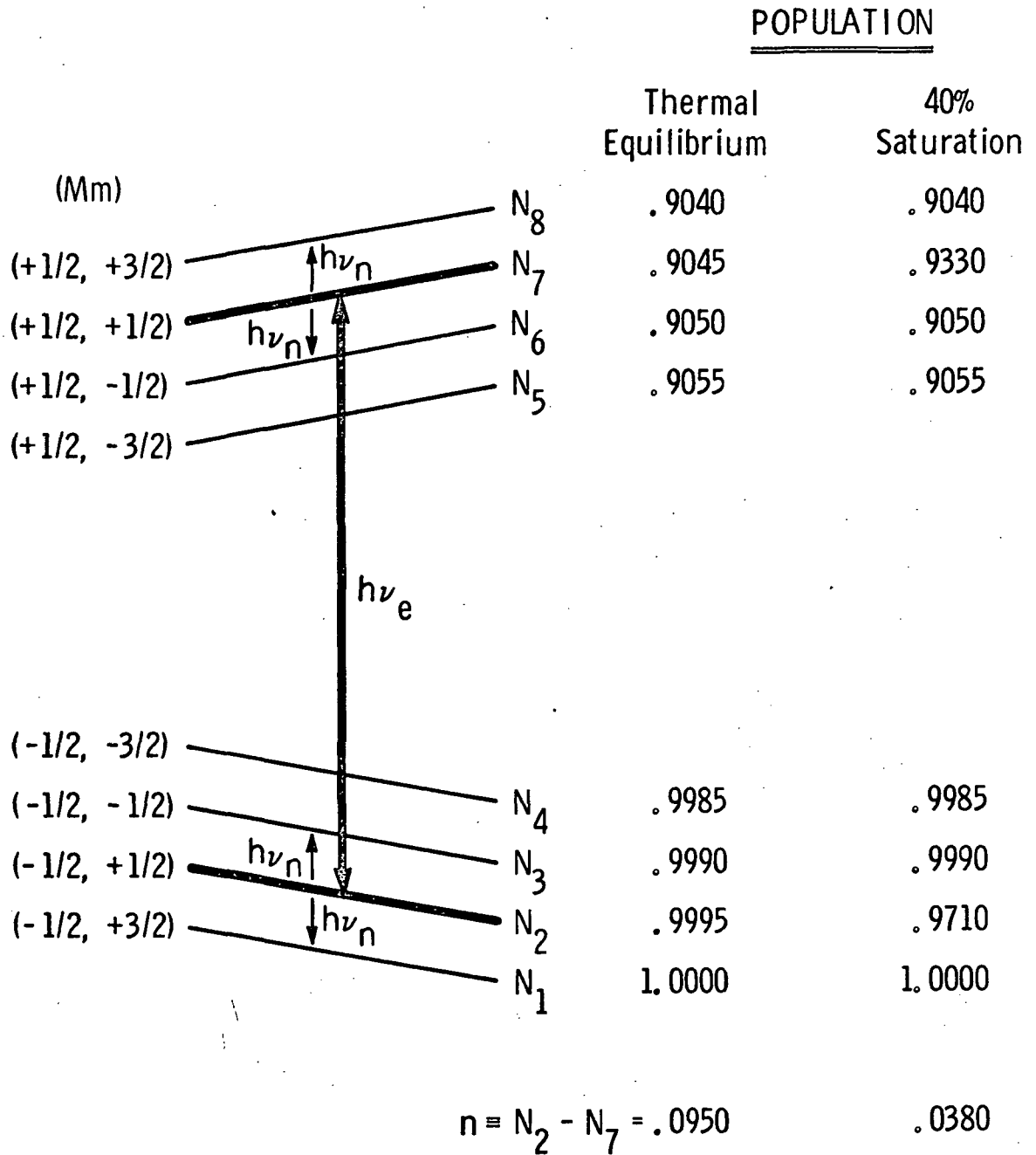


Fig. 2. Spin population for thermal equilibrium and partially saturated cases.

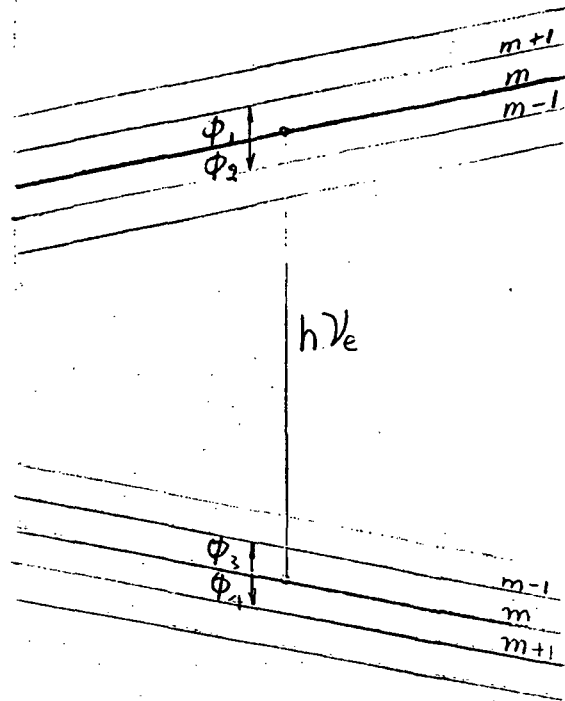
state $(-\frac{1}{2}, \frac{1}{2})$ is increased by the ENDOR signal. On the other hand the same signal will cause the population of the $(+\frac{1}{2}, +\frac{1}{2})$ state to decrease. Hence the application of the RF signal causes the population difference for the EPR transition to increase, thus the degree of saturation decreases and the EPR signal intensity increases. If the d.c. magnetic field and the microwave frequency are kept fixed at the peak of the EPR line while the RF signal generator sweeps through the range of the nuclear resonance the result will be an ENDOR spectrum corresponding to a resonant nuclear transition (see Fig. 16 on page 86). This is sometimes called the "ENDOR-induced EPR spectrum".⁽⁴¹⁾ Since, in general, the hyperfine splittings do not have exactly equal spacings, four ENDOR lines are obtained but only two when the EPR transition is between an outer hyperfine pair of levels.

B. ENDOR Signal

In ENDOR experiments, transitions between adjacent nuclear magnetic states are induced. Hence the observed frequencies are obtained from Eqs. (24') and (65) keeping in mind the selection rules $\Delta M = 0$ and $\Delta m = \pm 1$. These ENDOR frequencies are given by Eq. (66).

$$M = \frac{1}{2}$$

$$M = -\frac{1}{2}$$



$$A > 0$$

$$\phi_1 = h\nu^{\frac{1}{2}} (+) \equiv E_{\frac{1}{2}m+1} - E_{\frac{1}{2}m}$$

$$\phi_2 = h\nu^{\frac{1}{2}} (-) \equiv E_{\frac{1}{2}m} - E_{\frac{1}{2}m-1}$$

$$\phi_3 = h\nu^{-\frac{1}{2}} (-) \equiv E_{-\frac{1}{2}m-1} - E_{-\frac{1}{2}m}$$

$$\phi_4 = h\nu^{-\frac{1}{2}} (+) \equiv E_{-\frac{1}{2}m} - E_{-\frac{1}{2}m+1}$$

(65)

$$\phi_1 = \frac{A}{2} - g_n \beta_n H_m - \frac{m+1}{2h\nu_e} A^2 + (2m+1)f_u + \frac{V}{2} - W(3m^2+3m+1)$$

$$\phi_2 = \frac{A}{2} - g_n \beta_n H_m - \frac{m}{2h\nu_e} A^2 + (2m-1)f_u + \frac{V}{2} - W(3m^2-3m+1)$$

$$\left. \begin{aligned} \phi &= \frac{A}{2} + g_n \beta_n H_m - \frac{m-1}{2h\nu_e} A^2 - (2m-1)f_4 + \frac{V}{2} - W(3m^2-3m+1) \\ \phi &= \frac{A}{2} + g_n \beta_n H_m - \frac{m}{2h\nu_e} A^2 - (2m+1)f_4 + \frac{V}{2} - W(3m^2+3m+1) \end{aligned} \right\} \quad (66)$$

where ϕ_1, ϕ_2, ϕ_3 and ϕ_4 are the ENDOR frequencies measured at the d.c. magnetic field H_m corresponding to the quantum number m , and V and W are defined as

$$V = 8 [2I(I+1)-1]f_5 + [-4I(I+1)+1]f_6 \quad (67)$$

$$W = 8 (f_5 - 4f_6) \quad (68)$$

When Eq. (66) is plotted as ENDOR frequencies versus m , there will be four curves. Since the term $g_n \beta_n H_m$ ($\sim 3.3 \text{ MHz}$) is very much smaller than A and to the first approximation H_m is linear to m (see Eq. (26)), this term will have only minor effect on the shape of these curves. Thus if W is small, these curves become four straight lines, while if W is big, they are four parabolas.

From Eq. (66) we derive the following relations between the measured quantities of ENDOR experiment and the parameters f_4, V, W and A . These relations are important because through them we can calculate the quadrupole coupling constant Q , nuclear g -factor g_n and hyperfine coupling constant A .

$$\phi_1 - \phi_2 + \phi_3 - \phi_4 = 4f_4 \quad (69)$$

$$\phi_1 - \phi_2 - \phi_3 + \phi_4 = -\frac{A}{h\nu_e} - 12mW \quad (70)$$

$$\phi_1 + \phi_2 - \phi_3 - \phi_4 = -4g_n \beta_n H_m - \frac{A^2}{h\nu_e} + 8mf_4 \quad (71)$$

$$\phi_1 + \phi_2 + \phi_3 + \phi_4 = 2(A+V) - \frac{2m}{h\nu_e} A^2 - 4(3m^2+1)W \quad (72)$$

These equations are valid for $m = -7/2, -5/2, \dots, +5/2, +7/2$.

A plot of the left hand side (the various algebraic sums of frequencies) of Eqs. (69) to (72) versus m reveals the correctness of the method we employed to attack the problem. For example, the plot of the left hand side of Eq. (69) against m should be a horizontal line since f_4 is independent of m . If the plot does not appear as a horizontal line, then we have to go back to the original Eq. (24') from which the ϕ 's are derived. The fact is that this plot is a parabola instead of a straight line. To explain this phenomenon we note that had we started from Eq. (24) instead of Eq. (24') we would obtain the result:

$$\phi_1 - \phi_2 + \phi_3 - \phi_4 = 4f_4 + (f_5 K_5(m) + f_6 K_6(m)) \quad (69')$$

in which

$$\begin{aligned} K_5(m) &= \left[\frac{99}{4} - (m+1)(m+2) \right] \left[\frac{99}{4} - (m+2)(m+3) \right] \frac{8 \left(\frac{f_4}{A} \right)^2 (m+2)}{1 - 16 \left(\frac{f_4}{A} \right)^2 (m-2)^2} \\ &+ 2 \left[\frac{99}{4} - m(m+1) \right] \left[\frac{99}{4} - (m+1)(m+2) \right] \frac{-8 \left(\frac{f_4}{A} \right) (m+1)}{1 - 16 \left(\frac{f_4}{A} \right)^2 (m+1)^2} \\ &+ 2 \left[\frac{99}{4} - m(m-1) \right] \left[\frac{99}{4} - (m-1)(m-2) \right] \frac{8 \left(\frac{f_4}{A} \right) (m-1)}{1 - 16 \left(\frac{f_4}{A} \right)^2 (m-1)^2} \\ &+ \left[\frac{99}{4} - (m-1)(m-2) \right] \left[\frac{99}{4} - (m-2)(m-3) \right] \frac{-8 \left(\frac{f_4}{A} \right) (m-2)}{1 - 16 \left(\frac{f_4}{A} \right)^2 (m-2)^2} \\ &\approx 24 \left(-\frac{99}{4} + 5m^2 \right) \left(\frac{8f_4}{A} \right) \end{aligned}$$

$$\begin{aligned}
K_6(m) &= (2m+3)^2 \left[\frac{99}{4} - (m+1)(m+2) \right] \frac{8 \left(\frac{f_4}{A} \right) (2m+3)}{1-4 \left(\frac{f_4}{A} \right)^2 (2m+3)^2} \\
&+ 3(2m+1)^2 \left[\frac{99}{4} - m(m+1) \right] \frac{-8 \left(\frac{f_4}{A} \right) (2m+1)}{1-4 \left(\frac{f_4}{A} \right)^2 (2m+1)^2} \\
&+ 3(2m-1)^2 \left[\frac{99}{4} - m(m-1) \right] \frac{8 \left(\frac{f_4}{A} \right) (2m-1)}{1-4 \left(\frac{f_4}{A} \right)^2 (2m-1)^2} \\
&+ (2m-3)^2 \left[\frac{99}{4} - (m-1)(m-2) \right] \frac{-8 \left(\frac{f_4}{A} \right) (2m-3)}{1-4 \left(\frac{f_4}{A} \right)^2 (2m-3)^2} \\
&\approx 12(90-40m^2) \left(\frac{8f_4}{A} \right) \tag{73}
\end{aligned}$$

where we have written $I(I+1) = 99/4$ so that

$$\begin{aligned}
\phi_1 - \phi_2 + \phi_3 - \phi_4 &\approx 4f_4 - (4368 \frac{f_5}{A} - 8640 \frac{f_6}{A}) f_4 \\
&+ m^2 (960 \frac{f_5}{A} - 3840 \frac{f_6}{A}) f_4 \tag{69"}
\end{aligned}$$

We will use this equation to find the more accurate value of f_4 .

Summing up the expressions of "-m" and "+m", Eqs. (70)

to (72) become:

$$(\phi_1 - \phi_2 - \phi_3 + \phi_4)_m + (\phi_1 - \phi_2 - \phi_3 + \phi_4)_{-m} = -\frac{2A^2}{h\nu_e} \tag{74}$$

$$\begin{aligned}
(\phi_1 + \phi_2 - \phi_3 - \phi_4)_m + (\phi_1 + \phi_2 - \phi_3 - \phi_4)_{-m} \\
= -4g_n \beta_n (H_{+m} + H_{-m}) - \frac{2A^2}{h\nu_e} \tag{75}
\end{aligned}$$

$$\begin{aligned}
(\phi_1 + \phi_2 + \phi_3 + \phi_4)_m + (\phi_1 + \phi_2 + \phi_3 + \phi_4)_{-m} \\
= 4(A+V) - 8(3m^2+1)W \tag{76}
\end{aligned}$$

These equations give more accurate results for A and g_n

because of the cancellation of the odd-order errors. The magnitude of A is found in the following manner: Q' and Q'' are first calculated from the f_4 of Eq. (69"). Then f_5 and f_6 are calculated from Eq. (25) by using a value of A from the first approximation. The parameters V and W are calculated from Eqs. (67) and (68). The final value of A is then found by the help of Eq. (76). For example, along the principal axes X_Q , Y_Q and Z_Q of the Q-tensor, we have

$$(f_4)_i = \frac{3}{2} Q_i \quad (77)$$

$$(f_5)_i = \frac{(Q_j - Q_k)^2}{16A_i} \quad (78)$$

$$(f_6)_i = 0 \quad (79)$$

$$(V)_i = 388(f_5)_i \quad (80)$$

$$(W)_i = 8(f_5)_i, \text{ and} \quad (81)$$

$$A_i = \frac{1}{4} (\sum_m \phi + \sum_{-m} \phi) + 2(3m^2 + 1)W_i - (V)_i \quad (82)$$

where i, j, k take X_Q, Y_Q and Z_Q cyclically and $\sum_m \phi$ denotes the summation of ENDOR frequencies measured at the niobium hyperfine line of quantum number m . Thus if we know the principal axes X_Q, Y_Q and Z_Q we can measure the ENDOR frequencies along these directions and calculate $(f_4)_i$ or Q_i by Eq. (69"). Once the parameters Q_i are known, we can find f_4, f_5 and f_6 along any direction through Eqs. (23) and (25). Then the A-value of a general direction can be found easily either by ENDOR technique, Eq. (76) or even by EPR technique, Eq. (32).

C. The Assumption of Negative A-Value

In order to see the consequence of a "-A" assumption we first have to obtain a formulation of ENDOR experiment for "-A". Since A and f_4 should have the same sign, we also assume f_4 to be "-". Under this assumption Eq. (65) and Eq. (66) becomes

$$\phi'_1 = E_{\frac{1}{2} m-1} - E_{\frac{1}{2} m}$$

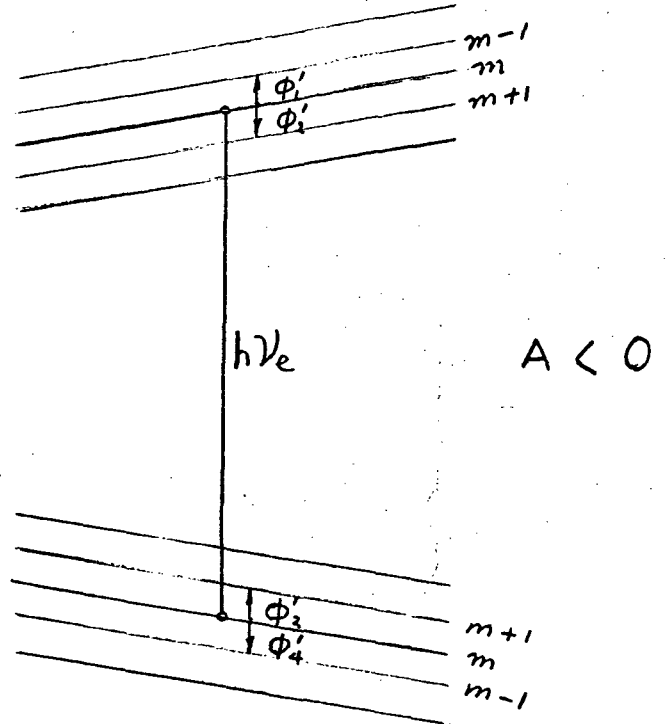
$$M = +\frac{1}{2}$$

$$\phi'_2 = E_{\frac{1}{2} m} - E_{\frac{1}{2} m+1}$$

$$\phi'_3 = E_{-\frac{1}{2} m+1} - E_{-\frac{1}{2} m}$$

$$\phi'_4 = E_{-\frac{1}{2} m} - E_{-\frac{1}{2} m-1}$$

$$M = -\frac{1}{2}$$



$$\phi'_1 = -\frac{A'}{2} + \beta_n g_n H_m + \frac{m A'^2}{2 h \nu_e} - (2m-1) f'_4 - \frac{1}{2} V' + (3m^2 - 3m + 1) W'$$

$$\phi'_2 = -\frac{A'}{2} + \beta_n g_n H_m + \frac{m+1}{2 h \nu_e} A'^2 - (2m+1) f'_4 - \frac{1}{2} V' + (3m^2 + 3m + 1) W'$$

$$\phi'_3 = -\frac{A'}{2} - \beta_n g_n H_m + \frac{m}{2 h \nu_e} A'^2 + (2m+1) f'_4 - \frac{1}{2} V' + (3m^2 + 3m + 1) W'$$

$$\phi'_4 = -\frac{A'}{2} - \beta_n g_n H_m + \frac{m-1}{2 h \nu_e} A'^2 + (2m-1) f'_4 - \frac{1}{2} V' + (3m^2 - 3m + 1) W'$$

where

$$A' = -A$$

$$\left. \begin{aligned} V' &= -V \\ W' &= -W \end{aligned} \right\} W \text{ and } V \text{ being } \propto \frac{1}{A}$$

$$f_4' = -f_4$$

Let

$$\phi_1'' = -\phi_1'$$

$$\phi_2'' = -\phi_2'$$

$$\phi_3'' = -\phi_3'$$

$$\phi_4'' = -\phi_4'$$

Then,

$$\phi_1' = \frac{A'}{2} - \beta_n g_n H_m - \frac{m}{2h\nu_e} A'^2 + (2m-1)f_4' + \frac{1}{2} V' - (3m^2-3m+1) W'$$

$$\phi_2' = \frac{A'}{2} - \beta_n g_n H_m - \frac{m+1}{2h\nu_e} A'^2 + (2m+1)f_4' + \frac{1}{2} V' - (3m^2+3m+1) W'$$

$$\phi_3' = \frac{A'}{2} + \beta_n g_n H_m - \frac{m}{2h\nu_e} A'^2 - (2m+1)f_4' + \frac{1}{2} V' - (3m^2+3m+1) W'$$

$$\phi_4' = \frac{A'}{2} + \beta_n g_n H_m - \frac{m-1}{2h\nu_e} A'^2 - (2m-1)f_4' + \frac{1}{2} V' - (3m^2-3m+1) W'$$

which leads to

$$\phi_1'' - \phi_2'' + \phi_3'' - \phi_4'' = -4f_4'$$

$$\phi_1'' - \phi_2'' - \phi_3'' + \phi_4'' = \frac{A'^2}{h\nu_e} + 12mW'$$

$$\phi_1'' + \phi_2'' - \phi_3'' - \phi_4'' = -4\beta_n g_n H_m - \frac{A'^2}{h\nu_e} + 8mf_4'$$

$$\phi_1'' + \phi_2'' + \phi_3'' + \phi_4'' = 2(A'+V') - \frac{2m}{h\nu_e} A'^2 - 4(3m^2+1)W'$$

Let

$$\phi_1'' \rightarrow -\phi_4$$

$$\phi_2'' \rightarrow -\phi_3$$

$$\phi_3'' \rightarrow -\phi_2$$

$$\phi_4'' \rightarrow -\phi_1$$

$$m \rightarrow -m$$

$$A' \rightarrow -A$$

$$f_4' \rightarrow -f_4$$

$$g_n \rightarrow +g_n$$

$$V' \rightarrow -V$$

$$W' \rightarrow -W$$

Then we obtain

$$-\phi_4 + \phi_3 - \phi_2 + \phi_1 = 4f_4$$

$$-\phi_4 + \phi_3 + \phi_2 - \phi_1 = \frac{A^2}{h\nu_e} + 12 \text{ mW}$$

$$-\phi_4 - \phi_3 + \phi_2 + \phi_1 = -4\beta_n g_n H_m - \frac{A^2}{h\nu_e} + 8mf_4$$

$$-\phi_4 - \phi_3 - \phi_2 - \phi_1 = -2(A+V) + \frac{2m}{h\nu_e} A^2 + 4(3m^2+1)W$$

or

$$\phi_1 - \phi_2 + \phi_3 - \phi_4 = 4f_4$$

$$\phi_1 - \phi_2 - \phi_3 + \phi_4 = -\frac{A^2}{h\nu_e} - 12\text{mW}$$

$$\phi_1 + \phi_2 - \phi_3 - \phi_4 = -4g_n \beta_n H_m - \frac{A^2}{\hbar v_e} + 8 m f_4$$

$$\phi_1 + \phi_2 + \phi_3 + \phi_4 = 2(A+V) - \frac{2m}{\hbar v_e} A^2 - 4(3m+1)W$$

which are just Eqs. (69) to (72). Therefore the g_n value will be the same for the assumption of either +A and +Q (i.e. f_4), or -A and -Q (i.e. $-f_4$).

Chapter V

EXPERIMENTAL SETUP

A. EPR Spectrometer System

The entire instrumentation is shown in the block diagram, Fig. 10. Functionally it may be grouped into four parts, namely, the x-band microwave circuitry, the low frequency equipment (the console), the DC electromagnet, and the low temperature dewar system (not included in the figure). Although the diagram is self-explanatory, a few qualitative comments will be made to clarify a few points that are not immediately obvious.

The microwave power is provided by a type VA-153 / 6315 mechanically tunable klystron, 8.5-10.0 GHz, rated at 300 mW maximum power output. The klystron power is taken out through the terminals marked "high" and "low" indicated by the letters A' and A in Fig. 10. The power from the "low" outlet flows along the path A, B, and C, back into B, and then into D. The letter C designates the cavity, containing the sample under investigation. The power absorption of the sample gives rise to an amplitude modulated wave containing information about the magnetic susceptibility $\chi(\omega)$ of the sample.

The wave from the "high" outlet flows along A' B' C', then into D', which is port #2 of the balanced detector. At C', the 30 MHz signal on the 1N23 diode gives rise to a reference signal

30 MHz away from the klystron output frequency.

The circuits associated with the hybrid tee and the crystal mount work as a substitute for a local oscillator of a superheterodyne detector. In a conventional heterodyne detection technique, ^(63, 64) the local oscillator microwave power is generated by a separate klystron operated at a frequency of $f_0 + 30$ MHz (or $f_0 - 30$ MHz) and incorporated with an additional frequency stabilization network. The electronic circuit required is more complicated and the dynamic range of frequency operation is limited. In the present setup the local oscillator klystron and its associated components are all eliminated. Only one klystron supplies the power to the whole system. The frequency is stabilized by an automatic frequency control (AFC) circuit with the sample cavity as the frequency reference. This circuit resembles the homodyne balanced mixer introduced by Henning ⁽⁶⁵⁾ with the modification of an addition of IF signal circuit which helps to eliminate the crystal noise. ⁽⁶⁴⁾ The IF generator has a stability of better than ± 200 Hz per hour when operated in the 30 MHz range. Hence, there is no drift problem. The operation is simple, and once the IF signal generator is aligned to the IF amplifier no more adjustment is required. The superheterodyne is always in optimum condition no matter how the klystron frequency is changed.

The electromagnet system contains a Varian 12-inch magnet of 3" gap, a Varian 2100 B regulated magnet power supply and a V-4280 Precession Field Scanning Unit. The regulated power supply can produce a current of 20 ma to 2 amperes to the magnet. The corresponding maximum magnetic field obtainable is more than 11,000

gauss. The regulation is one part per 100,000 with 10% line voltage fluctuation. Field scanning is obtained by rotating the arm of a precision potentiometer with a constant speed motor and gear train in the Precession Field Scanning Unit. A scanning speed of from 1 gauss/min to 500 gauss/min is available in the range of magnetic field 0 to 10,000 by selecting a proper resistance in series with the precision potentiometer.

In the 3" pole gap a double glass dewar system is installed for low temperature operation, consisting of an outer and an inner dewar. The cavity system is housed in the inner dewar. (See the drawing, Fig. 3). The liquid nitrogen fills the space between the outer and inner dewars. This is a capacity of 1.5 liter of liquid nitrogen which can maintain the temperature for 15 hours after reaching equilibrium. Liquid helium is transferred into the inner dewar for ENDOR experiments. It can take 0.9 liter of liquid helium which will last for about 4 to 5 hours.

The magnetic field was measured by using a Varian Nuclear Fluxmeter Model F-8 with a proton probe located outside the dewar vessel. The NMR frequency of the fluxmeter was first beat against a Beckman Transfer Oscillator Model 7580, and then monitored by a Beckman Universal EPUT and Timer Model 7370. The inaccuracy of the fluxmeter is ± 0.04 gauss at 3000 gauss mainly due to the proton line width. The frequency stability of the transfer oscillator is 10^{-6} per min. and the accuracy is ± 1 kHz.

The microwave frequency of the klystron is monitored by an hp-X532 B frequency meter, which can be read to ± 1 MHz with

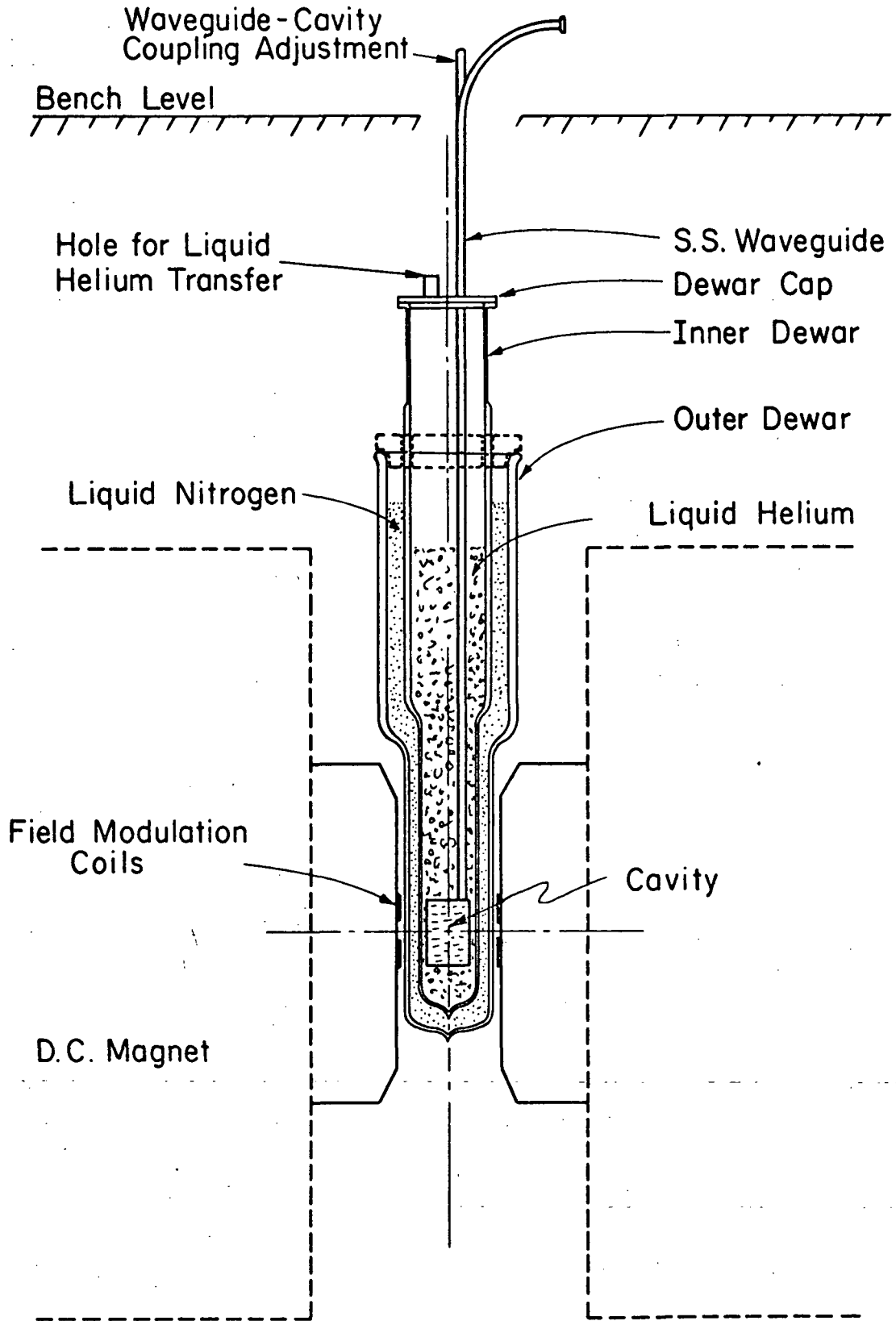


Fig. 3. The Magnet and Dewar System

good reproducibility. A higher accuracy is obtained by using the transfer oscillator and EPUT equipment. When the klystron oscillates in the 9200 to 9700 MHz range, the 66th harmonics of the transfer oscillator frequency (75-150 MHz) beats strongly with the microwave, and the EPUT counter gives the frequency in six figures, e.g., 9297.55 MHz \pm .05 MHz.

B. The ENDOR Arrangement

The ENDOR instrumentation includes the signal generator the wide band voltage amplifiers and the power amplifiers in addition to the whole EPR arrangement. (See Fig. 10). There is also a modification in the cavity design as will be seen later.

1. The Signal Generator

The radio frequency (RF) signal is generated by an FM-AM Standard Signal Generator of Type MS27 made by Radiometer, Denmark. This instrument covers a frequency band from 0.3 up to 240 MHz in five ranges. It has a voltage output adjustable from 0.1 μ Volt to 0.1 volt across a 50-ohm load; with a frequency stability of 5×10^{-5} per hour for frequencies from 15 MHz to 240 MHz. For external FM, a source of approximately 3 volts into a 200 Kohm load is required. The maximum frequency deviation obtainable is 600 KHz. For this measurement, a 400 Hz external modulating frequency is used and the deviation frequency is about 80 KHz. The 400 Hz modulating signal is generated by the low frequency oscillator amplifier in the console for EPR use and is switched to the signal generator when ENDOR measurement starts. Frequency

modulation is used rather than amplitude modulation because FM is found to be more effective for the observation of ENDOR signal in this experiment. A low speed drive unit has been installed on the frequency tuning dial for ENDOR field scanning. In the range of 30 MHz to 60 MHz the scanning rate is about 1.4 MHz per minute. The frequency of the signal generator is accurately measured by an hp-5246L Electronic Counter with an hp-5251A Frequency Converter as a plug-in unit.

2. The Voltage Amplifier

The output of the signal generator is boosted by two (or three) hp-460 AR wide band amplifiers connected in cascade. Each amplifier has a band pass from 100 KHz to 120 MHz and a voltage gain of 20 db. These amplifiers can be substituted by two (or three) solid state distributed amplifiers of Model 3007 from C-COR Electronics, Inc., State College, Pa. The latter provides a wider band pass of 100 KHz to 225 MHz with at least 36 db total gain. However, neither type of amplifiers gives sufficient power output to drive the ENDOR coil.

3. The Power Amplifier

The ENDOR coil is powered by two Model ifi 500 wide band amplifiers via a few feet of coaxial cable. These amplifiers are connected for series operation following the voltage amplifiers. Each power amplifier has a band pass of 200 KHz to 220 MHz, a gain of 10 db, input impedance of 90 ohms, output impedance of 180 ohms and a power output capability of 3 watts cw. It was found hard to match the ENDOR coil with the output of the amplifier for the

whole working frequency band. However, since the power of the amplifier was high enough, the mismatch did not constitute a problem in this experiment.

4. The Cavity

The cylindrical cavity has dimensions of 40 mm ID x 50 mm length with 3mm wall thickness. The mode of the standing wave inside the cavity is TE_{011} . The resonant frequency f_r can be estimated from the formula (83) (66):

$$(f_r D)^2 = A + B \left(\frac{D}{L}\right)^2 \quad (83)$$

where f_r is in MHz

D = inside diameter in inches

L = inside length in inches

A = $(c r_1 / \pi)^2 = 2.0707 \times 10^8$

B = $(c/2)^2 = 0.34799 \times 10^8$

c = Velocity of light = 1.17981×10^{10} inches/sec.

r_1 = the 1st non-zero root of the cylindrical Bessel

Function $J'_1(r)$

= 3.83171

The raw material for the cavity is Lava, grade A, made by American Lava Corporation. Chemically it is an hydrous aluminum silicate. It is machinable; but there is a 1.5% shrinkage under heat treatment. Hence just after machining, the cavity size should be proportionally larger than that specified in Fig. 4. It is then fired up to 2000°F, the furnace is shut off and left to

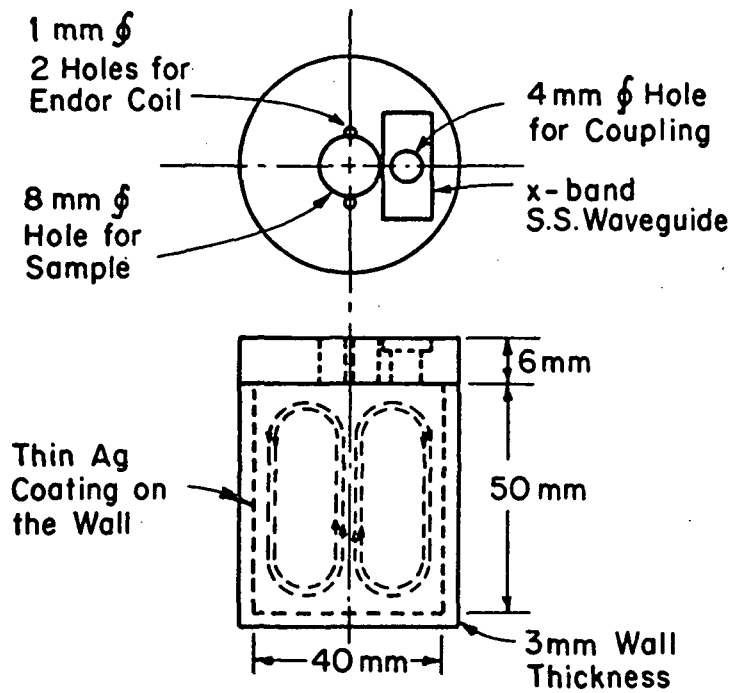


Fig. 4. Details of a Lava Cavity and the Magnetic field of mode TE_{011}

cool down to room temperature by itself. The inside wall of the cavity is painted with Du Pont Silver #4731 and fired up to 1100°F. This makes the silver adhere to the wall. The painting and firing can be repeated for two or three times if the silver coating appears uneven at first.

A schematic of the cavity is given in Fig. 4 and the assembly drawing of cavity and wave guide is shown in Fig. 5. A hole of 8mm diameter at the center of the cavity cap is provided for the insertion of samples and another hole of 4mm diameter inside the waveguide for microwave coupling. For optimal operation, the coupling hole is positioned at about half the cavity radius from the center.⁽⁶⁶⁾ The coupling is achieved by a small loop of copper wire in a figure of 8 embedded in a piece of teflon fixed at the end of a long quartz tubing. This tubing passes through the center of the stainless steel (S.S) waveguide and protrudes out of the waveguide bend. Thus the degree of coupling can be adjusted on top of the dewar vessel during the experiment. (See Fig. 3).

The ENDOR coil is formed by two turns of enamel wire about SWG #30 passed through four small holes on the cavity top and bottom. The area of the coil is 11mm x 59mm. The center of the coil coincides approximately with that of the cavity, where the sample is positioned. One terminal of the coil is grounded on the waveguide surface while the other is soldered to the central wire of the S.S. coaxial cable. The coaxial cable, approximately 29" in length, is clamped at the surface of the S.S. waveguide, and after passing through the dewar cap, the outer end of the

cable is terminated with a BNC connector.

The RF magnetic field generated at the center of the coil was checked by a search coil before the sample was placed in the cavity. The voltage induced in the search coil was measured by the Tektronix Oscilloscope 545 with type 1S1 Sampling Unit and a cathode follower probe. Alternately, the RF field can be calculated from the ENDOR coil area and the current passing through the coil. The current is measured by a Tektronix current probe P6020. Its output, in milliamperes, is then directly read from the 1S1 Sampling Unit and Scope. The latter method can monitor the field when the sample is in position. The results from both methods agree well, the RF field is found to be about 1 gauss peak to peak in the 15-60 MHz frequency range.

When the dc magnet is set at zero degree, the plane of ENDOR coil is parallel with the dc magnetic field. Since this field is located horizontally and the cavity with dewar stands vertically, the three fields, i.e., the dc magnetic field, the microwave field, and the ENDOR field are mutually perpendicular.

C. The Sample

Calcium tungstate has the scheelite structure. It contains four molecules per unit cell and is characterized by the space group C_{4h}^6 symmetry. ⁽⁹⁾ The size of the unit cell is

$$c = 11.376 \pm .003 \text{ \AA}$$

$$a = b = 5.243 \pm .002 \text{ \AA}$$

The crystal $CaWO_4$ can be considered as a composition of WO_4^{--} ions

and Ca^{++} ions bonded together ionically. The radical WO_4^{--} is formed by a tungsten ion W^{6+} covalently bonded to four oxygen ions O^{--} . These four oxygens form a squashed tetrahedron (bisphenoid) with the tungsten ion at the center. The dimension of the squashed tetrahedron is $2.11\text{\AA} \times 2.11\text{\AA} \times 1.96\text{\AA}$ with short side along the c-axis. The W-O distance is 1.78\AA . The diagonal plane of the tetrahedron makes an angle of $31^\circ 54'$ with the a-axis. A schematic diagram of the unit cell is given in Figs. 6 and 7.

The orientation of the crystal was determined by an GE XRD - 5D/F x-ray diffraction unit. The Laue pattern of the crystal was taken by using a Polaroid XR-7 system. Two pictures showing the Laue image along crystal c-axis and a- (or b-) axis are given in Figs. 8 and 9, respectively.

All the crystals were obtained from the Harry Diamond Laboratories. The orientation of the boule of crystal was first checked by the x-ray Laue picture. Small pieces (about 5mm x 5mm x 5mm) were cut off the boule by a diamond saw. After cutting, the orientation of the sample was checked again using the x-ray Laue technique, and then glued to the end of a 6mm diameter VYCOR quartz tube with Pliobond cement and left to dry. The orientation of the sample was so chosen that the dc magnetic field would move in either the ab-plane, or the ac-plane, or the (110)-plane, or the diagonal (d-) plane defined by the two diagonal oxygens and the c-axis of the tetrahedron.

Before putting into the cavity, the sample was irradiated at 77°K with a 10 thousand curie Co-60 gamma source for 1 to 2 hours. The dose rate was about 200 Krads per hour. At the end

of irradiation the sample was transferred into the cavity as fast as possible.

D. Operating Procedure

1. EPR measurements

The measurements of the g-tensor and A-tensor of Nb^{4+} in CaWO_4 single crystals have been made at 77°K using the apparatus described in Section A. The sample cavity is housed in a dry inner dewar with the outer dewar filled with liquid nitrogen. The gamma-irradiated sample is transferred into the cavity after precooling to 77°K .

The EPR absorption spectrum is very complex. The nuclear spin I of the 100% abundant Nb^{93} is $9/2$. Consequently the hyperfine structure consists of 10 components. There are 4 inequivalent Nb sites, corresponding to the 4 oxygens to which the Nb is bonded. The spectrum is complicated further by the presence of "forbidden" transitions. Consequently, extreme care is needed in identifying the different components with the proper groups. Measurements, therefore, were made by rotating the magnetic field about 5° each time.

2. ENDOR measurement

ENDOR measurements were carried out at liquid helium temperature (4.2°K). As the liquid helium is inside the inner dewar, the cavity resonant frequency, f_r drops to a lower value than the one at liquid nitrogen temperature. The cavity Q is usually better at 4.2°K .

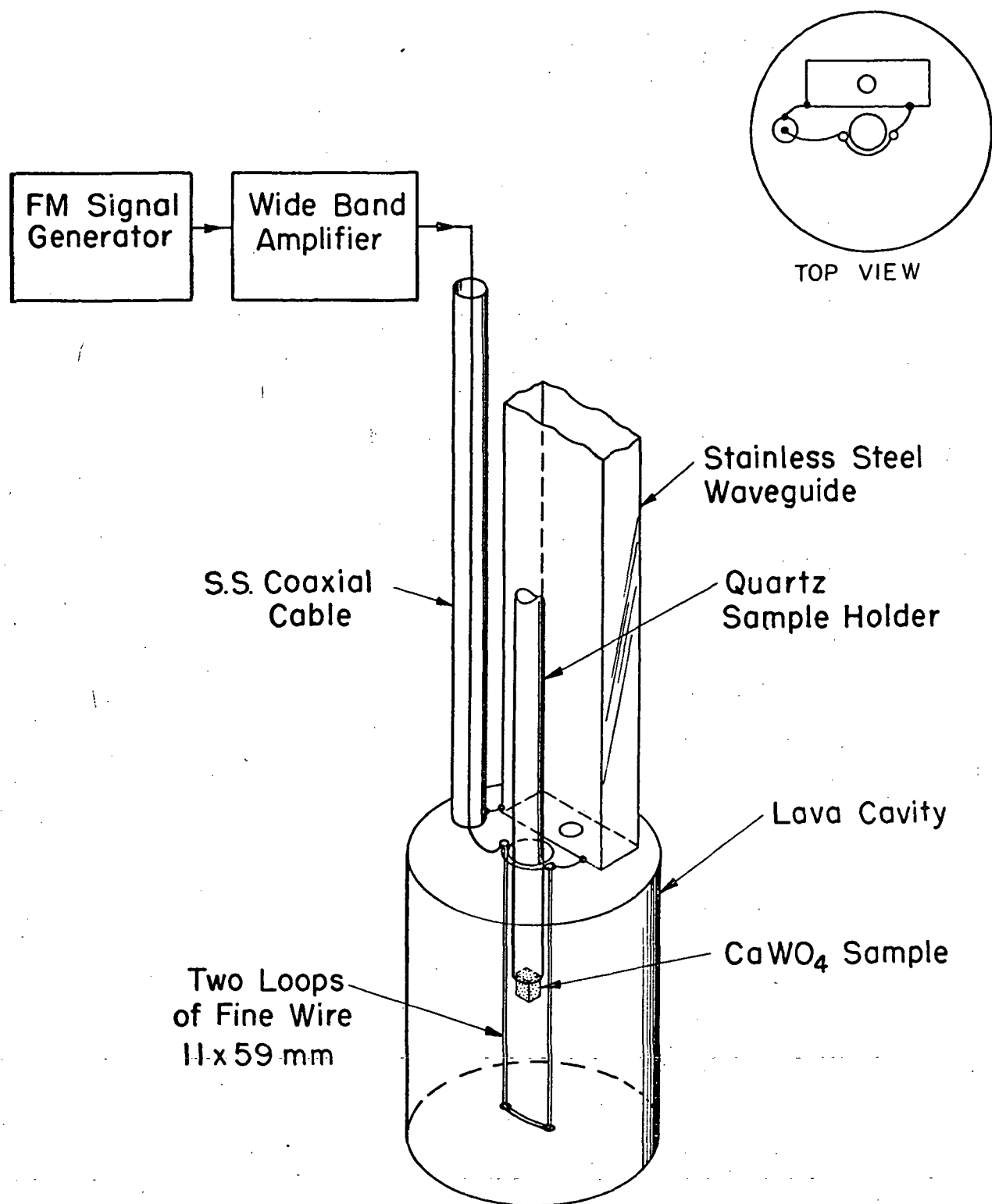
The spectrum is observed at a very low power level (more than 70 db attenuation) so that the line shape does not show any saturation effect. The beginning of saturation can be recognized as the line starts to broaden and its amplitude tends to decrease. Further saturation makes the line shape asymmetric. The line appears one-sided as the saturation increases.

After identification of the line sets, the magnetic field is set on one of the line peaks. The power level is increased a few db above the value at which saturation commences. Too much saturation will reduce the s/n ratio of the ENDOR signal. The optimal degree of saturation is found by trial and error. The 400 Hz magnet field modulation is switched to the input of the "Ext. Mod." of the RF signal generator. The power level of the source of 400 cycle is increased to give a proper frequency deviation of FM signal. The gains of the signal generator and its following amplifiers are controlled to obtain an adequate RF field in the ENDOR coil. The frequency of the signal generator is scanned over an appropriate range, in the present experiment from 20 MHz to 70 MHz. When the ENDOR signal has been initially located, the following readjustments are made to optimize the s/n ratio:

1. The exact position of the magnetic field around the peak of the EPR line.
2. The degree of saturation
3. The deviation frequency (~ 80 kHz)
4. The RF field strength (~ 1 gauss)

There will be 4 ENDOR lines corresponding to $\Delta m = \pm 1$ and

$\Delta M = 0$ for each of the EPR line of all allowable quantum numbers, except $m = \pm 9/2$ which represent the end lines of a line set. For each of these end lines only two ENDOR lines corresponding to $\Delta m = \pm 1$ and $\Delta M = 0$ can be observed. For each ENDOR line the following data were taken: the microwave frequency, the magnetic field at which the EPR line occurred, and the RF frequency.



Schematic of Cavity System for
ENDOR Experiments

Fig. 5. The cavity system of ENDOR Experiments.

- W-Ion
- Calcium Ion
- Oxygen Ion
- ⊗ Nb-Ion

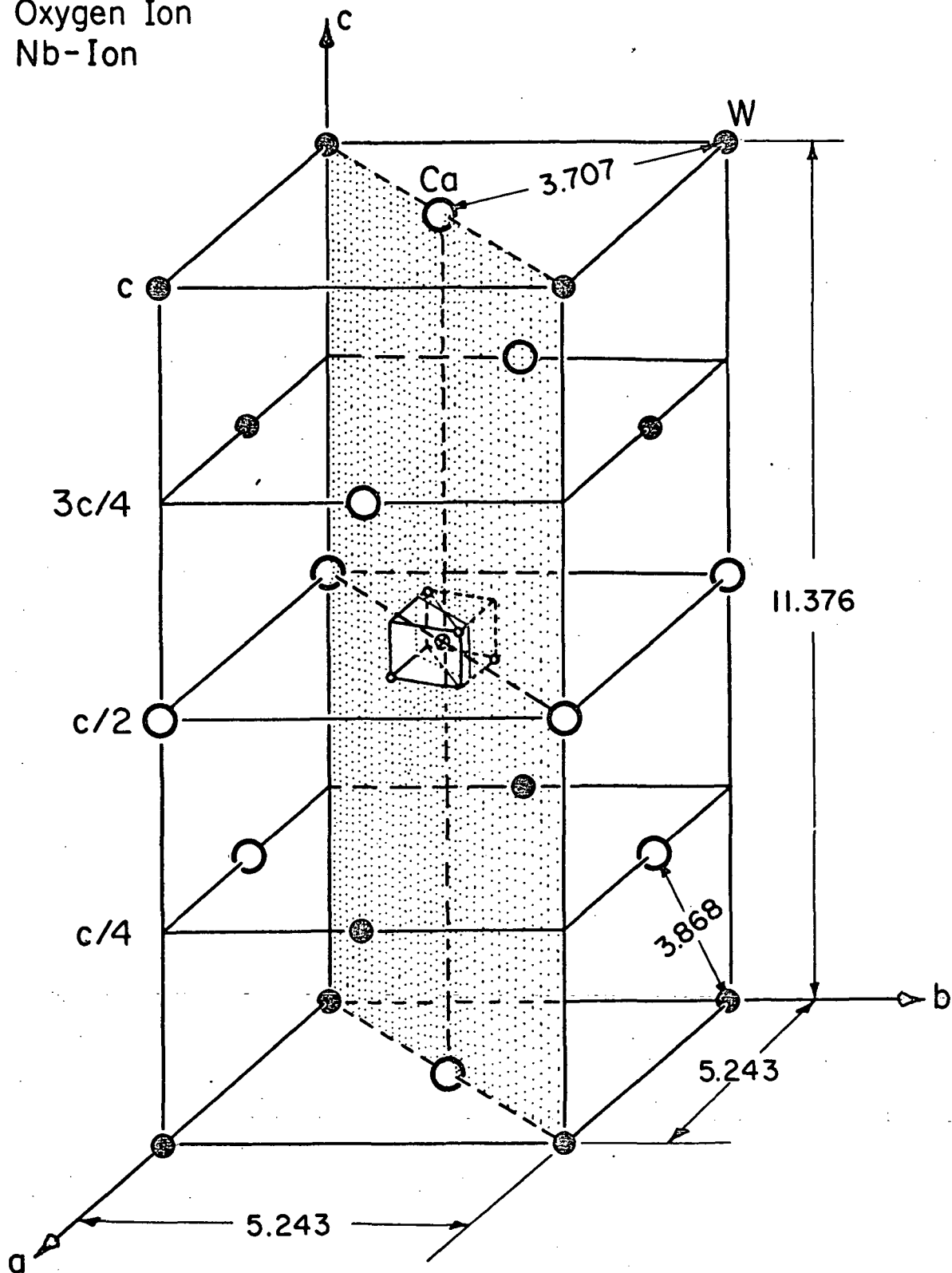


Fig. 6. A Unit Cell of CaWO_4 .

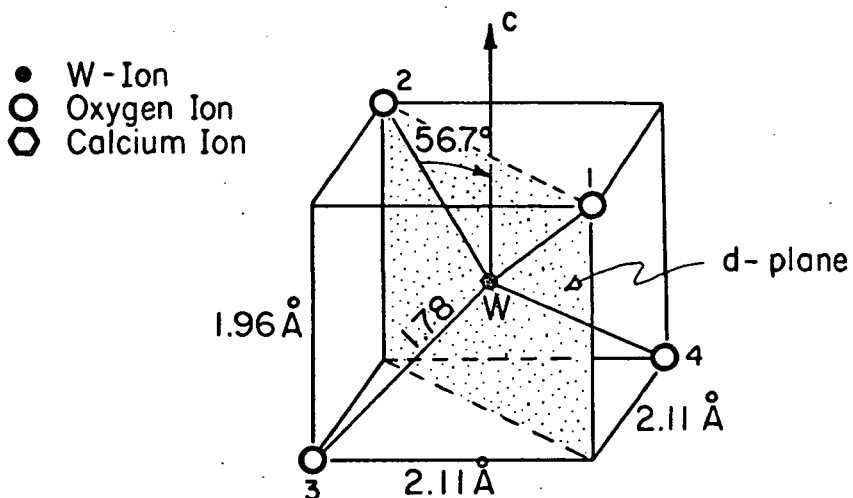


Fig. 7. --
 a) WO_4^{--}
 Tetrahedron

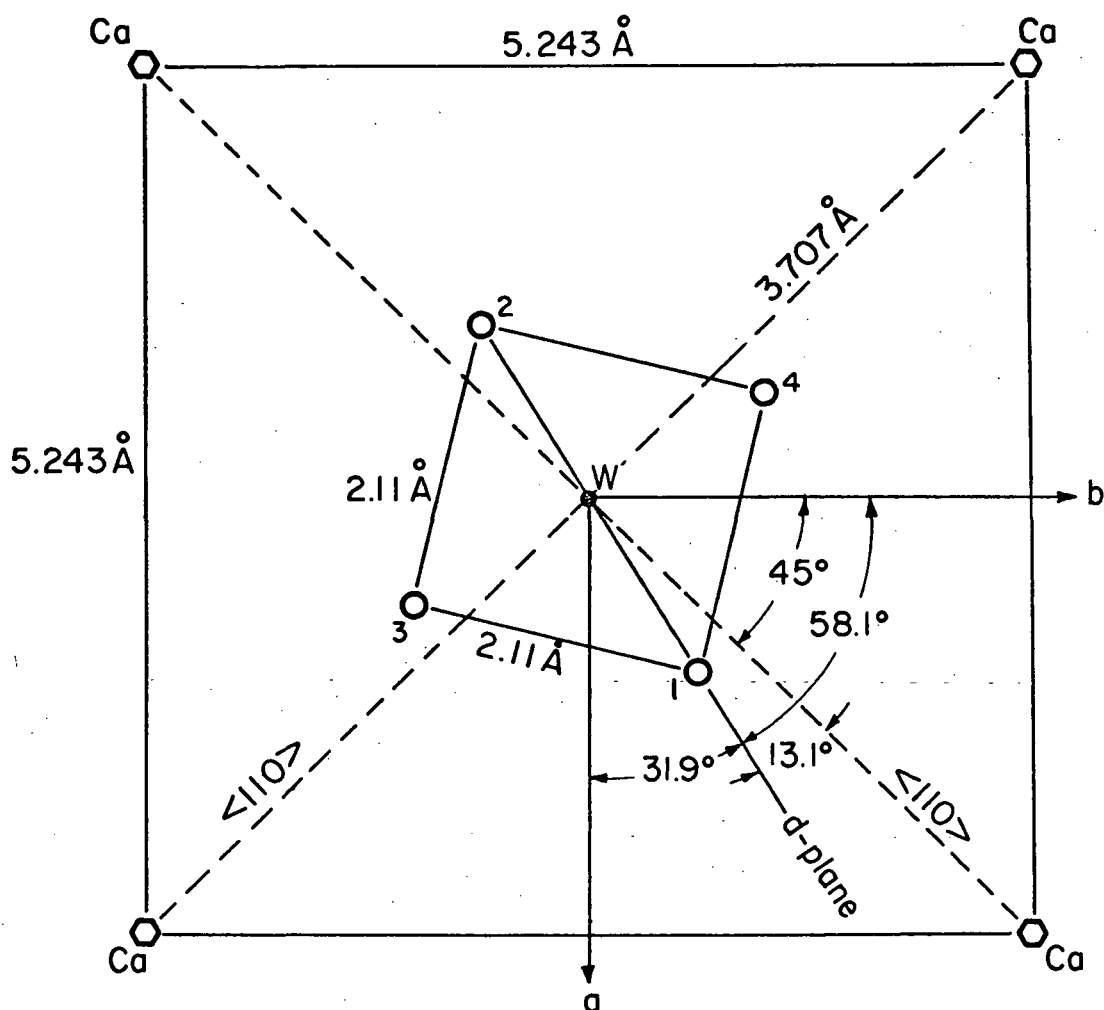
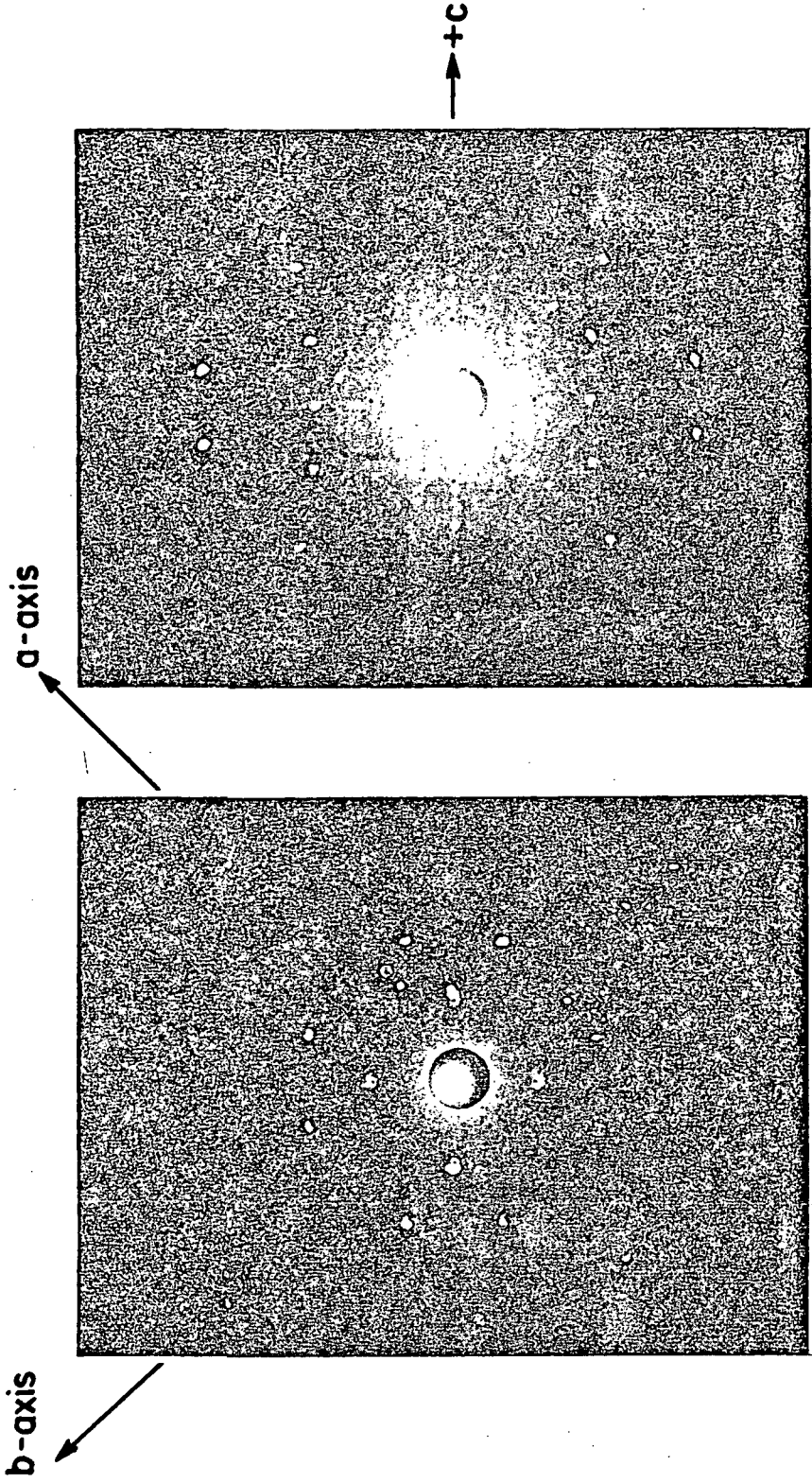


Fig. 7. b) Projection of WO_4^{--} on the ab-plane.



Laue Picture
of c-axis

Fig. 8. Laue Picture
of c-axis

+b

Laue Picture
of a-axis

Fig. 9. Laue Picture
of a-axis

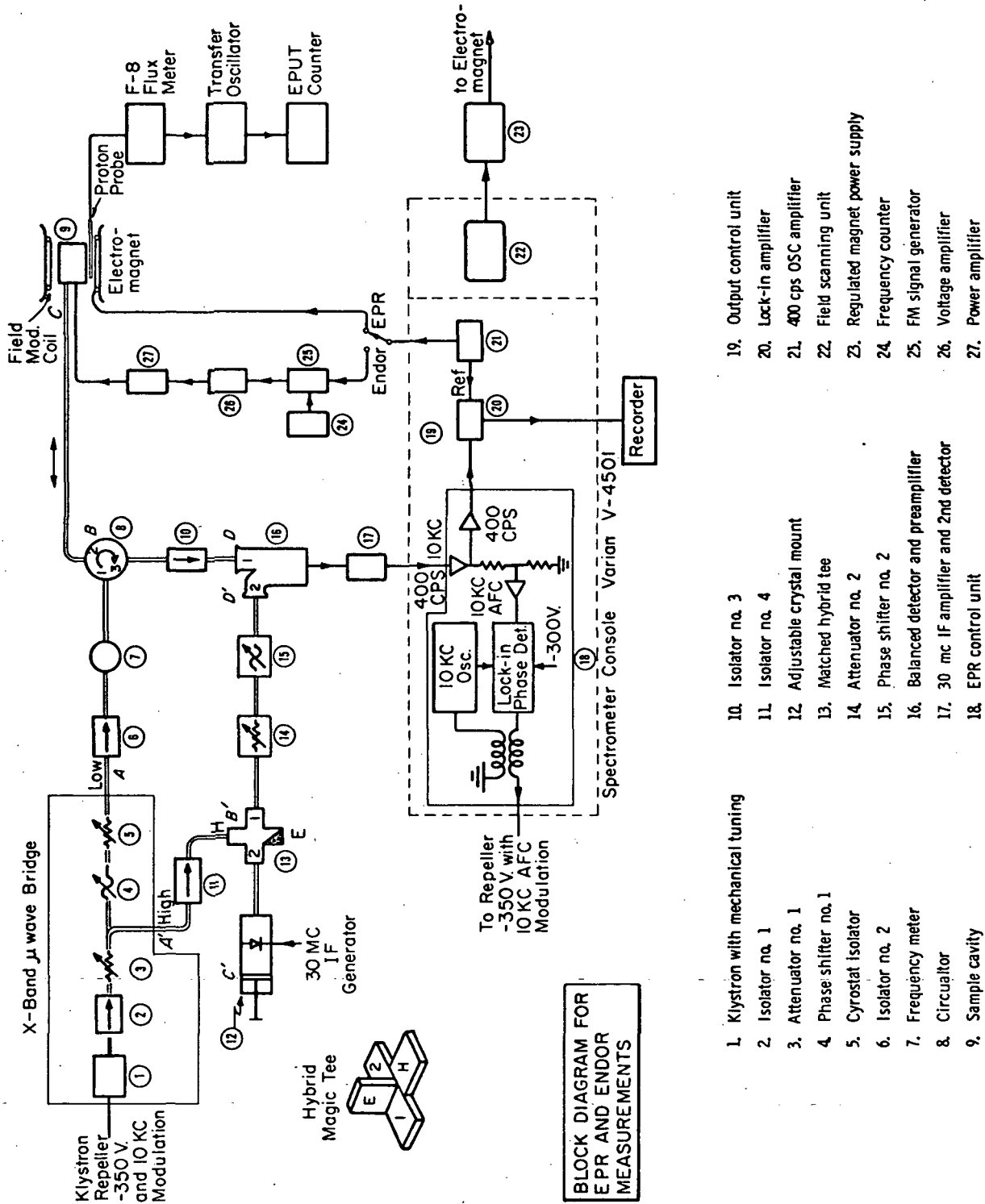


Fig. 10. Block diagram of the EPR/ENDOR System.

Chapter VI

EXPERIMENTAL RESULTS

A. EPR

1. Samples

All the samples utilized in this study were obtained from the Harry Diamond Laboratories, Washington, D.C. These samples include: #A-11, CaWO_4 : 0.5% U_2O_3 , and 1% Nb_2O_5 in melt (Mar. 31, 1967), #A-12, CaWO_4 : 1% Tm and 1% Nb in melt (June 6, 1967); #A-17, CaWO_4 : 0.1% Nd and 0.1% Nb in melt, polished platelet (Sept. 6, 1967); and #A-18, CaWO_4 : 0.1% Nd and 0.1% Nb in melt (Sept. 13, 1967). The last two samples have the same impurity contents but were grown at different times. The date in the brackets indicates the time the sample was received. Different samples cut from the same boule were marked by the same number but with different greek subscripts, e.g. #A-18 $_{\alpha}$, #A-18 $_{\beta}$, #A-18 $_{\gamma}$, etc.

2. Spectra

A typical EPR spectrum when the magnetic field is along the c-axis is shown in Fig. 11. This spectrum shows several striking features. One is the spacing of the allowed ($\Delta M = 1$, $\Delta m = 0$) HFS lines. The spacing is the narrowest at the central portion and widest in the wings of the spectrum. (See Fig. 28). Also the intensities of the lines near the center, ($m = \pm \frac{1}{2}$)

are the greatest, least for the lines $m = \pm 7/2$, while the end lines $m = \pm 9/2$ have some intermediate intensities. For the forbidden lines ($\Delta M = 1, \Delta m = \pm 1$), the doublet separation is the greatest at the ends, and decreases toward the center of the spectrum. The greatest doublet separation is at the high field end. See Fig. 17. The intensities of these doublets are greatest in the wings and drops steadily to zero at the center. Another point is the slight shoulder on each of the HFS lines; some tentative studies⁽⁷⁶⁾ indicate that the structure may be due to nearby tungstens, W^{183} . However, definitive studies have not been carried out.

When the magnetic field is off from the c-axis, the spectrum is complex consisting of 4 groups of lines, as shown in Fig. 13. However, in the ab-plane, the EPR spectrum consists of only 2 groups instead of 4. (See Fig. 12). These symmetry properties of the EPR spectrum suggest that the Nb ion is bonded preferentially to one of the 4 nearest neighbor oxygens.

In Figs. 14 and 15 it is noted that the forbidden lines are conspicuously absent. These directions correspond to the direction of the Q-tensor axes, as will be discussed later.

In the plot of the A-values along the c-axis, Fig. 30, it is seen that for the sample of #A-18₆ at 4.2°K, the A-value at $m = \pm \frac{1}{2}$ is given as 83.97 MHz which is about 0.6% higher than the other values. This sudden jump is an error introduced because of the even isotope Nd^{144} which gives a strong line at $g \approx 2$. This line happens to be broad and close to the niobium HFS of $m = + \frac{1}{2}$.

The values of A and A' along Z_0 -axis at $m = \pm 3/2$ and $T = 4.2^\circ\text{K}$ of Fig. 36 are much too higher than normal due to the interference of an adjacent line belonging to line set #4.

3. Data Analysis

a) Determination of g- and A- Tensor Principal Axes.

The angular variations of the A'- and g'- values for several magnetic field planes are shown in Figs. 18 to 25, in which g' and A' are defined by

$$g' \equiv \frac{h}{\beta} \frac{v_e}{H'_0}$$

where

$$H'_0 \equiv \frac{1}{2} (H_m + H_{-m}), \quad m = I$$

and

$$A' \equiv \frac{1}{2m} (H_{-m} - H_m), \quad m = I$$

The quantities g' and A' represent the first approximation to the correct g- and A- values, as will be discussed later.

The principal axes of the g-tensor were determined from the extremum values in the angular variation plots. According to Fig. 18, the extremum occurs near $\phi = 30^\circ$, in the ab-plane, and from Fig. 20, the angles $\theta = 30^\circ$ and 60° were suggested. Consequently the angular variations of the g'-value were compared for several azimuthal planes. ($\phi = 22^\circ, 26^\circ, 28^\circ, 32^\circ, 45^\circ$) and the one for $\phi = 28^\circ$ was found to yield the largest g-value, at $\theta = 62^\circ$. See Fig. 22. These values are to be compared to

$\theta = 56.7^\circ$ and $\phi = 31.9^\circ$ for the W-O bond direction. (Fig. 7).

Repeating similar procedures for the other directions and also for the A-tensor, the following directions and values were obtained:

g- tensor

	θ	ϕ	g
Z_g	62°	28°	2.0534
X_g	28°	208°	2.0133
Y_g	90°	-62°	2.0077

A- tensor

	θ	ϕ	A (MHz)
Z_A	62.5°	46°	88.388
X_A	27.5°	225°	80.979
Y_A	90°	-45°	75.159

b) g- and A- values

Measurements indicate that the principal axes of the g-, A- and Q- tensors do not coincide so that the evaluation of the

Spin-Hamiltonian parameters is difficult and also tedious. Fortunately good estimates of the g- and A- values can be obtained by using the first order perturbation calculation results:

$$H'_O = \frac{1}{2} (H_m + H_{-m})$$

$$g' = \frac{h}{\beta} \frac{\nu_e}{H'_O} \quad (30)$$

and

$$A' = \frac{1}{2m} (H_{-m} - H_m) \quad (33)$$

where ν_e and H_m are the EPR resonant frequency and magnetic field respectively. The angular variation of g' and A' for various planes are plotted in Figs. 18, 19, 20, 21, 22, 23, 24, and 25. The errors introduced by using Eq. (30) and (33) are estimated to about $\pm 0.3\%$ and $\pm 5\%$ for the g- and A- values respectively.

For the principal values of A and g presented in Table 1, the results from the second order perturbation calculation have been used. The g-values obtained by using Eq. (28)

$$H_O = \frac{1}{2} (H_m + H_{-m}) + \frac{\frac{99}{4} - m^2}{2(2m+1)} [H_{m+1} + H_{-(m+1)} - (H_m + H_{-m})]$$

$$g = \frac{h}{\beta} \frac{\nu_e}{H_O} \quad (28)$$

are plotted in Figs. 26 and 27, for various orientations of the magnetic field at both liquid nitrogen and liquid helium temperatures. Also, A-values calculated by Eq. (32)

$$A = \frac{1}{2m} (H_{-m} - H_m) g \beta - 8 [2I(I+1) - (2m^2+1)] f_5$$

$$- 8 [-4I(I+1) + 8m^2+1] f_6 \quad (32)$$

are plotted in Figs. 30 to 36. For these plots the H_m 's were taken from the EPR measurements and the f_5 and f_6 computed from ENDOR measurements.

These corrections reduce the error in the g -values to about 0.04% and the A -values to less than 1%. The quantities f_5 and f_6 (See Eq. (21) or (25)) are calculated from the constants appearing in f_4 , which in turn is estimated from the positions of the forbidden lines or measured accurately by ENDOR. Note that there is a difference of A -value existing between 4.2°K and 77°K. This difference is about 1%. This temperature dependence will be explained later on.

c) Adjacent HF Line Separation

As indicated earlier, the separation between the adjacent HFS lines is smallest at the center and largest in the wings of the spectrum (Fig. 11). This phenomenon can be explained easily if the quadrupole coupling term is the dominant perturbation in the Spin Hamiltonian. Eq. (24') leads to the adjacent HFS separation as

$$\begin{aligned} \Delta H &\equiv g\beta(H_{m-1} - H_m) \\ &= A + V - \frac{2m^2-1}{2h\nu_e} A^2 - 2W(3m^2-3m+1) \end{aligned} \quad (84)$$

where W and V are as defined by Eqs. (67) and (68), and are independent of m . Eq. (84) is an equation of parabola. The experimental results for the c -axis are plotted in Fig. 28. The bold curve represents the average value obtained from 7 measurements in the range of temperature from 77°K to 4.2°K. The range mark

at each point indicates the data spread.

d) Fit of the g^2 - Equation

Eq. (17) can be written in the form

$$g^2 = g_{\perp}^2 + (g_z^2 - g_{\perp}^2) \cos^2 \textcircled{H} \quad (17')$$

This represents a straight line equation if g^2 is plotted against $\cos^2 \textcircled{H}$, where \textcircled{H} is the aximuthal angle between the applied field H and the Z-axis of the g-tensor. g_{\perp} is the g-value in the direction perpendicular to the Z_g -axis. The result of measurements made in the d-plane is given in Table 2 and plotted in Fig. 29 in which the g^2 has been calculated by using the first order perturbation result, Eq. (30). In the d-plane, the point where $\cos^2 \textcircled{H} = 0$, gives $g_{\perp} = g_x$ and $\cos^2 \textcircled{H} = 1$ gives g_z . From the plot, we obtain $g'_x = 2.0129$ and $g'_z = 2.0527$ which should be compared with the exact values: $g_x = 2.0137$ and $g_z = 2.0534$, respectively.

e) Q_{33} and g_n from Forbidden Doublets

The first forbidden doublets, arising from the transitions $\Delta M = \pm 1$, $\Delta m = \pm 1$, can be used to obtain estimates of the quadrupole coupling constant (Q_{33}) and the nuclear g-value (g_n). According to Eq. (60), the doublet separation is given by

$$g\beta(H_m^+ - H_{m+1}^-) = 3(2m+1)Q_{33} - g_n\beta_n(H_{m+1}^- + H_m^+) - \frac{A^2}{2h\nu_e} \quad (60)$$

Measurements were made for both H // Y_g and H // c-axis (See Fig. 17). The results obtained are

	Q_{33} (MHz)	g_n
Y_g -axis	-.68	1.28 - 1.33
c-axis	+.72	1.38 - 1.42

These values are to be compared to $Q_{33}(Y_g) = -.835$ MHz and $Q_{33}(c) = +.748$ MHz obtained from ENDOR measurements, as will be discussed presently. Also the ENDOR measurements of g_n give 1.357 and 1.398 along the Y_g - and c-axes respectively. (See Table 5).

Table 1
Principal Values of A and g

Axis	θ				ϕ				g				A (MHz)			
	Line Set No.		Line Set No.		Line Set No.		Line Set No.		Sample A-11	Sample A-12	Sample A-17	Sample A-18	Sample A-11	Sample A-12	Sample A-17	Sample A-18
	1	2	3	4	1	2	3	4								
X _g	28°	28°	152°	152°	208°	28°	118°	-62°	2 0137	2 0133	2 0137	2 0125	80.334	80.117	80.097	80.300
Y _g	90°	90°	90°	90°	-62°	118°	28°	208°	2 0076	2 0077	2 0080	2 0069	75.952	76.785	76.490	76.074
Z _g	62°	62°	118°	118°	28°	208°	-62°	118°	2 0534 (2.0552)*	2 0535	2 0542	2 0531	87.668 (87.722)*	87.610	87.812	88.047
X _A	27.5°	27.5°	152.5°	152.5°	225°	45°	135°	-45°				2 0136				80.979
Y _A	90°	90°	90°	90°	-45°	135°	45°	225°				2 0113				75.159
Z _A	62.5°	62.5°	117.5°	117.5°	45°	225°	-45°	135°				2 0492				88.388
a	90°	90°	90°	90°	0°	0°	90°	90°	2 0364		2 0366		80.717		81.121	
b	90°	90°	90°	90°	90°	90°	0°	0°	2 0153		2 0145		81.885		81.506	
c	0°	0°	0°	0°	---	---	---	---	2 0217	2 0223**	2 0226**	2 0217	82.646	82.710	82.579	82.507

Note: * Values obtained with KU-band spectrometer
** First order calculation

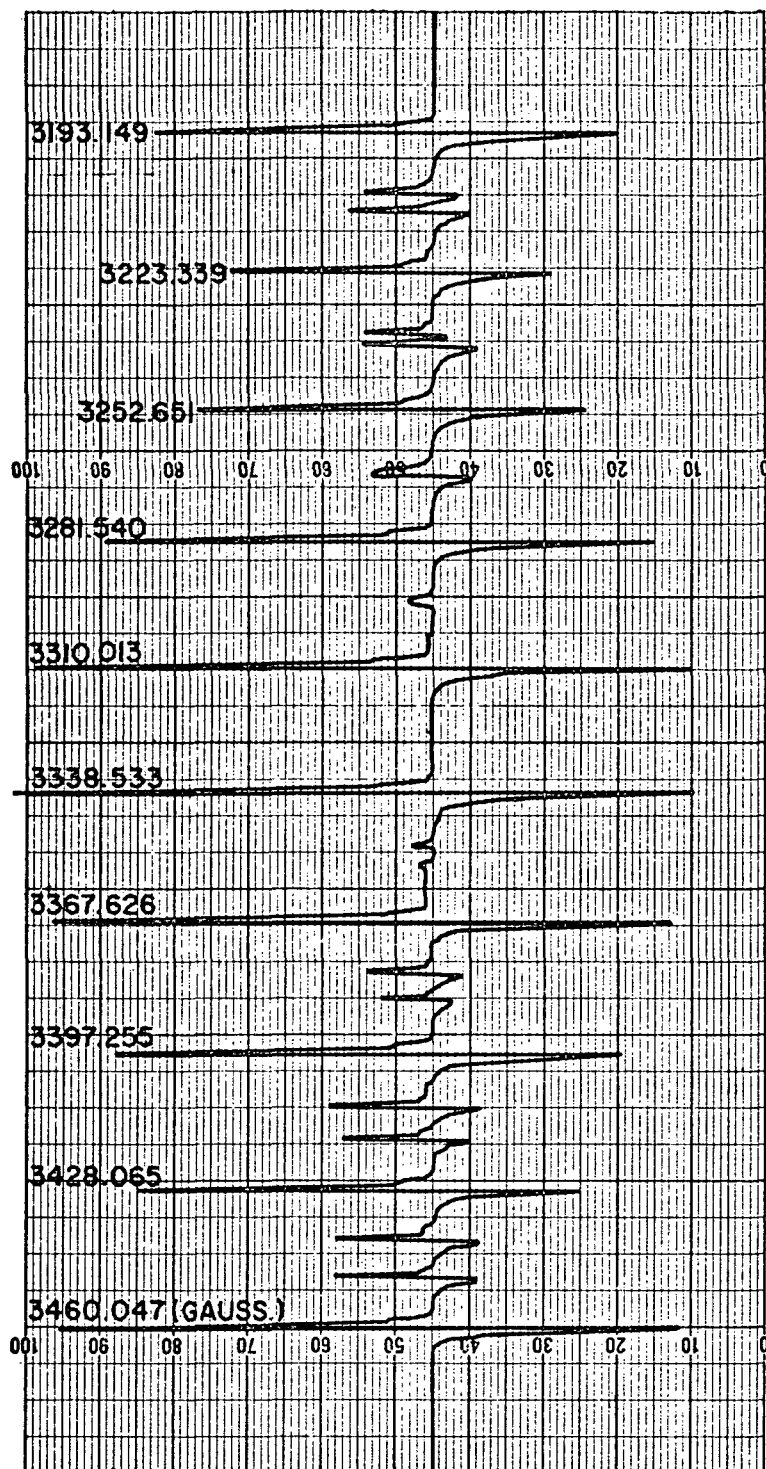


Fig. 11. Spectrum a) along c-axis

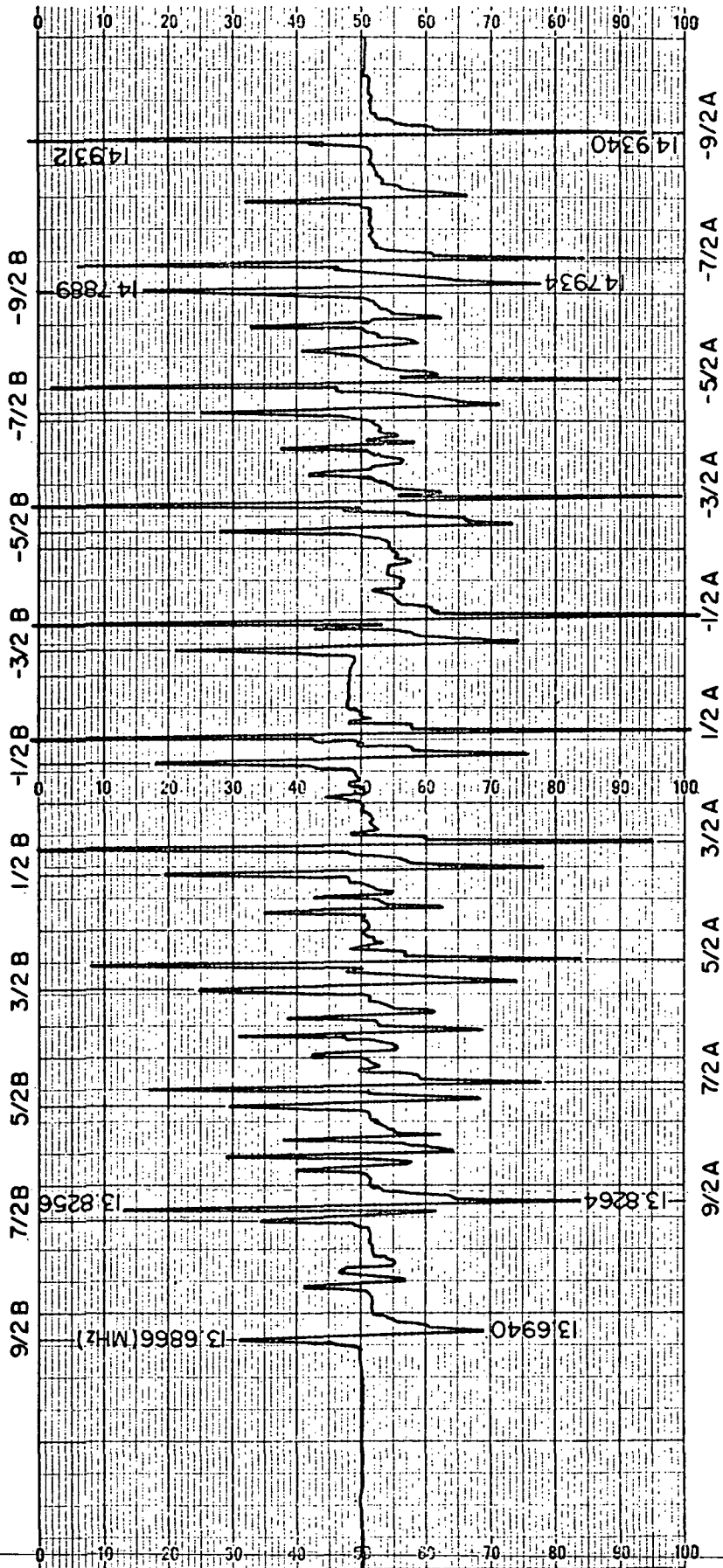


Fig. 12. Spectrum b) along a-axis.

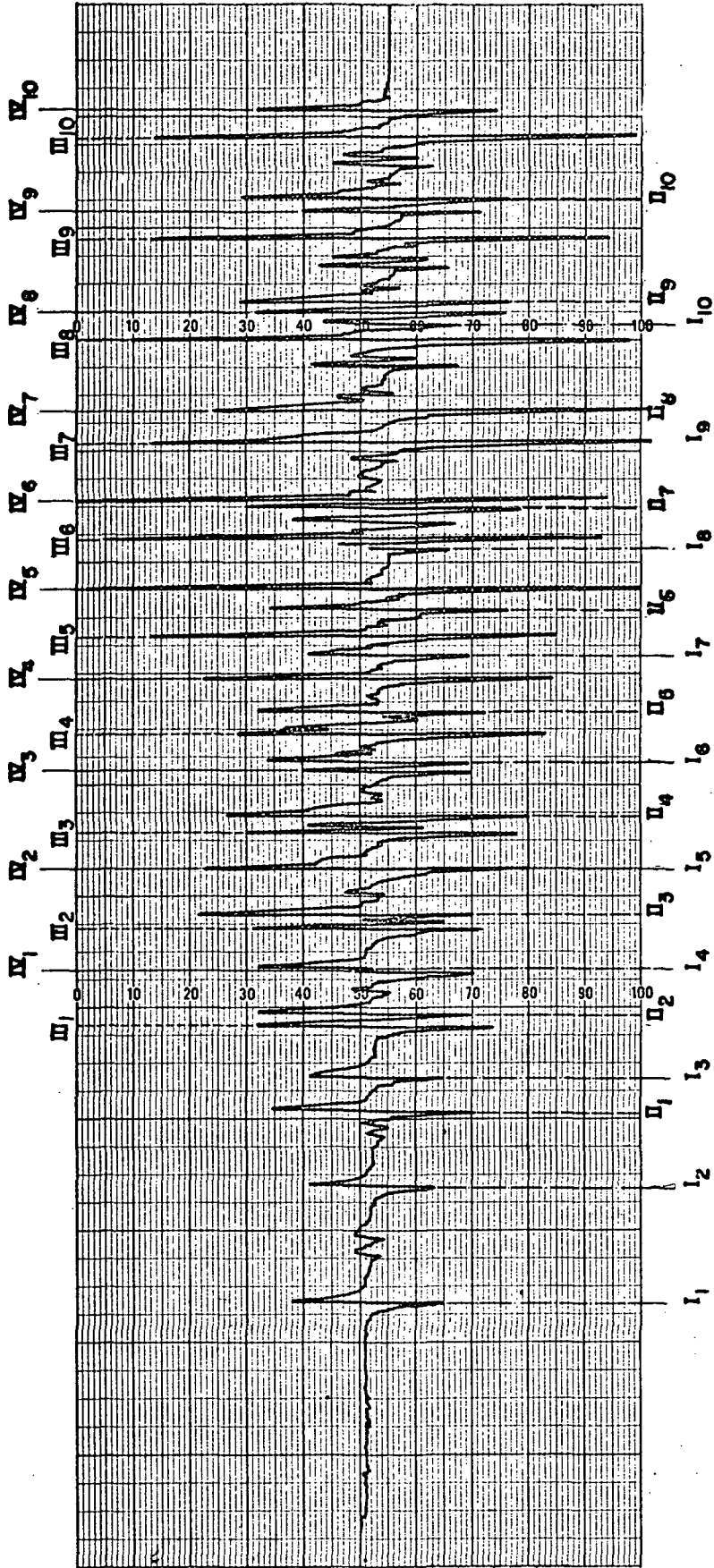


Fig. 13. Spectrum c) along Z_g -axis.

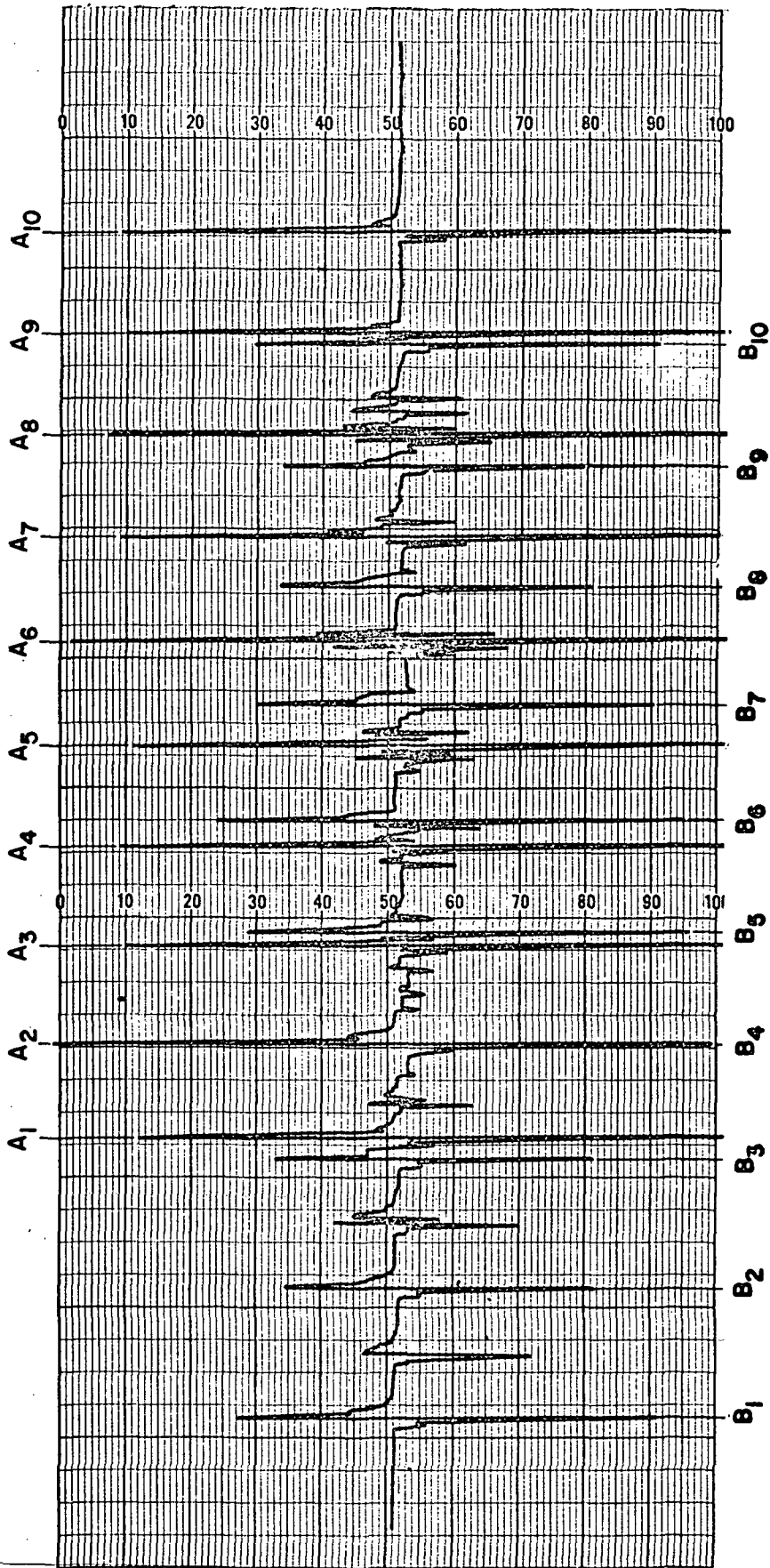


Fig. 14. Spectrum d) along Y_Q or Y_A -axis; $\langle 110 \rangle$ direction.

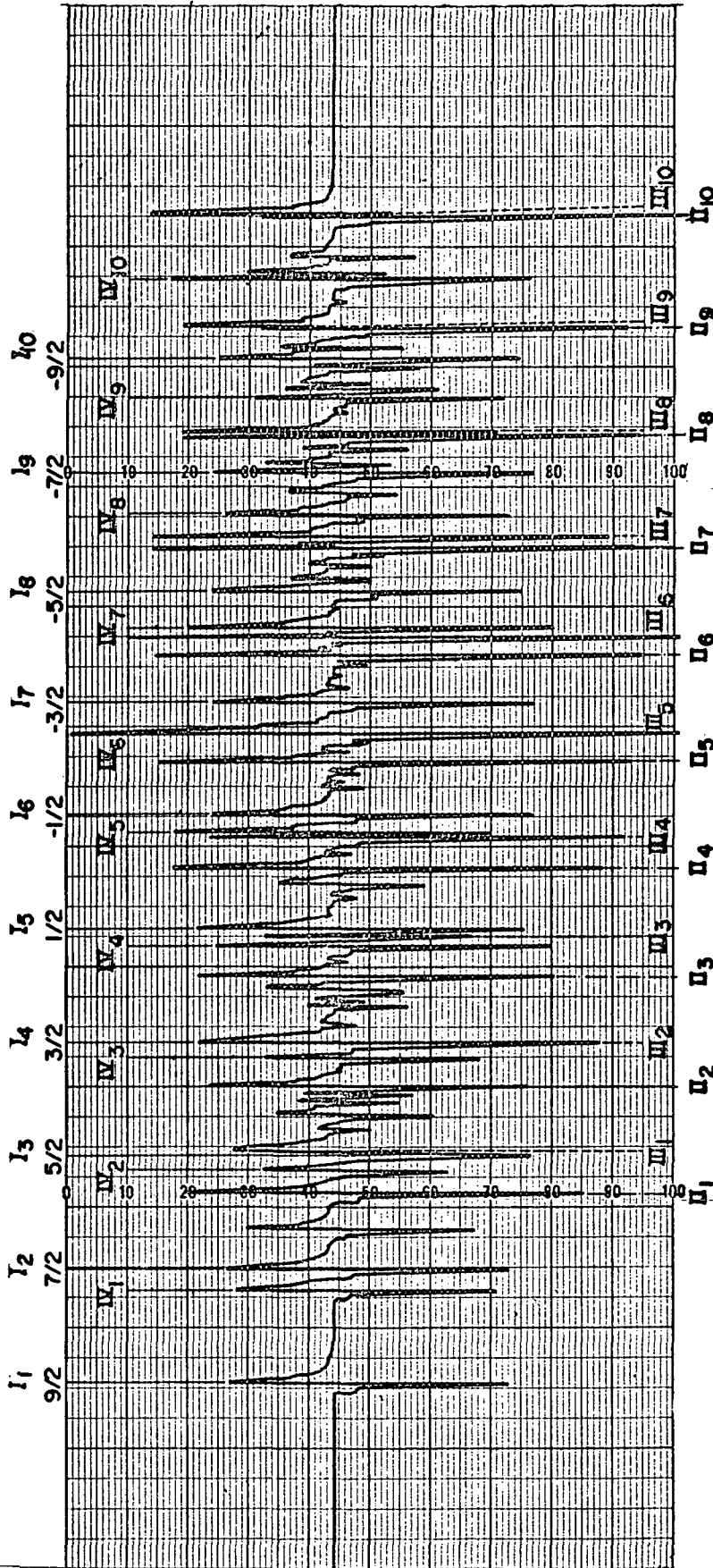


Fig. 15. Spectrum e) along Z_Q -axis.

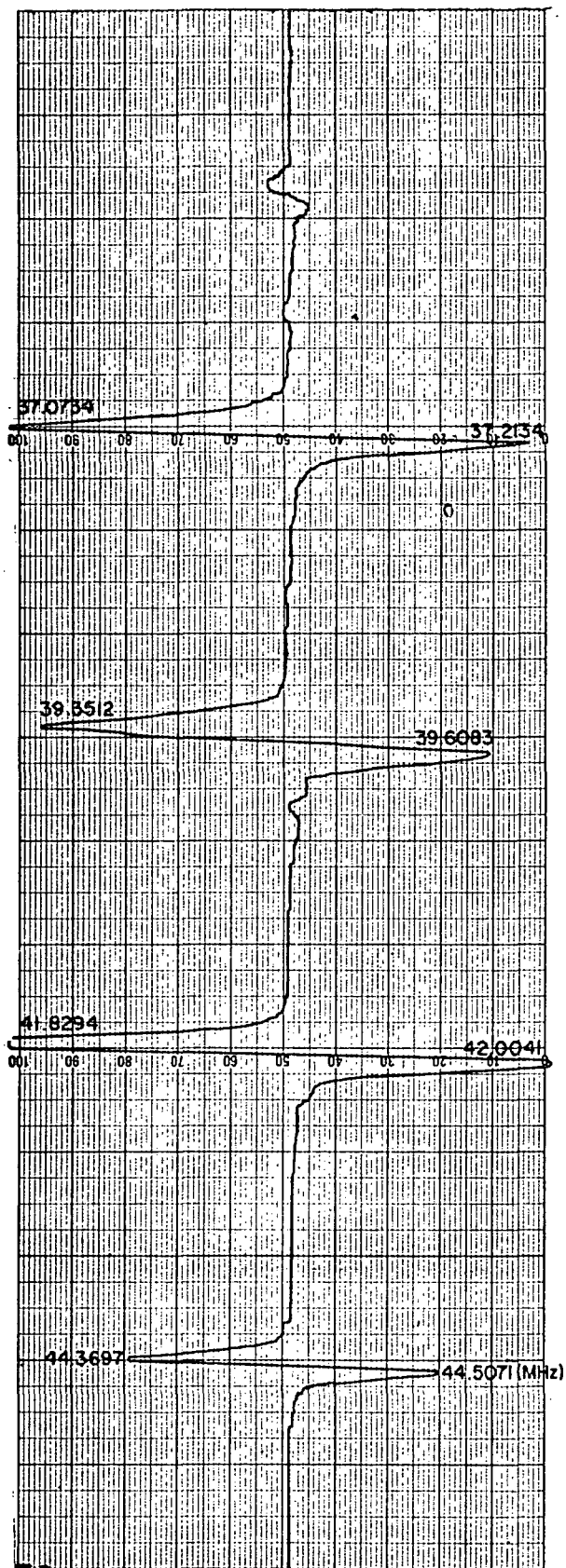


Fig. 16. Spectrum f) ENDOR pattern, c-axis,
 $m = +\frac{1}{2}$

Adjacent HF Separation

77°K	30.251	29.429	28.654	28.490	28.560	28.936	29.687	30.744	32.013 gauss
4.2°K	30.51	29.67	29.10	28.60	29.01	29.29	29.97	31.35	32.48 gauss

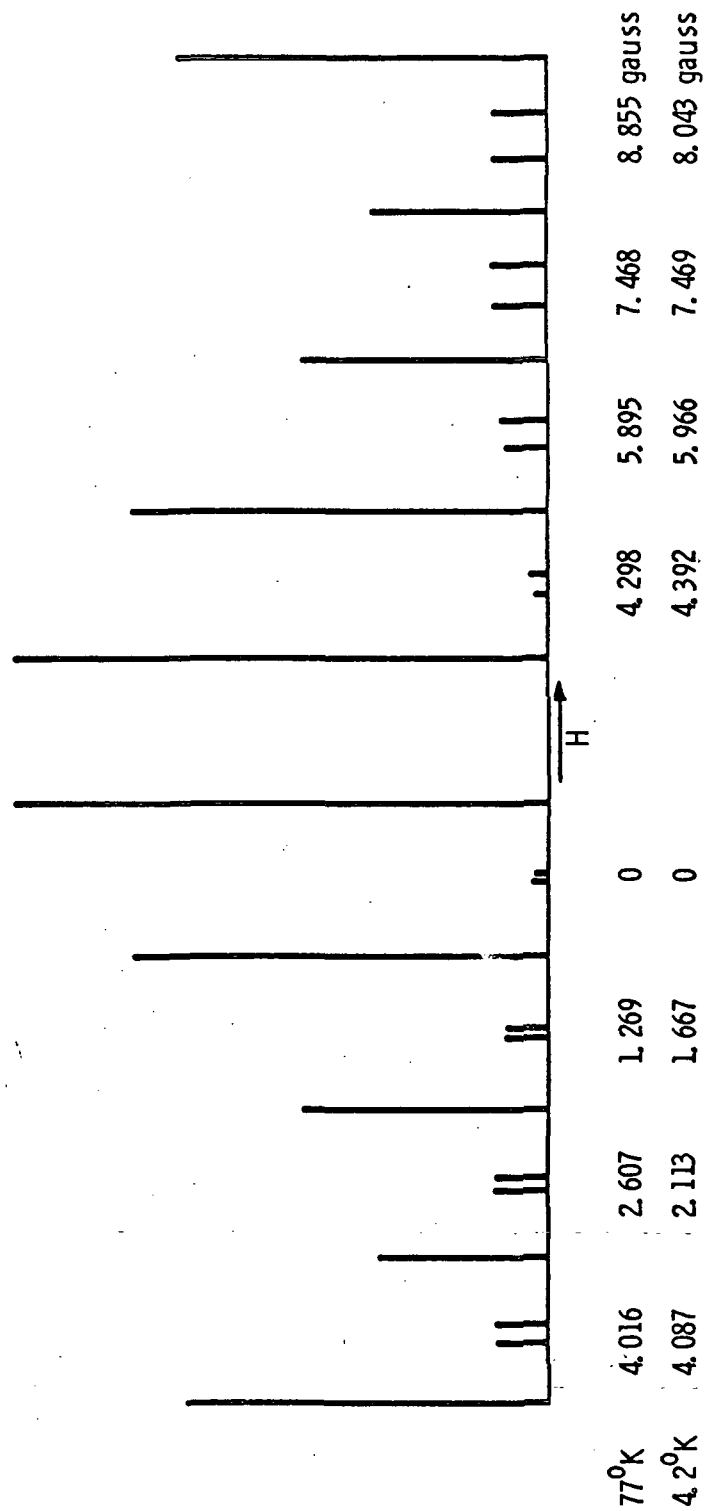


Fig. 17. Separation of adjacent HF Lines and Forbidden Doublet Along c-Axis.

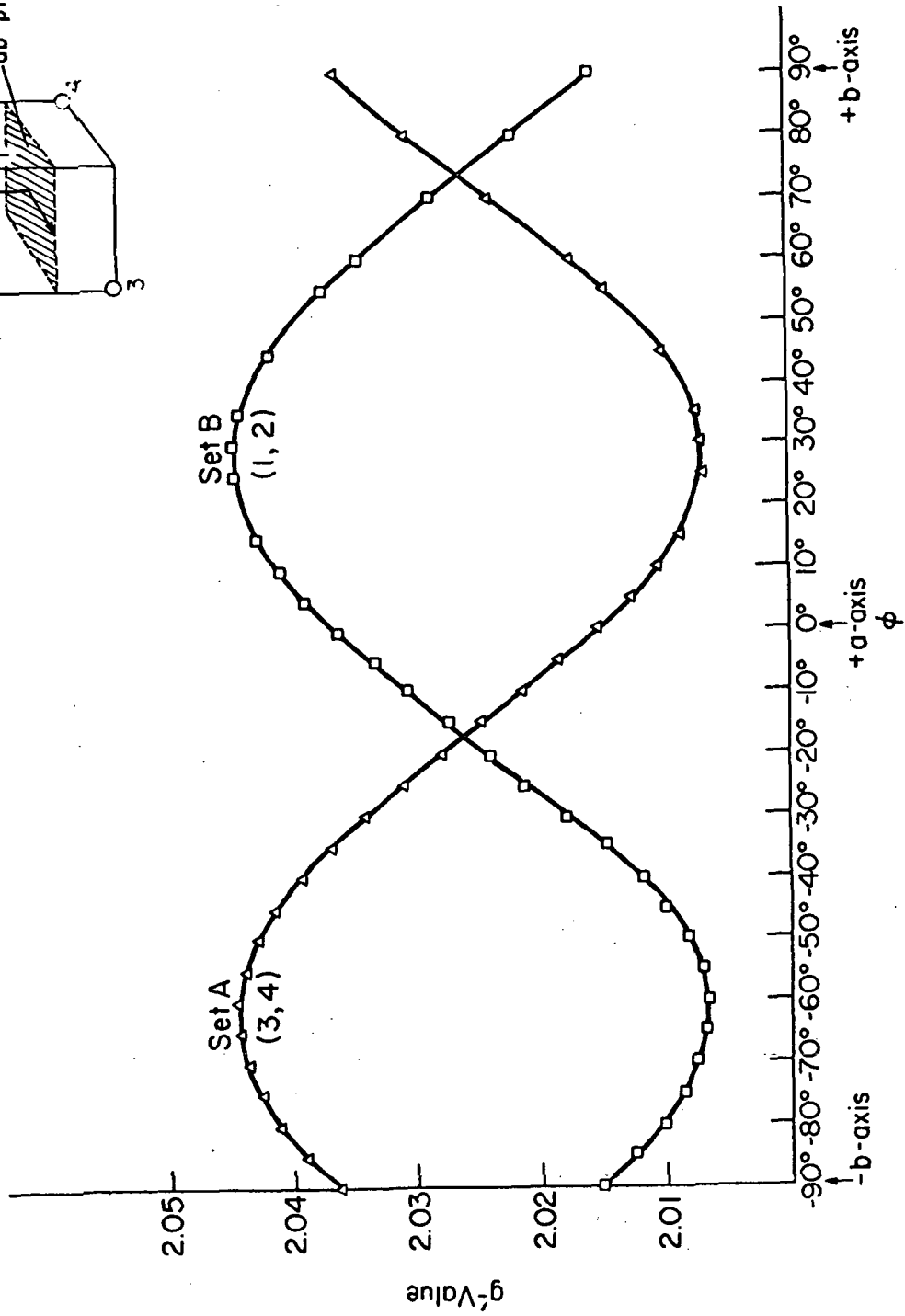
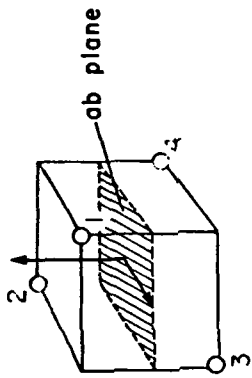


Fig. 18. g' -value. Angular Variation in ab -plane.

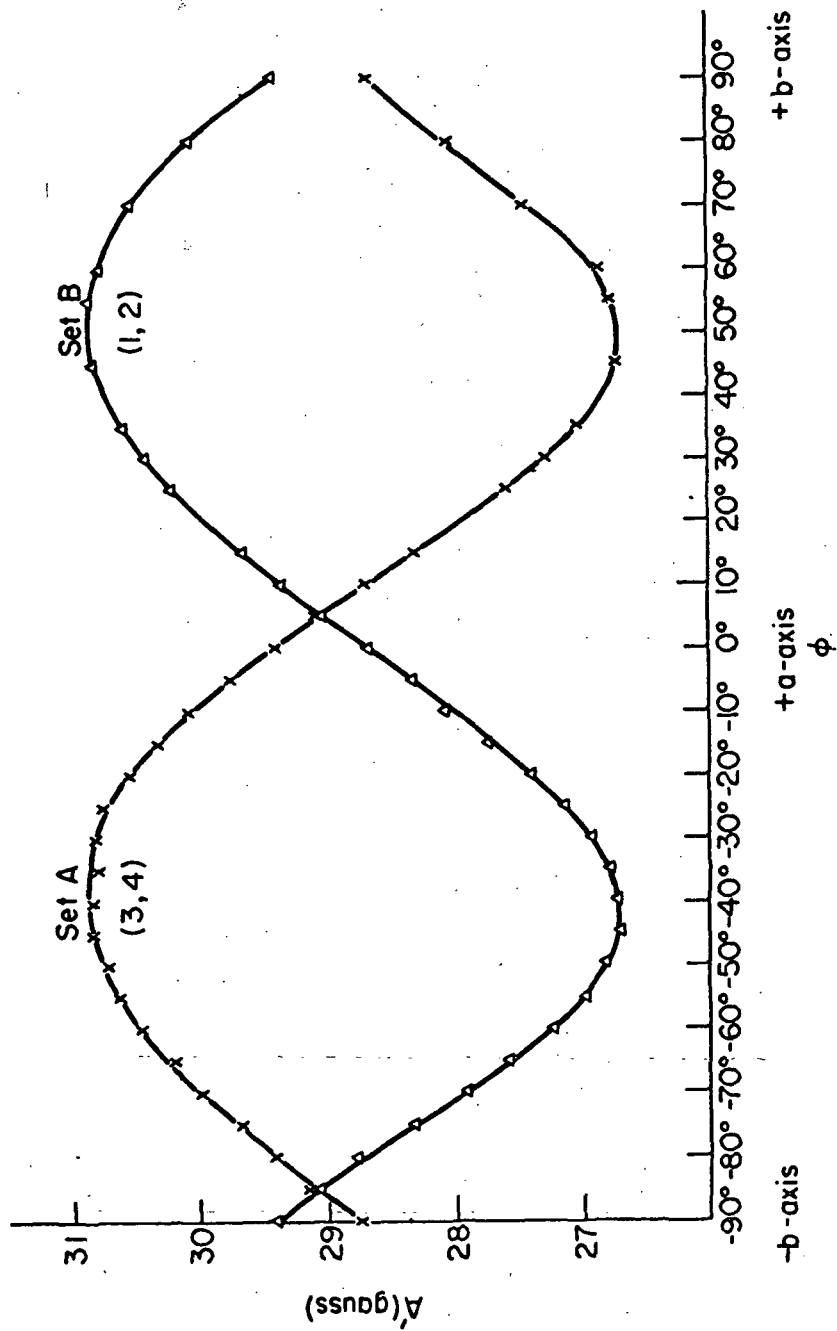
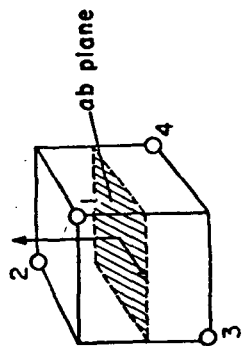


Fig. 19. A'-value, Angular Variation in ab-plane.

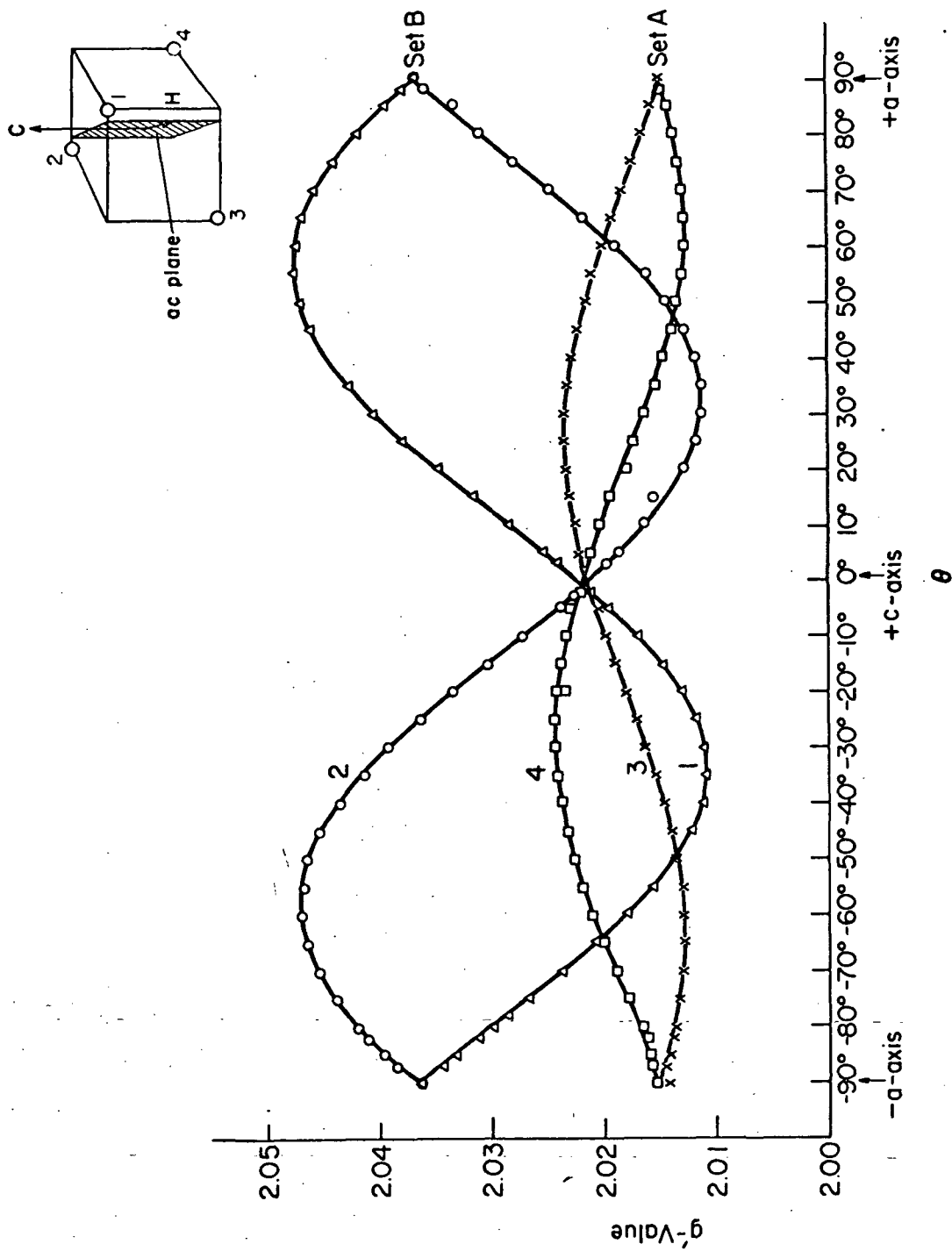


Fig. 20. g' -value, Angular Variation in ac -plane.

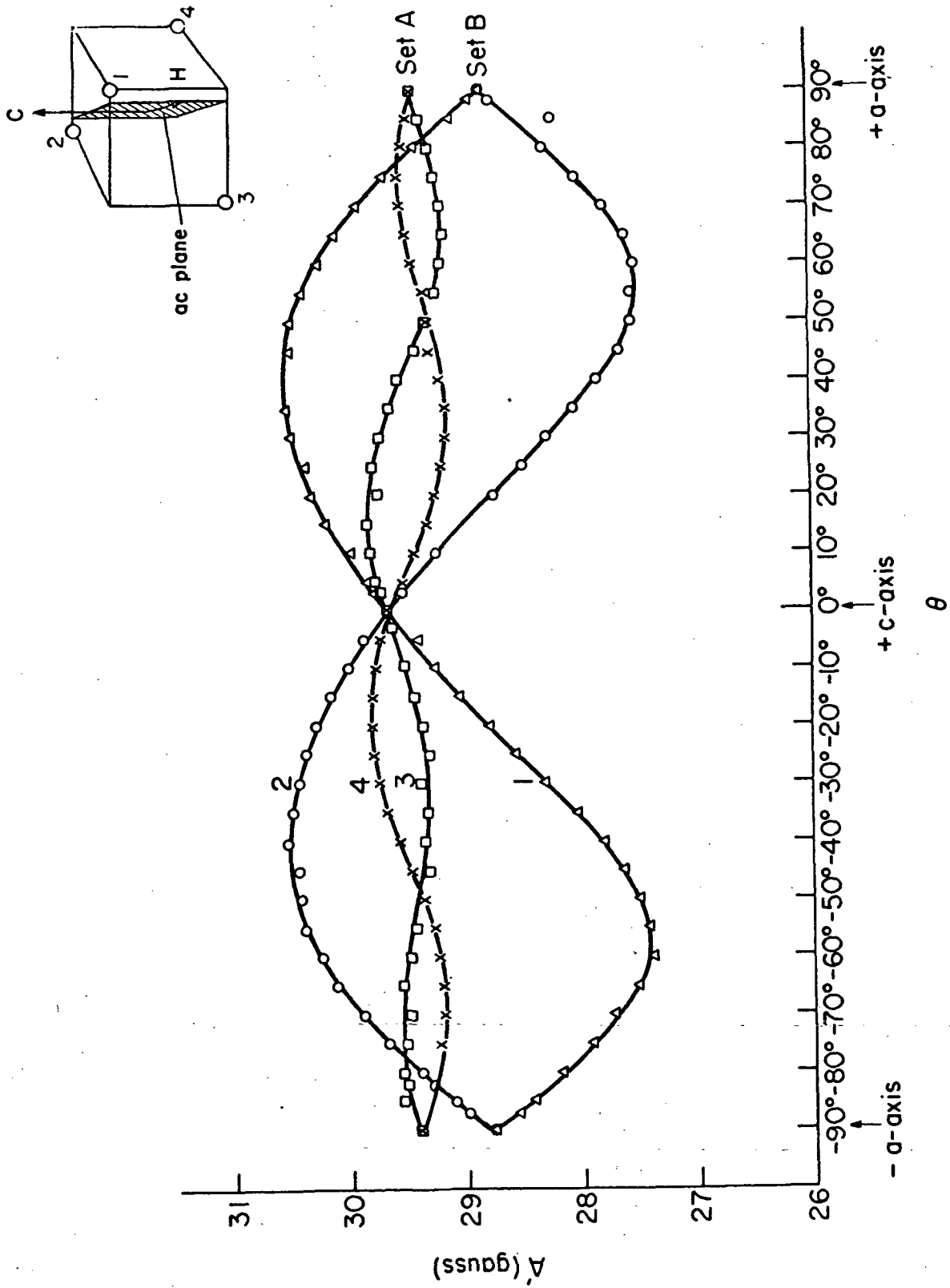


Fig. 21. A' -value, Angular Variation in ac-plane.

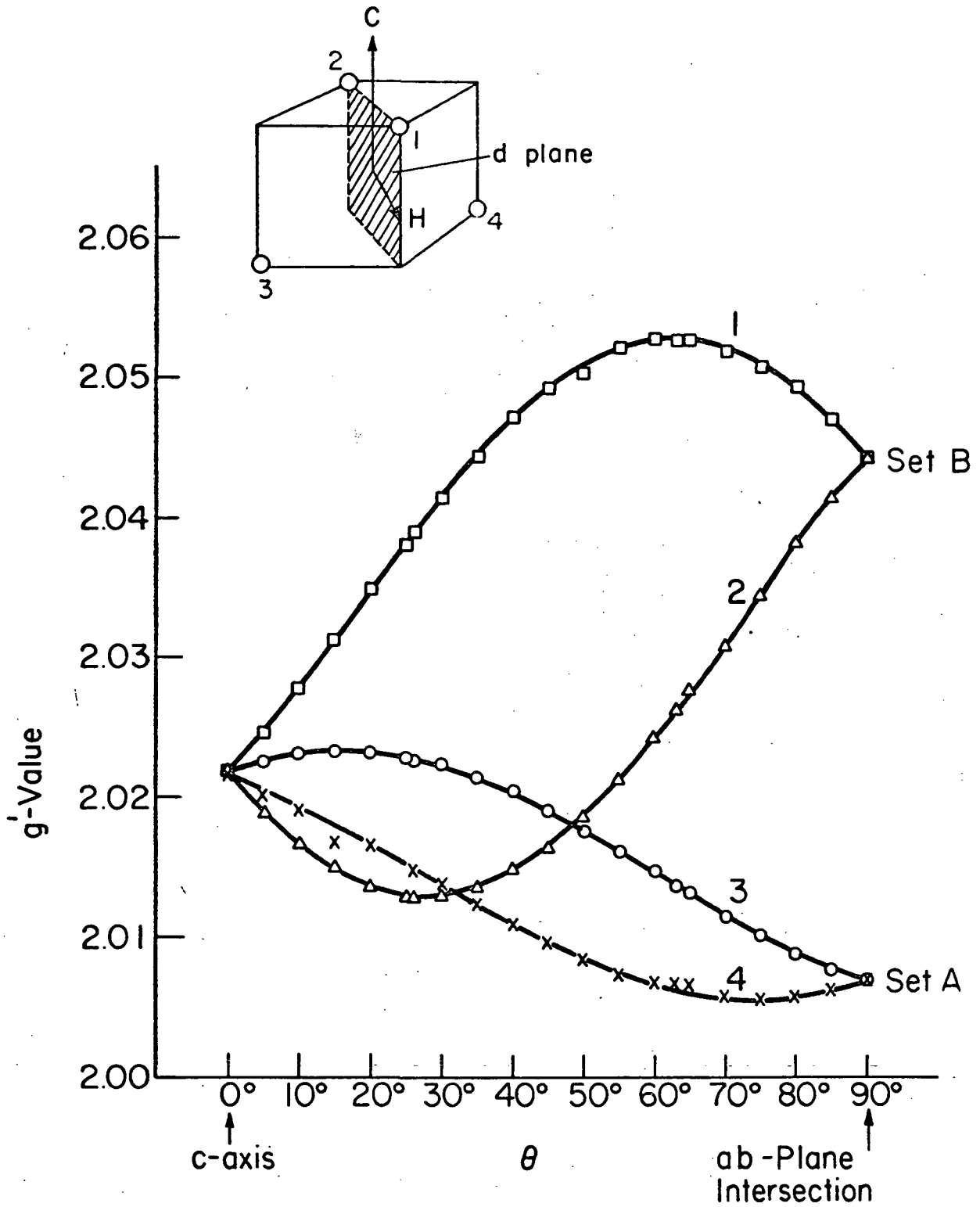


Fig. 22. g' -value, Angular Variation in d-plane (28°).

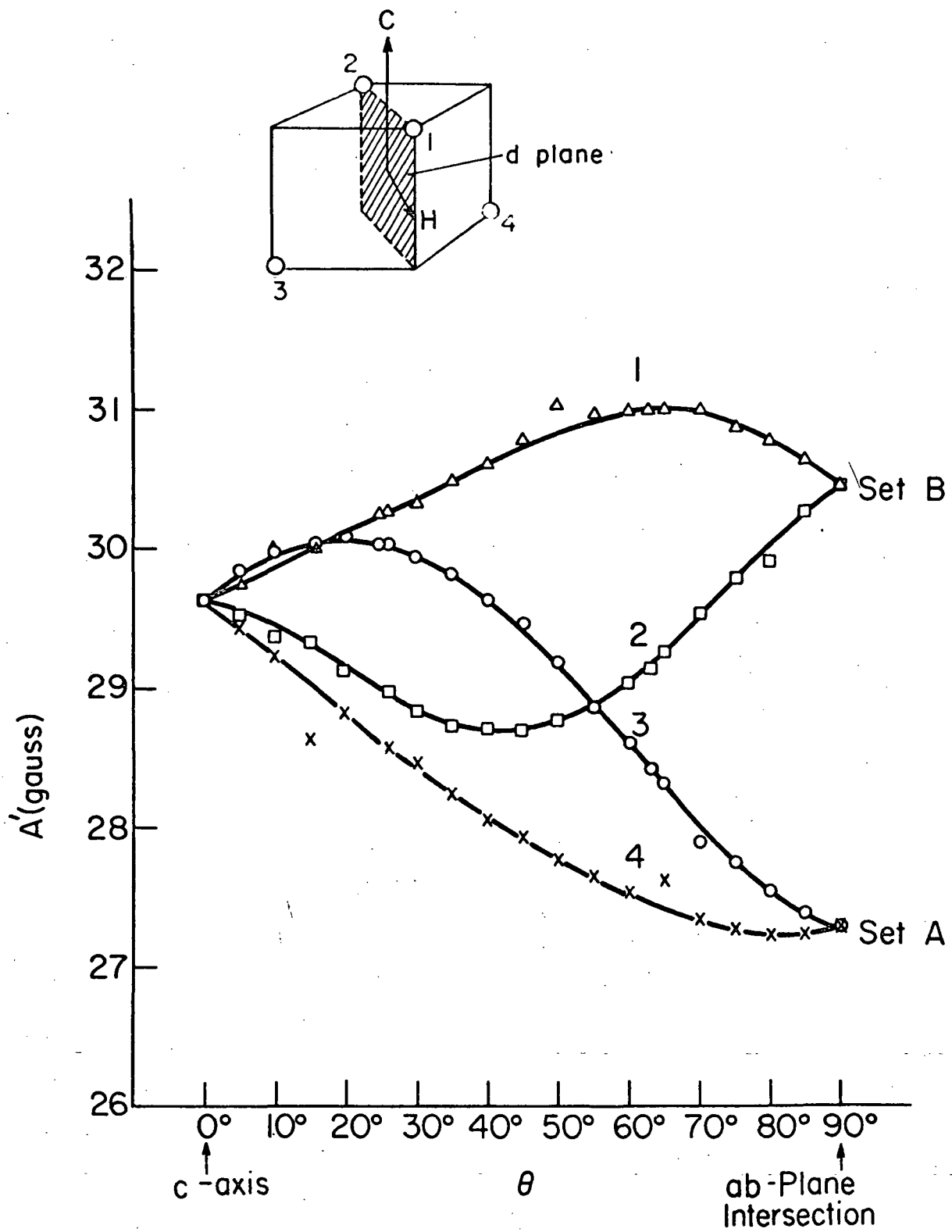


Fig. 23. A' -value, Angular Variation in d -plane (28°).

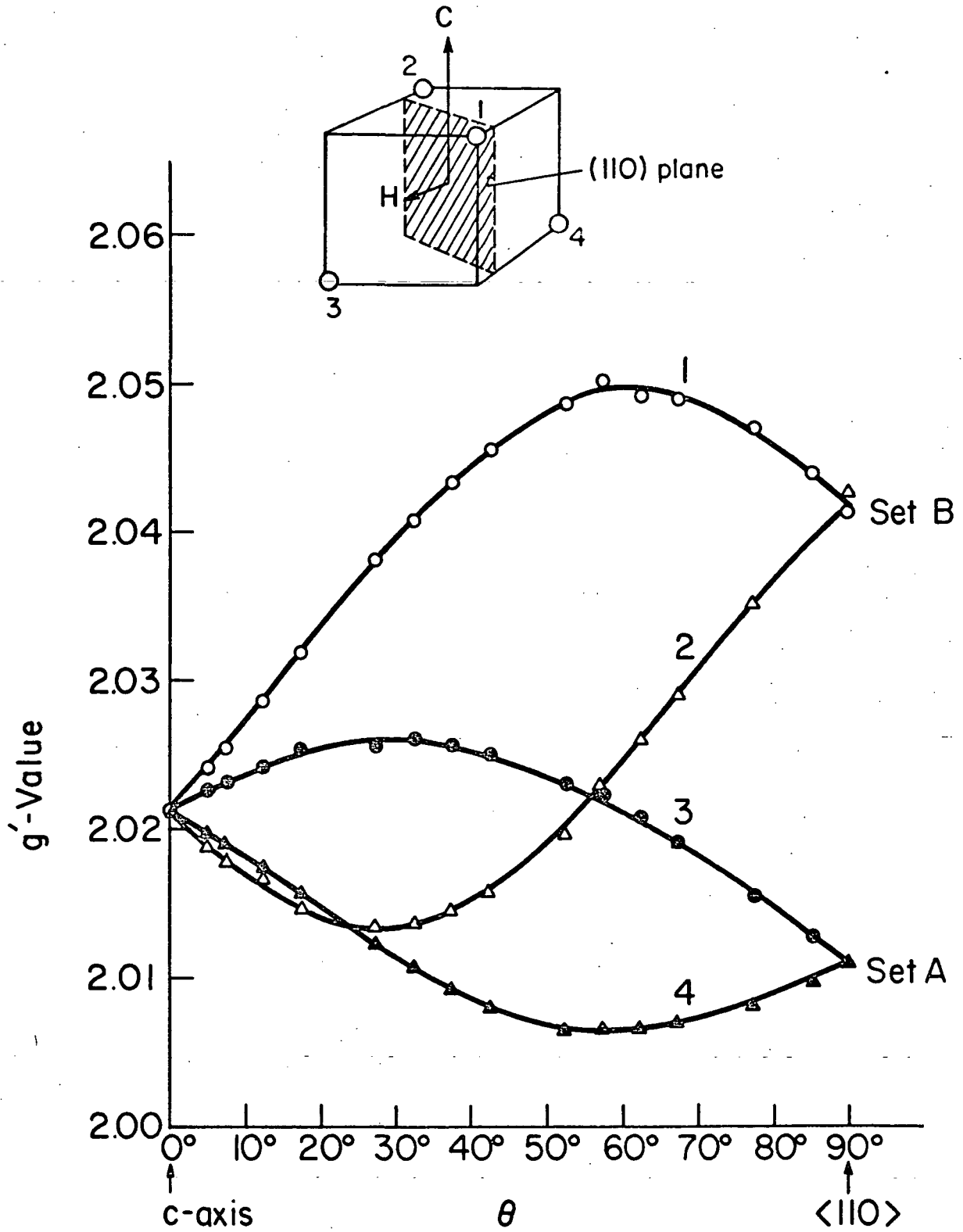


Fig. 24. g' -value, Angular Variation in (110)-plane*

*Due to C. Y. Huang

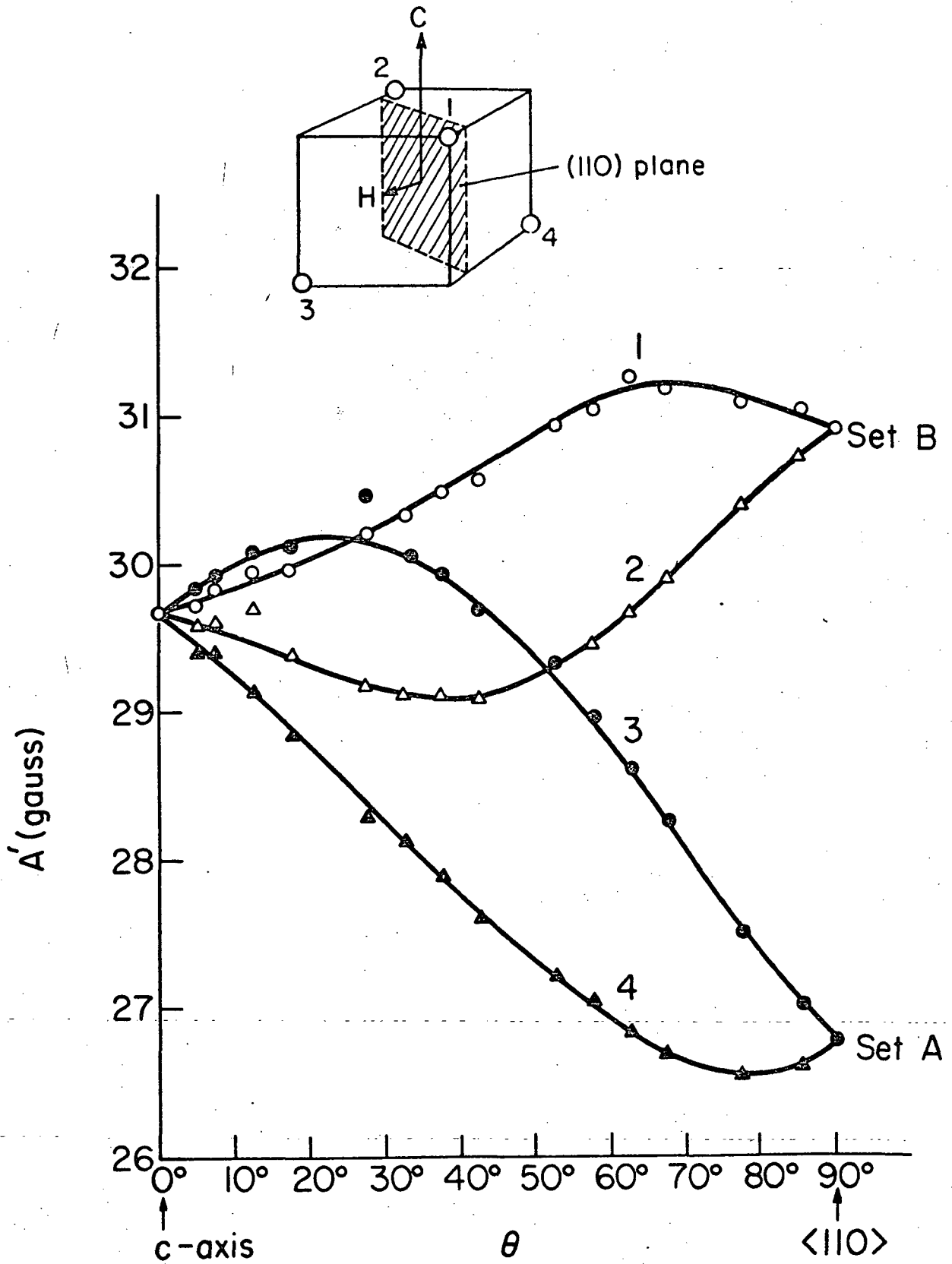


Fig. 25. A' -value, Angular Variation in (110)-plane*

- | | |
|---|---|
| 1. g_z (No. A-18 _γ) Liq. He | 6. g_y (No. A-18 _γ) Liq. He |
| 2. g_z (No. A-18 _γ) Liq. N ₂ | 7. g_y (No. A-18 _γ) Liq. N ₂ |
| 3. g_x (No. A-18 _γ) Liq. N ₂ | 8. g_y (No. A-17) Liq. He |
| 4. g_x (No. A-17) Liq. N ₂ | 9. g_y (No. A-17) Liq. N ₂ |
| 5. g_x (No. A-17) Liq. He | |

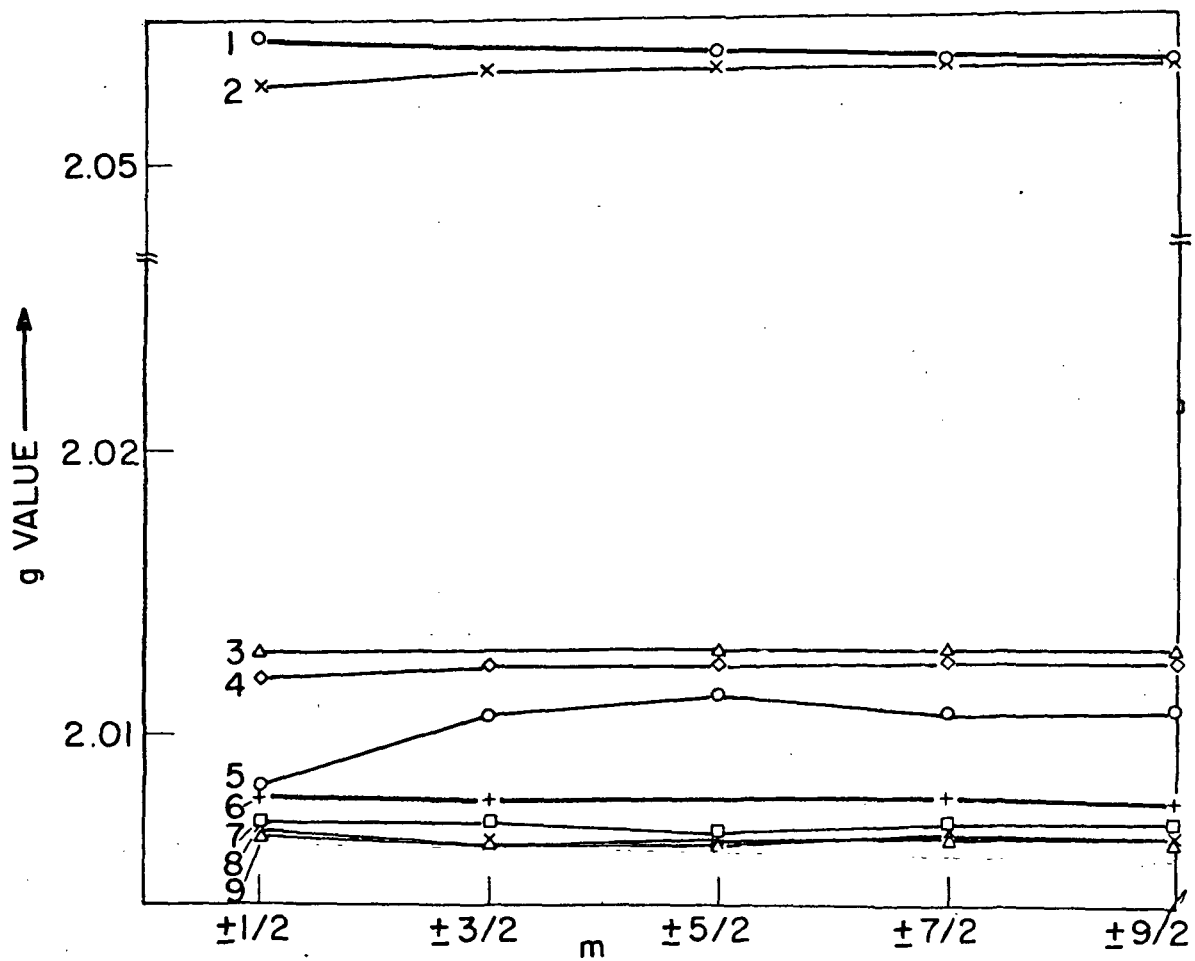


Fig. 26. g -value vs. m (i) d -plane (28°).

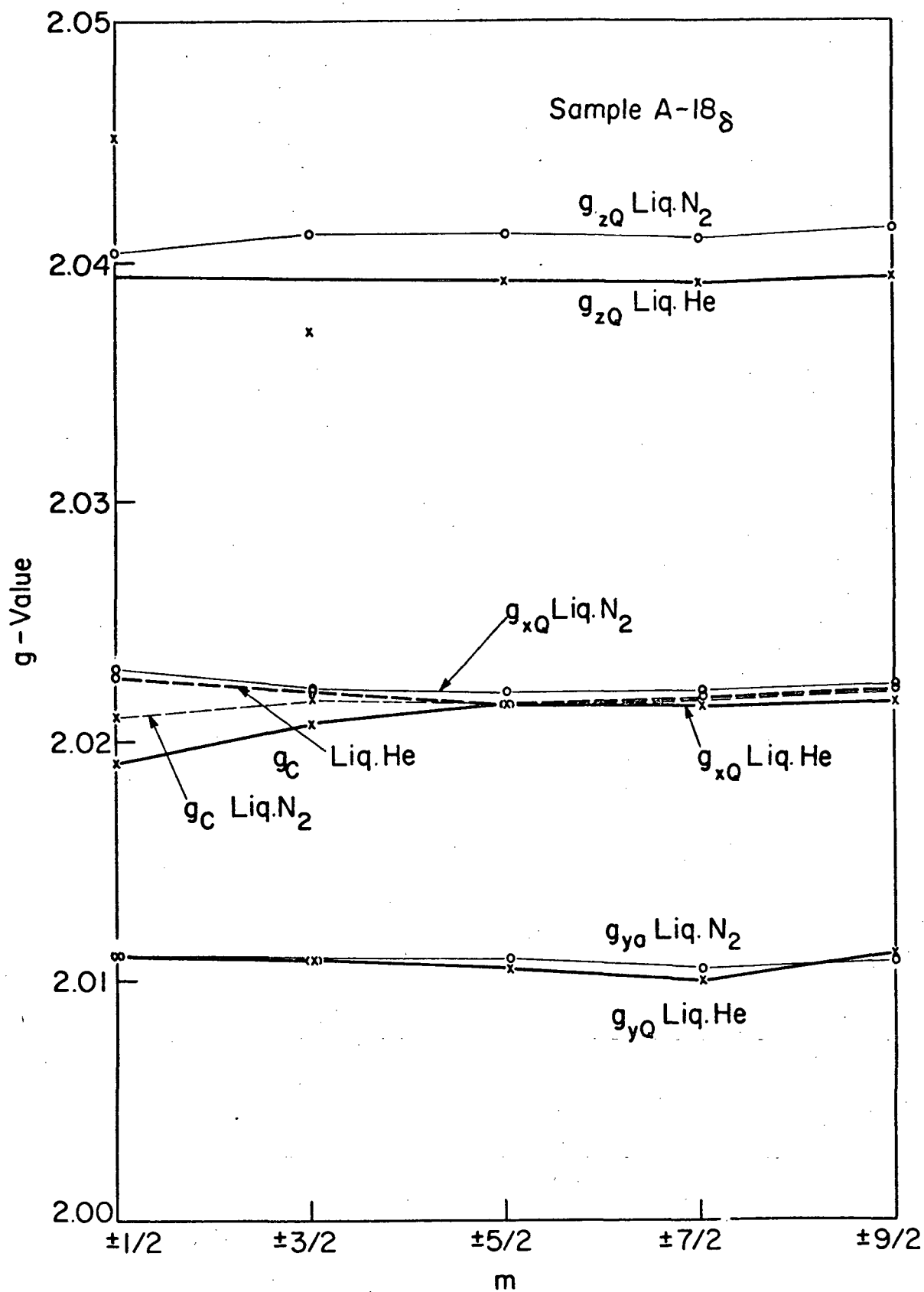


Fig. 27. g-value vs. m ii) (110)-plane

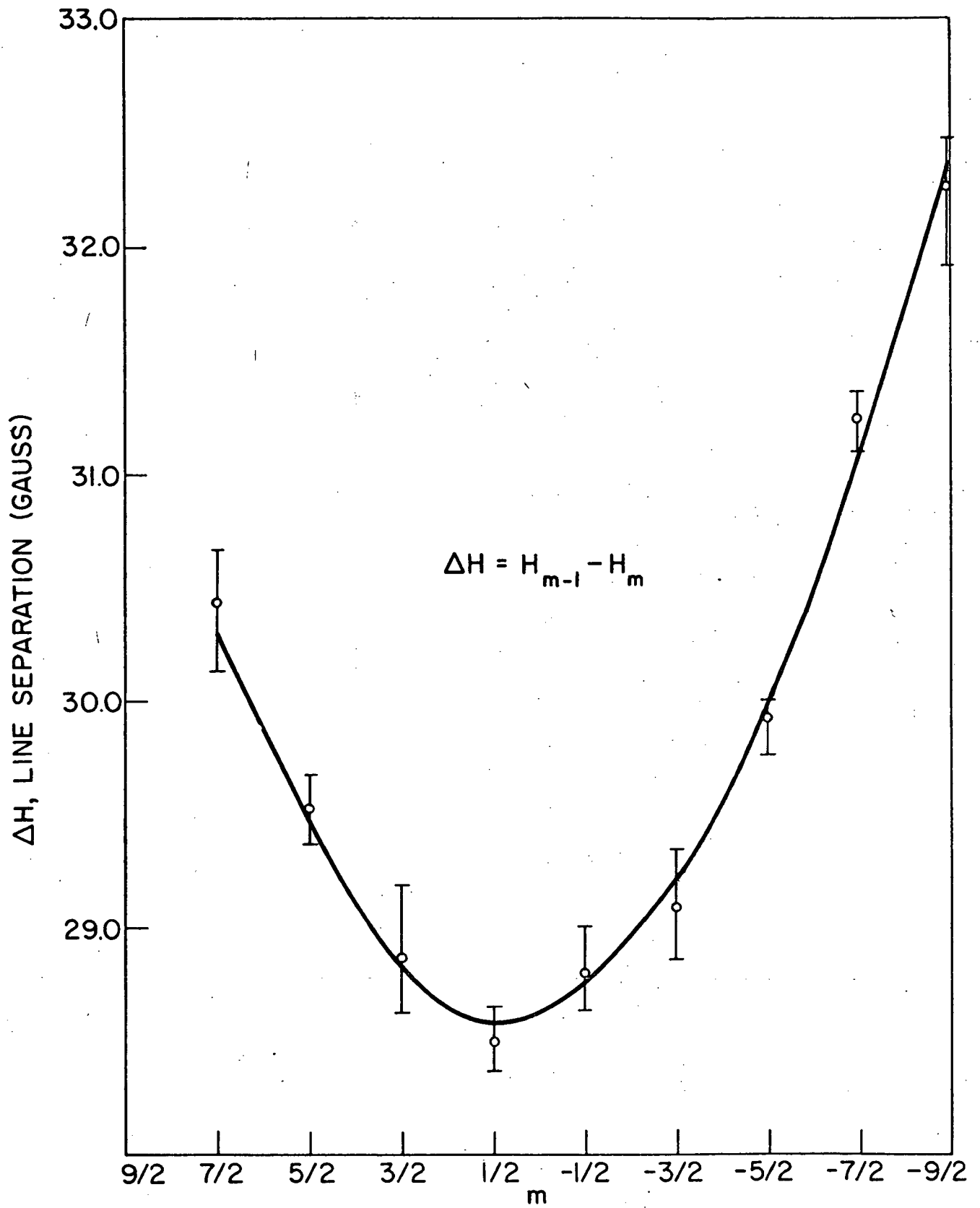


Fig. 28. Adjacent Line Separation (c-axis)

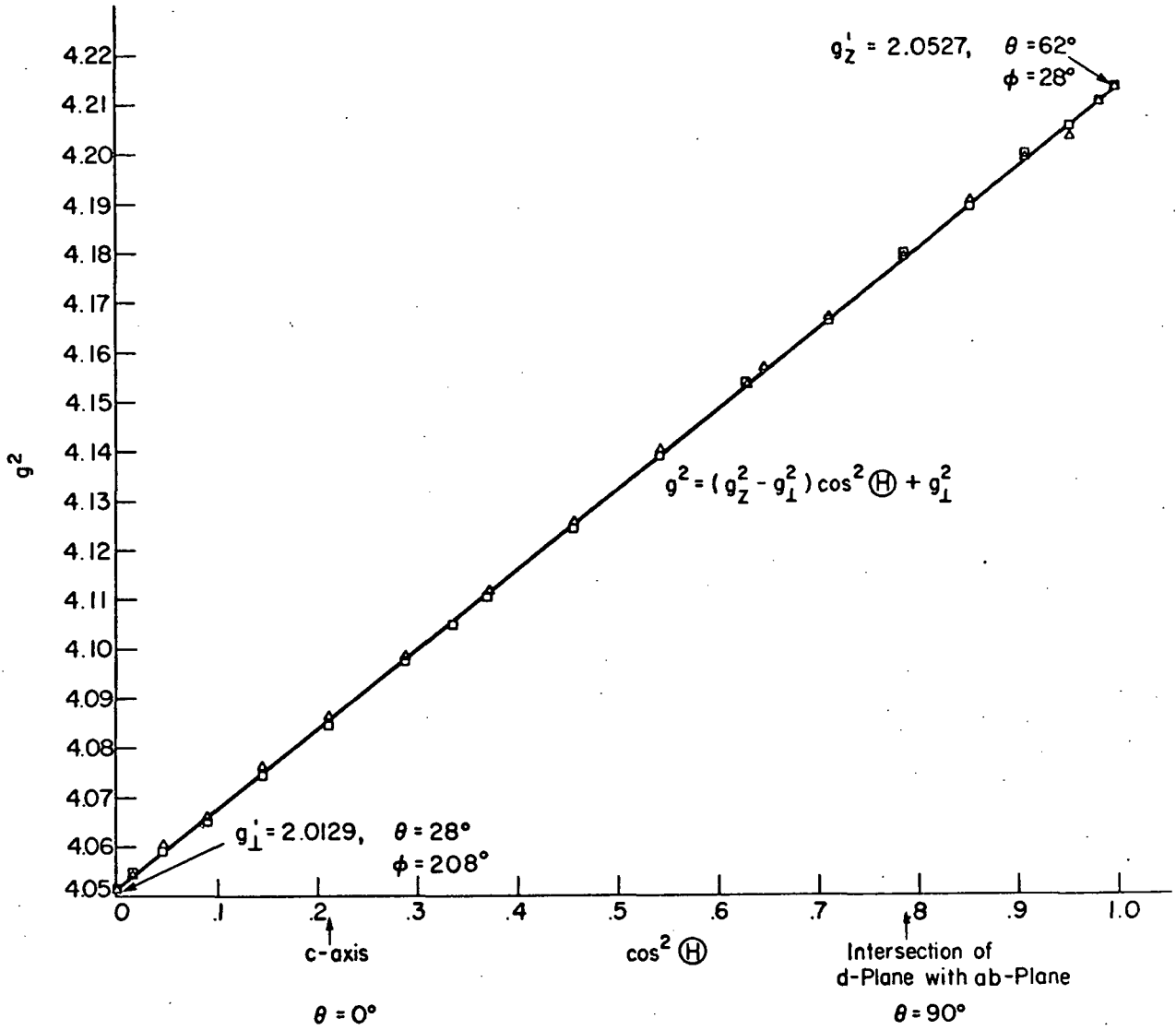


Fig. 29. Fit of g^2 -Equation

Table 2

 g^2 vs. $\cos^2 H$

$$g^2 = (g_z^2 - g_{\perp}^2) \cos^2(H) + g_{\perp}^2$$

	(H)	$\cos^2(H)$	g^2
z-axis	0.5 ⁰	.99992	4 21333
	2.5	.99810	4 21370
	7.5	.98295	4 21095
	12.5	.95316	4 20357
	17.5	.90958	4 19938
	22.5	.95459	4 19037
	27.5	.78679	4 17957
	32.5	.71131	4 16731
	36.5	.64619	4 15695
	37.5	.62940	4 15348
	42.5	.54358	4 14033
	47.5	.45642	4 12585
	52.5	.37059	4 11177
	57.5	.28869	4 08896
	c-axis	62.5	.21321
67.5		.14644	4 07604
72.5		.09043	4 06643
77.5		.04685	4 06023
82.5		.01704	4 05446
87.5		.00190	4 05197
x-axis		88.5	.00069
	92.5	.00190	4 05189
	97.5	.01704	4 05454
	102.5	.04685	4 05910
	107.5	.09043	4 06510
	112.5	.14644	4 07467
	117.5	.21321	4 08493
	122.5	.28869	4 09755
	125.5	.33721	4 10500
	127.5	.37059	4 11080
	132.5	.45642	4 12419
	137.5	.54358	4 13895
	142.5	.62940	4 15365
	147.5	.71131	4 16666
	on ab-plane	152.5	.78679
157.5		.85459	4 19013
162.5		.90958	4 19971
167.5		.95316	4 20544
172.5		.98295	4 21066
177.5		.99810	4 21358
179.5		.99992	4 21333

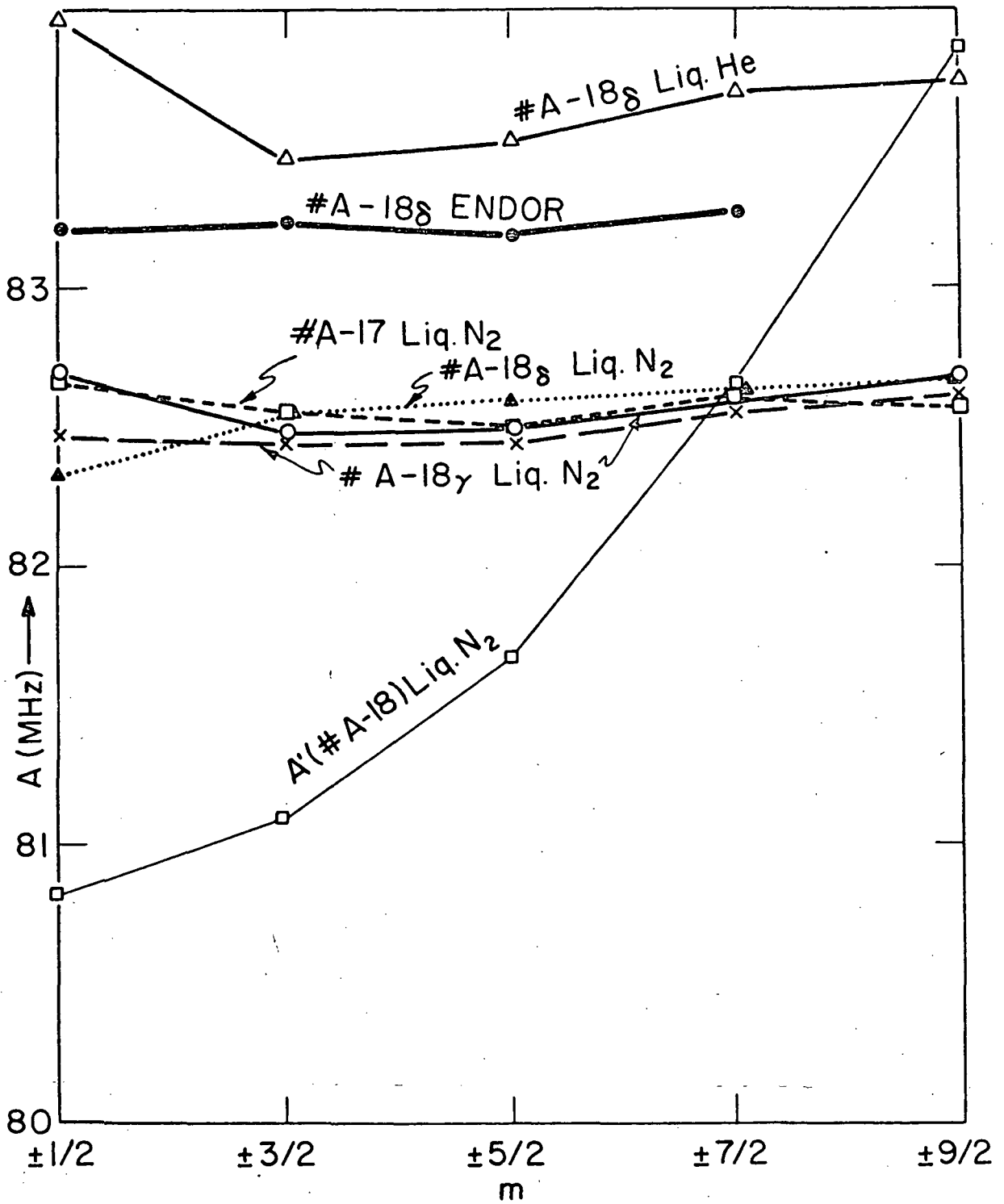


Fig. 30. A-value vs. m, c-axis

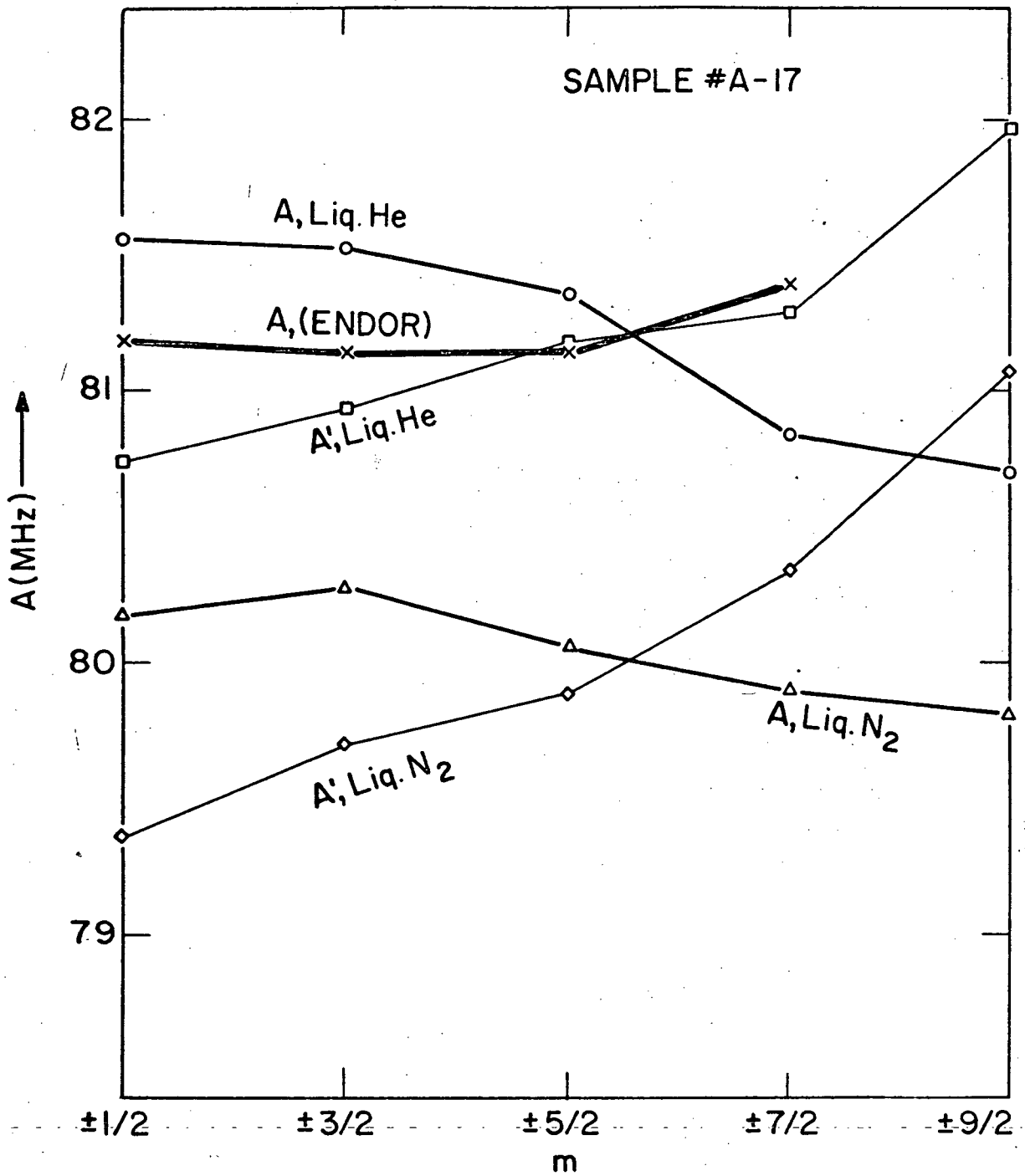


Fig. 31. A-value vs. m, X_g-axis

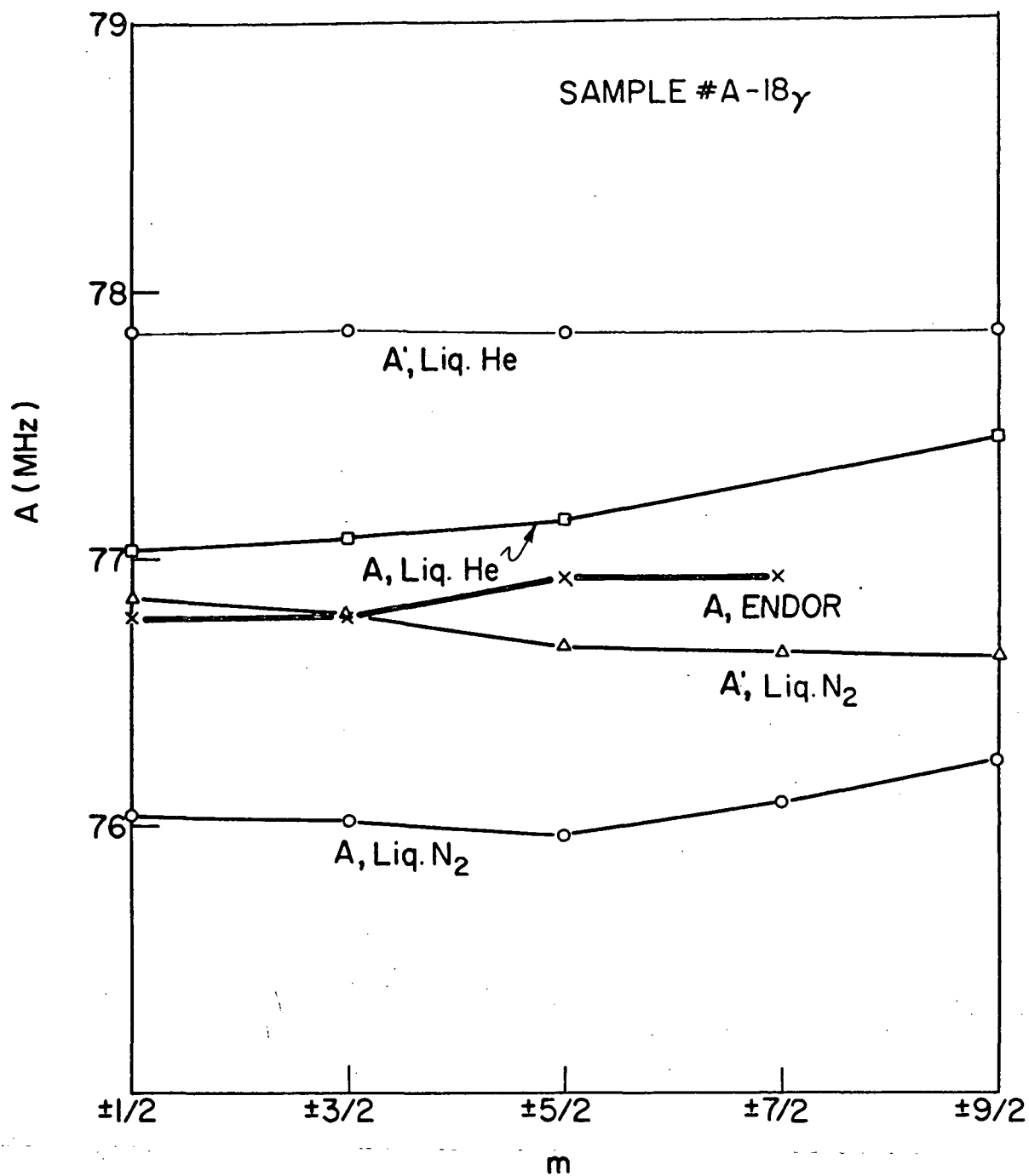


Fig. 32. A-value vs. m, Y_g-axis

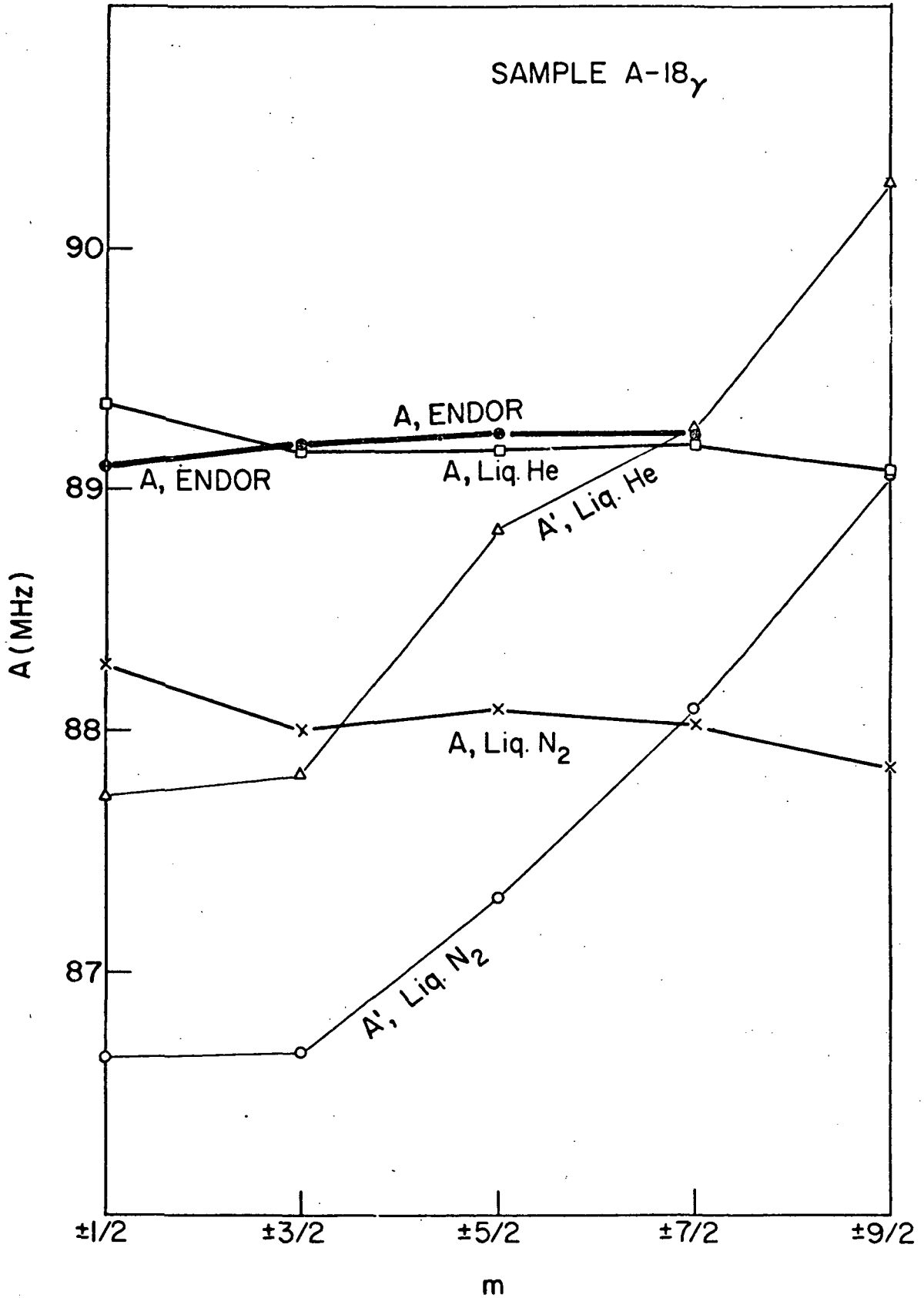
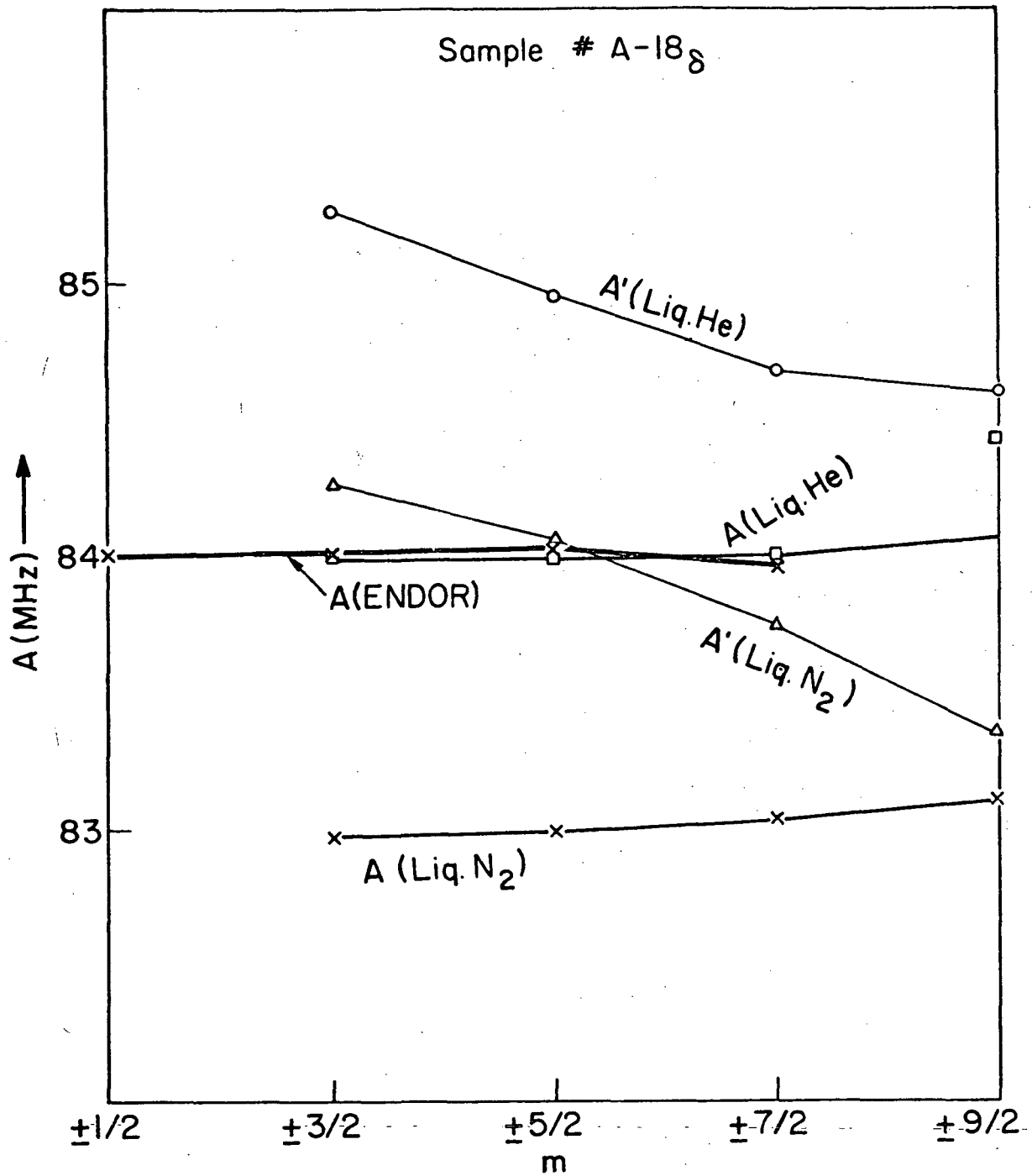


Fig. 33. A-value vs. m, Z_g-axis

Fig. 34. A-value vs. m, X_Q -axis

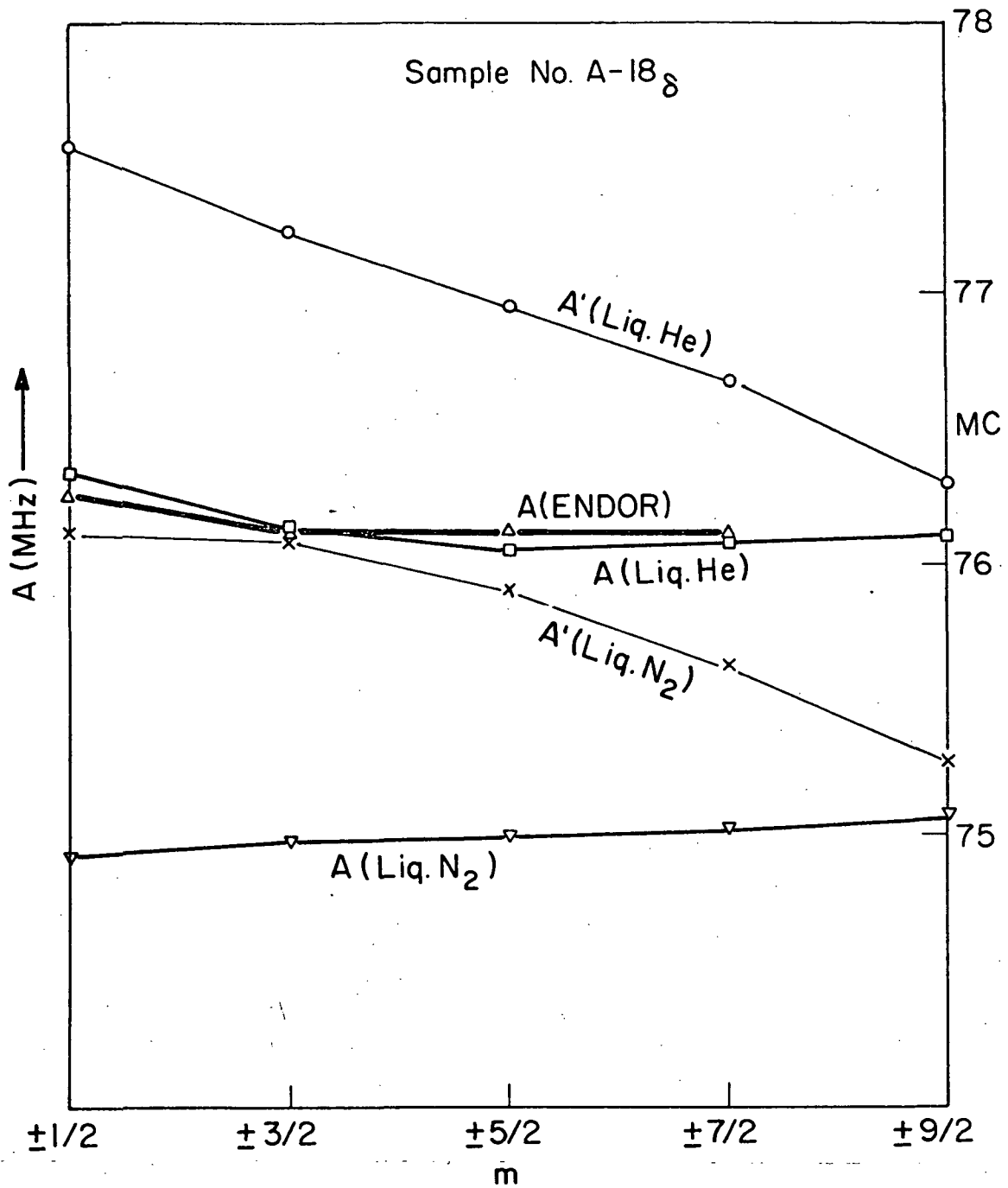


Fig. 35. A-value vs. m , Y_c axis

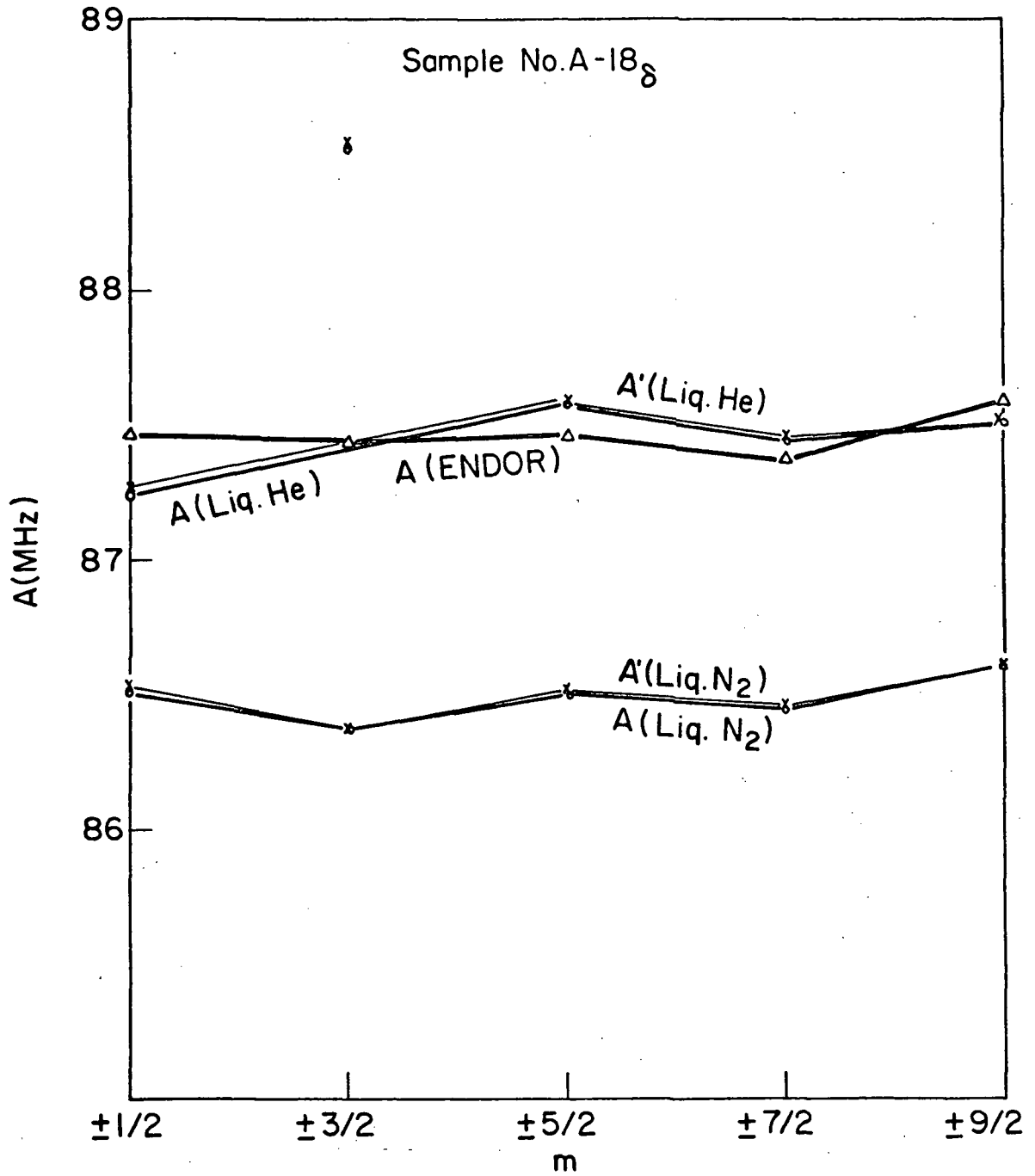


Fig. 36. A-value vs. m, B_Q -axis

B. ENDOR

1. ENDOR Frequency Identification

The ENDOR frequencies were measured from spectra, such as shown in Fig. 16. These spectra are obtained by applying saturating microwave power at the resonance magnetic field of each of the $2I + 1$ HFS lines and then scanning with an RF generator from about 20 to about 70 MHz. In general, there are four frequencies for each value of m , excepting for $m = \pm I$, for which there are only two.

We shall show how the partial identification of the ENDOR frequencies given in Eq. (66) is correlated with the experimental curves given in Figs. 38 to 44. Two characteristics of the plots are that (1) they occur in pairs, i.e. two of the 4 branches have a positive slope, the other two have a negative one, and (2) that the curvature of the 4 branches are all positive, zero or negative.

These features can be readily understood from Eq. (66) in which, if we assume the terms containing f_4 to be the dominant ones in determining the slope of the plots. We note that the first two equations giving ϕ_1 and ϕ_2 have the same, or nearly the same slope, and the remaining two have also nearly the same slope but with a sign opposite to that of the former pair. The first two frequencies ϕ_1 and ϕ_2 are associated with the nuclear spin transition for $M = +\frac{1}{2}$. See Fig. 37a.

From the fact that the nuclear spectroscopic splitting factor g_n is positive for Nb^{93} , it is deduced from both EPR and ENDOR measurements

that A and f_4 have the same sign.

2. ENDOR Frequency Plots

The ENDOR frequencies measured along several directions ($X_g, Y_g, Z_g, X_Q, Y_Q, Z_Q$ and c-axis) are presented in Figs. 38 to 44. These frequency plots show clearly the importance of the quadrupole interaction term of the spin Hamiltonian. Ordinarily, the dominant nuclear interaction terms such as the HFS and the nuclear Zeeman terms in the spin Hamiltonian are linear in the nuclear spin operator I , so that the second order contributions to the nuclear energy levels are proportional to matrix elements of the form

$$|\langle m \pm 1 | I_{\pm} | m \rangle|^2$$

and therefore are quadratic functions of m . The ENDOR frequencies then, being given by the separation of adjacent nuclear spin magnetic levels, are linear in m , and hence the ENDOR frequencies plots are expected to be straight lines. On the other hand, if an interaction term quadratic in the operator I is dominant, such as the nuclear quadrupole interaction, then relevant matrix elements are of the form

$$|\langle m' | I_i I_j | m \rangle|^2$$

so that the second order contributions to the energy levels will be quartic in m . Consequently, the expressions for the ENDOR frequencies are expected to depend upon m^2 and m^3 . The frequency plots, Figs. 38 to 44 reveal that the behavior of Nb^{4+} ion in $CaWO_4$ favours the latter case, that is the quadrupole interaction

dominates. Equations of ENDOR frequencies derived under the assumption of dominant quadrupole interaction are given by Eq. (66). The curvatures of the plots depend upon W , given by

$$W = 8 (f_5 - 4f_6) \quad (68)$$

where

$$f_5 = \frac{(Q_{11} - Q_{22})^2 - 4Q_{12}^2}{16A}$$

$$f_6 = \frac{Q_{13}^2 + Q_{23}^2}{4A}$$

As indicated earlier, the components of the quadrupole tensor, Q_{ij} , are measured in a coordinate system for which the 3-axis is the direction of magnetic field.

Consider the ENDOR plots in Fig. 40. For this case, the magnetic field is along the quadrupole principal axis, Z_Q , so that

$$f_5 = \frac{(Q_{11} - Q_{22})^2}{16A}$$

$$f_6 = 0$$

and

$$W = 8f_5 = \frac{(Q_{11} - Q_{22})^2}{2A}$$

The fact that the plots are straight lines, or nearly so, indicates that

$$W \approx 0$$

and

$$Q_{11} \approx Q_{22}$$

The value of W can also be obtained directly from the plot of Eq. (70), namely

$$\phi_1 - \phi_2 - \phi_3 + \phi_4 = -\frac{A^2}{h\nu_e} - 12mW \quad (70)$$

When the left-hand-side of Eq. (70) is plotted against m , the slope of the plot gives W . The result of fitting the ENDOR frequencies to the expressions of Eq. (66), using the W found in the preceding manner, is shown in Table 4.

3. Quadrupole Principal Axes and Values

The inadequacy of the usual perturbation calculation is revealed by Eq. (69). Combining this with Eq. (25') we find

$$(Q_{33})_{\text{approx.}} = \frac{1}{6} (\phi_1 - \phi_2 + \phi_3 - \phi_4) \quad (85)$$

which should be a constant (independent of m). The plots of this quantity versus m are given in Figs. 45 to 51. These plots show appreciable deviation from horizontal straight lines, although along the Z_Q axis, the $(Q_{33})_{\text{approx.}}$ for different m values is almost a constant. To account for these deviations, we use the more nearly correct expression Eq. (69''), which indicates that the plot of $\phi_1 - \phi_2 + \phi_3 - \phi_4$ is a parabola:

$$(Q_{33})_{\text{approx.}} = Q_{33} \left[1 - \frac{8}{A} (91f - 180f_6) + m^2 \frac{160}{A} (f_5 - 4f_6) \right] \quad (86)$$

or

$$(Q_{33})_{\text{approx.}} = Q_{33} \left[1 - \frac{2}{A} (V - 16W) + m^2 \left(\frac{20W}{A} \right) \right] \quad (86')$$

where use has been made of the relations of Eqs. (67) and (68). The curvatures of these plots depend upon the sign of the quantity $Q_{33} \frac{160}{A} (f_5 - 4f_6)$ of Eq. (86), or the quantity $Q_{33} \left(\frac{20W}{A} \right)$ of Eq. (86'). Fitting the ENDOR frequencies to Eq. (86') leads to the results given in Table 4, in which f_5 and f_6 have been calculated by using the average value of $(Q_{33})_{\text{approx.}}$ and the Eqs. (23) and (25); W is calculated from Eq. (68) and A is taken as a positive. Using the values of f_5 and f_6 given in Table 4, Q_{33} is calculated according to Eq. (86). The principal values of the quadrupole tensor given in Table 5 were obtained after correcting for this m^2 dependence.

The principal axis of quadrupole tensor can be readily obtained by noting that the intensities of the first forbidden lines are proportional to

$$I_{\text{forbidden}} \propto \frac{Q_{13}^2 + Q_{23}^2}{A}$$

$$\propto f_6$$

where the 3-axis denotes the direction of the magnetic field. Consequently, if the magnetic field direction coincides with one of the principal axes, then both Q_{13} and Q_{23} are zero, and so is f_6 (See Eq. (25')), so that the forbidden lines disappear as shown in Figs. 14 and 15.

4. Nuclear g-Value

Use was made of the positive sign of g_n to show that A_{ii} and Q_{ii} have the same sign. The numerical value of g_n can be estimated from the ENDOR frequencies according to the formula:

$$g_n \beta_n H_m = \frac{1}{2} (\phi_4 - \phi_1) + m(2f_4 + 3W) \quad (87)$$

This equation is obtained by combining Eq. (70) with Eq. (71). When $3/2 (Q_{33})_{\text{approx.}}$ is substituted into Eq. (87) for f_4 , the values of g_n calculated from this equation for different m 's are plotted as the first approximation of g_n . (See Fig. 52 to Fig. 55). More accurate values of g_n are found from Eq. (75). The latter gives the horizontal straight line shown in the same figures. Note that the difference between the g_n 's of various axes is less than 5% and that the quantity $g_n \beta_n H_m$ is small (~ 3.3 MHz in the x-band), so that the assumption of an isotropic g_n in the spin Hamiltonian is plausible. The average value of g_n determined by ENDOR is $1.366 \pm .036$ compared to 1.3652 obtained by nuclear magnetic resonance. (67)

5. The A-Values

The hyperfine structure tensor A is obtained through Eq. (72) or Eq. (76) or Eq. (82) in which the quantities W and V are calculated from Eqs. (67) and (68) by using the f_5 and f_6 presented in Table 4. Along the principal axes of quadrupole, the values of A calculated for different values of m are plotted in Fig. 56. The near independence of A upon m provides considerable confidence to the precision of the A-values. For other directions, A-values

have been computed by Eq. (76) and plotted in Fig. 30 to Fig. 33 (labeled ENDOR) along with the A-values obtained by EPR technique. The ENDOR result should be comparable to the EPR result measured at 4.2°K. This is true for all the directions except the c-axis, X_g-axis and Y_g-axis, Fig. 30 to Fig. 32. For these directions the A-values obtained by ENDOR technique are about 2% smaller than by EPR technique. The reason behind this is not well understood. However, an interpretation is given as following. First of all we note that the EPR results for the hyperfine coupling constant A have been calculated from the Eq. (32):

$$\begin{aligned} \text{EPR: } A &\approx g\beta \frac{H_{-m} - H_m}{2m} \\ &- 8[2I(I+1) - 2m^2 - 1] f_5 \\ &- 8[-4I(I+1) + 8m^2 + 1] f_6 \end{aligned} \quad (32)$$

Using the definitions given previously:

$$V \approx 8 \left\{ [2I(I+1) - 1] f_5 + [-4I(I+1) + 1] f_6 \right\} \quad (67)$$

$$W \approx 8(f_5 - 4f_6) \quad (68)$$

Eq. (32) becomes

$$\text{EPR} \quad A = g\beta \frac{H_{-m} - H_m}{2m} - V + 2m^2 W \quad (32')$$

The ENDOR results have been obtained by using Eq. (82):

$$\text{ENDOR:} \quad A = \frac{1}{2} \left(\sum_m \phi + \sum_{-m} \phi \right) - V + 2(3m^2 + 1)W \quad (82)$$

The second and third terms in Eqs. (32') and (82) are the

correction terms due to quadrupole coupling. We expect A (EPR) and A (ENDOR) to be the same because both Eq. (32') and Eq. (82) are derived from the same energy level formula Eq. (24'). The question is then why for c-axis, X_g -axis and Y_g -axis, the experimental values of A (EPR) and A (ENDOR) are different. Suppose we imagine an ideal case without the quadrupole interaction, nuclear Zeeman interaction, or the second order HF effect. Then we would have instead of Eqs. (32') and (82),

$$\text{EPR:} \quad A = g\beta \frac{H_{-m} - H_m}{2m} \quad (32a)$$

$$\text{ENDOR:} \quad A = \frac{1}{4} (\sum_m \phi + \sum_{-m} \phi) \quad (82a)$$

The idealized energy levels are depicted as shown in Fig. 37b, in which $h\nu_e$ is the EPR frequency and ϕ_1, ϕ_2, ϕ_3 and ϕ_4 are the ENDOR frequencies. The energy levels are two sets of parallel lines, $M = +\frac{1}{2}$ and $M = -\frac{1}{2}$, with equal spacing, $\phi_1 = \phi_2 = \phi_3 = \phi_4 = \frac{1}{4} \sum_m \phi$. The HF lines $h\nu_e$ are vertical lines which are also parallel to each other and with equal spacing given by $\frac{H_{-m} - H_m}{2m}$. Therefore the A-values measured by EPR and ENDOR methods can be represented by a tetragonal like abcd which is, in this case, a parallelogram and has a constant area $\propto \frac{1}{2} A^2$. In the EPR method, what we measured is the diagonal distance \overline{bd} , while in the ENDOR method, the sum of sides \overline{ab} and \overline{cd} , that is

$$\overline{bd} = g\beta \frac{H_{-m} - H_m}{2m}$$

$$\overline{ab} + \overline{cd} = \frac{1}{4} (\sum_m \phi + \sum_{-m} \phi)$$

and

$$\overline{bd} \cdot (\overline{ab} + \overline{cd}) = A^2 = 2 \times \text{area of abcd}$$

When the effects of nuclear Zeeman interaction or/ and the second order HF interaction are taken into consideration, the energy levels become non-parallel lines for each set of $M = \pm \frac{1}{2}$. However these terms are cancelled out and have no influence on the calculation of A. In our case, the quadrupole coupling effect is important. When this effect is included, the spacing between the energy levels at a given magnetic field become unequal, and the area of the parallelogram abcd is no longer proportional to $\frac{1}{2} A^2$. In order to keep this proportionality, correction factors are to be introduced into the linear dimensions of the parallelogram abcd. The correction on the diagonal appears on the second and third terms of Eq. (32') and that on the sides, $ab+cd$, appears on the second and third terms of Eq. (82). Thus any error introduced in the estimation of these correction terms would show up as the difference in A (EPR) and A (ENDOR). Since both Eq. (32') and Eq. (82) contain the same V, this term does not lead to different values in A. However, the third term of Eq. (32'), $2m^2W$ and that of Eq. (82), $2(3m^2+1)W$ are important. They carry the same factor W but the coefficients $2m^2$ and $2(3m^2+1)$ are different. Thus along the c-axis, since W has a negative sign, an over estimated magnitude of W leads to an A(ENDOR) smaller than A(EPR). The same situation occurs on X_g -axis. Along Y_g -axis, W is found to have a positive sign. Hence an under estimation of the magnitude of W leads to an A(ENDOR) too smaller than it should be. Note that from Eq. (68), the magnitude of W is in turn determined by f_5 and f_6 . A small error in the estimation of f_5 and/or f_6 can produce an error 10 times as

bit in W. This argument indicates that the difference in the two A values obtained by EPR and ENDOR methods could come from errors introduced in the estimation of f_6 .

The final result of ENDOR experiment, including Q , g_n and A is summarized in Table 5. For comparison purposes, the data of EPR experiment are also included if possible.

Table 3

The W Value fitting to the Expressions of Eq. (66)

Direction	W		Concavity of Φ - Plots (Figs. 36 to 42)	
	Calculated from Eq. (68) KHz	Experimentally Measured from the slope of the plot of Eq. (70) KHz	Predicted by Eq. (66) using the left hand side value of W	Experimental Plot Shows
X _Q	+29	+24	Concave Down	Same as Prediction
Y _Q	+25	+36	Concave Down	Same as Prediction
Z _Q	+0.4	-5	Small Curvature	Straight Line
X _g	-52	-41	Concave up	Same as Prediction
Y _g	+11	+5	Small Curvature	Straight Line
Z _g	-70	-64	Concave up	Same as Prediction
C	-73	-84	Concave up	Same as Prediction

Table 4

Fitting of ENDOR Frequencies
to Eq. (86)

Direction	Sign of (Q_{33}) Approx.	f_5 KHz	f_6 KHz	W	A MHz	Sign of $Q_{33} \left(\frac{20W}{A} \right)$	Curvature of (Q_{33}) approx. -plot	
							Predicted Concavity	Actual Concavity
X_Q	-	3.7	0	+29	+84.008	-	down	down
Y_Q	-	3.1	0	+25	+75.734	-	down	down
Z_Q	+	0.05	0	+0.4	+87.442	+	up	Slightly down
X_g	-	2.3	2.2	-52	+81.208	+	up	up
Y_g	-	2.9	0.4	+11	+76.934	-	down	Slightly up
Z_g	+	0.36	2.29	-70	+89.234	-	down	down
C	+	0.56	2.41	-73	+83.150	-	down	down

Table 5

Constants of Spin Hamiltonian

Axis	Spherical co-ordinates referred to oxygen # 1		Q_{33} (MHz)		g_n (ENDOR)	A (MHz)			g EPR	
						ENDOR	EPR		4.2°K	77°K
	θ	ϕ	ENDOR	Calculated			4.2°K	77°K		
X_Q	57°	1225°	-0.561	-----	1.3446	84.008	83.930	82.841	2.0223	2.0222
Y_Q	90°	-45°	-0.835	-----	1.3568	75.734	76.147	74.997	2.0121	2.0108
Z_Q	33°	45°	1.392	-----	1.3657	87.442	87.823	86.485	2.0428	2.0409
X_g	28°	208°	-0.095	-0.084	1.3448	81.208	81.190	80.300	2.0104	2.0125
Y_g	90°	-62°	-0.739	-0.762	1.3497	76.934	77.252	76.074	2.0077	2.0069
Z_g	62°	28°	0.895	0.846	1.4019	89.234	89.274	87.844	2.0534	2.0531
X_A	27.5°	225°		-0.069				80.979		2.0136
Y_A	90°	-45°		-0.835				75.159		2.0113
Z_A	62.5°	45°		0.904				88.388		2.0492
a	90°	0°		-0.408			82.132	81.121		2.0366
b	90°	90°		-0.408			82.848	81.506		2.0145
c	0°	-----	0.748	0.816	1.3983	83.150	83.686	82.507	2.0240	2.0217

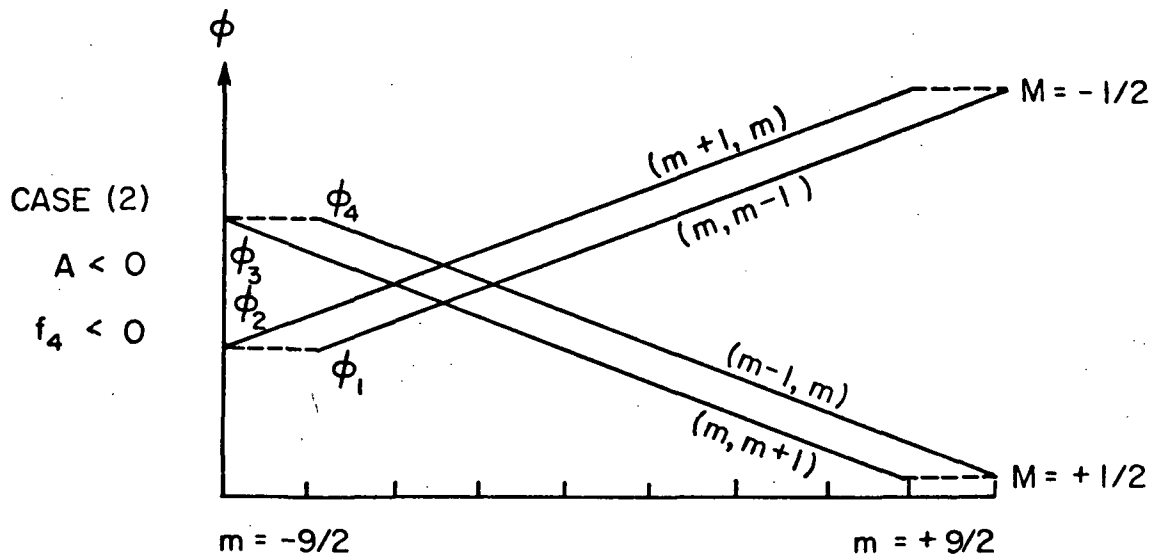
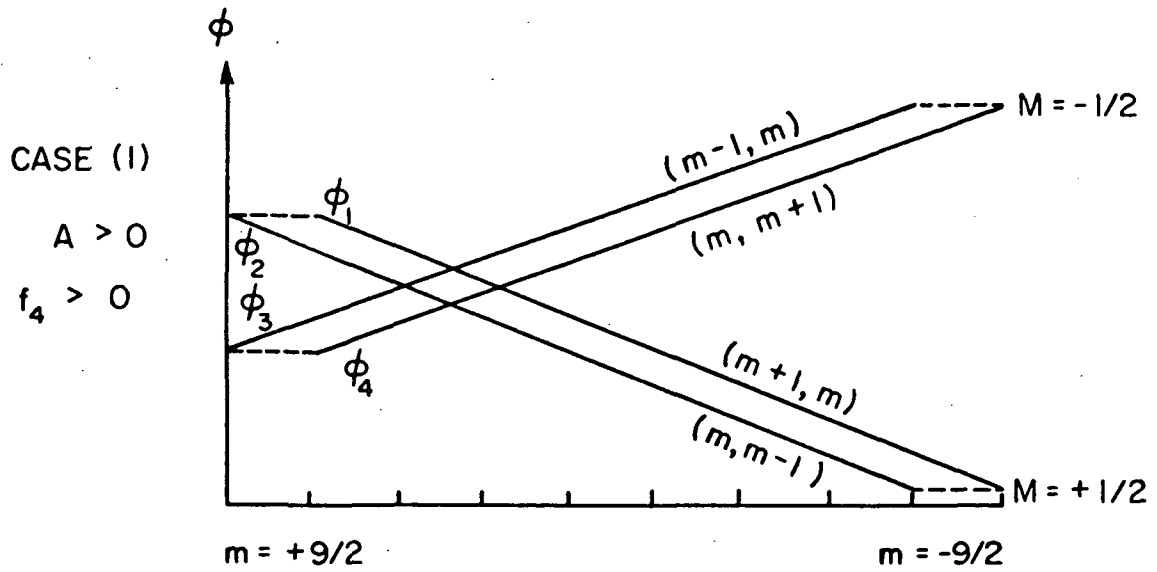


Fig. 37a. ENDOR Frequency Identification

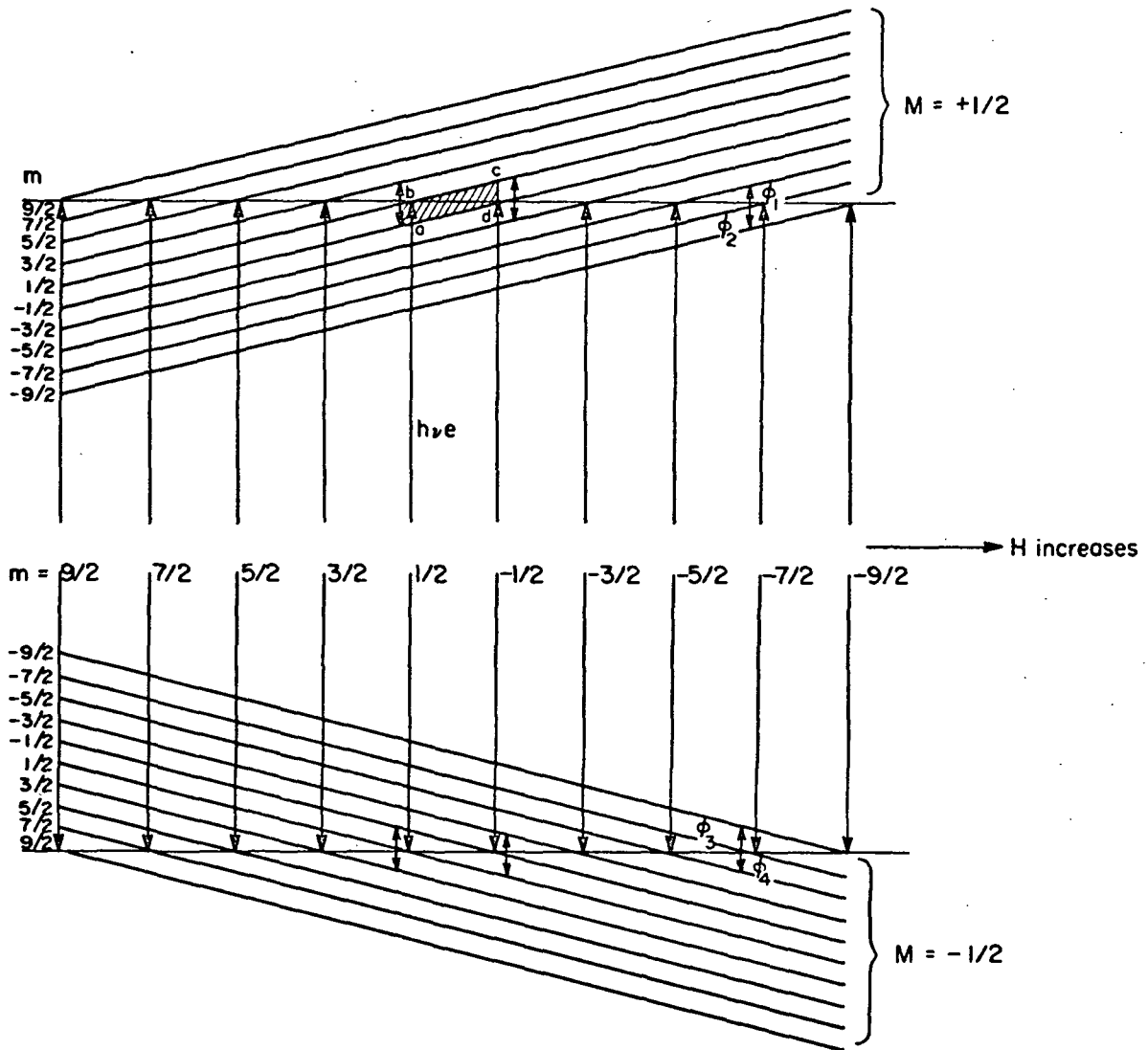


Fig. 37b. Idealized Energy Level Diagram with $E_{Mm} = g\beta H_m + AMm$

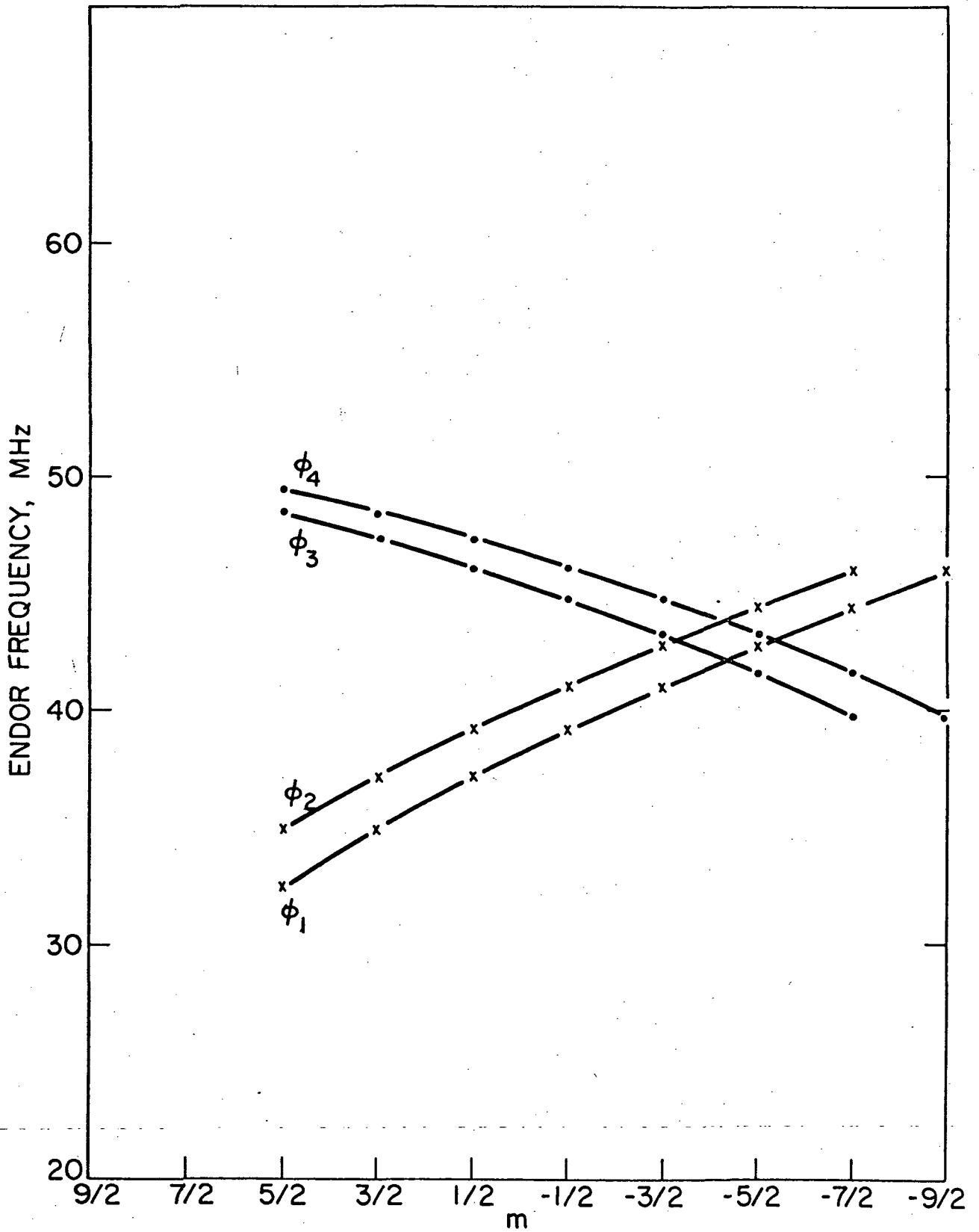


Fig. 38. ENDOR frequency vs. m , X_0 -axis.

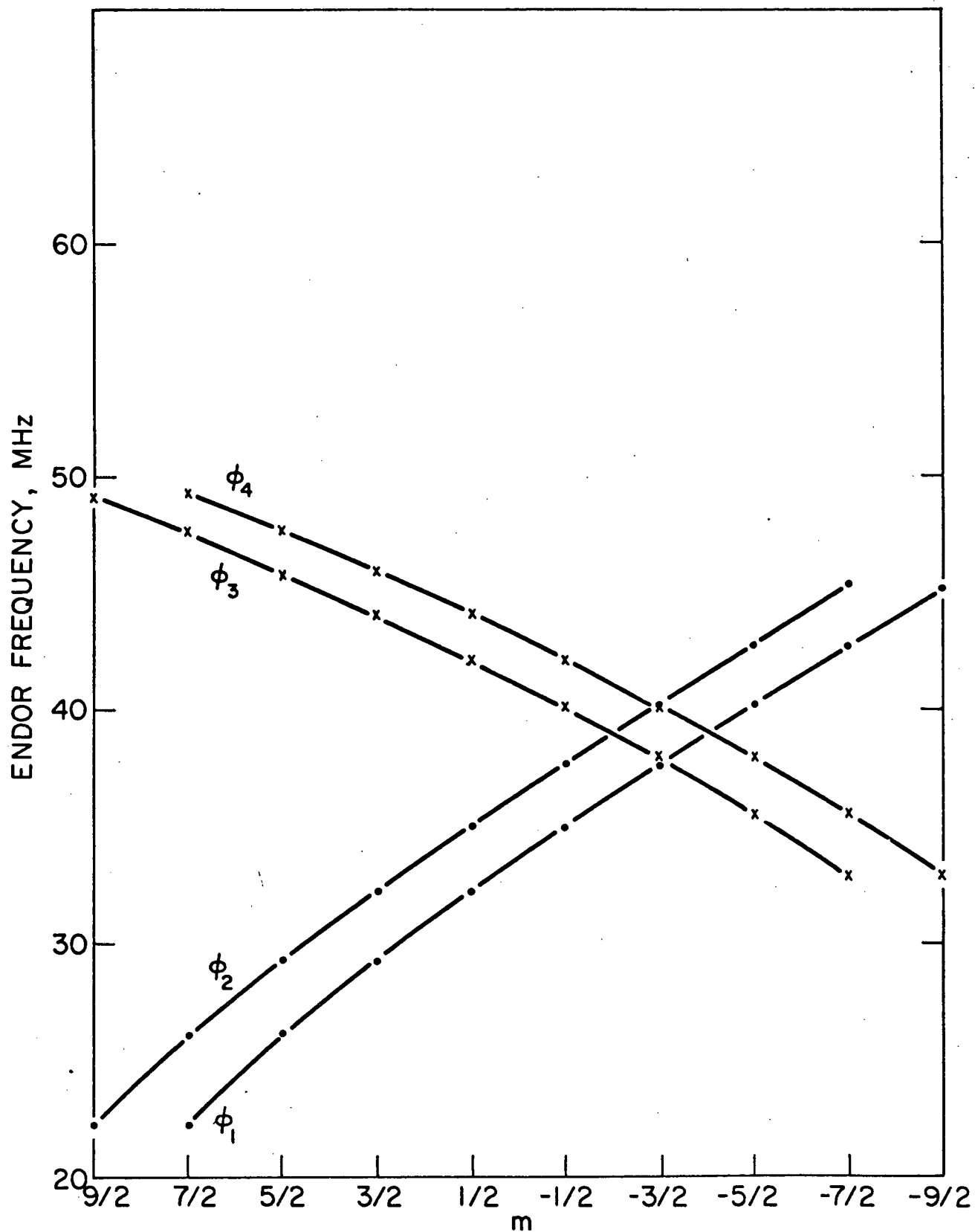


Fig. 39. ENDOR frequency vs. m , Y_Q -axis.

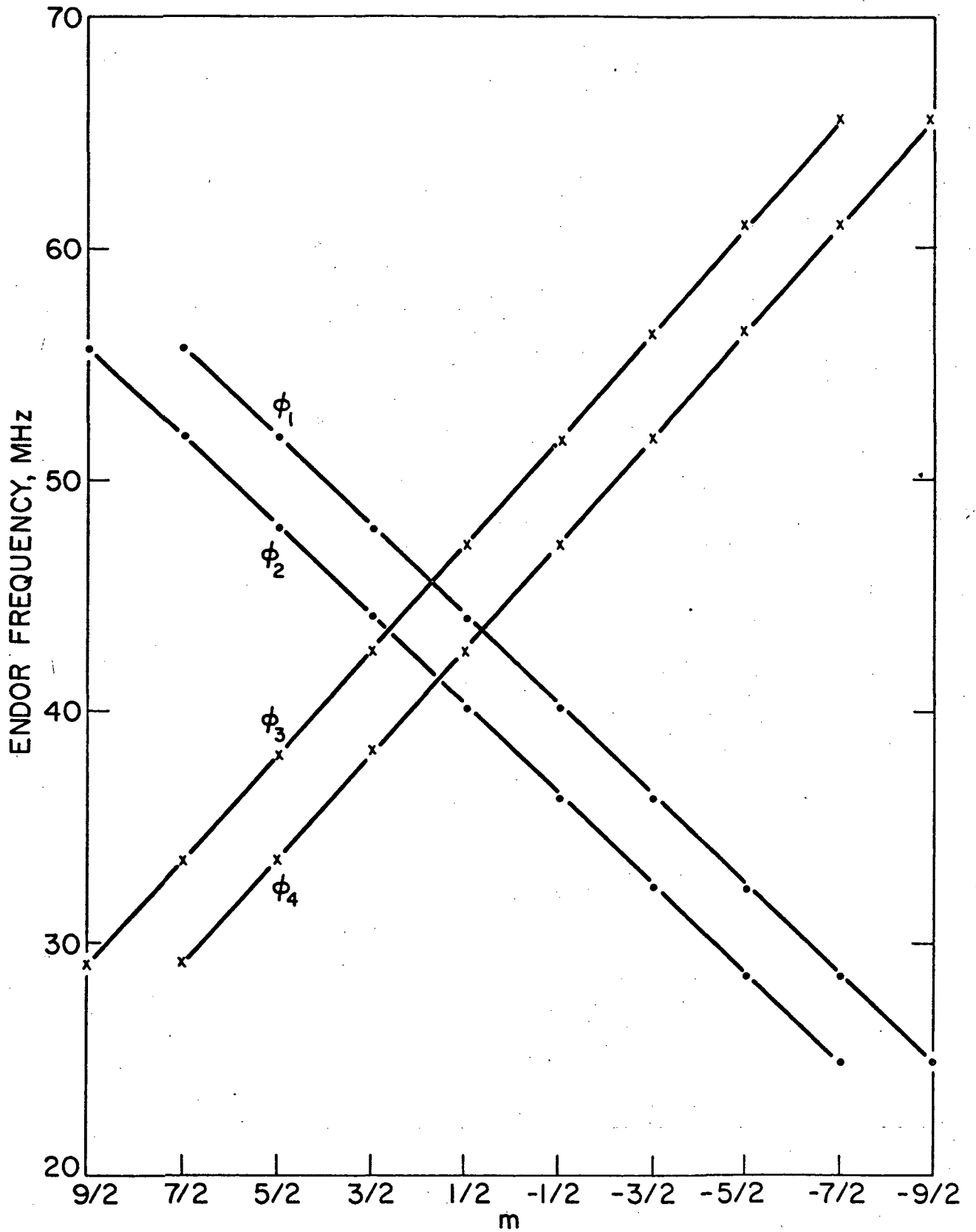


Fig. 40. ENDOR frequency vs. m , Z_0 -axis.

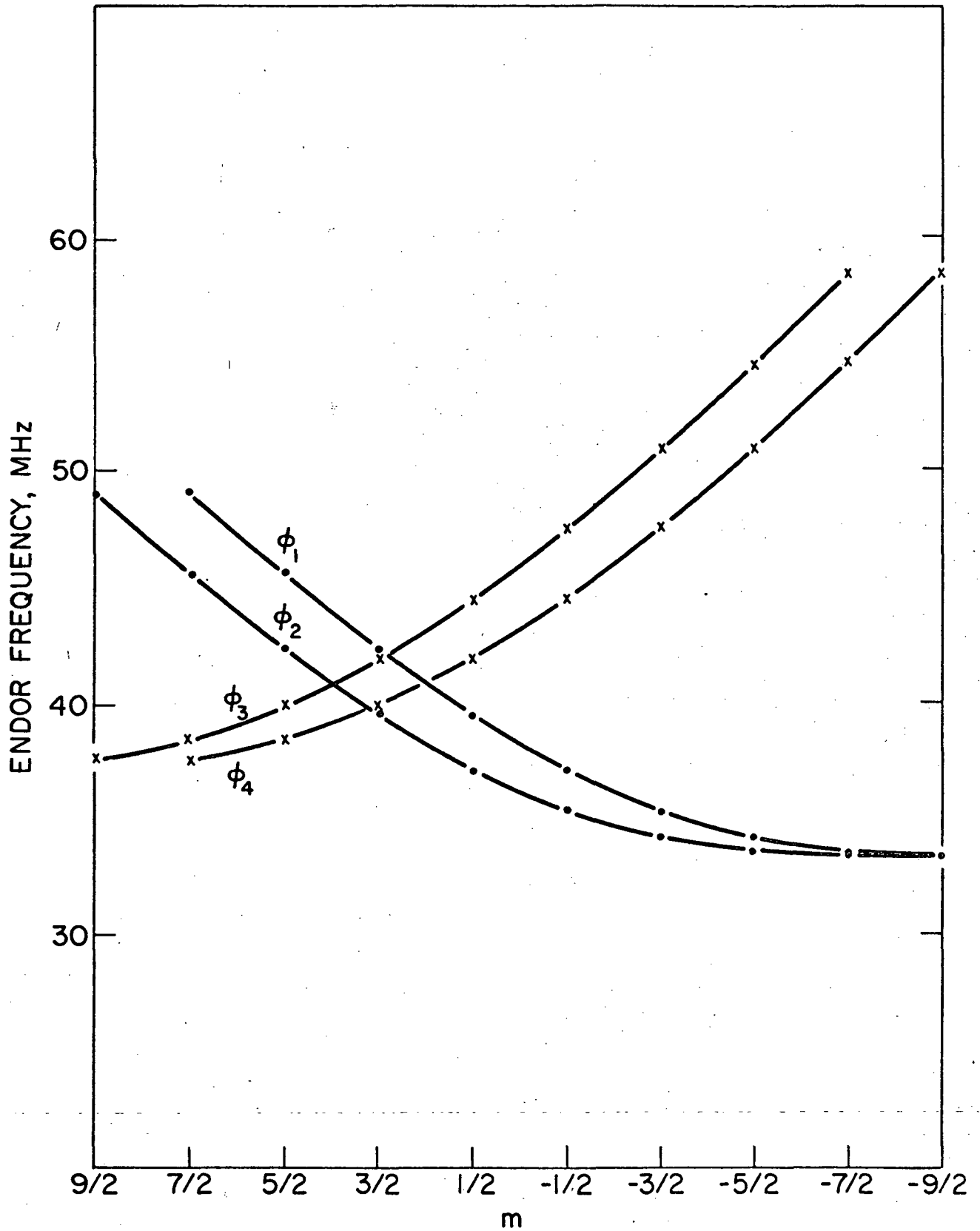


Fig. 41. ENDOR frequency vs. m , c-axis.

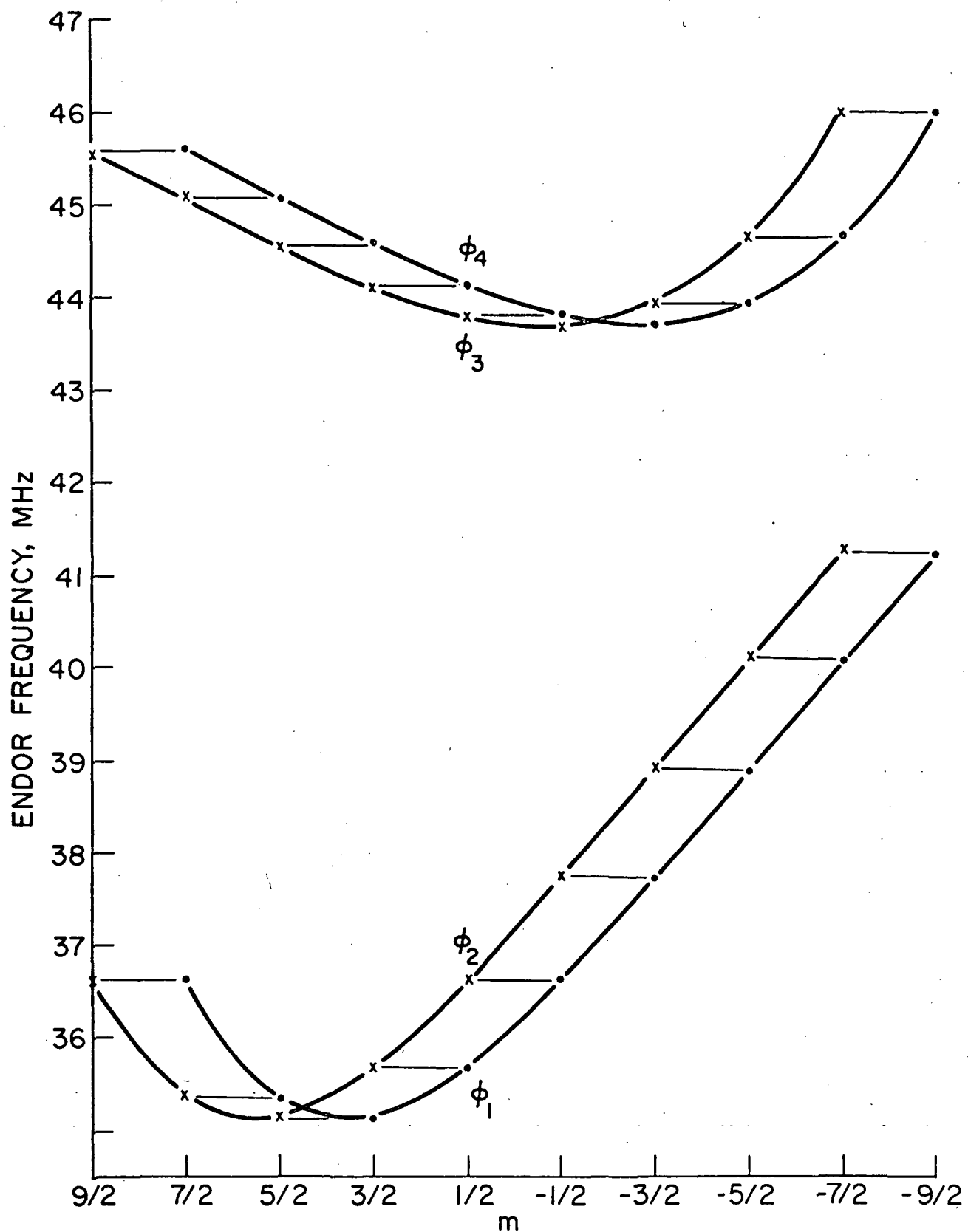


Fig. 42. ENDOR frequency vs. m , X_g -axis.

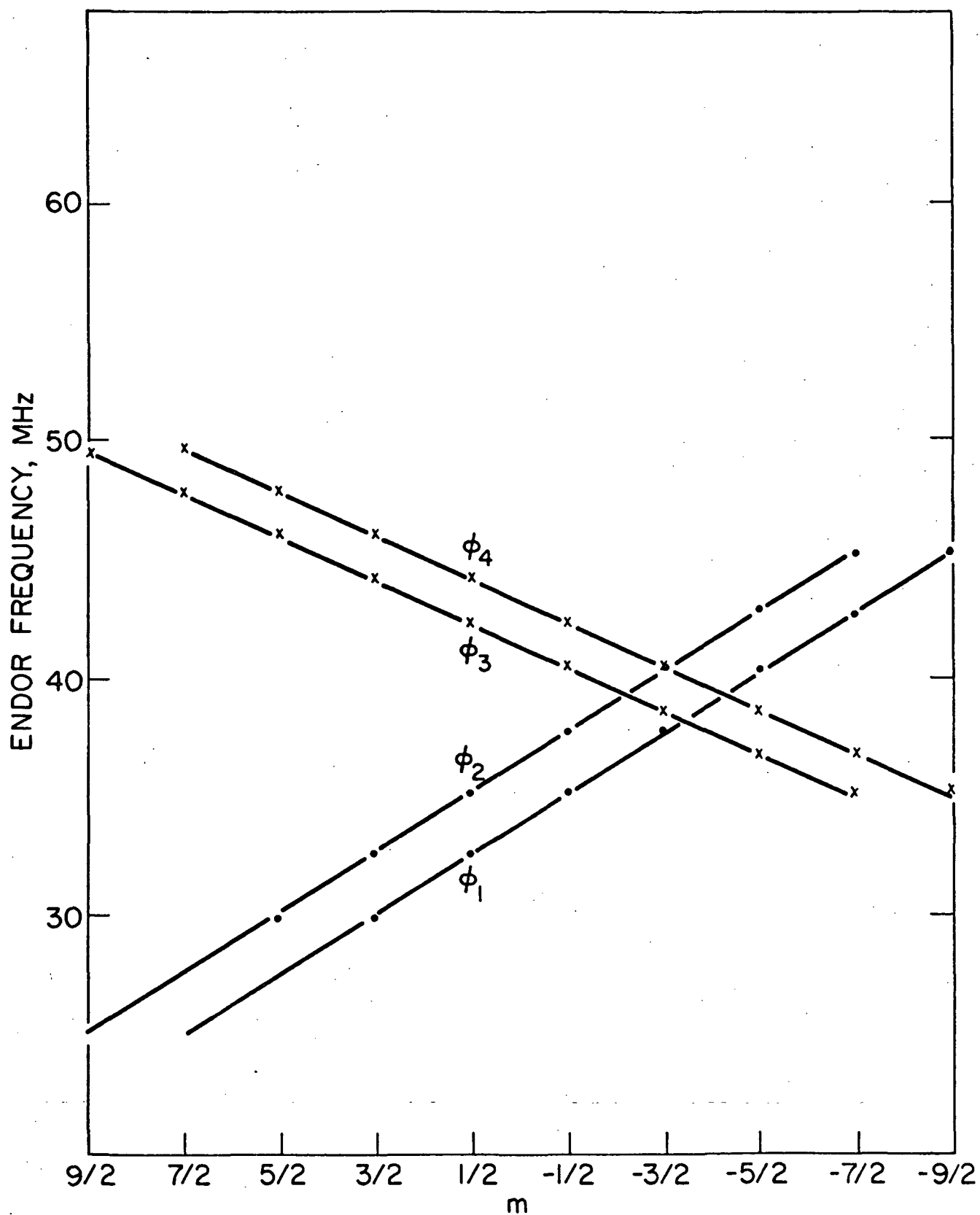


Fig. 43. ENDOR frequency vs. m , Y_g -axis.

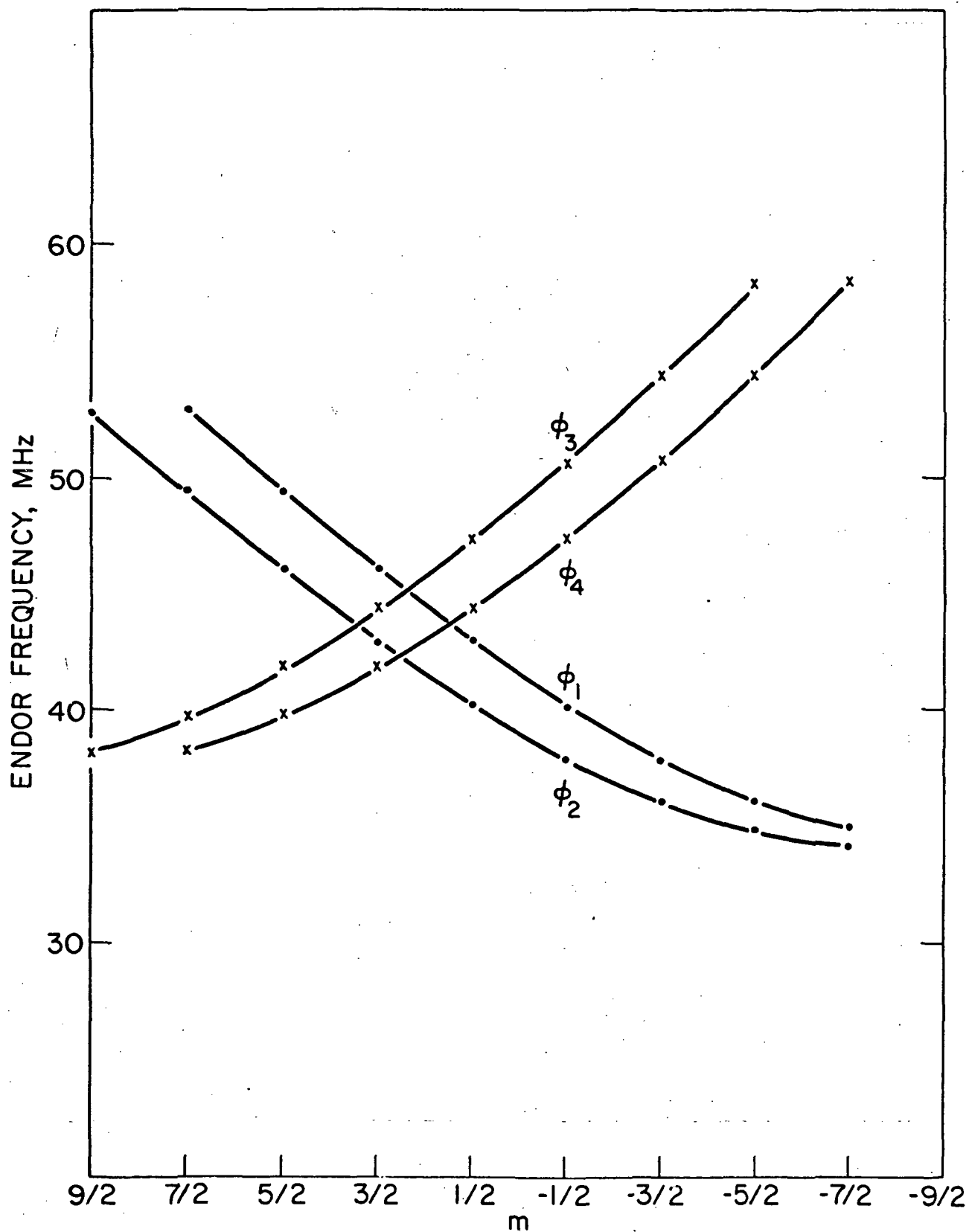


Fig. 44. ENDOR frequency vs. m , Z_g -axis.

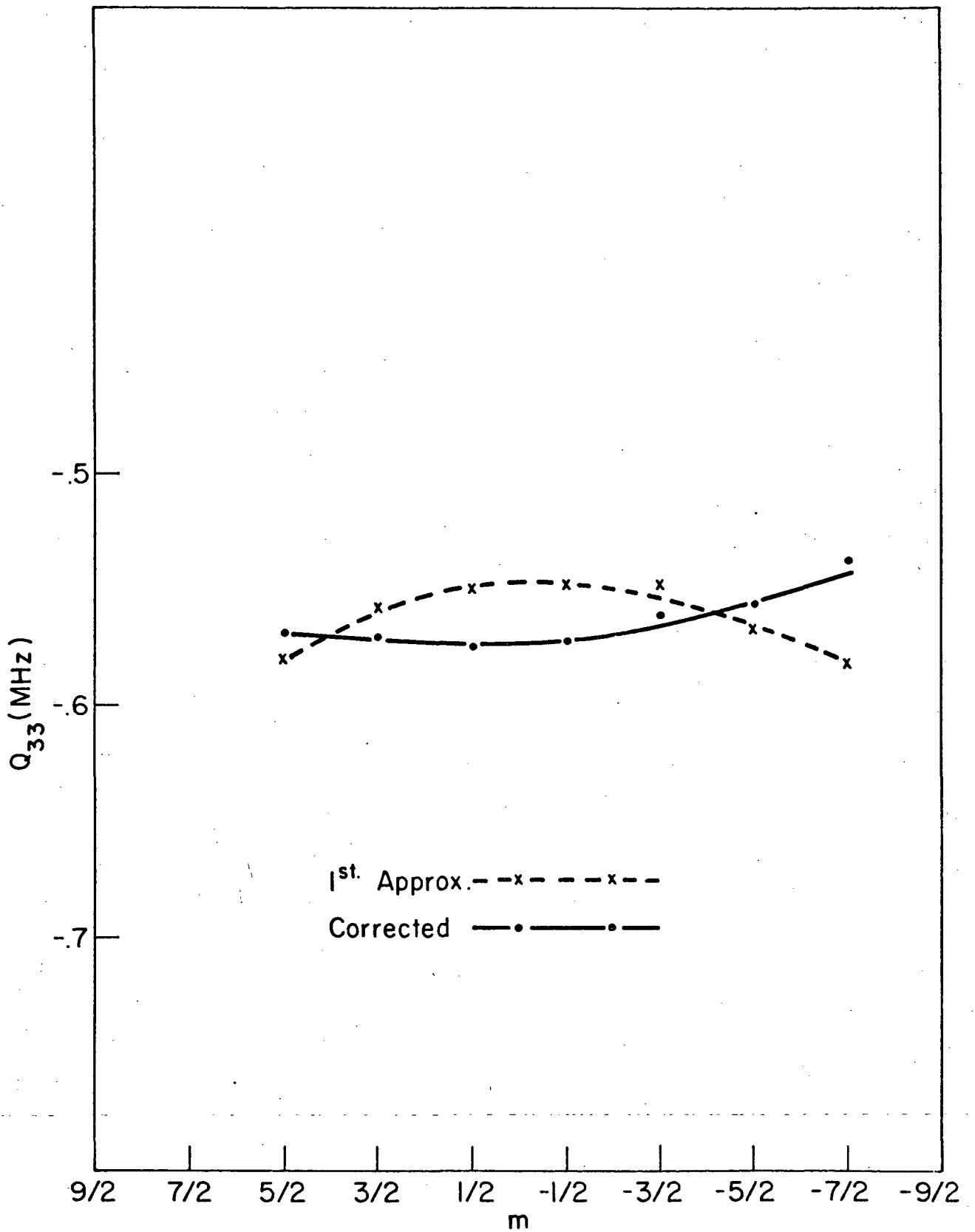
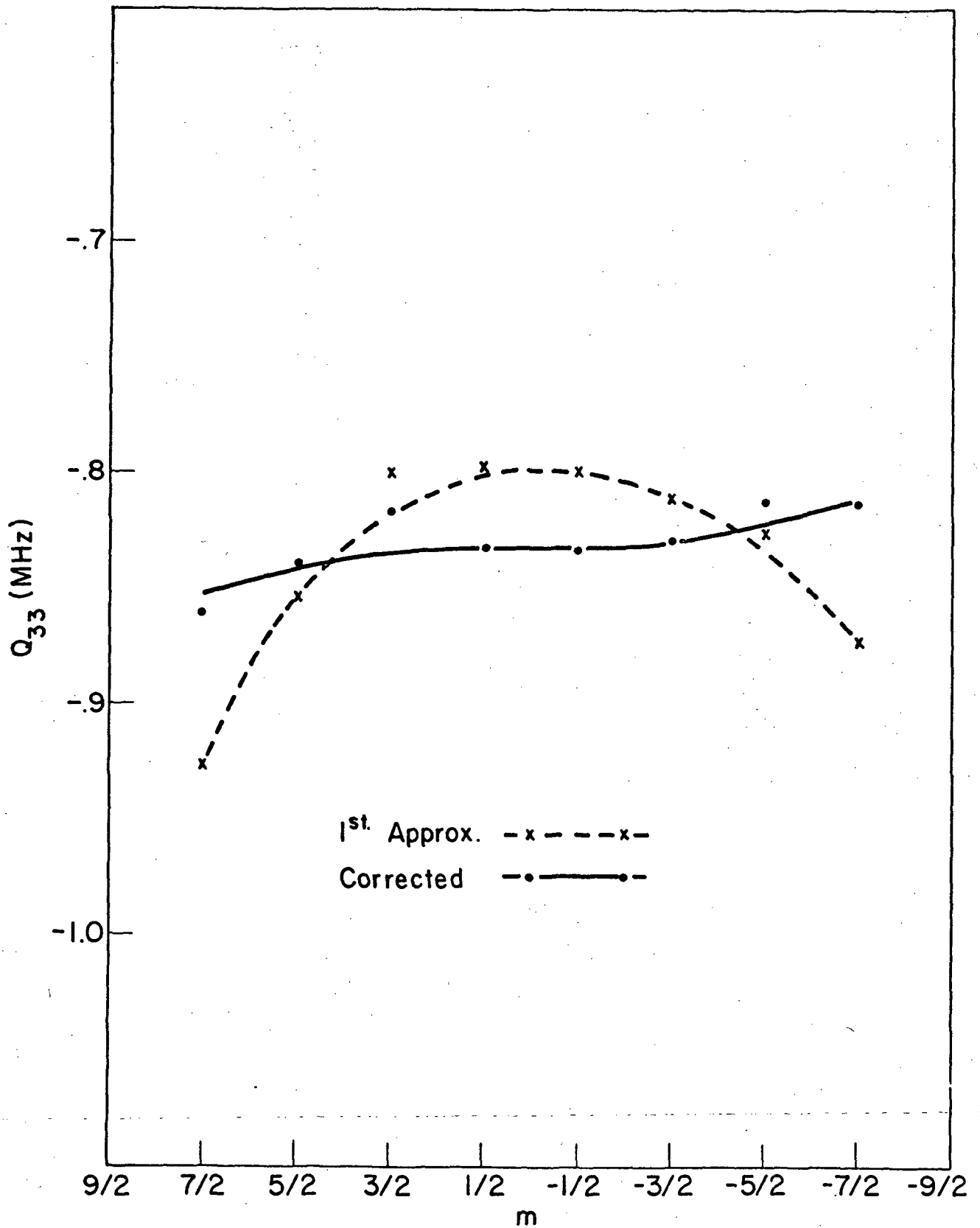
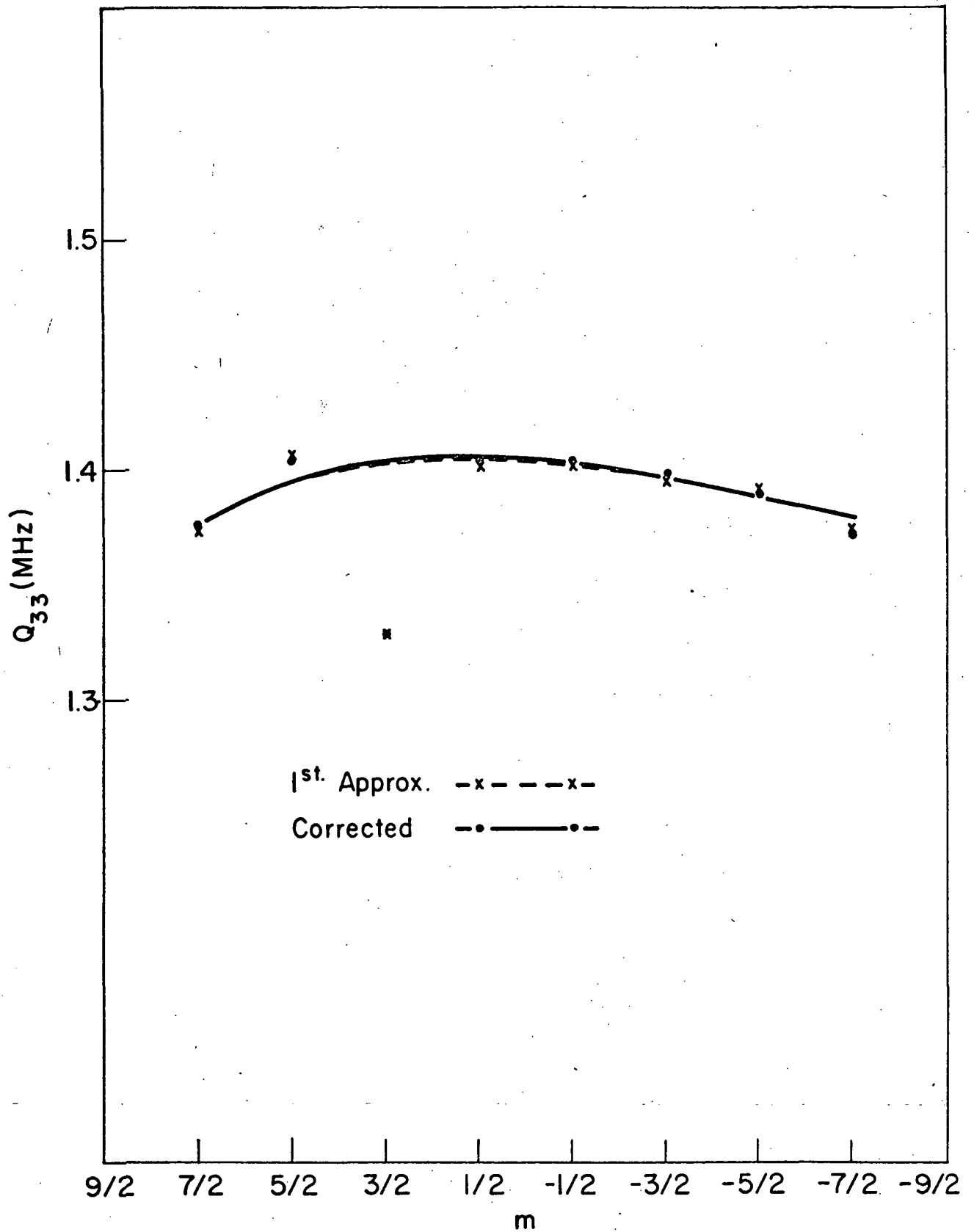
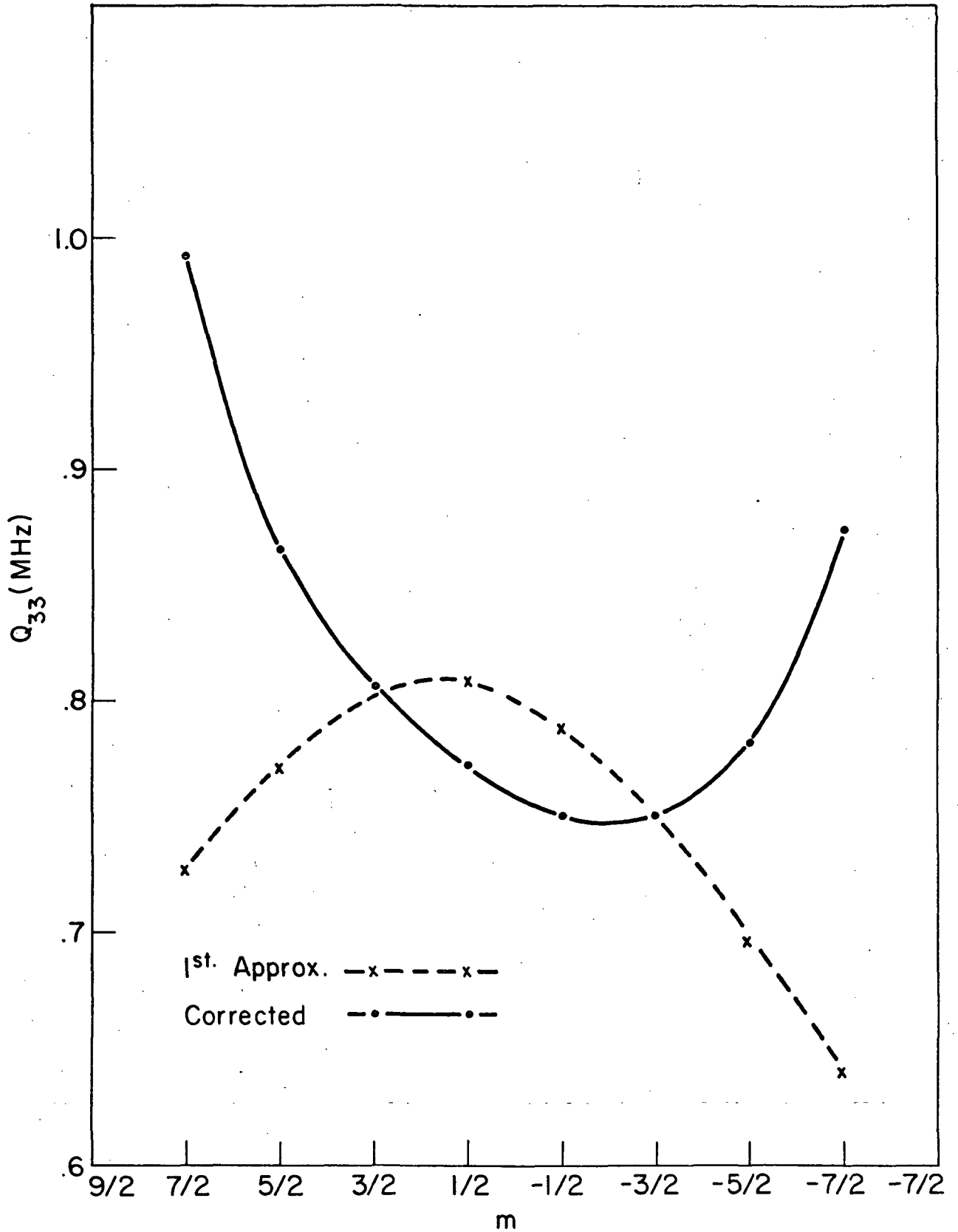
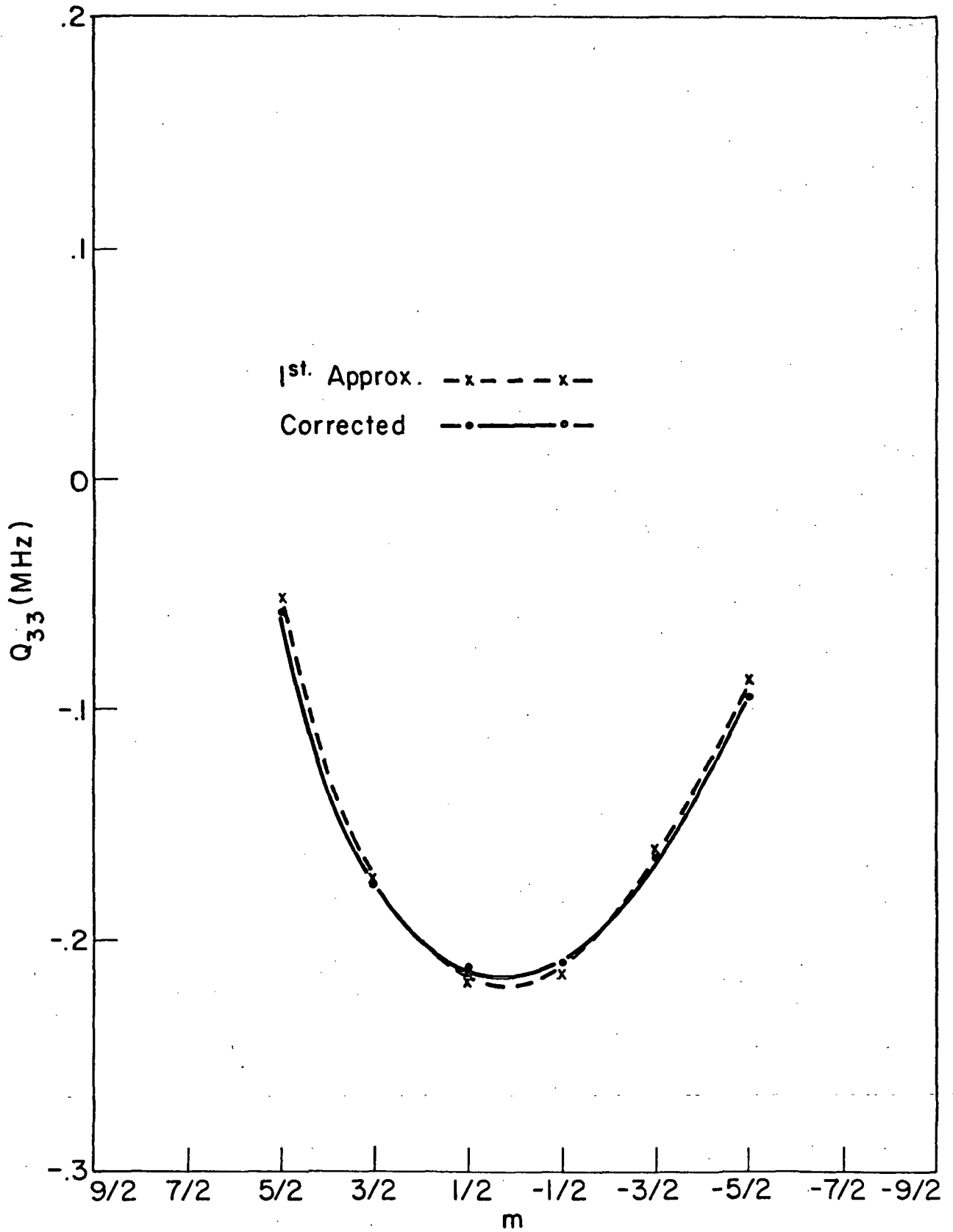


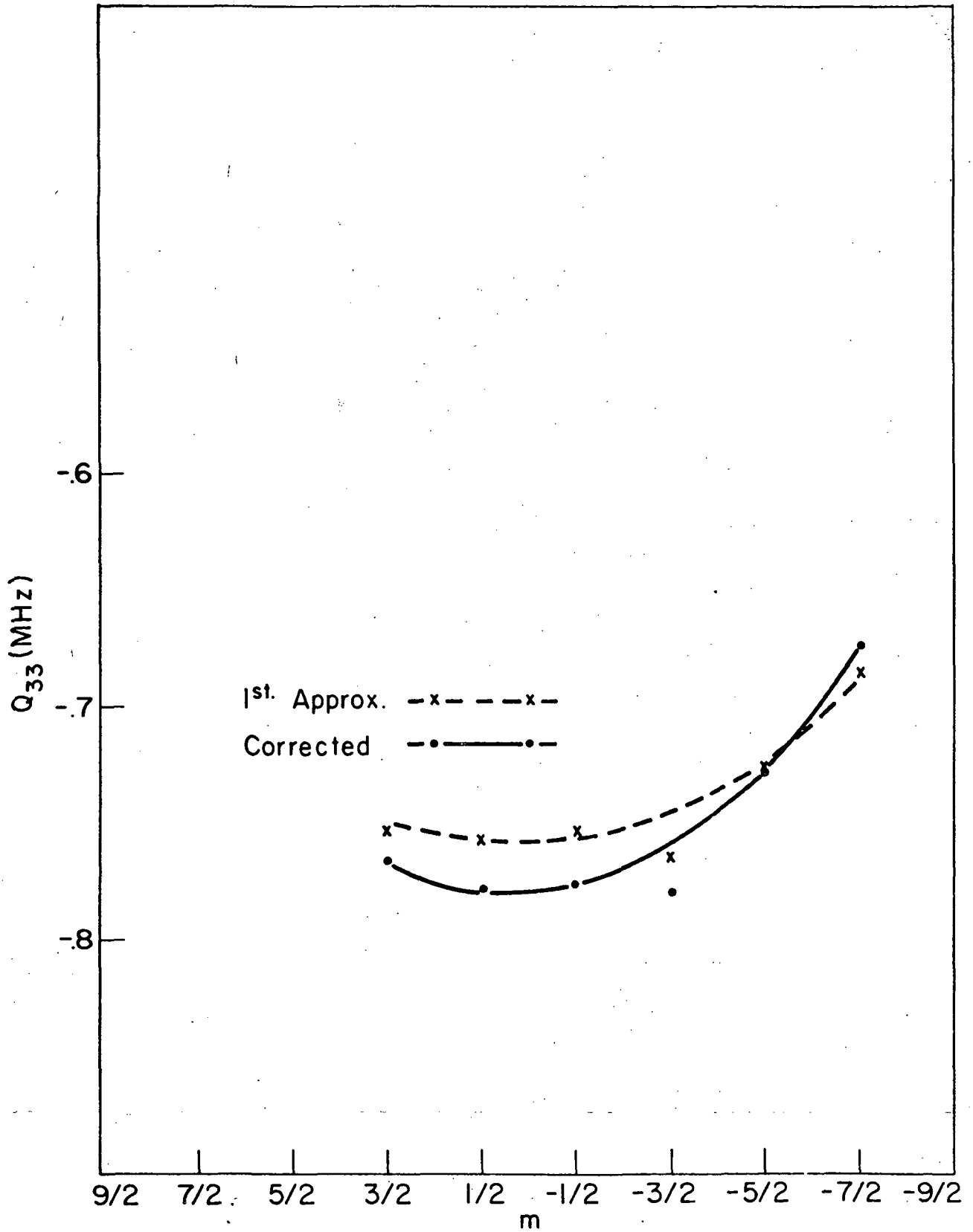
Fig. 45. Q_{33} vs. m , X_Q -axis

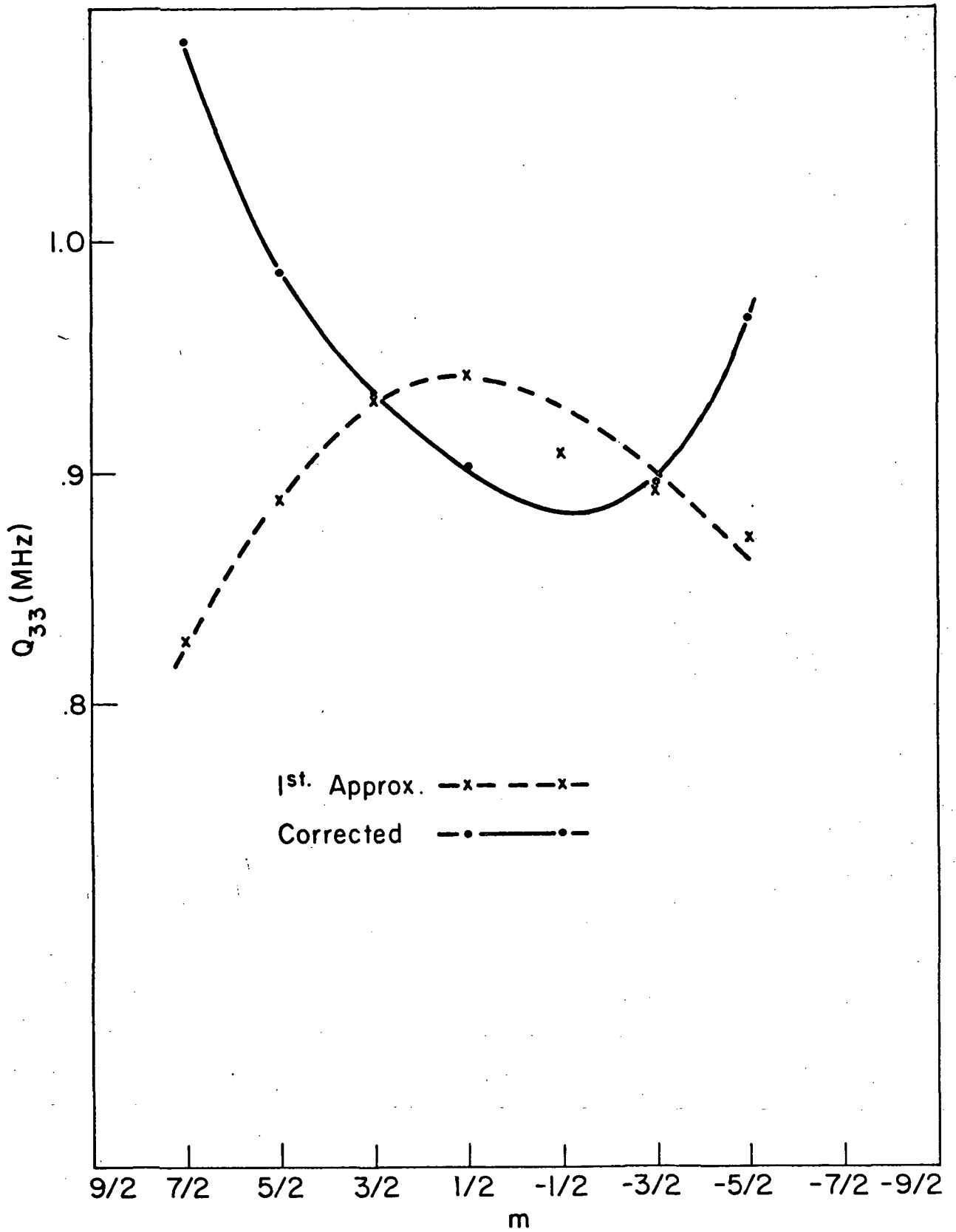
Fig. 46. Q_{33} vs. m , Y_Q -axis

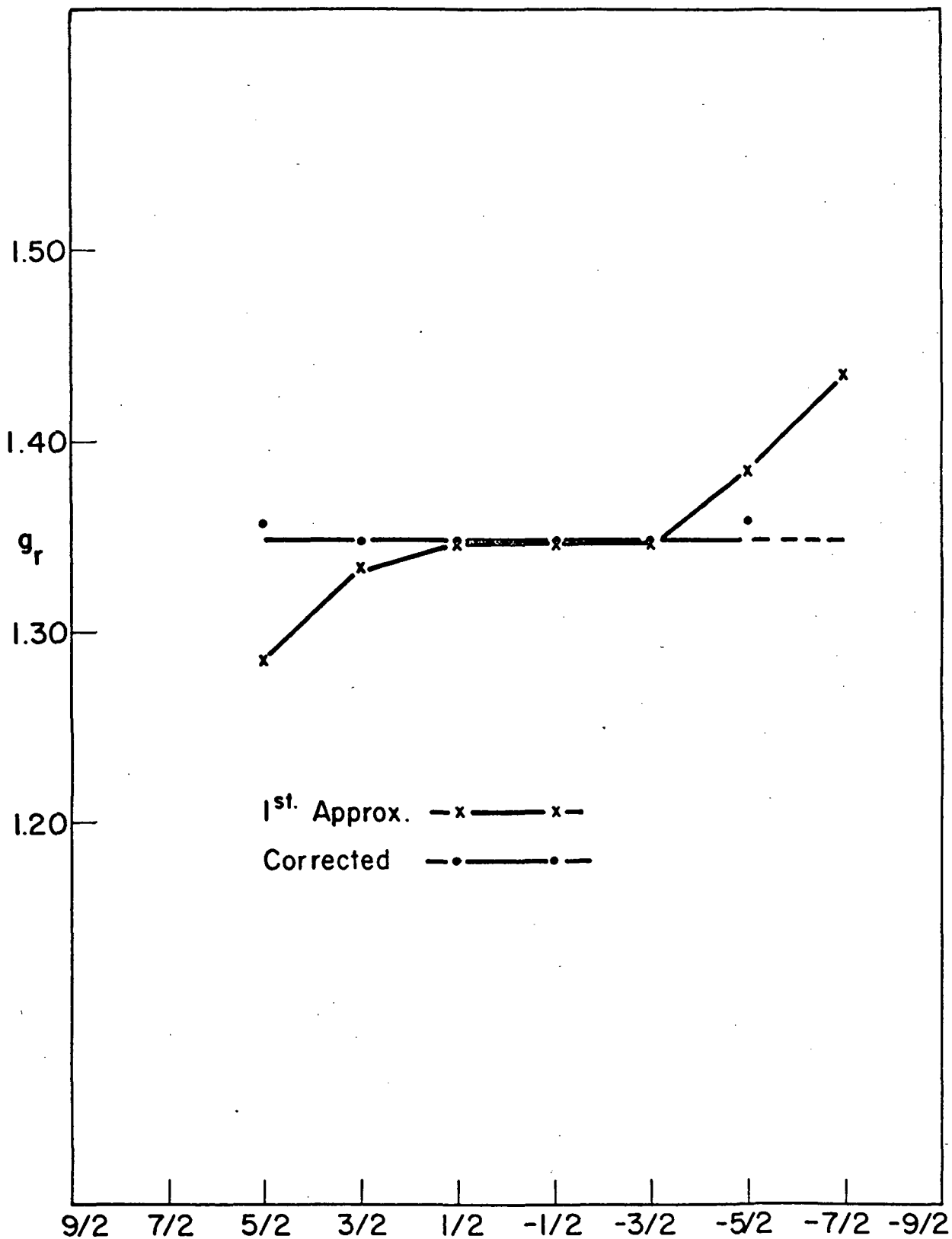
Fig. 47. Q_{33} vs. m , Z_Q -axis

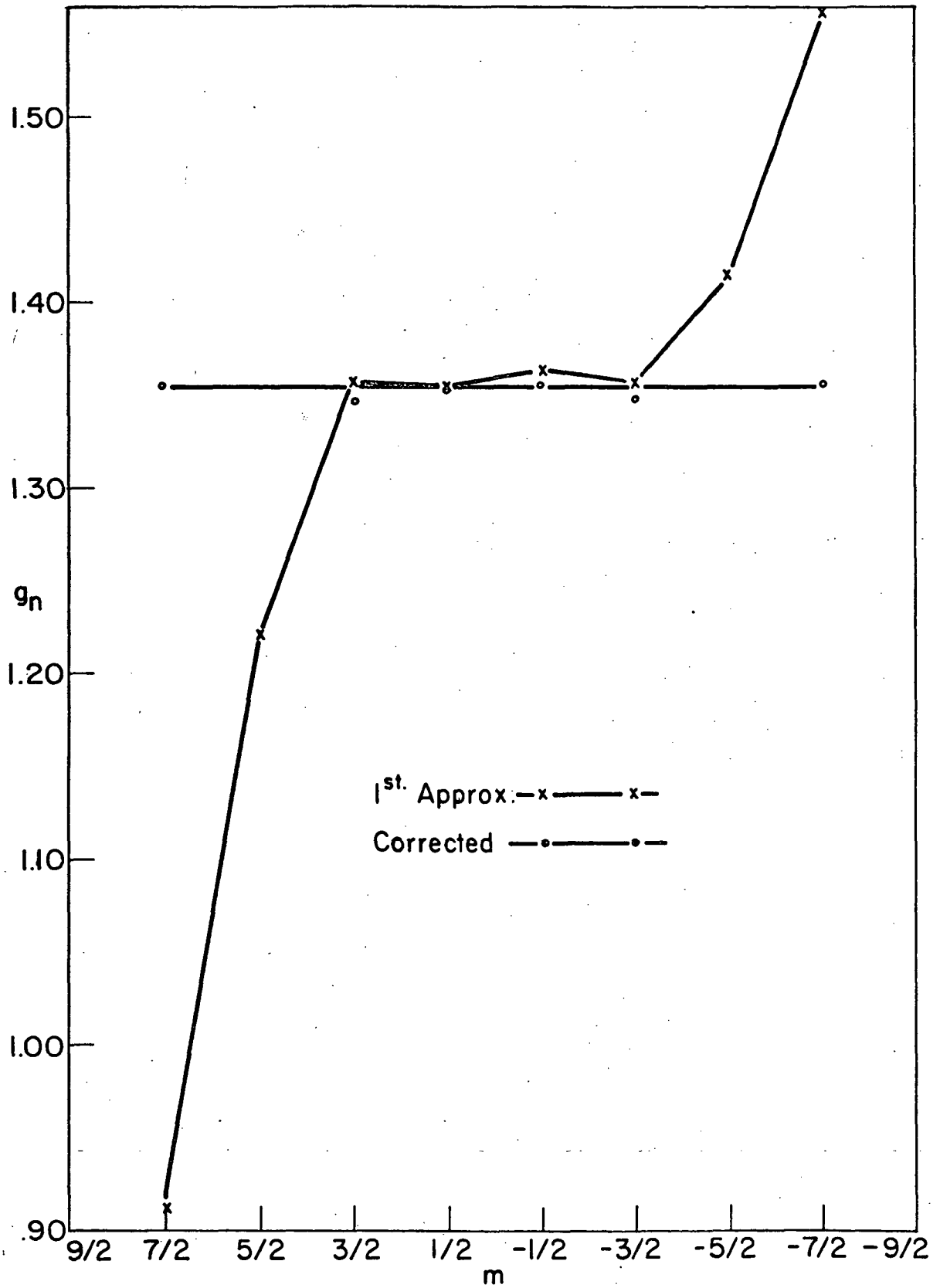
Fig. 48. Q_{33} vs. m , c-axis

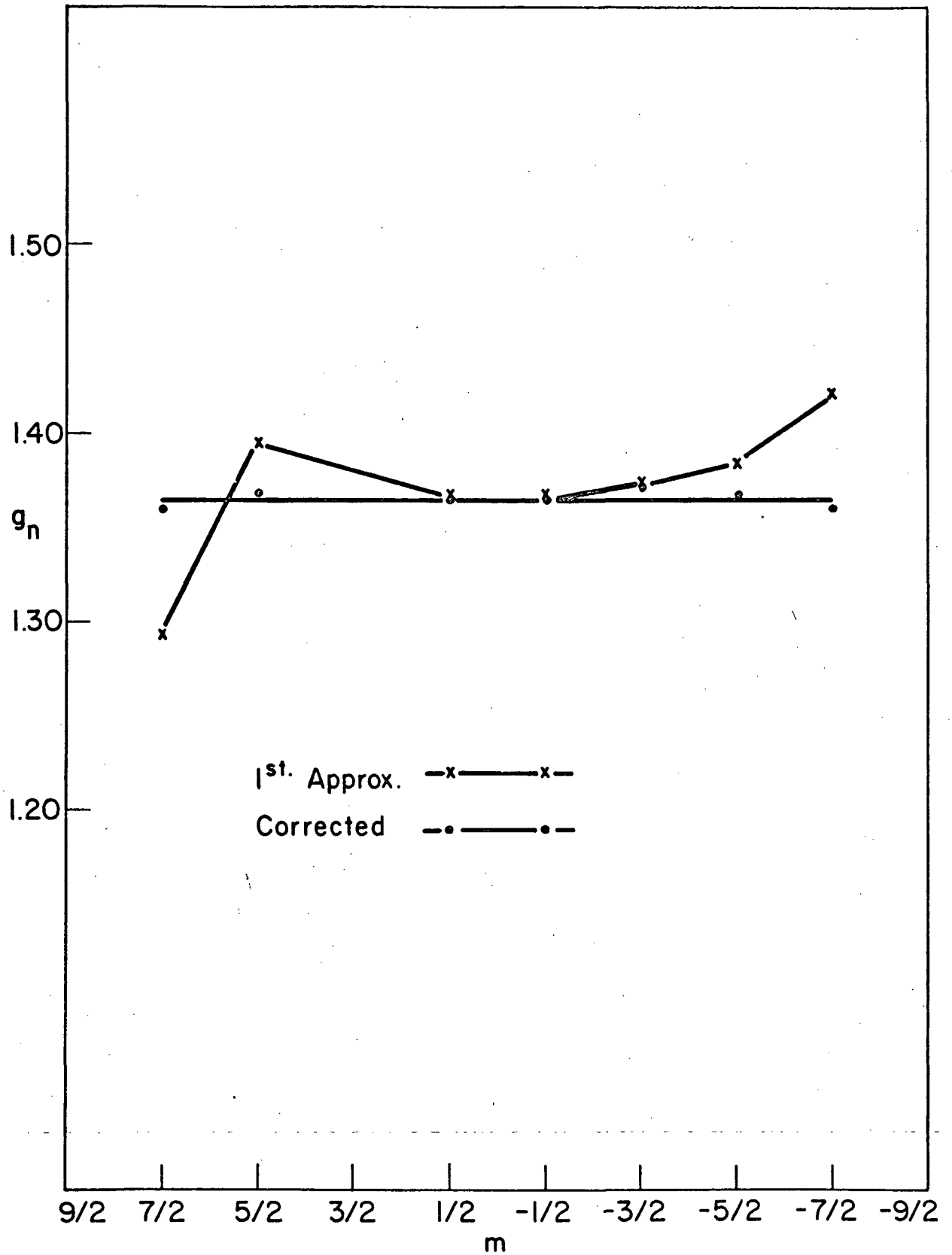
Fig. 49. Q_{33} vs. m , X_g -axis

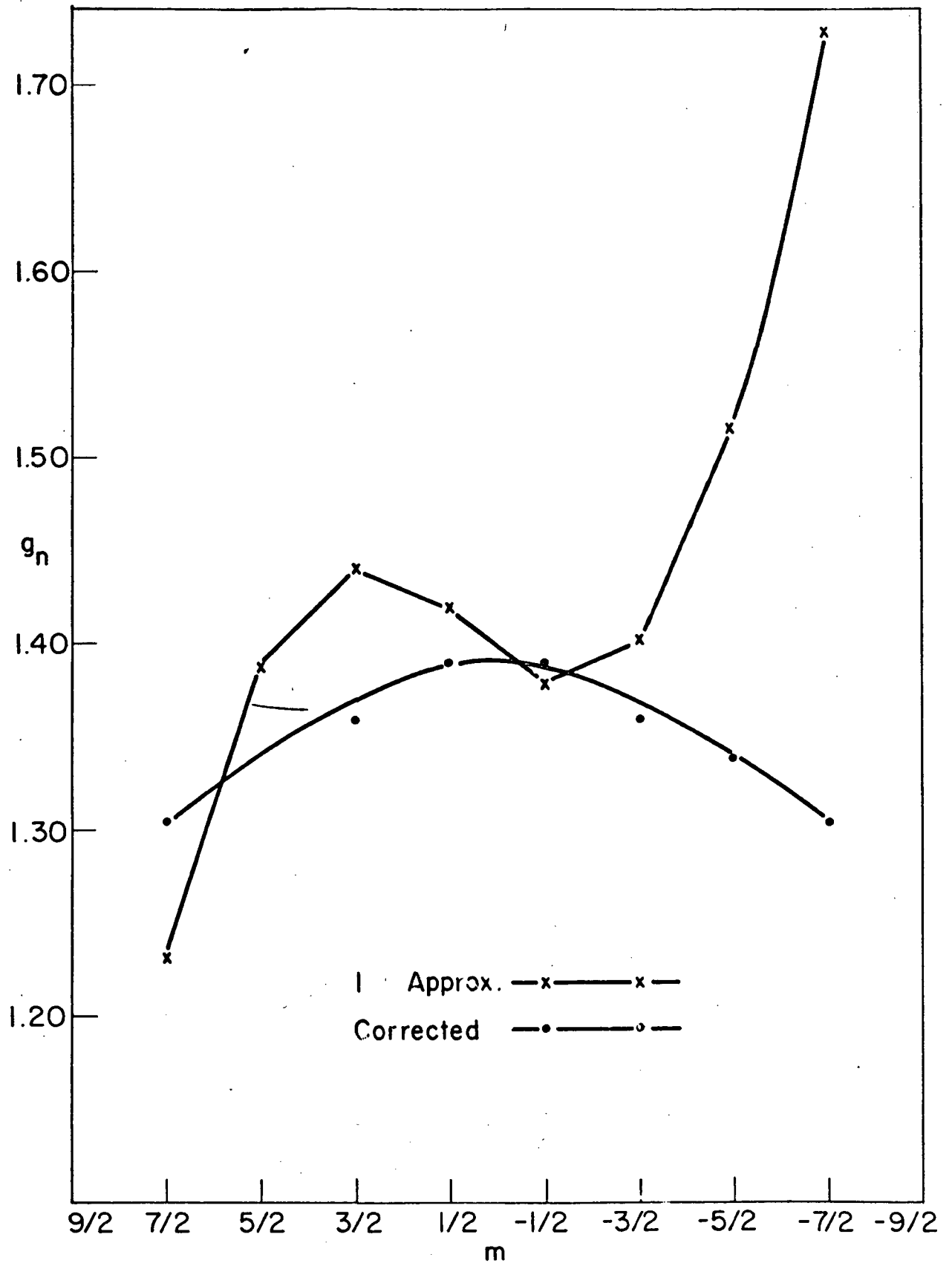
Fig. 50. Q_{33} vs. m , Y_g -axis

Fig. 51. Q_{33} vs. m , Z_g -axis

Fig. 52. g_n vs. $m, X_0\text{-axis}$

Fig. 53. g_n vs. m , Y_Q -axis

Fig. 54. g_n vs. m , Z_0 -axis

Fig. 55. g_n vs. m , c-axis

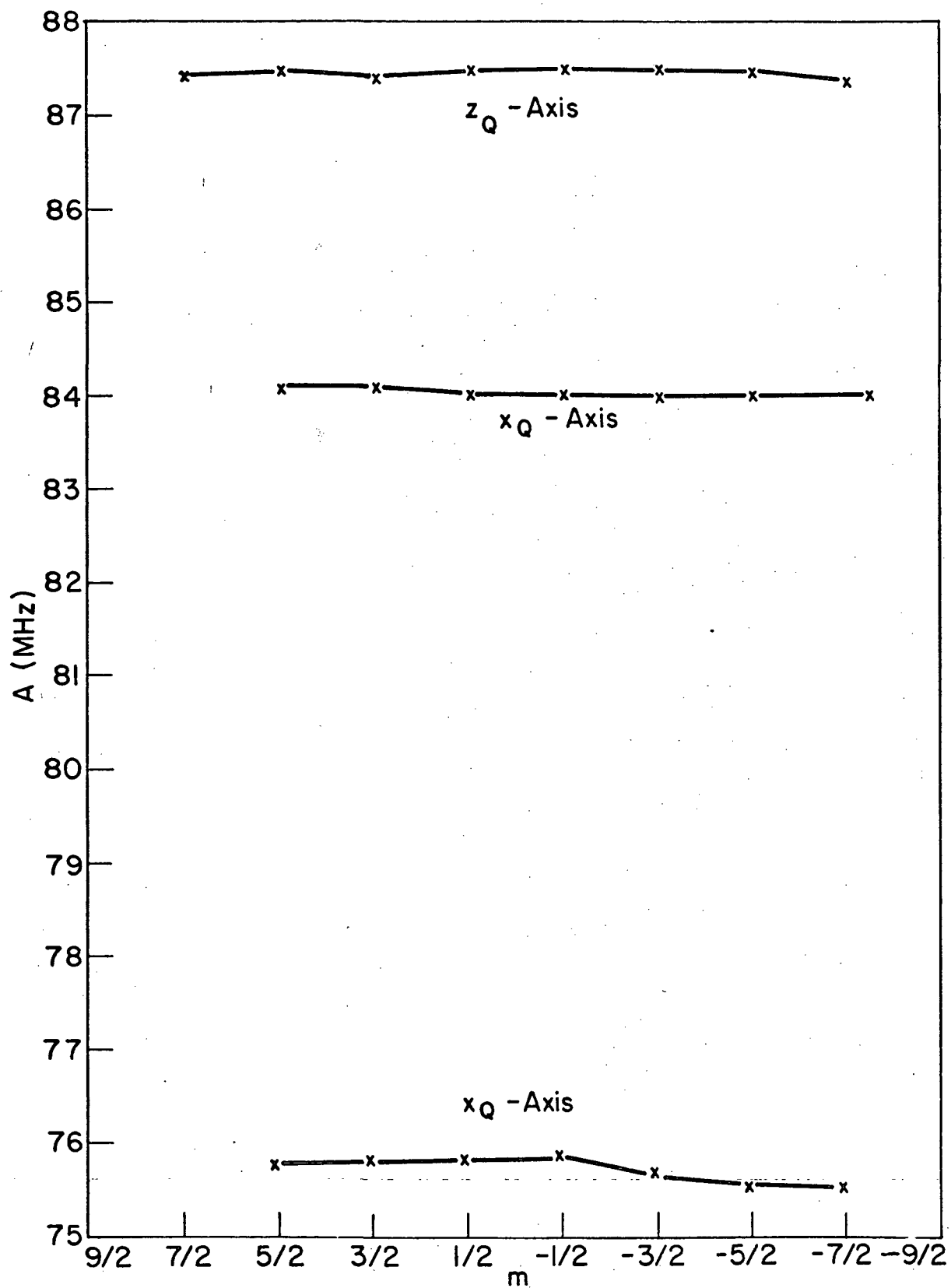


Fig. 56. A vs. m , Along principal axes of quadrupole by ENDOR measurements.

Chapter VII

DISCUSSION AND CONCLUSION

A. Various Charge Compensators

The hyperfine structures of Nb-93 in crystal CaWO_4 of different charge compensators Nd, U, and Tm have been measured and analyzed with spin resonance technique. The results are presented in Tables 1 and 5. No significant difference in the magnitudes of g or A for Nb with different charge compensators has been found from the EPR measurements of Nb spectra. Nevertheless, sufficient ENDOR data are not available to show whether differences in Q or g_n exist for these different compensators.

B. Temperature Effect

When the sample temperature varies from 77°K down to 4.2°K, a change of 1-2% in HFS line separation is observed. This implies, from Eq. (32), that a corresponding change must exist in the A -value. That this is the case can be seen from the plots of A -value versus m shown in Fig. 30 to Fig. 36. The reason why the A -value should change with temperature is not well understood. Experiments have only been performed at two temperatures, 77°K and 4.2°K. Thus, it is hard to assert a model to explain this effect. However, a similar change of A -value due to temperature variation has been observed for V^{2+} , Cr^{3+} , Mn^{2+}

and Fe^{3+} ions in cubic crystals like MgO , ZnS , CaO , SrO and CaF_2 by Walsh et al. (78) and others. (80, 81, 82) Walsh's experiment indicated an almost linear decrease of A-value in the range of temperature from 77°K up to 800°K . He also predicted a small increase of A-value as the temperature range extended from 77°K to 4.2°K . To explain this behavior, Simanek and Orbach (79) proposed a mechanism in which s-like configurations were admixed into the $3d^5$ configuration by the orbit-lattice interaction. Using a Debye model for the thermal vibrations of crystal, these authors obtained for Mn^{2+} and V^{2+} in cubic hosts a temperature dependence of A-value in good agreement with the experimental values of Walsh et al. Since the local symmetry of Nb^{4+} ion in crystal CaWO_4 is not a cubic one and the experiments have been carried out at only two points (77°K and 4.2°K) in the temperature scale, we are not sure whether or not the above theory can be applied to our case, although the observed temperature dependence of A-value is qualitatively in agreement with Walsh's result.

C. Sign of A and Q

ENDOR measurements show that g_n is almost isotropic and has a magnitude of $1.366 \pm .036$ which is close to the published value $+ 1.3652$. (67) Taking the nuclear g-value to be positive, the relative sign of A and Q can be determined from the experimental result. In this work we have assumed A to be positive. Then ENDOR measurements (Table 5) reveal that along the directions of Z_Q^- , Z_g^- and c-axis, Q has positive values and Q and A are of

the same sign. A check of the correctness of the ENDOR result has been made by measuring the separation of the doublets of EPR forbidden spectrum along c-axis and y-axis. The result is given in Table 6. With the argument on page 34, the measured separation of forbidden doublets indicates that along c-axis, A and Q have the same sign, while along y-axis, an opposite one. Thus both the ENDOR and the EPR measurements give a consistent result, that is, A and Q are of the same sign. However, they can be both positive or both negative. (See Chapter IV. C). The absolute sign can not be determined by the experimental technique used here.

D. Field Gradient of Nb⁴⁺ site

The niobium quadrupole coupling constant Q_{zz} (Abbreviated as Q_z), has been measured by the ENDOR technique. Literature⁽⁶⁸⁻⁷¹⁾ and Eq. (11') show that the measurement of this constant sheds some light on the nuclear quadrupole moment and the crystalline field gradient. To be sure, the interpretation of the result is not an easy matter. The difficulty is as following: The quadrupole coupling constant evaluated directly from the experiment is

$$Q_z = \frac{3e^2qQ}{4I(2I-1)} = \frac{1}{48} e^2qQ \quad (84)$$

where we have put $I = 9/2$; and Q is the scalar quadrupole moment of the nucleus defined as

$$eQ = \int \rho_{II}(X) (3Z^2 - r^2) d^3X \quad (85)$$

in which $\rho_{II}(X)$ denotes the expectation value of the nuclear

charge density in the state where $M = I$. The quantity q in Eq. (84) is proportional to the field gradient in the crystal (see page 15) and is approximated by: ⁽⁷⁰⁾

$$q = (1 + R) q_v + (1 + \gamma_\infty) q_i \quad (86)$$

where

eq_v = the field gradient due to the valence electrons, especially the p electrons. In our case, this is an unknown factor.

R = the core correction factor. This factor comes because the quadrupolar field of the nucleus distorts the electron charge density of Nb^{5-} ion core. This is another unknown. However, the value is always smaller than unity. For W, this factor is 0.51. ⁽⁷¹⁾

γ_∞ = the Sternheimer antishielding factor due to the radial shift of the electron charges. This "radial excitation" gives rise to a positive electronic quadrupole moment, that is, to antishielding of Q . For heavy ions γ_∞ is always large and positive, e.g., 18.2 for K^+ , 70.7 for Rb^+ and 143.5 for Cs^+ . ⁽⁷⁰⁾ But no such estimation is available for Nb^{4+} .

eq_i = the local field gradient of crystal $CaWO_4$ at the nucleus of Nb, arising from all other atoms by regarding the latter as point charges.

Probably the data most welcome to solid state physicists are the quadrupole moment Q and the local field gradient eq_i in the

crystal. But in view of the above complexity, it is hard to predict either of them here. However, if only the effective field gradient eq , instead of the local crystalline field gradient eq_i , is sought for, a rough estimation is ready to be obtained from the result of our measurements. The approximate value of the nuclear quadrupole moment Q of Nb has been given by many authors. (73, 74) The most up to date value was given by Arnold L. Bloom of Varian Associates using NMR technique. (67) It reads $Q = -0.2$ barn. Putting this value of Q into Eq. (84) we get

$$eq = -3.32 \times 10^{15} Q_Z \text{ esu/cm}^3 \quad (87)$$

where Q_Z is the quadrupole coupling constant measured in MHz. Table 5 gives $Q_Z = 1.3924$ MHz, or

$$\left(\frac{e^2 q Q}{h}\right)_{\text{CaWO}_4} = 66.835 \text{ MHz}$$

from which we find $eq \approx -4.51 \times 10^{15} \text{ esu/cm}^3$. Using the nuclear resonance method, Cotts and Knight obtained for Nb in the orthorhombic phase of KNbO_3 :

$$\left(\frac{e^2 q Q}{h}\right)_{\text{KNbO}_3} = 23.120 \text{ MHz.}$$

Thus

$$\frac{\left(\frac{e^2 q Q}{h}\right)_{\text{CaWO}_4}}{\left(\frac{e q Q}{h}\right)_{\text{KNbO}_3}} = 2.89$$

Cotts and Knight assumed a Q of the order of $0.1 \times 10^{-24} \text{ cm}^2$, and

estimated the field gradient eq at the Nb nucleus of crystal KNbO_3 to be 3×10^{15} esu/cm³.

E. Orientation of Z_g , Z_A and Z_Q -Axes

Experimental results indicate that the principal axes of g-, A-, and Q- tensors are not coincident. Nevertheless, all the Z-axes, (Z_g , Z_A , and Z_Q) and the Nb-O bond lie within a cone of 29° having the Nb nucleus as its vertex. Thus the principal axes form three cones designated by X, Y and Z as shown in Fig. 57. Note that instead of pointing to the oxygen ion #1, the Z_Q axis is pointing to the tungsten ion at the corner of the rectangle on the (1 $\bar{1}$ 0)-plane of the crystalline unit cell. See Fig. 58. The Y_Q axis is pointing to the Ca-ion at the $\langle 1\bar{1}0 \rangle$ -axis on ab-plane.

The fact that the Z_Q -axis points to $\langle 111 \rangle$ direction, that is to the W ion at one of the corners of the unit cell, is difficult to explain. According to the preceding discussion, the orientation of the Z_Q -axis means that there exists a strong field gradient directing from the Nb ion toward the W ion at the corner of the unit cell. Since there are 8 equivalent W ions at the corners of the unit cell plus 4 other W ions inside the unit cell, which are even closer to the Nb-ion than those at the corners, there is no obvious reason to suppose that this particular W ion should produce a stronger field gradient at the Nb site. One possibility is that a foreign ion like Nd^{3+} might have substitutionally occupied this W site. The ion radius of Nd^{3+} (1.08Å) is much larger than that of W^{6+} (0.62 Å). The substitution thus

stirs up a big perturbation to the crystal field around this ion, extending to the Nb nucleus site. There is evidence to support that ions with a valence of 3+ can take the W^{6+} site. Kedzie et al. have found that Fe^{3+} and Nd^{3+} do occupy the W site substitutionally in $CaWO_4$.^(72, 75) Thus the EPR and ENDOR results can be interpreted in the following way: Assume that after the crystal growing the Nb-ion and the Nd-ion have already substituted the W-ions at the center and the corner of the unit cell, respectively. After γ -irradiation the Nb-ion picks up an electron and becomes paramagnetic. According to Chu's model,⁽¹⁾ 4 equally probable potential traps at $\phi = \pi/4, 3\pi/4, 5\pi/4$ and $7\pi/4$ exist in the NbO_4 bisphenoid corresponding to the 4 oxygens because of the Jahn-Teller effect. This paramagnetic electron is caught by the trap at $\phi = \pi/4$ which is also the direction of high field gradient produced by the Nd^{3+} ion. This is why all the z-axes are directed around the oxygen #1 and $\langle 111 \rangle$ axis. In order to clarify this situation more studies should be made.

It has been observed⁽⁷⁶⁾ that there are superhyperfine structure (SHFS) due to W-183 around each niobium HF line. This implies that the paramagnetic electron produced by the γ -irradiation not only is covalently bonded to the oxygen ion but also spreads far out into the space of other cations. The SHFS can be studied by the ENDOR technique.

F. Conclusion

To conclude this work, we review that the orientation, sign and magnitude of the following quantities have been determined by

the EPR/ENDOR technique:

	θ	ϕ
$g_x = 2.0133 \pm .0028$	28°	208°
$g_y = 2.0077 \pm .0002$	90°	-62°
$g_z = 2.0534 \pm .0010$	62°	28°
$A_x = 81.0 \pm 0.9$ MHz	27.5°	225°
$A_y = 75.2 \pm 1.2$ MHz	90°	-45°
$A_z = 88.4 \pm 1.4$ MHz	62.5°	45°
$Q_x = -0.561 \pm .023$ MHz	57°	225°
$Q_y = -0.835 \pm .025$ MHz	90°	-45°
$Q_z = +1.392 \pm .050$ MHz	33°	45°
$g_n = 1.366 \pm .036$	--	--

From these experimental results, arguments lead to the tentative charge compensation scheme as shown in Fig. 57, i.e., a Nb-ion substitutes the W-ion at the center of the unit cell while a charge compensator ion might substitute the W ion at the corner of the same cell.

Table 6

Relations Between the Separation
of Forbidden Doublet and the Sign
Of A and Q

Direction	Sample	ν_e (GHz) at Liq. N ₂ Temp.	Separation and Average Position of Forbidden Doublet (G)		Signs of A and Q Predicted from For- bidden Doublets	ENDOR Result	
			Low Field Side	High Field Side		A (MHz)	Q (MHz)
c - axis	# A-12	9.5112	4.415	8.737	Same Sign	+82.5	+.75
			3242.720	3478.290			
			4.016	8.855			
y - axis	# A-18 _y	9.4470	3219.614	3455.279	Opposite Sign	+76.1	-.74
			8.362	3.311			
			3252.001	3471.277			
y - axis	# A-18 _a	9.5250	8.197	3.076	Opposite Sign	+76.1	-.74
			3281.097	3500.541			
			8.173	3.241			
	# A-18 _a	9.5260	3280.850	3500.459			

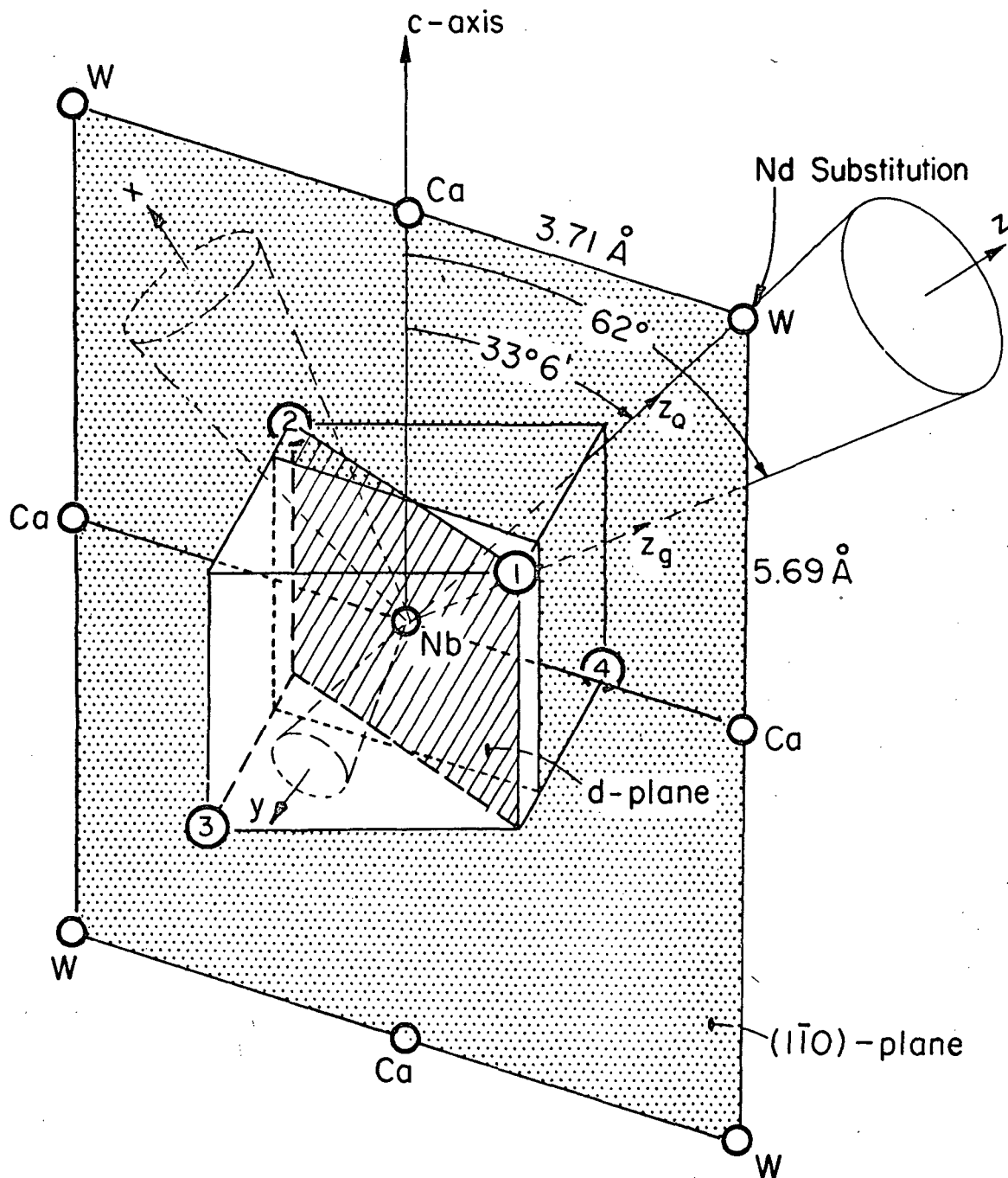


Fig. 57. Three cones confining the x , y and z axes of g -, A - and Q -tensors.

APPENDICES

- A. Derivation of Energy Level Formula
- B. Relation between the Principal Coordinates and the Crystal Symmetry Coordinates.

A. Derivation of Energy Level Formula

In deriving the energy level formula from the general spin Hamiltonian (13) we make three assumptions to simplify the mathematics, namely: 1) the local symmetry of crystal is rhombic, 2) the axes of tensors, g , A , Q and g_n are in parallel, 3) the principal axes of these tensors are taken as the coordinate system, X , Y , and Z . Under these assumptions Eq. (13) becomes

$$\begin{aligned}
 \mathcal{H} = & \beta (g_z H_z S_z + g_x H_x S_x + g_y H_y S_y) \\
 & + A_z I_z S_z + A_x I_x S_x + A_y I_y S_y \\
 & + Q_z I_z^2 + Q_x I_x^2 + Q_y I_y^2 \\
 & - \beta_n (g'_{nz} H_z I_z + g'_{nx} H_x I_x + g'_{ny} H_y I_y)
 \end{aligned} \tag{13'}$$

Defining

$$Q' \equiv Q_z - \frac{1}{2} (Q_x + Q_y)$$

and

$$Q'' \equiv \frac{1}{2} (Q_x - Q_y)$$

Eq. (13') can be put into the conventional form:

$$\begin{aligned}
 \mathcal{H} = & \beta(g_z H_z S_z + g_x H_x S_x + g_y H_y S_y) && \dots\dots\dots \text{Zeeman} \\
 & + A_z I_z S_z + A_x I_x S_x + A_y I_y S_y && \dots\dots\dots \text{HF} \\
 & + Q' [I_z^2 - \frac{1}{3} I(I+1)] + Q'' (I_x^2 - I_y^2) && \dots\dots\dots \text{Quadrupole} \\
 & - \beta_n (g'_{nz} H_z I_z + g'_{nx} H_x I_x + g'_{ny} H_y I_y) && \dots\dots\dots \text{Nuclear Zeeman}
 \end{aligned}
 \tag{14}$$

where use has been made of the fact that

$$I(I+1) \rightarrow \mathbf{I}^2, \text{ the operator,}$$

$$\mathbf{I}^2 = I_z^2 + I_x^2 + I_y^2, \text{ and}$$

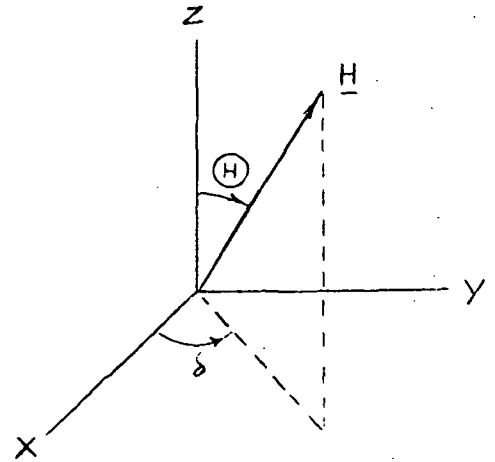
$$Q_x + Q_y + Q_z = 0$$

The last equation comes because \underline{Q} is a symmetric tensor with zero trace. (70)

Before the diagonalization of Eq. (14) we recognize that the Zeeman term is about 9000 MHz, the HF term is around 100 MHz and both the Quadrupole interaction term and the nuclear Zeeman term are of the same order of magnitude, about 10 MHz. Thus the perturbation theories are qualified. In the following we will diagonalize Eq. (14) term by term while the interaction between the quadrupole and nuclear Zeeman terms is neglected. After the diagonalization the corresponding energy level of Eq. (14) takes the form:

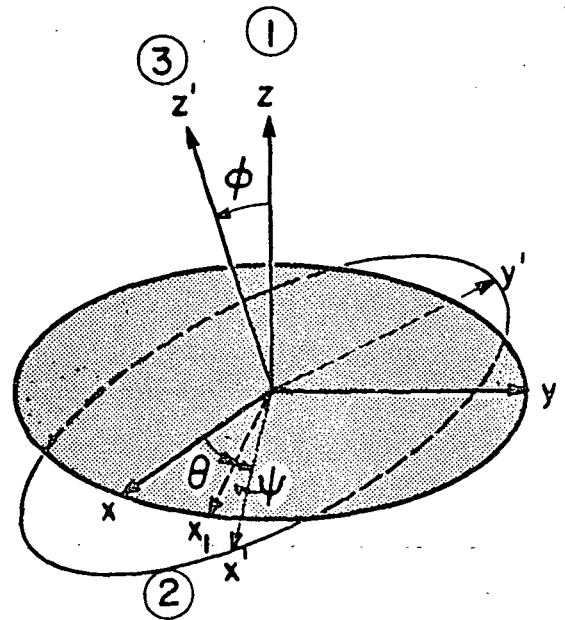
$$E = E_z + E_{\text{HF}} + E_Q + E_{\text{nz}} \tag{A-1}$$

The following relations are required and we will indicate their origin at the proper time:



The Relation between the field vector and the principal coordinates.

$$\left. \begin{aligned} H_x &= H \sin \textcircled{H} \cos \delta \\ H_y &= H \sin \textcircled{H} \sin \delta \\ H_z &= H \cos \textcircled{H} \end{aligned} \right\} \text{(A-2)}$$



The Generation of Eulerian Angles (after Goldstein)

$$\left. \begin{aligned} \cos \theta &= - \frac{g_y}{g_z} \sin \delta \\ \sin \theta &= \frac{g_x}{g_z} \cos \delta \\ \sin \varphi &= \frac{g_z}{g} \sin \textcircled{H} \\ \cos \varphi &= \frac{g_z}{g} \cos \textcircled{H} \end{aligned} \right\} \text{(A-3)}$$

$$\begin{aligned}
\text{i)} \quad g^2 &= g_z^2 \cos^2 \Theta + g_{\perp}^2 \sin^2 \Theta \\
\text{ii)} \quad g_{\perp}^2 &= g_x^2 \cos^2 \delta + g_y^2 \sin^2 \delta \\
\text{iii)} \quad K^2 &= A_z^2 \cos^2 \varphi + A_{\perp}^2 \sin^2 \varphi \\
\text{iv)} \quad A_{\perp}^2 &= A_x^2 \sin^2 \theta + A_y^2 \cos^2 \theta \\
\text{v)} \quad A_{\perp}^2 g_{\perp}^2 &= A_x^2 g_x^2 \cos^2 \delta + A_y^2 g_y^2 \sin^2 \delta \\
\text{vi)} \quad K^2 g^2 &= A_z^2 g_z^2 \cos^2 \Theta + A_{\perp}^2 g_{\perp}^2 \sin^2 \Theta
\end{aligned} \tag{A-4}$$

1. Zeeman Term

The Zeeman term can be written as

$$\beta (g_x H_x S_x + g_y H_y S_y + g_z H_z S_z) \equiv \beta \underline{H} \cdot \underline{g} \cdot \underline{S} \tag{A-5}$$

where \underline{g} is a diagonal matrix because we are using the principal coordinate system. To diagonalize (A-5) the first step is to rotate the existing coordinate system to a prime (') system such that

$$\underline{H} \cdot \underline{g} \cdot \underline{S} \rightarrow H g S'_z$$

Suppose such a prime system is related to the original system by the Eulerian angle, (θ, φ, ψ) . Then according to Goldstein, (83) the rotation operators are

$$\begin{aligned}
P_z(\theta) &= \begin{pmatrix} \cos\theta & \sin\theta & 0 \\ -\sin\theta & \cos\theta & 0 \\ 0 & 0 & 1 \end{pmatrix} \\
P_x(\varphi) &= \begin{pmatrix} 1 & 0 & 0 \\ 0 & \cos\varphi & \sin\varphi \\ 0 & -\sin\varphi & \cos\varphi \end{pmatrix}
\end{aligned}$$

and

$$P_{z'}(\Psi) = \begin{pmatrix} \cos \Psi & \sin \Psi & 0 \\ -\sin \Psi & \cos \Psi & 0 \\ 0 & 0 & 1 \end{pmatrix}$$

After rotation the spin vector becomes

$$\begin{aligned} \underline{S}' &= P_{z'}(\Psi) P_{x_1}(\varphi) P_z(\theta) \underline{S} \\ &\equiv P(\Psi, \varphi, \theta) \underline{S} \\ &\equiv P \underline{S} \end{aligned} \quad (\text{A-6})$$

where

$$\begin{aligned} P &= \begin{pmatrix} \cos \Psi & \sin \Psi & 0 \\ -\sin \Psi & \cos \Psi & 0 \\ 0 & 0 & 1 \end{pmatrix} \begin{pmatrix} 1 & 0 & 0 \\ 0 & \cos \varphi & \sin \varphi \\ 0 & -\sin \varphi & \cos \varphi \end{pmatrix} \begin{pmatrix} \cos \theta & \sin \theta & 0 \\ -\sin \theta & \cos \theta & 0 \\ 0 & 0 & 1 \end{pmatrix} \\ &= \begin{pmatrix} \cos \Psi \cos \theta - \cos \varphi \sin \theta \sin \Psi & \cos \Psi \sin \theta + \cos \varphi \sin \theta \sin \Psi & \sin \Psi \sin \varphi \\ -\sin \Psi \cos \theta - \cos \varphi \sin \theta \cos \Psi & -\sin \Psi \sin \theta + \cos \varphi \cos \theta \cos \Psi & \cos \Psi \sin \varphi \\ \sin \varphi \sin \theta & -\sin \varphi \cos \theta & \cos \varphi \end{pmatrix} \end{aligned} \quad (\text{A-7})$$

Note that P is orthogonal; $P^{-1} = \tilde{P}$. Also, $\det P = 1$. From (A-7), it is easy to derive

$$P^{-1} \equiv P^{-1}(\Psi, \varphi, \theta) = \tilde{P}(\Psi, \varphi, \theta)$$

$$\begin{aligned} &= \begin{pmatrix} \cos \Psi \cos \theta - \cos \varphi \sin \theta \sin \Psi & -\sin \Psi \cos \theta - \cos \varphi \sin \theta \cos \Psi & \sin \varphi \sin \theta \\ \cos \Psi \sin \theta + \cos \varphi \cos \theta \sin \Psi & -\sin \Psi \sin \theta + \cos \varphi \cos \theta \cos \Psi & -\sin \varphi \cos \theta \\ \sin \varphi \sin \Psi & \sin \varphi \cos \Psi & \cos \varphi \end{pmatrix} \end{aligned} \quad (\text{A-8})$$

Using these relations and the fact that a scalar product will not

change under a coordinate rotation, (A-5) becomes

$$\begin{aligned}
 \beta \underline{H} \cdot \underline{g} \cdot \underline{S} &= \beta [(\underline{H} \cdot \underline{g}) \cdot P^{-1}] \cdot P \cdot \underline{S} \\
 &= \beta [(\underline{H} \cdot \underline{g}) \cdot P^{-1} \underline{S}'] \\
 &= \beta (H_x g_x \quad H_y g_y \quad H_z g_z) P^{-1} \begin{pmatrix} S'_x \\ S'_y \\ S'_z \end{pmatrix} \\
 &= \beta \begin{pmatrix} H_x g_x (\cos \Psi \cos \theta & H_x g_x (-\sin \Psi \cos \theta & H_x g_x \sin \varphi \sin \theta \\ & -\cos \varphi \sin \theta \sin \Psi) & -\cos \varphi \sin \theta \cos \Psi) \\ H_y g_y (\cos \Psi \sin \theta & +H_y g_y (-\sin \Psi \sin \theta & +H_y g_y (-\sin \varphi \cos \theta) \\ & +\cos \varphi \cos \theta \sin \Psi) & +\cos \varphi \cos \theta \cos \Psi) \\ H_z g_z (\sin \varphi \sin \Psi) & + H_z g_z \sin \varphi \cos \Psi & + H_z g_z \cos \theta \end{pmatrix} \begin{pmatrix} S'_x \\ S'_y \\ S'_z \end{pmatrix} \\
 &= \beta (\textcircled{1} \quad \textcircled{2} \quad \textcircled{3}) \begin{pmatrix} S'_x \\ S'_y \\ S'_z \end{pmatrix} \\
 &= \beta (\textcircled{1} S'_x + \textcircled{2} S'_y + \textcircled{3} S'_z) \tag{A-9}
 \end{aligned}$$

where

$$\begin{aligned} \textcircled{1} &= H_x g_x (\cos\psi \cos\theta - \cos\varphi \sin\theta \sin\psi) \\ &+ H_y g_y (\cos\psi \sin\theta + \cos\varphi \cos\theta \sin\psi) \\ &+ H_z g_z (\sin\varphi \sin\psi) \end{aligned}$$

$$\begin{aligned} \textcircled{2} &= H_x g_x (-\sin\psi \cos\theta - \cos\varphi \sin\theta \cos\psi) \\ &+ H_y g_y (-\sin\psi \sin\theta + \cos\varphi \cos\theta \cos\psi) \\ &+ H_z g_z \sin\varphi \cos\psi \end{aligned}$$

$$\textcircled{3} = H_z g_z \sin\varphi \sin\theta + H_y g_y (-\sin\varphi \cos\theta) + H_z g_z \cos\theta$$

Using relations (A-2), (A-3) and i) and ii) of (A-4) we obtain from $\textcircled{3}$:

$$\begin{aligned} \textcircled{3} &= H [g_x \sin \textcircled{H} \cos \delta \sin\varphi \sin\theta \\ &- g_y \sin \textcircled{H} \sin\delta \sin\varphi \cos\theta \\ &+ g_z \cos \textcircled{H} \cos\varphi] \\ &= H [g_x \sin \textcircled{H} \cos\delta \frac{g_\perp}{g} \sin \textcircled{H} \frac{g_x}{g_\perp} \cos\delta \\ &- g_y \sin \textcircled{H} \sin\delta \frac{g_\perp}{g} \sin \textcircled{H} (-\frac{g_y}{g_\perp} \sin\delta) \\ &+ g_z \cos \textcircled{H} \frac{g_z}{g} \cos \textcircled{H}] \\ &= H \frac{1}{g} [(g_x^2 \cos^2\delta + g_y^2 \sin^2\delta) \sin^2 \textcircled{H} + g_z^2 \cos^2 \textcircled{H}] \\ &= H \frac{1}{g} (g_\perp^2 \sin^2 \textcircled{H} + g_z^2 \cos^2 \textcircled{H}) \\ &= Hg \end{aligned}$$

From (1):

$$\begin{aligned}
 (1) &= H[g_x \sin(\theta) \cos \delta (\cos \psi \cos \theta - \cos \varphi \sin \theta \sin \psi) \\
 &\quad + g_y \sin(\theta) \sin \delta (\cos \psi \sin \theta + \cos \varphi \cos \theta \sin \psi) \\
 &\quad + g_z \cos(\theta) \sin \varphi \sin \psi] \\
 &= H[g_x \sin(\theta) \cos \delta (\cos \psi (-\frac{g_y}{g_\perp}) \sin \delta - \frac{g_z}{g} \cos(\theta) \frac{g_x}{g_\perp} \cos \delta \sin \psi) \\
 &\quad + g_y \sin(\theta) \sin \delta (\cos \psi \frac{g_x}{g_\perp} \cos \delta + \frac{g_z}{g} \cos(\theta) (-\frac{g_y}{g_\perp}) \sin \delta \sin \psi) \\
 &\quad + g_z \cos(\theta) \frac{g_\perp}{g} \sin(\theta) \sin \psi] \\
 &= H[-\frac{g_x g_y}{g_\perp} \sin(\theta) \cos \delta \sin \delta \cos \psi - \frac{g_x^2 g_z}{g g_\perp} \sin(\theta) \cos(\theta) \cos^2 \delta \sin \psi \\
 &\quad + \frac{g_x g_y}{g_\perp} \sin(\theta) \cos \delta \sin \delta \cos \psi - \frac{g_z g_y^2}{g g_\perp} \sin(\theta) \cos(\theta) \sin^2 \delta \sin \psi \\
 &\quad + \frac{g_z g_\perp}{g} \sin(\theta) \cos(\theta) \sin \psi] \\
 &= H[-\frac{g_z}{g g_\perp} \sin(\theta) \cos(\theta) \sin \psi (g_x^2 \cos^2 \delta + g_y^2 \sin^2 \delta) \\
 &\quad + \frac{g_z g_\perp}{g} \sin(\theta) \cos(\theta) \sin \psi] \\
 &= H[-\frac{g_z}{g g_\perp} \sin(\theta) \cos(\theta) \sin \psi (g_\perp^2) + \frac{g_z g_\perp}{g} \sin(\theta) \cos(\theta) \sin \psi] \\
 &= 0
 \end{aligned}$$

Similarly we can show

$$(2) = 0$$

Thus (A-9) becomes

$$\beta \underline{H} \cdot \underline{g} \cdot \underline{S} = \beta \textcircled{3} S'_z = \beta g H S'_z \quad (\text{A-10})$$

which is what we claimed for. The diagonalization of the Zeeman term is, therefore

$$\begin{aligned} E_z &= \langle M | \beta \underline{H} \cdot \underline{g} \cdot \underline{S} | M \rangle \\ &= \beta g H \langle M | S'_z | M \rangle \\ &= \beta g H M \end{aligned} \quad (\text{A-11})$$

2. Hyperfine Term

In order to diagonalize the HF, quadrupole and nuclear Zeeman terms, we have to introduce a rotation operator P_I for the nuclear spin vector \underline{I} defined as

$$P_I \equiv P_I(\Psi, \varphi, \theta) \equiv P_{IZ'}(\Psi) P_{IX_1}(\varphi) P_{IZ}(\theta) \quad (\text{A-12})$$

where

$$P_{IZ}(\theta) = \begin{pmatrix} \frac{A_y}{A_\perp} \cos \theta & \frac{A_x}{A_\perp} \sin \theta & 0 \\ -\frac{A_x}{A_\perp} \sin \theta & \frac{A_y}{A_\perp} \cos \theta & 0 \\ 0 & 0 & 1 \end{pmatrix} \quad (\text{see p. 60 of ref. 13})$$

$$P_{IX_1}(\varphi) = \begin{pmatrix} 1 & 0 & 0 \\ 0 & \frac{A_z}{K} \cos \varphi & \frac{A_\perp}{K} \sin \varphi \\ 0 & -\frac{A_\perp}{K} \sin \varphi & \frac{A_z}{K} \cos \varphi \end{pmatrix}$$

$$P_{IZ'}(\Psi) = \begin{pmatrix} \cos \Psi & \sin \Psi & 0 \\ -\sin \Psi & \cos \Psi & 0 \\ 0 & 0 & 1 \end{pmatrix}$$

and (θ, φ, ψ) is the Eulerian angle defined previously.

Each of the above rotation matrix should be an orthogonal one and its determinant should be unity. In order to fulfill these requirements we set

$$\left. \begin{aligned} A_{\perp}^2 &= A_x^2 \sin^2 \theta + A_y^2 \cos^2 \theta \\ \text{and } K^2 &= A_z^2 \cos^2 \varphi + A_{\perp}^2 \sin^2 \varphi \end{aligned} \right\} \quad (\text{A-13})$$

Upon using the relation (A-3), Eq. (A-13) becomes

$$\left. \begin{aligned} A_{\perp}^2 g_{\perp}^2 &= A_x^2 g_x^2 \cos^2 \delta + A_y^2 g_y^2 \sin^2 \delta \\ K^2 g^2 &= A_z^2 g_z^2 \cos^2 (\text{H}) + A_{\perp}^2 g_{\perp}^2 \sin^2 (\text{H}) \end{aligned} \right\} \quad (\text{A-14})$$

Putting $P_{IZ}(\theta)$, $P_{IX_1}(\varphi)$ and $P_{IY}(\psi)$ into (A-12) we obtain

$$P_I = P_I(\psi, \varphi, \theta)$$

$$= \begin{pmatrix} \cos \psi \frac{A_y}{A_{\perp}} \cos \psi \cos \theta & \cos \psi \frac{A_x}{A_{\perp}} \sin \theta & \sin \psi \frac{A_{\perp}}{K} \sin \varphi \\ -\sin \psi \frac{A_z}{K} \cos \varphi \frac{A_x}{A_{\perp}} \sin \theta & +\sin \psi \frac{A_z}{K} \cos \varphi \frac{A_y}{A_{\perp}} \cos \theta & \\ -\sin \psi \frac{A_y}{A_{\perp}} \cos \theta & -\sin \psi \frac{A_x}{A_{\perp}} \sin \theta & \cos \psi \frac{A_{\perp}}{K} \sin \varphi \\ -\cos \psi \frac{A_z}{K} \cos \varphi \frac{A_x}{A_{\perp}} \sin \theta & +\cos \psi \frac{A_z}{K} \cos \varphi \frac{A_y}{A_{\perp}} \cos \theta & \\ \frac{A_{\perp}}{K} \sin \varphi \frac{A_x}{A_{\perp}} \sin \theta & -\frac{A_{\perp}}{K} \sin \varphi \frac{A_y}{A_{\perp}} \cos \theta & \frac{A_z}{K} \cos \varphi \end{pmatrix}$$

$$P_I^{-1} = \tilde{P}_I(\psi, \varphi, \theta)$$

$$= \begin{pmatrix} \cos\psi \frac{A_y}{A_\perp} \cos\theta & -\sin\psi \frac{A_y}{A_\perp} \cos\theta & \frac{A_\perp}{K} \sin\psi \frac{A_x}{A_\perp} \sin\theta \\ -\sin\psi \frac{A_z}{K} \cos\psi \frac{A_x}{A_\perp} \sin\theta & -\cos\psi \frac{A_z}{K} \cos\psi \frac{A_x}{A_\perp} \sin\theta & \\ \cos\psi \frac{A_x}{A_\perp} \sin\theta & -\sin\psi \frac{A_x}{A_\perp} \sin\theta & -\frac{A_\perp}{K} \sin\psi \frac{A_y}{A_\perp} \cos\theta \\ +\sin\psi \frac{A_z}{K} \cos\psi \frac{A_y}{A_\perp} \cos\theta & +\cos\psi \frac{A_z}{K} \cos\psi \frac{A_y}{A_\perp} \cos\theta & \\ \sin\psi \frac{A_\perp}{K} \sin\psi & \cos\psi \frac{A_\perp}{K} \sin\psi & \frac{A_z}{K} \cos\psi \end{pmatrix}$$

The hyperfine term can be written as

$$A_x I_x S_x + A_y I_y S_y + A_z I_z S_z$$

$$= \underline{I} \cdot \underline{A} \cdot \underline{S}$$

$$= \underline{I} P_I^{-1} \cdot P_{I\underline{A}} P^{-1} \cdot P \underline{S}$$

$$= \underline{I}' \cdot \underline{A}' \cdot \underline{S}'$$

(A-15)

where

\underline{I}' and \underline{I} are row vectors related by $\underline{I}' = \underline{I} P_I^{-1}$,

\underline{S}' is a column vector defined by (A-6),

\underline{A} is a diagonal matrix, and

$$\underline{A}' = P_{I\underline{A}} P^{-1}$$

$$= \begin{pmatrix} a_{11} & a_{12} & a_{13} \\ a_{21} & a_{22} & a_{23} \\ a_{31} & a_{32} & a_{33} \end{pmatrix}$$

with

$$a_{11} = \left(\cos\psi \frac{A_Y}{A_{\perp}} \cos\theta - \sin\psi \frac{A_Z}{K} \cos\varphi \frac{A_X}{A_{\perp}} \sin\theta \right) A_x (\cos\psi \cos\theta - \cos\varphi \sin\theta \sin\psi) \\ + \left(\cos\psi \frac{A_X}{A_{\perp}} \sin\theta + \sin\psi \frac{A_Z}{K} \cos\varphi \frac{A_Y}{A_{\perp}} \cos\theta \right) A_y (\cos\psi \sin\theta + \cos\varphi \cos\theta \sin\psi) \\ + \left(\sin\psi \frac{A_{\perp}}{K} \sin\varphi \right) A_z (\sin\varphi \sin\psi)$$

$$a_{12} = \left(\cos\psi \frac{A_Y}{A_{\perp}} \cos\theta - \sin\psi \frac{A_Z}{K} \cos\varphi \frac{A_X}{A_{\perp}} \sin\theta \right) A_x (-\sin\psi \cos\theta - \cos\varphi \sin\theta \cos\psi) \\ + \left(\cos\psi \frac{A_X}{A_{\perp}} \sin\theta + \sin\psi \frac{A_Z}{K} \cos\varphi \frac{A_Y}{A_{\perp}} \cos\theta \right) A_y (-\sin\psi \sin\theta + \cos\varphi \cos\theta \cos\psi) \\ + \left(\sin\psi \frac{A_{\perp}}{K} \sin\varphi \right) A_z (\sin\varphi \cos\psi)$$

$$a_{13} = \left(\cos\psi \frac{A_Y}{A_{\perp}} \cos\theta - \sin\psi \frac{A_Z}{K} \cos\varphi \frac{A_X}{A_{\perp}} \sin\theta \right) A_x \sin\varphi \sin\theta \\ + \left(\cos\psi \frac{A_X}{A_{\perp}} \sin\theta + \sin\psi \frac{A_Z}{K} \cos\varphi \frac{A_Y}{A_{\perp}} \cos\theta \right) A_y (-\sin\varphi \cos\theta) \\ + \left(\sin\psi \frac{A_{\perp}}{K} \sin\varphi \right) A_z (\cos\theta)$$

$$a_{21} = \left(-\sin\psi \frac{A_Y}{A_{\perp}} \cos\theta - \cos\psi \frac{A_Z}{K} \cos\varphi \frac{A_X}{A_{\perp}} \sin\theta \right) A_x (\cos\psi \cos\theta - \cos\varphi \sin\theta \sin\psi) \\ + \left(-\sin\psi \frac{A_X}{A_{\perp}} \sin\theta + \cos\psi \frac{A_Z}{K} \cos\varphi \frac{A_Y}{A_{\perp}} \cos\theta \right) A_y (\cos\psi \sin\theta + \cos\varphi \cos\theta \sin\psi) \\ + \left(\cos\psi \frac{A_{\perp}}{K} \sin\varphi \right) A_z (\sin\varphi \sin\psi)$$

$$a_{22} = \left(-\sin\psi \frac{A_Y}{A_{\perp}} \cos\theta - \cos\psi \frac{A_Z}{K} \cos\varphi \frac{A_X}{A_{\perp}} \sin\theta \right) A_x (-\sin\psi \cos\theta - \cos\varphi \sin\theta \cos\psi) \\ + \left(-\sin\psi \frac{A_X}{A_{\perp}} \sin\theta + \cos\psi \frac{A_Z}{K} \cos\varphi \frac{A_Y}{A_{\perp}} \cos\theta \right) A_y (-\sin\psi \sin\theta + \cos\varphi \cos\theta \cos\psi) \\ + \left(\cos\psi \frac{A_{\perp}}{K} \sin\varphi \right) A_z (\sin\varphi \cos\psi)$$

$$\begin{aligned}
a_{23} = & (-\sin\psi \frac{AY}{A_{\perp}} \cos\theta - \cos\psi \frac{AZ}{K} \cos\varphi \frac{AX}{A_{\perp}} \sin\theta) Ax (\sin\varphi \sin\theta) \\
& + (-\sin\psi \frac{AX}{A_{\perp}} \sin\theta + \cos\psi \frac{AZ}{K} \cos\varphi \frac{AY}{A_{\perp}} \cos\theta) Ay (-\sin\varphi \cos\theta) \\
& + (\cos\psi \frac{AZ}{K} \sin\varphi) Az \cos\theta
\end{aligned}$$

$$\begin{aligned}
a_{31} = & (\frac{AZ}{K} \sin\varphi \frac{AX}{A_{\perp}} \sin\theta) Ax (\cos\psi \cos\theta - \cos\varphi \sin\theta \sin\psi) \\
& + (-\frac{AZ}{K} \sin\varphi \frac{AY}{A_{\perp}} \cos\theta) Ay (\cos\psi \sin\theta + \cos\varphi \cos\theta \sin\psi) \\
& + (\frac{AZ}{K} \cos\varphi) Az (\sin\varphi \sin\psi)
\end{aligned}$$

$$\begin{aligned}
a_{32} = & (\frac{AZ}{K} \sin\varphi \frac{AX}{A_{\perp}} \sin\theta) Ax (-\sin\psi \cos\theta - \cos\varphi \sin\theta \cos\psi) \\
& + (-\frac{AZ}{K} \sin\varphi \frac{AY}{A_{\perp}} \cos\theta) Ay (-\sin\psi \sin\theta + \cos\varphi \cos\theta \cos\psi) \\
& + (\frac{AZ}{K} \cos\varphi) Az (\sin\varphi \cos\psi)
\end{aligned}$$

$$\begin{aligned}
a_{33} = & (\frac{AZ}{K} \sin\varphi \frac{AX}{A_{\perp}} \sin\theta) Ax (\sin\varphi \sin\theta) \\
& + (-\frac{AZ}{K} \sin\varphi \frac{AY}{A_{\perp}} \cos\theta) Ay (-\sin\varphi \cos\theta) \\
& + (\frac{AZ}{K} \cos\varphi) Az (\cos\theta)
\end{aligned}$$

Writing Eq. (A-15) out explicitly, the hyperfine term becomes

$$\begin{aligned}
\underline{I} \cdot \underline{A} \cdot \underline{S} &= \underline{I}' \cdot \underline{A}' \cdot \underline{S}' \\
&= \begin{pmatrix} I'_x & I'_y & I'_z \end{pmatrix} \cdot \begin{pmatrix} a_{11} & a_{12} & a_{13} \\ a_{21} & a_{22} & a_{23} \\ a_{31} & a_{32} & a_{33} \end{pmatrix} \cdot \begin{pmatrix} S'_x \\ S'_y \\ S'_z \end{pmatrix}
\end{aligned}$$

$$\begin{aligned}
&= \begin{pmatrix} I'_x & I'_y & I'_z \end{pmatrix} \cdot \begin{pmatrix} a_{11} S'_x + a_{12} S'_y + a_{13} S'_z \\ a_{21} S'_x + a_{22} S'_y + a_{23} S'_z \\ a_{31} S'_x + a_{32} S'_y + a_{33} S'_z \end{pmatrix} \\
&= a_{11} I'_x S'_x + a_{12} I'_x S'_y + a_{13} I'_x S'_z \\
&\quad + a_{21} I'_y S'_x + a_{22} I'_y S'_y + a_{23} I'_y S'_z \\
&\quad + a_{31} I'_z S'_x + a_{32} I'_z S'_y + a_{33} I'_z S'_z
\end{aligned} \tag{A-16}$$

Substituting into (A-16) a_{ij} and the following relation,

$$\begin{aligned}
I'_x &= \frac{1}{2}(I'_+ + I'_-) & S'_x &= \frac{1}{2}(S'_+ + S'_-) \\
I'_y &= \frac{-i}{2}(I'_+ - I'_-) & S'_y &= \frac{-i}{2}(S'_+ - S'_-)
\end{aligned}$$

and also writing $\cos \Psi \pm i \sin \Psi = e^{\pm i\Psi}$, we have

$$\underline{I}' \cdot \underline{A}' \cdot \underline{S}' = A_x \textcircled{4} + A_y \textcircled{5} + A_z \textcircled{6} \tag{A-17}$$

where

$$\begin{aligned}
\textcircled{4} &= I'_+ S'_+ \frac{e^{i2\Psi}}{4} \left(\frac{A_y}{A_\perp} \cos\theta + i \frac{A_z}{K} \cos\varphi \frac{A_x}{A_\perp} \sin\theta \right) (\cos\theta + i \sin\theta \cos\varphi) \\
&+ I'_+ S'_- \frac{1}{4} \left(\frac{A_y}{A_\perp} \cos\theta + i \frac{A_z}{K} \cos\varphi \frac{A_x}{A_\perp} \sin\theta \right) (\cos\theta - i \sin\theta \cos\varphi) \\
&+ I'_+ S'_z \frac{e^{i\Psi}}{2} \left(\frac{A_y}{A_\perp} \cos\theta + i \frac{A_z}{K} \cos\varphi \frac{A_x}{A_\perp} \sin\theta \right) \sin\theta \sin\varphi \\
&+ I'_- S'_+ \frac{1}{4} \left(\frac{A_y}{A_\perp} \cos\theta - i \frac{A_z}{K} \cos\varphi \frac{A_x}{A_\perp} \sin\theta \right) (\cos\theta + i \sin\theta \cos\varphi) \\
&+ I'_- S'_- \frac{e^{-i2\Psi}}{4} \left(\frac{A_y}{A_\perp} \cos\theta - i \frac{A_z}{K} \cos\varphi \frac{A_x}{A_\perp} \sin\theta \right) (\cos\theta - i \sin\theta \cos\varphi) \\
&+ I'_- S'_z \frac{e^{-i\Psi}}{2} \left(\frac{A_y}{A_\perp} \cos\theta - i \frac{A_z}{K} \cos\varphi \frac{A_x}{A_\perp} \sin\theta \right) (\sin\theta \sin\varphi) \\
&+ I'_z S'_+ \frac{e^{i\Psi}}{2} \left(\frac{A_\perp}{K} \sin\varphi \frac{A_x}{A_\perp} \sin\theta \right) (\cos\theta + i \sin\theta \cos\varphi) \\
&+ I'_z S'_- \frac{e^{-i\Psi}}{2} \left(\frac{A_\perp}{K} \sin\varphi \frac{A_x}{A_\perp} \sin\theta \right) (\cos\theta - i \sin\theta \cos\varphi)
\end{aligned}$$

$$+ I'_z S'_z \left(\frac{A^\perp}{K} \sin \varphi \frac{Ax}{A_\perp} \sin \theta \right) (\sin \theta \sin \varphi)$$

$$\begin{aligned} \textcircled{5} = & I'_{++} S'_{++} \frac{e^{i2\psi}}{4} \left(\frac{Ax}{A_\perp} \sin \theta - i \frac{Az}{K} \cos \varphi \frac{Ay}{A_\perp} \cos \theta \right) (\sin \theta - i \cos \theta \cos \varphi) \\ & + I'_{+-} S'_{+-} \frac{1}{4} \left(\frac{Ax}{A_\perp} \sin \theta - i \frac{Az}{K} \cos \varphi \frac{Ay}{A_\perp} \cos \theta \right) (\sin \theta + i \cos \theta \cos \varphi) \\ & + I'_{+z} S'_{+z} \frac{e^{+i\psi}}{2} \left(\frac{Ax}{A_\perp} \sin \theta - i \frac{Az}{K} \cos \varphi \frac{Ay}{A_\perp} \cos \theta \right) (-\cos \theta \sin \varphi) \\ & + I'_{-+} S'_{-+} \frac{1}{4} \left(\frac{Ax}{A_\perp} \sin \theta + i \frac{Az}{K} \cos \varphi \frac{Ay}{A_\perp} \cos \theta \right) (\sin \theta - i \cos \theta \cos \varphi) \\ & + I'_{--} S'_{--} \frac{e^{-i2\psi}}{4} \left(\frac{Ax}{A_\perp} \sin \theta + i \frac{Az}{K} \cos \varphi \frac{Ay}{A_\perp} \cos \theta \right) (\sin \theta + i \cos \theta \cos \varphi) \\ & + I'_{-z} S'_{-z} \frac{e^{-i\psi}}{2} \left(\frac{Ax}{A_\perp} \sin \theta + i \frac{Az}{K} \cos \varphi \frac{Ay}{A_\perp} \cos \theta \right) (-\cos \theta \sin \varphi) \\ & + I'_{z+} S'_{z+} \frac{e^{i\psi}}{2} \left(-\frac{A^\perp}{K} \sin \varphi \frac{Ay}{A_\perp} \cos \theta \right) (\sin \theta - i \cos \theta \cos \varphi) \\ & + I'_{z-} S'_{z-} \frac{e^{-i\psi}}{2} \left(-\frac{A^\perp}{K} \sin \varphi \frac{Ay}{A_\perp} \cos \theta \right) (\sin \theta + i \cos \theta \cos \varphi) \\ & + I'_{zz} S'_{zz} \left(\frac{A^\perp}{K} \sin \varphi \frac{Ay}{A_\perp} \cos \theta \right) (\cos \theta \sin \varphi) \end{aligned}$$

$$\begin{aligned} \textcircled{6} = & I'_{++} S'_{++} \frac{-e^{i2\psi}}{4} \frac{A^\perp}{K} \sin^2 \varphi \\ & + I'_{+-} S'_{+-} \frac{1}{4} \frac{A^\perp}{K} \sin^2 \varphi \\ & + I'_{+z} S'_{+z} \frac{-ie^{i\psi}}{2} \frac{A^\perp}{K} \sin \varphi \cos \varphi \\ & + I'_{-+} S'_{-+} \frac{1}{4} \frac{A^\perp}{K} \sin^2 \varphi \\ & + I'_{--} S'_{--} \frac{-e^{-i2\psi}}{4} \frac{A^\perp}{K} \sin^2 \varphi \\ & + I'_{-z} S'_{-z} \frac{ie^{-i\psi}}{2} \frac{A^\perp}{K} \sin \varphi \cos \varphi \\ & + I'_{z+} S'_{z+} \frac{-ie^{i\psi}}{2} \frac{Az}{K} \sin \varphi \cos \varphi \\ & + I'_{z-} S'_{z-} \frac{ie^{-i\psi}}{2} \frac{Az}{K} \sin \varphi \cos \varphi + I'_{zz} S'_{zz} \frac{Az}{K} \cos^2 \varphi \end{aligned}$$

The change of energy level, E_{HF} , due to the hyperfine term is obtained by the perturbation calculation to the second order:

$$\begin{aligned}
 E_{HF} &= \langle Mm | \underline{I}' \cdot \underline{A}' \cdot \underline{S}' | Mm \rangle \\
 &+ \sum_{M' \neq M} \frac{|\langle M'm' | \underline{I}' \cdot \underline{A}' \cdot \underline{S}' | Mm \rangle|^2}{E_{ZM} - E_{ZM'}} \\
 &\equiv E_{HF}' + E_{HF}'' \quad (A-18)
 \end{aligned}$$

Substituting (4), (5), and (6) into (A-18) we obtain:

$$\begin{aligned}
 E_{HF}' &= \langle Mm | A_x \text{ (4)} + A_y \text{ (5)} + A_z \text{ (6)} | Mm \rangle \\
 &= \left(\frac{A_x^2}{K} \sin^2 \varphi \sin^2 \theta + \frac{A_y^2}{K} \sin^2 \varphi \cos^2 \theta + \frac{A_z^2}{K} \cos^2 \varphi \right) \langle Mm | I_z' S_z' | Mm \rangle \\
 &= Mm \left[\frac{g^2}{g^2} \sin^2 \text{(H)} \frac{1}{K} (A_x^2 \sin^2 \theta + A_y^2 \cos^2 \theta) + \frac{A_z^2}{K} \frac{g_z^2}{g^2} \cos^2 \text{(H)} \right] \\
 &= Mm \left(\frac{A^2}{K} \frac{g^2}{g^2} \sin^2 \text{(H)} + \frac{A_z^2}{K} \frac{g_z^2}{g^2} \cos^2 \text{(H)} \right) = MmK \quad (A-19)
 \end{aligned}$$

$$\begin{aligned}
 E_{HF}'' &= \sum_{M' \neq M} \frac{|\langle M'm' | A_x \text{ (4)} + A_y \text{ (5)} + A_z \text{ (6)} | Mm \rangle|^2}{E_{ZM} - E_{ZM'}} \\
 &= \frac{\alpha_1}{E_{ZM} - E_{ZM'}} |\langle M'm' | I_+ S_+ | Mm \rangle|^2 \\
 &+ \frac{\alpha_2}{E_{ZM} - E_{ZM'}} |\langle M'm' | I_+ S_- | Mm \rangle|^2 \\
 &+ \frac{\alpha_3}{E_{ZM} - E_{ZM'}} |\langle M'm' | I_+ S_z' | mm \rangle|^2 \\
 &+ \frac{\alpha_4}{E_{ZM} - E_{ZM'}} |\langle M'm' | I_- S_+ | Mm \rangle|^2 \\
 &+ \frac{\alpha_5}{E_{ZM} - E_{ZM'}} |\langle M'm' | I_- S_- | Mm \rangle|^2 \\
 &+ \frac{\alpha_6}{E_{ZM} - E_{ZM'}} |\langle M'm' | I_- S_z' | Mm \rangle|^2
 \end{aligned}$$

$$\begin{aligned}
& + \frac{\alpha_7}{E_{ZM} - E_{ZM'}} |\langle M'm' | I'_Z S'_+ | Mm \rangle|^2 \\
& + \frac{\alpha_8}{E_{ZM} - E_{ZM'}} |\langle M'm' | I'_Z S'_- | Mm \rangle|^2
\end{aligned} \tag{A-20}$$

$$\begin{aligned}
E''_{HF} = & \frac{\alpha_1}{-g\beta H_0} [s(s+1) - M(M+1)] [I(I+1) - m(m+1)] \\
& + \frac{\alpha_2}{+g\beta H_0} [s(s+1) - M(M-1)] [I(I+1) - m(m+1)] \\
& + \frac{\alpha_4}{-g\beta H_0} [s(s+1) - M(M+1)] [I(I+1) - m(m-1)] \\
& + \frac{\alpha_5}{+g\beta H_0} [s(s+1) - M(M-1)] [I(I+1) - m(m-1)] \\
& + \frac{\alpha_7}{-g\beta H_0} m^2 [s(s+1) - M(M+1)] \\
& + \frac{\alpha_8}{+g\beta H_0} m^2 [s(s+1) - M(M-1)]
\end{aligned} \tag{A-21}$$

where we have taken

$$|E_{ZM} - E_{ZM\pm 1}| = g\beta H_0 \approx h\nu_e$$

and

$$\begin{aligned}
\alpha_1 = \alpha_5 &= \frac{1}{16} \left[\left(\frac{AZA_{\perp}}{K} - \frac{AXAY}{A_{\perp}} \right)^2 + \frac{AZ^2 (AX - AY)^2}{K^2 A_{\perp}^2} \frac{g_z^2 g_x^2 g_y^2}{g^2 g_{\perp}^4} \cos^2 \Theta \sin^2 \delta \cos^2 \delta \right] \\
\alpha_2 = \alpha_4 &= \frac{1}{16} \left[\left(\frac{AZA_{\perp}}{K} + \frac{AXAY}{A_{\perp}} \right)^2 + \frac{AZ^2 (AX - AY)^2}{K^2 A_{\perp}^2} \frac{g_z^2 g_x^2 g_y^2}{g^2 g_{\perp}^4} \cos^2 \Theta \sin^2 \delta \cos^2 \delta \right] \\
\alpha_3 = \alpha_6 &= 0 \\
\alpha_7 = \alpha_8 &= \frac{1}{4} \frac{g_{\perp}^2}{K^2 g^2} \sin^2 \Theta \left[(A_z^2 - A_{\perp}^2)^2 \frac{g_z^2}{g^2} \cos^2 \Theta + (A_x^2 - A_y^2)^2 \frac{g_x g_y^2}{g_{\perp}^4} \sin^2 \delta \cos^2 \delta \right]
\end{aligned}$$

Putting the relations between the α 's into (A-21) we have

$$\begin{aligned}
E_{HF}^n &= \frac{\alpha_1}{g\beta H_0} \cdot 2 [s(s+1)m + I(I+1)M - Mm(M+m)] \\
&+ \frac{\alpha_2}{g\beta H_0} \cdot 2 [-s(s+1)m + I(I+1)M + Mm(M-m)] \\
&+ \frac{\alpha_7}{g\beta H_0} \cdot 2 Mm^2 \\
&= \frac{Mm^2}{2g\beta H_0} \cdot \frac{g_{\perp}^2}{K^2 g^2} \sin^2 \textcircled{H} [(A_z^2 - A_{\perp}^2)^2 \frac{g_z^2}{g^2} \cos^2 \textcircled{H} + (A_x^2 - A_y^2) \frac{g_x g_y}{g_{\perp}^4} \sin^2 \delta \cos^2 \delta] \\
&+ \frac{-s(s+1)m + I(I+1)M + Mm(M-m)}{8g\beta H_0} [A_{\perp}^2 (\frac{A_z^2 - K^2}{K^2}) + (A_x^2 + A_y^2 + 2 \frac{A_x A_y A_z}{K}) \\
&\quad - \frac{(A_x^2 - A_y^2)^2}{K^2} \cdot \frac{g_x g_y}{g^2 g_{\perp}^2} \sin^2 \textcircled{H} \sin^2 \delta \cos^2 \delta] \\
&+ \frac{s(s+1)m + I(I+1)M - Mm(M+m)}{8g\beta H_0} [A_{\perp}^2 (\frac{A_z^2 - K^2}{K^2}) + (A_x^2 + A_y^2 - 2 \frac{A_x A_y A_z}{K}) \\
&\quad - \frac{(A_x^2 - A_y^2)^2}{K^2} \cdot \frac{g_x g_y}{g^2 g_{\perp}^2} \sin^2 \textcircled{H} \sin^2 \delta \cos^2 \delta] \quad (A-22)
\end{aligned}$$

Putting (A-19) and (A-22) into (A-18) we obtain:

$$\begin{aligned}
E_{HF} &= MmK + \frac{1}{2} Mm f_1 \\
&+ \frac{1}{8} [-s(s+1)m + I(I+1)M + Mm(M-m)] f_2 \\
&+ \frac{1}{8} [s(s+1)m + I(I+1)M - Mm(M+m)] f_3 \quad (A-23)
\end{aligned}$$

where

$$\begin{aligned}
f_1 &= \frac{1}{g\beta H_0} \cdot \frac{g_{\perp}^2}{K^2 g^2} \sin^2 \textcircled{H} [(A_z^2 - A_{\perp}^2)^2 \frac{g_z^2}{g^2} \cos^2 \textcircled{H} + (A_x^2 - A_y^2) \frac{g_x g_y}{g_{\perp}^4} \sin^2 \delta \cos^2 \delta] \\
f_2 &= \frac{1}{g\beta H_0} [A_{\perp}^2 (\frac{A_z^2 - K^2}{K^2}) + (A_x^2 + A_y^2 + 2 \frac{A_x A_y A_z}{K}) \\
&\quad - \frac{(A_x^2 - A_y^2)^2}{K^2} \cdot \frac{g_x g_y}{g^2 g_{\perp}^2} \sin^2 \textcircled{H} \sin^2 \delta \cos^2 \delta] \\
f_3 &= \frac{1}{g\beta H_0} [A_{\perp}^2 (\frac{A_z^2 - K^2}{K^2}) + (A_x^2 + A_y^2 - 2 \frac{A_x A_y A_z}{K}) \\
&\quad - \frac{(A_x^2 - A_y^2)^2}{K^2} \cdot \frac{g_x g_y}{g^2 g_{\perp}^2} \sin^2 \textcircled{H} \sin^2 \delta \cos^2 \delta] \quad (A-24)
\end{aligned}$$

3. Quadrupole Term

The quadrupole term is

$$\underline{I} \cdot \underline{Q} \cdot \underline{I} = Q_x I_x^2 + Q_y I_y^2 + Q_z I_z^2 \quad (\text{A-25})$$

$$= Q' [I_z^2 - \frac{1}{3} I(I+1)] + Q'' (I_x^2 - I_y^2) \quad (\text{A-26})$$

We could diagonalize the quadrupole term expressed as (A-25) by the same method used for the diagonalization of the hyperfine term. However, since it is preferred to use the expression (A-26) for the quadrupole term, we will adopt a different treatment in the following way: Writing the nuclear angular momentum operator \underline{I} as a column vector, and applying the rotation operator P_I , we have

$$\underline{I}' = P_I \underline{I}$$

Hence

$$\underline{I} = P_I^{-1} \underline{I}' \quad (\text{A-27})$$

Writing (A-27) in component form and substituting for \underline{I}' the relation

$$\left. \begin{aligned} I'_x &= \frac{1}{2} (I'_+ + I'_-) \\ I'_y &= \frac{-i}{2} (I'_+ - I'_-) \\ I'_z &= I'_z \end{aligned} \right\} \quad (\text{A-28})$$

we obtain:

$$\begin{aligned}
I_x &= I'_+ \frac{e^{i\psi}}{2} \left(\frac{A_y}{A_\perp} \cos\theta + i \frac{A_z}{K} \cos\varphi \frac{A_x}{A_\perp} \sin\theta \right) \\
&+ I'_- \frac{e^{-i\psi}}{2} \left(\frac{A_y}{A_\perp} \cos\theta - i \frac{A_z}{K} \cos\varphi \frac{A_x}{A_\perp} \sin\theta \right) \\
&+ I'_z \left(\frac{A_\perp}{K} \sin\varphi \frac{A_x}{A_\perp} \sin\theta \right) \\
I_y &= I'_+ \frac{e^{i\psi}}{2} \left(\frac{A_x}{A_\perp} \sin\theta - i \frac{A_z}{K} \cos\varphi \frac{A_y}{A_\perp} \cos\theta \right) \\
&+ I'_- \frac{e^{-i\psi}}{2} \left(\frac{A_x}{A_\perp} \sin\theta + i \frac{A_z}{K} \cos\varphi \frac{A_y}{A_\perp} \cos\theta \right) \\
&+ I'_z \left(-\frac{A_\perp}{K} \sin\varphi \frac{A_y}{A_\perp} \cos\theta \right) \\
I_z &= I'_+ \frac{-ie^{i\psi}}{2} \frac{A_\perp}{K} \sin\varphi \\
&+ I'_- \frac{ie^{-i\psi}}{2} \frac{A_\perp}{K} \sin\varphi \\
&+ I'_z \frac{A_\perp}{K} \cos\varphi
\end{aligned} \tag{A-29}$$

Equation (A-29) leads to

$$\begin{aligned}
I_x^2 &= I'_+{}^2 \frac{e^{i2\psi}}{4} \left(\frac{A_y}{A_\perp} \cos\theta + i \frac{A_z}{K} \frac{A_x}{A_\perp} \cos\varphi \sin\theta \right)^2 \\
&+ I'_-{}^2 \frac{e^{-i2\psi}}{4} \left(\frac{A_y}{A_\perp} \cos\theta - i \frac{A_z A_x}{K A_\perp} \cos\varphi \sin\theta \right)^2 \\
&+ I'_z{}^2 \frac{A_x^2}{K} \sin^2\varphi \sin^2\theta \\
&+ \frac{I'_+ I'_- + I'_- I'_+}{4} \left(\frac{A_y^2}{A_\perp^2} \cos^2\theta + \frac{A_z^2 A_x^2}{K^2 A_\perp^2} \cos^2\varphi \sin^2\theta \right) \\
&+ (I'_+ I'_z + I'_z I'_+) e^{i\psi} \frac{A_x}{2K} \sin\varphi \sin\theta \left(\frac{A_y}{A_\perp} \cos\theta + i \frac{A_z A_x}{K A_\perp} \cos\varphi \sin\theta \right) \\
&+ (I'_- I'_z + I'_z I'_-) e^{-i\psi} \frac{A_x}{2K} \sin\varphi \sin\theta \left(\frac{A_y}{A_\perp} \cos\theta - i \frac{A_z A_x}{K A_\perp} \cos\varphi \sin\theta \right)
\end{aligned}$$

$$\begin{aligned}
I_Y^2 &= I_+^{\prime 2} \frac{e^{i2\Psi}}{4} \left(\frac{A_X}{A_\perp} \sin\theta - i \frac{A_Z A_Y}{K A_\perp} \cos\varphi \cos\theta \right)^2 \\
&+ I_-^{\prime 2} \frac{e^{-i2\Psi}}{4} \left(\frac{A_X}{A_\perp} \sin\theta + i \frac{A_Z A_Y}{K A_\perp} \cos\varphi \cos\theta \right)^2 \\
&+ I_Z' \frac{A_Y^2}{K^2} \sin^2\varphi \cos^2\theta \\
&+ \frac{I_+^{\prime} I_-^{\prime} + I_-^{\prime} I_+^{\prime}}{4} \left(\frac{A_X^2}{A_\perp^2} \sin^2\theta + \frac{A_Z^2 A_Y^2}{K^2 A_\perp^2} \cos^2\varphi \cos^2\theta \right) \\
&+ (I_+^{\prime} I_Z' + I_Z' I_+^{\prime}) e^{i\Psi} \frac{-A_Y}{2K} \sin\varphi \cos\theta \left(\frac{A_X}{A_\perp} \sin\theta - i \frac{A_Z A_Y}{K A_\perp} \cos\varphi \cos\theta \right) \\
&+ (I_-^{\prime} I_Z' + I_Z' I_-^{\prime}) e^{-i\Psi} \frac{-A_Y}{2K} \sin\varphi \cos\theta \left(\frac{A_X}{A_\perp} \sin\theta + i \frac{A_Z A_Y}{K A_\perp} \cos\varphi \cos\theta \right)
\end{aligned}$$

$$\begin{aligned}
I_Z^2 &= (I_+^{\prime 2} e^{i2\Psi} + I_-^{\prime 2} e^{-i2\Psi}) \frac{-A_\perp^2}{4K^2} \sin^2\varphi + I_Z^{\prime 2} \frac{A_Z^2}{K^2} \cos^2\varphi \\
&+ (I_+^{\prime} I_-^{\prime} + I_-^{\prime} I_+^{\prime}) \frac{A_\perp^2}{4K^2} \sin^2\varphi \\
&- (I_+^{\prime} I_Z' + I_Z' I_+^{\prime}) \frac{ie^{i\Psi}}{2K^2} A_Z A_\perp \cos\varphi \sin\varphi \\
&+ (I_-^{\prime} I_Z' + I_Z' I_-^{\prime}) \frac{ie^{-i\Psi}}{2K^2} A_Z A_\perp \cos\varphi \sin\varphi
\end{aligned} \tag{A-30}$$

With these preparations, the diagonalization of the quadrupole term, $\underline{I} \cdot \underline{Q} \cdot \underline{I}$ is straight forward:

$$\begin{aligned}
E_Q &= \langle Mm | Q' [I_Z^2 - \frac{1}{3} I(I+1)] + Q'' (I_X^2 - I_Y^2) | Mm \rangle \\
&+ \sum_{m' \neq m} \frac{|\langle Mm' | Q' [I_Z^2 - \frac{1}{3} I(I+1)] + Q'' (I_X^2 - I_Y^2) | Mm \rangle|^2}{E_m - E_{m'}} \\
&\equiv E_Q' + E_Q''
\end{aligned} \tag{A-31}$$

Substituting (A-30) into the first term of (A-31) we obtain

$$\begin{aligned}
E'_Q &= \langle Mm | Q' [I_Z^2 - \frac{1}{3} I(I+1)] + Q'' (I_X^2 - I_Y^2) | Mm \rangle \\
&= \langle Mm | Q' [I_Z'^2 \frac{A_z^2}{K^2} \cos^2 \varphi + (I_+ I_- + I_- I_+) \frac{A_+^2}{4K^2} \sin^2 \varphi - \frac{1}{3} I(I+1)] \\
&\quad + Q'' [I_Z'^2 \frac{1}{K^2} \sin^2 \varphi (A_x^2 \sin^2 \theta - A_y^2 \cos^2 \theta) \\
&\quad + (I_+ I_- + I_- I_+) \frac{(-) \sin^2 \varphi}{4K^2} (A_x^2 \sin^2 \theta - A_y^2 \cos^2 \theta)] | Mm \rangle \\
&= m^2 [Q' (1 - \frac{3}{2} \frac{A_z^2 g_z^2}{K^2 g^2} \sin^2 \textcircled{H}) + Q'' \frac{3}{2} \frac{1}{K^2 g^2} \sin^2 \textcircled{H} (A_x^2 g_x^2 \cos^2 \delta \\
&\quad - A_y^2 g_y^2 \sin^2 \delta)] \\
&\quad + \frac{I(I+1)}{3} [Q' (-1 + \frac{3A_+^2 g_+^2}{2K^2 g^2} \sin^2 \textcircled{H}) - Q'' \frac{3}{2} \frac{\sin^2 \textcircled{H}}{K^2 g^2} \\
&\quad \cdot (A_x^2 g_x^2 \cos^2 \delta - A_y^2 g_y^2 \sin^2 \delta)] \\
&\equiv [m^2 - \frac{1}{3} I(I+1)] f_4
\end{aligned}$$

where we have made use of Eq. (A-3) to go from the second step to the third step; and

$$f_4 = Q' (1 - \frac{3}{2} \cdot \frac{A_z^2 g_z^2}{K^2 g^2} \sin^2 \textcircled{H}) + Q'' \frac{3}{2} \frac{\sin^2 \textcircled{H}}{K^2 g^2} (A_x^2 g_x^2 \cos^2 \delta - A_y^2 g_y^2 \sin^2 \delta).$$

$$\begin{aligned}
E_Q'' &= \sum_{m' \neq m} \frac{|\langle Mm' | Q' [I_z^2 - \frac{1}{3} I(I+1)] + Q'' (I_x^2 - I_y^2) | Mm \rangle|^2}{E_m - E_{m'}} \\
&= \beta_1 \frac{|\langle m+2 | I_+^2 | m \rangle|^2}{E_m - E_{m+2}} + \beta_2 \frac{|\langle m-2 | I_-^2 | m \rangle|^2}{E_m - E_{m-2}} \\
&\quad + \beta_3 \frac{|\langle m+1 | I_+ I_z + I_z I_+ | m \rangle|^2}{E_m - E_{m+1}} + \beta_4 \frac{|\langle m-1 | I_- I_z + I_z I_- | m \rangle|^2}{E_m - E_{m-1}} \\
&= \beta_1 \frac{[I(I+1) - m(m+1)][I(I+1) - (m+1)(m+2)]}{-2MK - 4(m+1)f_4} \\
&\quad + \beta_2 \frac{[I(I+1) - m(m-1)][I(I+1) - (m-1)(m-2)]}{2MK + 4(m-1)f_4} \\
&\quad + \beta_3 \frac{(2m+1)^2 [I(I+1) - m(m+1)]}{-MK - (2m+1)f_4} \\
&\quad + \beta_4 \frac{(2m-1)^2 [I(I+1) - m(m+1)]}{MK + (2m-1)f_4} \tag{A-33}
\end{aligned}$$

where β_1, \dots, β_4 are angular dependent coefficients:

$$\begin{aligned}
\beta_1 &= \beta_2 \\
&= [Q' \frac{A_z^2 g_z^2}{4K^2 g^2} \sin^2 \Theta + \frac{Q''}{4A_z^2 g_z^2} (1 + \frac{A_z^2 g_z^2}{K^2 g^2} \cos \Theta) (A_x^2 g_x^2 \cos^2 \delta - A_y^2 g_y^2 \sin^2 \delta)]^2 + Q''^2 \frac{A_z^2 A_x^2 A_y^2}{K^2 A_z^4} \cdot \frac{g_z^2 g_x^2 g_y^2}{g^2 g_z^4} \cos \Theta \sin^2 \delta \cos^2 \delta \\
&\equiv Kf_5 \tag{A-34}
\end{aligned}$$

$$\begin{aligned}
\beta_3 &= \beta_4 \\
&= \frac{A_z^2 g_z^2}{4K^4 A_z^2 g_z^4 g^2} \sin^2 \Theta \cos^2 \Theta [-Q' A_z^2 g_z^2 + Q'' (A_x^2 g_x^2 \cos^2 \delta - A_y^2 g_y^2 \sin^2 \delta)]^2 \\
&\quad + Q''^2 \frac{A_z^2 A_x^2}{K^2 A_z^2} \cdot \frac{g_x^2 g_y^2}{g^2 g_z^2} \sin^2 \Theta \sin^2 \delta \cos^2 \delta \\
&\equiv Kf_6 \tag{A-35}
\end{aligned}$$

Putting (A-32) to (A-35) into (A-31) we obtain the result of diagonalization of the quadrupole term as

$$\begin{aligned}
 E_Q = & [m^2 - \frac{1}{3} I(I+1)] f_4 \\
 & + \frac{K[I(I+1) - m(m+1)][I(I+1) - (m+1)(m+2)]}{-2MK - 4(m+1)f_4} f_5 \\
 & + \frac{K[I(I+1) - m(m-1)][I(I+1) - (m-1)(m-2)]}{2MK + 4(m-1)f_4} f_5 \\
 & + \frac{K(2m+1)^2 [I(I+1) - m(m+1)]}{-MK - (2m+1)f_4} f_6 \\
 & + \frac{K(2m-1)^2 [I(I+1) - m(m-1)]}{MK + (2m-1)f_4} f_6
 \end{aligned} \tag{A-36}$$

4. Nuclear Zeeman Term

The nuclear interaction term is

$$-\beta_n \underline{H} \cdot \underline{g}'_n \cdot \underline{I} = -\beta_n (g'_{nx} H_x I_x + g'_{ny} H_y I_y + g'_{nz} H_z I_z). \tag{A-37}$$

Substituting (A-29) into (A-37) we get

$$\begin{aligned}
 \underline{H} \cdot \underline{g}'_n \cdot \underline{I} = & I'_+ \frac{e^{i\psi}}{2} [g'_{nx} H_x \left(\frac{A_y}{A_\perp} \cos\theta + i \frac{A_z A_x}{K A_\perp} \cos\varphi \sin\theta \right) \\
 & + g'_{ny} H_y \left(\frac{A_x}{A_\perp} \sin\theta - i \frac{A_z A_y}{K A_\perp} \cos\varphi \cos\theta \right) \\
 & - g'_{nz} H_z \frac{i A_\perp}{K} \sin\varphi] \\
 & + I'_- \frac{e^{-i\psi}}{2} [g'_{nx} H_x \left(\frac{A_y}{A_\perp} \cos\theta - i \frac{A_z A_x}{K A_\perp} \cos\varphi \sin\theta \right) \\
 & + g'_{ny} H_y \left(\frac{A_x}{A_\perp} \sin\theta + i \frac{A_z A_y}{K A_\perp} \cos\varphi \cos\theta \right) \\
 & + g'_{nz} H_z \frac{i A_\perp}{K} \sin\varphi]
 \end{aligned}$$

$$\begin{aligned}
& + I'_z \left[g'_{nx} H_x \frac{A_x}{K} \sin\varphi \sin\theta - g'_{ny} H_y \frac{A_y}{K} \sin\varphi \cos\theta \right. \\
& \quad \left. + g'_{nz} H_z \frac{A_z}{K} \cos\varphi \right] \tag{A-38}
\end{aligned}$$

The change of energy level, E_{NZ} , due to the nuclear Zeeman term is obtained by the perturbation method to the second order:

$$\begin{aligned}
E_{nz} &= \langle Mm | -\beta_n \underline{H} \cdot \underline{g}_n \cdot \underline{I} | Mm \rangle \\
&+ \sum_{m' \neq m} \frac{|\langle Mm' | -\beta_n \underline{H} \cdot \underline{g}_n \cdot \underline{I} | Mm \rangle|^2}{E_m - E_{m'}} \\
&\equiv E'_{nz} + E''_{nz} \tag{A-39}
\end{aligned}$$

With Eq. (A-38),

$$\begin{aligned}
E'_{nz} &= \langle Mm | -\beta_n \underline{H} \cdot \underline{g}'_n \cdot \underline{I} | Mm \rangle \\
&= -\beta_n \left(g'_{nx} H_x \frac{A_x}{K} \sin\varphi \sin\theta - g'_{ny} H_y \frac{A_y}{K} \sin\varphi \cos\theta \right. \\
&\quad \left. + g'_{nz} H_z \frac{A_z}{K} \cos\varphi \right) \langle Mm | I'_z | Mm \rangle \\
&= -m\beta_n H \frac{1}{Kg} \left[\sin^2 \textcircled{H} (g'_{nx} g'_x A_x \cos^2 \delta + g'_{ny} g'_y A_y \sin^2 \delta) \right. \\
&\quad \left. + g'_{nz} g'_z A_z \cos^2 \textcircled{H} \right] \\
&= -m\beta_n H f_7 \tag{A-40}
\end{aligned}$$

where

$$f_7 \equiv \frac{1}{Kg} \left[\sin^2 \textcircled{H} (A_x g'_x g'_{nx} \cos^2 \delta + A_y g'_y g'_{ny} \sin^2 \delta) + A_z g'_z g'_{nz} \cos^2 \textcircled{H} \right]$$

Also,

$$\begin{aligned}
E''_{nz} &= \sum_{m' \neq m} \frac{|\langle Mm' | -\beta_n \underline{H} \cdot \underline{g}' \cdot \underline{I} | Mm \rangle|^2}{E_m - E_{m'}} \\
&= \gamma_1 \frac{|\langle Mm+1 | I_+ | Mm \rangle|^2}{E_m - E_{m+1}} + \gamma_2 \frac{|\langle Mm-1 | I_- | Mm \rangle|^2}{E_m - E_{m-1}} \\
&= \gamma_1 \frac{I(I+1) - m(m+1)}{-MK} + \gamma_2 \frac{I(I+1) - m(m-1)}{MK} \quad (A-41)
\end{aligned}$$

where

$$\begin{aligned}
\gamma_1 = \gamma_2 &= \frac{\beta_n^2}{4} \left[(g'_{nx} H_x \frac{A_y}{A_{\perp}} \cos\theta + g'_{ny} H_y \frac{A_x}{A_{\perp}} \sin\theta)^2 \right. \\
&\quad \left. + (g'_{nx} H_x \frac{A_z A_x}{K A_{\perp}} \cos\varphi \sin\theta - g'_{ny} H_y \frac{A_z A_y}{K A_{\perp}} \cos\varphi \cos\theta - g'_{nz} H_z \frac{A_{\perp}}{K} \sin\varphi)^2 \right]
\end{aligned}$$

Using the relations (A-2) to (A-4), γ_1 becomes

$$\begin{aligned}
\gamma_1 &= \frac{\beta_n^2 H^2}{4} \cdot \frac{1}{A_{\perp}^2 g_{\perp}^2} \sin^2 \textcircled{H} [\sin^2 \delta \cos^2 \delta (g'_{nx} g'_y A_y - g'_{ny} g'_x A_x)^2 \\
&\quad + \frac{1}{K^2 g^2} \cos^2 \textcircled{H} (g'_{nx} g'_x g'_z A_z A_x \cos^2 \delta + g'_{ny} g'_y g'_z A_z A_y \sin^2 \delta - g'_{nz} g_{\perp}^2 A_{\perp}^2)^2] \\
&\equiv \frac{\beta_n^2 H^2}{4} K f_8
\end{aligned}$$

$$\therefore E''_{nz} = \frac{2m}{KM} \gamma_1 = \frac{m}{2M} \beta_n^2 H^2 f_8 \quad (A-42)$$

where

$$\begin{aligned}
f_8 &= \frac{\sin^2 \textcircled{H}}{K A_{\perp}^2 g_{\perp}^2} \left[\frac{\cos^2 \textcircled{H}}{K^2 g^2} (A_z A_x g'_z g'_x g'_{nx} \cos^2 \delta + A_z A_y g'_z g'_y g'_{ny} \sin^2 \delta \right. \\
&\quad \left. - A_{\perp}^2 g_{\perp}^2 g'_{nz})^2 + \sin^2 \delta \cos^2 \delta (A_y g'_y g'_{nx} - A_x g'_x g'_{ny})^2 \right]
\end{aligned}$$

Therefore the result of diagonalization of the nuclear Zeeman term is, combining (A-39) with (A-40) and (A-42):

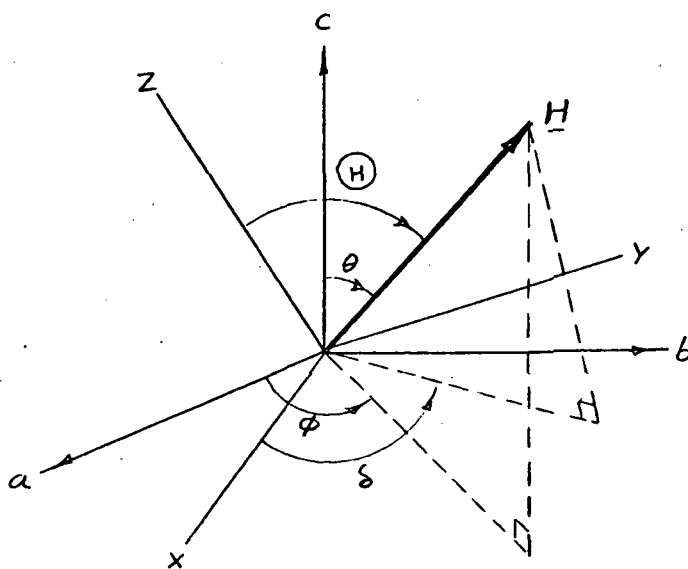
$$E_{nz} = -m\beta_n H f_7 + \frac{m}{2M} \beta_n^2 H^2 f_8 \quad (A-43)$$

5. Summary

Summing up Eqs. (A-11), (A-23), and (A-43) and putting the result into (A-1), we obtain the energy level formula corresponding to the spin Hamiltonian Eq. (14). This formula is given in Eq. (20) with the angular dependent coefficients defined by Eq. (21), on page 19.

B. Relation Between the Principal Coordinates and the Crystal Symmetry Coordinates

The formulation of both EPR and ENDOR signals has been made on the principal coordinate system x, y, z . Nevertheless, the experiment and data presentation are usually, for the sake of convenience, performed in the crystal symmetry coordinates a, b, c . It is the purpose of this appendix to derive the relation between the spherical coordinates of the a, b, c , system and the x, y, z system.



Let \underline{H} be the magnetic field vector

d_{aH}, d_{bH}, d_{cH} = direction cosines of \underline{H} in abc coordinates

d_{xH}, d_{yH}, d_{zH} = direction cosines of \underline{H} in xyz coordinates

$\underline{a}, \underline{b}, \underline{c}$ = unit vectors of a, b, c coordinates

$\underline{x}, \underline{y}, \underline{z}$ = unit vectors of x, y, z coordinates

$$\text{Since } \underline{H} = H(\underline{a} d_{aH} + \underline{b} d_{bH} + \underline{c} d_{cH}) \quad (\text{B-1})$$

$$= H(\underline{x} d_{xH} + \underline{y} d_{yH} + \underline{z} d_{zH}) \quad (\text{B-2})$$

then

$$\left. \begin{aligned} d_{aH} &= \sin\theta \cos\phi \\ d_{bH} &= \sin\theta \sin\phi \\ d_{cH} &= \cos\theta \end{aligned} \right\} \quad (\text{B-3})$$

where θ and ϕ are directly measured from experiment; and

$$\left. \begin{aligned} d_{xH} &= \sin(H) \cos\delta \\ d_{yH} &= \sin(H) \sin\delta \\ d_{zH} &= \cos(H) \end{aligned} \right\} \quad (\text{B-4})$$

Where (H) and δ are the unknowns to be found. Let the direction cosines of

the unit vector \underline{x} in abc system be d_{ax}, d_{bx}, d_{cx} ;

~~the unit vector \underline{y} in abc system be d_{ay}, d_{by}, d_{cy} ;~~

the unit vector \underline{z} in abc system be d_{az}, d_{bz}, d_{cz} .

Also let the direction cosines of

the unit vector \underline{a} in xyz system be d_{xa}, d_{ya}, d_{za} ;

the unit vector \underline{b} in xyz system be d_{xb}, d_{yb}, d_{zb} ;

the unit vector \underline{c} in xyz system be d_{xc}, d_{yc}, d_{zc} .

Then, because the cosines of the same angle are identical, we have

$$\begin{aligned}
 d_{ax} &= d_{xa} & d_{bx} &= d_{xb} & d_{cx} &= d_{xc} \\
 d_{ay} &= d_{ya} & d_{by} &= d_{yb} & d_{cy} &= d_{yc} \\
 d_{az} &= d_{za} & d_{bz} &= d_{zb} & d_{cz} &= d_{zc}
 \end{aligned} \tag{B-5}$$

Note that

$$\begin{aligned}
 d_{xH} &= d_{xa}d_{aH} + d_{xb}d_{bH} + d_{xc}d_{cH} \\
 d_{yH} &= d_{ya}d_{aH} + d_{yb}d_{bH} + d_{yc}d_{cH} \\
 d_{zH} &= d_{za}d_{aH} + d_{zb}d_{bH} + d_{zc}d_{cH}
 \end{aligned} \tag{B-6}$$

By (B-5), Eq. (B-6) becomes

$$\begin{aligned}
 d_{xH} &= d_{ax}d_{aH} + d_{bx}d_{bH} + d_{cx}d_{cH} \\
 d_{yH} &= d_{ay}d_{aH} + d_{by}d_{bH} + d_{cy}d_{cH} \\
 d_{zH} &= d_{az}d_{aH} + d_{bz}d_{bH} + d_{cz}d_{cH}
 \end{aligned} \tag{B-7}$$

Let the spherical coordinates of

$$\underline{x} \text{ in abc system be } \theta_x, \phi_x;$$

$$\underline{y} \text{ in abc system be } \theta_y, \phi_y;$$

$$\underline{z} \text{ in abc system be } \theta_z, \phi_z.$$

These angles are experimentally measured quantities.

Then

$$\left. \begin{aligned} d_{ax} &= \sin \theta_x \cos \phi_x \\ d_{bx} &= \sin \theta_x \sin \phi_x \\ d_{cx} &= \cos \theta_x \end{aligned} \right\} \quad (\text{B-8})$$

$$\left. \begin{aligned} d_{ay} &= \sin \theta_y \cos \phi_y \\ d_{by} &= \sin \theta_y \sin \phi_y \\ d_{cy} &= \cos \theta_y \end{aligned} \right\} \quad (\text{B-9})$$

$$\left. \begin{aligned} d_{az} &= \sin \theta_z \cos \phi_z \\ d_{bz} &= \sin \theta_z \sin \phi_z \\ d_{cz} &= \cos \theta_z \end{aligned} \right\} \quad (\text{B-10})$$

Combining (B-4) with (B-7) and utilizing relations (B-8) to (B-10) we have

$$\cos \textcircled{H} = \sin \theta_z \cos \phi_z \sin \theta \cos \phi + \sin \theta_z \sin \phi_z \sin \theta \sin \phi + \cos \theta_z \cos \theta \quad (\text{B-11})$$

and

$$\tan \delta = \frac{\sin\theta_y \cos\phi_y \sin\theta \cos\phi + \sin\theta_y \sin\phi_y \sin\theta \sin\phi + \cos\theta_y \cos\theta}{\sin\theta_x \cos\phi_x \sin\theta \cos\phi + \sin\theta_x \sin\phi_x \sin\theta \sin\phi + \cos\theta_x \cos\theta} \quad (\text{B-12})$$

All the angles, θ 's and ϕ 's, in the RHS of Eq. (B-11) and Eq. (B-12) are obtained directly from the experiment and referred to the abc-coordinates. \textcircled{H} and δ are the angles referred to the xyz-system and are used in Eq. (21).

REFERENCES

1. K.C. Chu, C. Kikuchi and W. Viehmann, "ESR of Niobium in CaWO_4 ", J. Chem. Phys. 46, 386 (1967). Also "Electron Spin Resonance of Paramagnetic Tungsten and Niobium Substitution in Calcium Tungstate", Ph.D. Dissertation of the first author, Univ. of Mich., 1967.
2. L.F. Johnson, "Characteristics of the $\text{CaWO}_4:\text{Nd}^{3+}$ Optical Masers", Quantum Electronics, Vol. 2, p. 1021. Columbia University Press, New York, 1963.
3. K. Nussan and G.M. Loiacono, "Calcium Tungstate - III, Trivalent Rare-Earth Substitution", J. Phys. Chem. Solids 24, 1503, 1511, (1963).
4. G.L. Miller, Tantalum and Niobium, Academic Press, Inc. Publishers, New York, Butterworths Scientific Publishers, London, 1959.
5. Frank T. Sisco and Edward Epreman, Columbium and Tantalum, John Wiley & Sons, Inc., New York, 1963.
6. N. Mahootian, "An Electron Spin Resonance Study of Vanadium in Calcium Tungstate Crystal", Ph.D. Dissertation, Univ. of Mich., 1966.
7. N. Mahootian and C. Kikuchi and W. Viehmann, "Spin-Resonance Properties of Scheelites, I. Vanadium in CaWO_4 ", J. Chem. Phys. 48, 1097, 1 Feb., 1968.
8. Robert B. Leighton, Principles of Modern Physics, McGraw-Hill Book Co., Inc., New York, (1959).
9. R.W.G. Wyckoff, Crystal Structures, Interscience Publishers, Inc., New York (1951), Vol. II, Chapter VIII; Also, International Tables for X-ray Crystallography, Vol. I, The Kynoch Press, Birmingham, England, (1952).
10. S. Karavelas and C. Kikuchi, "Molecular Orbital Calculation of Vanadium in the Tungsten Site of CaWO_4 ", Bull. Am. Phys. Soc. 10, 614 (1965); also University of Michigan Tech. report 06029-30-T, September, 1965.
11. J.D.E. Ingram, Spectroscopy at Radio and Microwave Frequencies, Academic Press (1955).

12. J.D.E. Ingram, Free Radicals as Studied by Electron Spin Resonance, Academic Press (1958).
13. W. Low, Paramagnetic Resonance in Solids, Academic Press, New York (1960).
14. G.E. Pake, Paramagnetic Resonance, W. A. Benjamin, Inc., New York (1962).
15. C.P. Slichter, Principles of Magnetic Resonance, Harper and Row Publishers, New York (1963).
16. M. Bersohn and J.C. Baird, An Introduction to Electron Paramagnetic Resonance, W. A. Benjamin, Inc., New York, 1966.
17. H.S. Jarrett, "Electron Spin Resonance Spectroscopy in Molecular Solids", Solid State Phys., Vol. 14 (1963).
18. S.A. Al'tschuler and B.M. Kozyrev, Electron Paramagnetic Resonance, (1959), translated by Scripta Technica, Inc., Academic Press, New York (1964).
19. Charles P. Poole, Jr. Electron Spin Resonance, A Comprehensive treaty on experimental technique, Interscience Publishers, New York, 1967.
20. H.M. Assenheim, Introduction to Electron Spin Resonance, Plenum Press, New York, 1967.
21. A.J. Freeman and R.B. Frankel, Hyperfine Interactions, Chapters 1 and 6, Academic Press, New York, 1967.
22. A. Carrington and A.D. McLachlan, Introduction to Magnetic Resonance, Harper and Row Publishers, New York, 1967.
23. B. Bleaney and K.W.H. Stevens, "Paramagnetic Resonance", Rep. Progr. Phys. 16, 108 (1953) (London: Physical Society).
24. K.D. Bowers and J. Owen "Paramagnetic Resonance II," Rep. Progr. Phys. 18, 304 (1955).
25. G. Feher, "Method of Polarizing Nuclei in Paramagnetic Substances", Phys. Rev. 103, 500 (1956).
26. G. Feher and E.A. Gere, "Polarization of Phosphorus Nuclei in Silicon", Phys. Rev. 103, 501 (1956).
27. G. Feher, "Observation of Nuclear Magnetic Resonances Via the Electron Spin Resonance Line", Phys. Rev. 103, 834 (1956).

28. G. Feher, "Electronic Structure of F Centers in KCl by the Electron Spin Double-Resonance Technique", Phys. Rev. 105, 1122 (1957).
 29. J. Eisinger and G. Feher, "HFS Anomaly of Sb¹²¹ and Sb¹²³ Determined by the Electron Nuclear-Double Resonance Technique", Phys. Rev., 109, 1172 (1958).
 30. Donald Halford, Clyde A. Hutchinson, Jr. and Peter M. Llewellyn, "Electron Nuclear Double Resonance of Neodymium", Phys. Rev., 110, 284, (1958).
 31. G. Feher, "Electron Spin Resonance Experiments on Donors in Silicon. I. Electronic Structure of Donors by the Electron Nuclear Double Resonance Technique", Phys. Rev. 114, 1219, (1959).
 32. G. Feher, "Electron Spin Resonance Experiments on Donors in Silicon. II. Electron Spin Relaxation Effect," Phys. Rev. 114, 1245, (1959).
 33. J. Lambe, N. Laurance, E.C. McIrvine and R.W. Terhune, "Mechanisms of Double Resonance in Solids", Phys. Rev. 122, 1161, (1961).
 34. R.W. Terhune, J. Lambe, C. Kikuchi, and J. Baker, "Hyperfine Spectrum of Cr-53 in Al₂O₃", Phys. Rev. 123, 1265, (1961).
 35. D.J.I. Fry and P.N. Llewellyn, "The Double Resonance of Cobalt Ions in Magnesium Oxide", Proc. Roy. Soc. A 266, 84, (1962).
 36. J.M. Baker and F.I.B. Williams, "Electron Nuclear Double Resonance of the Divalent Europium Ion", Proc. Roy. Soc., A 267, 283 (1962).
 37. R. Kaplan and P.J. Bray, "Electron-Spin Paramagnetic Resonance Studies of Neutron-Irradiated LiF", Phys. Rev. 129, 1919 (1963).
 38. N. Laurance and J. Lambe, "Quadrupole Interactions of Vanadium and Manganese in Corundum", Phys. Rev. 132, 1029, Nov., 1963.
 39. C.D. Watkins and J.W. Corbett, "Defects in Irradiated Silicon (III) EPR and ENDOR of the Si-E Center", Phys. Rev. 134, A 1359 (1964).
 40. I. Chen, C. Kikuchi and H. Watanabe, "Superhyperfine Structures in ESR and ENDOR of Cubic CdTs: Mn²⁺", J. Chem. Phys. 42, 189 (1965).
-

41. James S. Hyde, "ENDOR of Free Radicals in Solution," J. Chem. Phys. 43, 1806 (1965).
42. P.R. Locher and S. Geschwind, "Electron Nuclear Double Resonance of Fe⁵⁷ in MgO", Phys. Rev. 139, A 991, August, 1965.
43. U. Ranon and James S. Hyde, "Electron-Nuclear-Double-Resonance and Electron-Paramagnetic-Resonance Analysis of Ytterbium-Fluorine Superhyperfine Interaction in CaFe³⁺", Phys. Rev. 141, 259 (1966).
44. J.J. Krebs and J. Lambe and N. Laurance, "Electron-Nuclear Double Resonance of Mn²⁺ in Al₂O₃", Phys. Rev. 141, 425 (1966).
45. J.L. Horner, "The Role of Cross Relaxation in the Extra ENDOR Spectrum of Vanadium in Tutton Salt Crystal", Ph.D. Dissertation, Univ. of Mich., 1967.
46. A. Abragam, The Principles of Nuclear Magnetism, Oxford at the Clarendon Press, 1961, p. 133: spin temperature.
47. M.H.L. Pryce, "A Modified Perturbation Procedure for a Problem in Paramagnetism", Proc. Phys. Soc. A 63, 25 (1950).
48. A. Abragam and M.H.L. Pryce, "Theory of the Nuclear Hyperfine Structure of Paramagnetic Resonance Spectra in Crystals", Proc. Roy. Soc. (London) A 205, 135 (1951).
49. J.H. Van Vleck, "Theory of the Variations in Paramagnetic Anisotropy Among Different Salts of Iron Group", Phys. Rev. 41, 208, July 15, 1932.
50. R. Schlapp and W.G. Penny, "Influence of Crystalline Fields on the Susceptibilities of Salts of Paramagnetic Ions. II. The Iron Group, Especially Ni, Cr and Co", Phys. Rev. 42, 666, Dec. 1, 1932.
51. K.W.H. Stevens, "Matrix Element and Operator Equivalents Connected with the Magnetic Properties of Rare Earth Ions", Proc. Phys. Soc. A 65, 209 (1952).
52. R.J. Elliott and K.W.H. Stevens, "The Theory of Magnetic Resonance Experiments on Salts of the Rare Earths", Proc. Roy. Soc. A 218, 553 (1953).
53. B.R. Judd, "Operator Equivalents and Matrix Elements for the Excited States of Rare Earth Ions", Proc. Roy. Soc. A 227, 552 (1955).

54. R.J. Elliott and K.W.H. Stevens, "The Theory of the Magnetic Properties of Rare Earth Salts: Cerium Ethyl Sulphate", Proc. Roy. Soc. A 215, 437 (1952).
55. R.J. Elliott and K.W.H. Stevens, "The Magnetic Properties of Certain Rare-Earth Ethyl Sulphates," Proc. Roy. Soc. A 219, 387 (1953).
56. J.H. Van Vleck, "Valence Strength and the Magnetism of Complex Salts," J. Chem. Phys. 3, 807 (1935).
57. K.W.H. Stevens, "On the Magnetic Properties of Covalent XY_6 Complexes", Proc. Roy. Soc. A 219, 542 (1953).
58. J. Owen, "The Colours and Magnetic Properties of Hydrated Iron Group Salts and Evidence for Covalent Bonding," Proc. Roy. Soc. A 227, 183 (1955).
59. Robert H. Borcherts, "An EPR Investigation of VO^{+2} and x-ray Produced V^{+2} in Tutton Salt", Ph.D. thesis, Univ. of Mich., 1963, or J. Chem. Phys. 40, 2270 (1964).
60. R.H. Borcherts, Private Communication.
61. C. Kikuchi, "Theory of Forbidden EPR Spectrum" unpublished, University of Michigan, 1968.
62. B. Bleaney, "Hyperfine Structure in Paramagnetic Salts and Nuclear Alignment", Philosophical Magazine, 42, 441 (1951).
63. Jack M. Hirshon and George K. Fraenkel, "Recording High-Sensitivity Paramagnetic Resonance Spectrometer", Rev. Sci. Instr. 26, 34, (1955).
64. G. Feher, "Sensitivity Considerations in Microwave Paramagnetic Resonance Absorption Techniques", Bell System Tech. J. 36, 449 (1957).
65. J.C.M. Henning, "Homodyne Balanced Mixer Electron Spin Resonance Spectrometer", Rev. Sci. Instr. 32, 35 (1961).
66. Bell Laboratory Staff, Radar Systems and Components, D. Van Nostrand Company, New York, 1949, especially the paper by J.P. Kinzer and I.G. Wilson, "Some Results on Cylindrical Resonators", and the bibliography with this paper; or I.G. Wilson, C.W. Schramm and J.P. Kinzer, "High Q Resonant Cavities for Microwave Testing", Bell System Tech. J. 25 408, (1946); and J.P. Kinzer and I.G. Wilson, "End Plate and Side Wall Currents in Circular Cylinder Cavity Resonator", Bell System Tech. J. 26, 31 (1947).

67. Robert E. Sheriff, William H. Chambers, and Dudley Williams, "The Nuclear Magnetic Moment of Niobium", *Phys. Rev.* 78, 476, 1950; also *Phys. Rev.* 82, 651, 1951. Also Arnold L. Bloom, "NMR Table, 5th ed." Varian Associates, Palo Alto, Calif., 1965.
68. Norman F. Ramsey, Nuclear Moments, John Wiley and Sons, Inc., New York, 1953.
69. R.M. Cotts and W.D. Knight, "Nuclear Resonance of Nb⁹³ in KNbO₃". *Phys. Rev.* 96, 1285, 1954.
70. M.H. Cohen and F. Reif, "Quadrupole Effects in Nuclear Magnetic Resonance Studies of Solids", Solid State Physics, Vol. 5, 321, Academic Press Inc., Publishers, New York, 1957 (a high field study).
71. T.P. Das and E.L. Hahn, "Nuclear Quadrupole Resonance Spectroscopy", Solid State Physics, Supplement 1, Academic Press Inc., Publishers, New York, 1958 (a low field study).
72. R.W. Kedzie, D.H. Lyons and M. Kestigian, "Paramagnetic Resonance of the Fe³⁺ ion in CaWO (Strong Tetragonal Crystal Field)", *Phys. Rev.* 138, A 918, 5 May, 1965.
73. D.R. Speck and F.A. Jenkins, "Preliminary Report on the Quadrupole Moment of Niobium," *Phys. Rev.* 98, 282, 1955.
74. Hisashi Horie and Akito Arima, "Configuration Mixing and Quadrupole Moments of Odd Nuclei", *Phys. Rev.* 99, 778, 1955.
75. R.W. Kedzie and M. Kestigian, "PMR of Nd³⁺ in CaWO₄ - Model for W Site Substitution", *App. Phys. Letters.* 4, 124, 1 April, 1964.
76. C.Y. Huang, Private Communication.
77. C. Kikuchi and R.D. Spence "Microwave Methods in Physics I. Microwave Spectroscopy", *Am. J. Phys.* 17, 288, 1949; Also "Microwave Methods in Physics II. Microwave absorption in Paramagnetic Substances", *Am. J. Phys.* 18, 167, 1950. (Also reprinted in Selected Reprints in NMR and EPR, Chapter II, American Inst. of Physics).
78. Walter M. Walsh, Jr. and Jean Jeener and N. Bloemberger, "Temperature-Dependent Crystal Field and Hyperfine Interactions", *Phys. Rev.* 139, A 1338, 1965.
79. E. Simanek and R. Orbach, "Temperature Dependence of Hyperfine Coupling of S-State Ions in Cubic Environment", *Phys. Rev.* 145, 1966.

80. Jack Rosenthal, Leonard Yarmus and R.H. Bartram, "Hyperfine Coupling Temperature Dependence: Mn^{2+} in CaO and SrO," Phys. Rev. 153, 407, 10 Jan. 1967.
 81. R. Calvo and R. Orbach, "Temperature Dependence of the Hyperfine Coupling of Mn^{2+} in the Oxides: Experimental and Theoretical," Phys. Rev. 164, 284, 10 Dec. 1967.
 82. R.A. Serway, "Hyperfine Coupling Temperature Dependence of Mn^{2+} in CaF_2 ," Physics Letters, 26A, No. 12, 6 May, 1968.
 83. Herbert Goldstein, Classical Mechanics, Addison-Wesley Publishing Company, Inc., London, England, 1950.
-